

SYNTHESIS OF POLYFLUOROACRYLATE EMULSION AND COATINGS FOR HYDROPHOBIC AND ICEPHOBIC APPLICATIONS

By

Tamal Barman, MSc (Advanced Materials), MSc (Chemistry)

Thesis submitted to the University of Nottingham for the degree of Doctor of Philosophy

Abstract

Low surface energy polymeric materials always attract great interest due to their effective non-stick feature when contacting with other materials. Surface roughness in addition to the low surface energy elevates the hydrophobicity of the surface and makes it superhydrophobic. Ice adhesion and formation is one of the major problems for many industries including aerospace, wind energy and transportation. Superhydrophobic surfaces are potentially used for icephobic applications.

In the present work, hydrophobic polyfluoroacrylates (PFAs) were synthesized using styrene, acrylic acid, and heptafluorobutyl acrylate via radical polymerization method. The synthesized PFA emulsions had a relatively low curing temperature (e.g. 80 °C), and different molar ratios of heptafluorobutyl acrylate were used to vary the fluorine content in the polymer. The polymerization is a random co-polymerization process and hence the exact arrangement of the groups cannot be predicted. X-ray photoelectron spectroscopy revealed that the maximum fluorine content in the PFA emulsion can reach up to 34 Wt%. Average ultimate tensile strength of the synthesized polyfluoroacrylate was measured at ~37 MPa which is comparable to that of PTFE ~35 MPa. From chemical analysis by Fourier transform infrared spectroscopy, X-ray photoelectron spectroscopy, and nuclear magnetic resonance, it was found that the synthesized PFA emulsion exhibited co-polymer structure consisting of the three monomer units.

For the study of surface morphology, three different processes were used: anodisation, chemical etching and Cu-nanoparticle deposition. From scanning electron microscopy (SEM) images and 3D profilometer measurement, it had been found that anodistion and chemical etching produced micrometer range surface

roughness and Cu-nanoparticle deposited surfaces had a nanometer range surface roughness. Below 10 °C, anodisation gave relatively uniform surface roughness in the range of 1-2 μm, and with the increase in temperature the surface roughness reached beyond 5 μm. When the aluminium surface was etched with a mixture of hydrochloric acid (HCl) and hydrogen peroxide (H_2O_2), average surface roughness of 1.5-1.8 μm was obtained. When Cu-nanoparticles were deposited, surface roughness reduced to nanometer range of 20-50 nm, but the Cu-nanoparticles tended to agglomerate and hence non uniform surface roughness was obtained. PFA was deposited on the modified surface by mainly spin coating process. The surface roughness of the coating decreased after the deposition of the PFA emulsion.

Hydrophobicity of the coatings was evaluated using water contact angle (WCA) and contact angle hysteresis (CAH). For anodised samples, the WCA and CAH values gradually increased with increasing surface roughness, indicating the decrease in hydrophobicity. Chemical etched surfaces had surface roughness in the range of 1.5 – 2 μm and hence hydrophobicity was almost maintained throughout. For Cu-nanoparticle deposited samples, hydrophobicity was also maintained, evidenced from the average WCA at ~140° and CAH below 10°. The coating erosion test indicated that the lowest coating adhesion was obtained on the nanoparticle deposited surfaces, as the nanoparticles were loosely bound on the substrate surface. Chemically etched hydrophobic surfaces showed the highest erosion resistance.

Ice adhesion strength and de-icing tests showed that anodised samples had the highest ice adhesion as compared to chemically etched and nanoparticle deposited hydrophobic surfaces as the ice anchored in the large cavities on the anodised surfaces. Anodisation also formed a thin layer of Al_2O_3 on the surface which was non conductive and hence de-icing time was higher. For Cu nanoparticle deposited

surfaces the de-icing time was least as the Cu-nanoparticle layer was thermally conductive, and hence when heat was applied on the coating, it can easily remove the ice and increase the efficiency of the coating.

Journal Publications

- **Barman T**., Chen H., Liu J., Yang G., Zhao W., Peng C.,Hou X., (2019) "Synthesis and characterisation of styrene-based polyfluoroacrylate film for hydrophobic/icephobic applications" Thin Solid Films **687** (2019) 137462.
- Liu J ., Wang J ., Memon H ., Fu Y., **Barman T**., Turnbull B., Choi K., Hou X (2019) "Hydrophobic/icephobic coatings based on thermal sprayed metallic layers with subsequent surface functionalization" Surface Coatings and Technology **357** (2019) 267-272.
- Liu J ., Wang J ., Mazzola L ., Memon H ., **Barman T**., Turnbull B., Mingione G ., Choi K., Hou X (2018) " Development and Evaluation of poly(dimethylsiloxane) based composite coatings for icephobic applications" Surface Coatings and Technology Volume **349** (2018) 980-985.
- Chen, H., **Barman, T.** (2018) "Thermo-Calc and DICTRA modelling of the β-phase depletion behaviour in CoNiCrAlY coating alloys at different Al contents." Computational Materials Science **147** (2018) 103-114.

Conferences

- **Barman T**., Chen H and Hou X., Synthesis and characterization of nanocomposite polyfluoroacrylate thin film for hydrophobic/icephobic applications**,** The 25th Joint Annual Conference of the Chinese Society of Chemical Science and Technology in the UK and Society of Chemical Industry's Chinese UK Regional Group (CSCST-SCI) – Manchester, September, 2018, (Best oral presentation prize)
- **Barman T**., Chen H and Hou X., Synthesis and deposition of polyfluoroacrylate film on anodised aluminium surface for hydrophobic applications, Fifth European Conference on Nanofilms (ECNF) – Cranfield, 2018, (Oral presentation)

Acknowledgement

I take this opportunity to profusely thank my supervisors Dr. Xianghui Hou, Dr. Hao Chen, Dr. Junpeng Liu and Prof. Shuguang Li for giving me the opportunity to be the part of the research group and guiding me throughout duration of my PhD research work. Their immense support through these years has helped me put together this PhD thesis. I also, thank The University of Nottingham for providing me Intercampus PhD scholarship for the successful completion of my research work for 3 years and Nanoscale and Microscale Research Centre (nmRC) of the university for all the help and analysis with the experimental work.

I thank The University of Nottingham and Advanced Materials Research Group for providing the necessary infrastructure for completion of my research work and lab technicains of Wolfson building Jason Greaves, Graham Malkinson and Max Mason for their help throughout my PhD work. I also thank the PGR support team which has been extremely cooperative and helpful. My sincere gratitude towards all at the department for providing me an experience at the international standards.

My sincere gratitude to my parents and my sisters for their emotional support during the PhD. Overall, this has been an enriching experience and will always be a memorable one. The exposure gained over this PhD work will boost my career prospects greatly and I look forward to my future endeavours with this invaluable experience.

Contents

1 Introduction 1

1.1 Background 1

1.2 Aims and objectives 4

1.2.1 Aims 4

1.2.2 Objectives 4

2 Literature review 6

2.1 Hydrophobicity and Superhydrophobicity 6

2.1.1 Fundamentals of hydrophobic and superhydrophobic surface 6

2.1.2 Applications of superhydrophobic surfaces 9

2.2 Icephobicity 12

2.2.1 Definition of icephobicity 12

2.2.2 Mechanism of ice formation 12

2.2.3 Anti-icing and de-icing 15

2.2.4 Applications of icephobic surfaces 16

2.3 Relation of surface superhydrophobicity and icephobicity 19

2.4 Surface energy and low surface energy polymers 21

2.4.1 Low surface energy via surface treatment 22

2.4.2 Polymer coatings 27

2.4.3 Polymer synthesis via chain growth and step growth process 34

2.5 Surface morphology 36

2.5.1 Anodisation 37

2.5.2 Chemical Etching 41

2.5.3 Growth of carbon nanotubes on substrate surface 44

2.5.4 Surface modification using nanoparticles 45

2.5.5 Surface modification using functionalised nanoparticles 49

3 Methodologies 52

3.1 Introduction 52

3.2 Raw materials, chemicals and substrates 53

3.2.1 Substrates 53

3.2.2 Chemicals for the synthesis of PFA emulsion 54

3.2.3 Surface modification process 54

3.3 Surface modification for aluminium substrates 54

3.3.1 Preparation of the substrates 54

3.3.2 Anodisation 55

3.3.3 Chemical etching process 60

3.3.4 Surface modification of the nanoparticles before deposition 62

3.3.5 Deposition of Cu nanoparticles on aluminium substrate 63

3.4 Synthesis and curing of Polyfluoroacrylate emulsion 63

3.4.1 Synthesis of polyfluoroacrylate emulsion 63

3.4.2 Preparation of polyfluoroacrylate coatings 64

3.5 Thermogravimetric and Differential Scanning Calorimetric analysis 66

3.6 Microstructural characterization 67

3.6.1 Sample preparation for microstructural characterisation 67

3.6.2 Measurement of surface roughness 67

3.6.3 Imaging and analysis 68

3.6.4 NMR analysis 69

3.6.5 X-ray photoelectron spectroscopy 70

3.6.6 Fourier transform Infrared spectroscopy 72

3.6.7 X-ray Fluoroscence Spectrometer (XRF) 73

3.7 Surface hydrophobicity measurement 74

3.7.1 Water contact angle and Contact angle hysteresis measurement 74

3.7.2 Surface energy measurement 76
3.8 Evaluation of material and coating performance 77
3.8.1 Water impinging tests 77
3.8.2 Tensile test 78
3.9 Ice adhesion tests 79
3.10 De-icing energy efficiency test 80
3.11 Statistical analysis 81
4 Synthesis, mechanism of polymerization and characterization of polymer properties of PFA emulsion 83
4.1 Introduction 83
4.2 Design of the polymer structure 84
4.3 Possible Structure and Reaction Mechanism of Polyfluoroacrylate Polymers 85
4.3.1 Possible structures of the polymers 85
4.4 Characterization of the polymers 87
4.4.1 Thermal Analysis 87
4.4.2 Characterization of different bonds 91
4.4.3 Detection of elements in Polyfluoroacrylate emulsion 97
4.4.4 Comparison of fluorine content in the polyfluoroacrylate emulsion 100
4.4.5 Elemental Analysis of the synthesised PFA emulsion 102
4.5 Mechanical testing for the polymer 104
4.6 Surface energy 105
4.7 Discussion 106
4.7.1 Effect of different fluorine content on the polymer composition 106
4.7.2 Reaction mechanism of the polymer 107
4.7.3 Role of concentration of fluorine in the polymerization process 109
4.7.4 Structure of the PFA polymer 111

4.8 Summary 112

5 Surface treatment of aluminium substrate and the deposition of polymer coating on the treated substrate 114

5.1 Introduction 114

5.2 Surface modification of aluminium substrate 115

5.2.1 Anodisation 115

5.2.2 Chemical etching 120

5.2.3 Deposition of Nanoparticles 124

5.3 Surface roughness study 127

5.3.1 Anodisation 127

5.3.2 Chemical Etching 129

5.3.3 Deposition of nanoparticles 136

5.4 Effect of deposition of polyfluoroacrylate polymer coating on the modified surfaces 138

5.5 Evaluation of coating water erosion resistance 140

5.5.1 PFA coating on anodised aluminium substrate 141

5.5.2 Coatings on chemically etched substrate 142

5.5.3 Coatings on nanoparticle deposited surface 143

5.6 Discussion 144

5.6.1 Comparison of Anodisation and Chemical etching for surface modification 144

5.6.2 Surface morphology of aluminium substrate deposited with Cu-nanoparticles 148

5.6.3 Effect of temperature in chemical etching process 149

5.6.4 Role of treatment time in chemical etching process 150

5.6.5 Influence of concentration of the etching agent 151

5.6.6 Effect of concentration of Cu-nanoparticles on surface roughness 156

5.6.7 Effect of PFA coating on the surface roughness 157

5.6.8 Coating erosion resistance 159

5.7 Summary 160

6 Hydrophobicity and Icephobicity of PFA coatings 163

6.1 Introduction 163

6.2 Characterization of hydrophobicity of the PFA coatings 164

6.2.1 Water contact angle analysis 164

6.2.2 Contact angle hysteresis study 171

6.3 Characterization of icephobicity of the surface 178

6.3.1 Ice adhesion strength analysis 178

6.3.2 De-icing energy evaluation 184

6.4 Discussion 190

6.4.1 Effect of different coating process 190

6.4.2 Comparison of hydrophobicity of different surfaces 192

6.4.3 Comparison of icephobicity of different surfaces 198

6.5 Summary 201

7 Conclusions 204

References 209

List of figures

Figure 2-1. Schematic representation of (a) Young's model [48], (b) Cassie Baxter model [49] and (c) Wenzel model [50] for surface wetting. 6

Figure 2-2. (a) Steady decrease of water contact angle on the hydrophobic i-PP films and (b) oscillatory water contact angle on the superhydrophobic i-PP film [53]. 8

Figure 2-3. Drop-by-drop accumulation and freezing of a growing supercooled water volume on aluminium surface: The time from the onset of deposition is indicated on each frame. (a) First impacted supercooled droplets have merged together to form one major unit. (b) The main drop has grown by the sequential impaction of inkjetted droplets from above and remains all liquid. (c) Frozen drop shortly after the first freezing stage, which rapidly converts the supercooled liquid into a mushy liquid plus ice phase. (d, e) The crystallization front (horizontal dashed line) starts at the liquid−solid contact area and gradually advances upward. (f) Completely frozen drop [23]. 14

Figure 2-4. (a) A framework for classifying recently developed icephobic coatings. (b) Phase diagram for water indicating three different pathways for formation of water-based solid by changes in temperature and/or pressure of water. (i) Vapor–solid desublimation deposition, (ii) vapor–liquid–solid or condensation followed by freezing, and (iii) liquid–solid or freezing [129]. 19

Figure 2-5. Frost formation on a microfabricated superhydrophobic surface. (a) Dry surface with a contact angle (for the flat material) of about 110°. The surface is maintained at −13 °C, and after the start of the experiment, the relative humidity is increased. (b–d) the time gradually increased from 4s to 10s to 36s. Frost formation is observed and occurs everywhere, including the top of the posts, the valleys, and the sides of the posts [98]. 20

Figure 2-6. Schematic diagram of modification of sodium hydroxide (NaOH) etched aluminium surface after treatment with stearic acid [140]. 22

Figure 2-7. SEM image of the aluminium substrate (a) after deposition of copper films at 0.8 V for 10 minutes and (b) after electrochemical modification of the deposited copper films in ethanolic stearic acid solution at 30 V for 30 mins [127]. 23

Figure 2-8. SEM micrograph of prepared films (a) Film prepared from suspension containing only boehmite and (b) Film prepared from a suspension containing boehmite and AACA [142]. 25

Figure 2-9. (a) SEM micrograph image of aluminium alloy substrate after etching and deposition of fluorinated hydrocarbon and (b)Image of a water drop suspended from a syringe needle during contact angle hysteresis measurement on fluorinated-hydrocarbon coated aluminium [145]. 26

Figure 2-10. SEM images of PP-PMMA surface (a) Micelles deposited on a surface cast from DMF solution at a PP-PMMA concentration of $1x10^{-4}$ gmL^{-1} and (b) Micelles aggregates deposited on a surface cast from DMF solution at a PP-PMMA concentration of $5x10^{-2}$ gmL^{-1}[154]. 30

Figure 2-11. Schematic diagram of stepwise procedure of plasma fluorination of polybutadiene coated substrate[155]. 31

Figure 2-12. Schematic diagram of the salinization of silica nanoparticles using FDTS [156]. 32

Figure 2-13. Illustration of steps leading to a polymer in step growth polymerization [166]. 36

Figure 2-14. SEM images of porous aluminium oxide film on substrate surface at electrolyte temperature of (a) 35 °C and (b) 55 °C [169]. 38

Figure 2-15. SEM images of aluminium surface after anodisation with (a) Malic acid [172] and (b) Selenic acid [171]. 40

Figure 2-16. SEM images of aluminium surfaces Polyfluoroalkyltryethoxysilane (PFO) coated and etched with mixed acid solution for (a) 10 s and (b) 20 s [127]. 41

Figure 2-17. (a) ESEM image of ultrathin rf-sputtered Teflon coated aluminium sample etched with 14.8 % HCl for 2.5 min and (b) Change in thickness of aluminium substrates with etching time [144]. 42

Figure 2-18. SEM image of aluminium surface treated with NaOH and fluoroalkyl silane (FAS-17) and inset shows a magnified image as well as a water drop image [145]. 44

Figure 2-19 .SEM images of the Polysiloxanes (POS)/ MWCNTs surfaces annealed at (a) 60 °C, (b) 70 °C, (c) 80 °C and (d) 90 °C for 1 h with different MWCNT activation temperature [122]. 45

Figure 2-20 . SEM images of aluminium substrate surface (a) Poly urethane (TPU) coating only and (b) silica deposited coating only and the insets are corresponding water drop profile[174]. 46

Figure 2-21. SEM images of fluorinated silica nanoparticles of sizes 169 ± 8 nm [5]. ... 48

Figure 2-22. SEM images of ZnO coated aluminium (a) by classical dipping method and (b) by ultrasonication method [138]. 49

Figure 2-23: SEM images of (PAH/PAA) films (a) After single acid treatment and (b) After a combined acid treatment [179]. 51

Figure 3-1. Schematic diagram of the experimental outline of the research. 52

Figure 3-2. Aluminium AA1050 plate samples (a) before electropolishing and (b) after electropolishing..... 55

Figure 3-3. Schematic diagram of anodisation process and the equipments needed for the process. 56

Figure 3-4. The temperature control instrument - Cole Parmer polystat R6LP for sulfuric acid anodisation. 57

Figure 3-5. SDT machine which simultaneously perform TGA and DSC analysis..... 66

Figure 3-6. Schematic of an Interferometric profilometer. 68

Figure 3-7. Spin quantization of the angular momentum of spin 1/2 nuclei [108]. 70

Figure 3-8. Schematic diagram of a X-ray photoelectron spectrometer [186]. 71

Figure 3-9. (a) FTIR instrument and (b) schematic diagram of mechanism of FTIR machine on ATR mode [187]. 73

Figure 3-10. Schematic diagram of mechanism of X-ray Fluoroscence Spectroscopy [188]. 74

Figure 3-11. (a) Water contact angle measurement instrument unit and (b) some important part of the instrument (ejecting tip, high resolution camera and sample bed). 75

Figure 3-12. Schematic diagram of water impinging test setup. 78

Figure 3-13. Schematic diagram of centrifuge ice adhesion test device with rotor driven by a motor in a stainless steel casing. The ice/substrate sample on one end and counterweight on the other end. The rotor was spun at increasing rate until detachment of ice [190]. 80

Figure 3-14. Schematic diagram of de-icing test set-up. 81

Figure 4-1. Possible polymer structures combining styrene, acrylic acid and heptafluorobutyl acrylate (a) co-polymer of Styrene and heptafluoro butyl acrylate, (b) co-polymer of styrene and acrylic acid, (c) co-polymer of styrene acrylic acid and heptafluorobutyl acrylate and (d) co-polymer of acrylic acid and heptafluorobutyl acrylate. The red atoms are oxygen atoms, the yellow is fluorine, the white atom corresponds to the hydrogen atoms while the grey atoms are carbon. 86

Figure 4-2 Variation of mass change (wt%) and heat flow of PFA emulsion (PFA 10.1) with increasing temperature. 87

Figure 4-3.TGA and DSC analysis data for PFA emulsion containing styrene, acrylic acid and heptafluorobutyl acrylate in the molar ratio of (a) 1:1:1 and (b) 1:1:2 respectively. 89

Figure 4-4. FTIR spectrum of heptafluorobutyl acrylate used as one of the raw materials for the synthesis of PFA emulsion. 91

Figure 4-5. Chemical Structure of 1H,1H- Heptafluorobutyl acrylic acid with all different bonds. 91

Figure 4-6. FTIR spectrum of styrene used as one of the raw materials for the synthesis of PFA emulsion. 92

Figure 4-7. Chemical structure of styrene with all different bonds. 93

Figure 4-8. FTIR spectrum of acrylic acid used as one of the raw materials for the synthesis of PFA emulsion. 94

Figure 4-9. Chemical Structure of acrylic acid with all the different bonds present. 94

Figure 4-10.FTIR spectra of PFA emulsion synthesized from 1:1:1 and 1:1:2 molar ratio of styrene, acrylic acid, and heptafluorobutyl acrylate PFA10.1 and PFA 10.2 respectively. 95

Figure 4-11. 1H NMR analysis data for PFA emulsion containing 16.6 wt% of fluorine. 97

Figure 4-12. ^{13}C NMR analysis data for PFA emulsion containing 16.6 wt% of fluorine.. 98

Figure 4-13. ^{19}F NMR analysis data for PFA emulsion containing 16.6 Wt% of fluorine.. 99

Figure 4-14. ^{19}F NMR analysis of (a) PFA10.1 and (b) PFA 10.2. 100

Figure 4-15. (a) ^{19} F NMR analysis of reference polytetrafluoroethylene (PTFE) and chemical structure of tertrafluoroethylene. 101

Figure 4-16. XPS spectra from one area on each sample, showing that all samples are similarly dominated by fluorine (F), oxygen (O), carbon (C) and sulphur (S) peaks. .. 102

Figure 4-17. High-resolution spectra for all PFA samples, key as wide scan in Figure 4-16. 103

Figure 4-18.(a) stress vs strain graph for PFA 10.1 and PFA 10.2 and (b)comparison of average ultimate tensile strength of PFA 10.1, PFA10.2 and PTFE. 104

Figure 4-19.(a) 2D and (b) 3D structures of probable co-polymer of styrene acrylic acid and heptafluorobutyl acrylate containing 1 unit of each. The red atoms are oxygen atoms, the yellow are fluorine, the white atom corresponds to the hydrogen atoms while the grey atoms are carbon. 111

Figure 5-1. ESEM image of surface morphology of untreated aluminium AA1050 sample at 2000x magnification with working distance (WD) 10 spot size 4 and accelerating voltage 20 KV. 115

Figure 5-2. ESEM image of surface morphology of anodised aluminium sample treated with 20.24 wt% sulphuric acid for 45 mins at a temperature of 30 °C(a) current density of 6 x 10^{-4} Acm^{-2} and (b)) current density of 18 x 10^{-4} A/cm^2 at 2000x magnification with working distance (WD) 10 spot size 4 and accelerating voltage 20 KV. 116

Figure 5-3. ESEM image of surface morphology of anodised aluminium sample treated at a current density of 9x10-4 A/cm^2 for 45 mins at ~30 °C (a) with 16.56 wt% sulfuric acidand (b) with 20.24 wt% sulfuric acid at 2000x magnification with working distance (WD) 10 spot size 4 and accelerating voltage 20 KV. 116

Figure 5-4. ESEM image of surface morphology of aluminium samples treated with 20.24 wt % sulfuric acid at a current density 9 x 10^{-4} A/cm^2 for 45 mins(a) at 15 °C and (b) at 50 °C at 2000x magnification with working distance (WD) 10 spot size 4 and accelerating voltage 20 KV. 116

Figure 5-5. ESEM-SE image of surface morphology of aluminium sample treated with 20.24 wt % sulfuric acid at a current density 9 x 10^{-4} A/cm^2 for 90 mins at room temperature. 117

Figure 5-6. ESEM image of surface morphology of aluminium AA1050 samples (a) SH610 at 500x magnification, (b) SH610 at 2000x magnification, (c) SH410 at 500x magnification and (d) SH410 at 200x magnification. In all the cases the accelerating voltage is 20 kV and spot size 4. 119

Figure 5-7. ESEM image of aluminium substrates etched with a mixture of 0.5 M HCl and 0.5 M H_2O_2 (a) Al.50.50.40.20, (b) Al.50.50.40.60, (c) Al.50.50.30.60 and (d) Al.50.50.60.60 with accelerating voltage of 20 kV and spot size 4. 120

Figure 5-8. ESEM image of aluminium substrates etched with a mixture of 1 M HCl and 0.25 M H_2O_2 (a) Al.1.25.40.20, (b) Al.1.25.40.60, (c) Al.1.25.30.60 and (d) Al.1.25.60.60 60 with accelerating voltage of 20 kV and spot size 4. 121

Figure 5-9. . ESEM-SE image of aluminium substrates etched with a mixture of 2 M HCl and 0.1 M H_2O_2 (a) Al.2.10.40.20, (b) Al.1.25.40.60, (c) Al.1.25.30.60 and (d) Al.2.10.60.60 60 with accelerating voltage of 20 kV and spot size 4. 122

Figure 5-10. ESEM-SE image of aluminium substrates etched with a mixture of 2 M HCl and 0.25 M H_2O_2 (a) Al.2.25.40.20, (b) Al.2.25.40.60, (c) Al.2.25.30.60 and (d) Al.2.25.60.60 60 with accelerating voltage of 20 kV and spot size 4. 123

Figure 5-11. ESEM image of aluminium substrates coated with a composite mixture of2 g/L Cu-nanoparticles and synthesized PFA 10.1 emulsion (a) 500x magnification cured at room temperature, (b) 8000x magnification cured at room temperature, (c) 4000x magnification cured at 80 °C and (d) 8000x magnification cured at 80 °C. 124

Figure 5-12. ESEM image of aluminium substrates coated with a composite mixture of 2 g/L Cu-nanopartcles with 0.1 M POTS in synthesized PFA 10.1 emulsion (a) 500x magnification cured at 80 °C, (b) 8000x magnification cured at 80 °C, (c) 4000x magnification cured at 120 °C and (d) 10000x magnification cured at 120 °C. 125

Figure 5-13. 2D model representation of aluminium substrates anodised under optimised conditions with controlled temperature at 10 °C and constant current density of $15x10^{-4}$ A/cm^2 (a) with anodising solution of 300 g/L H_2SO_4 for 40 mins, (b)with anodising solution of 300 g/L H_2SO_4 for 60 mins, (c) with anodising solution of 175 g/L H_2SO_4 for 40 mins, (d) with anodising solution of 175 g/L H_2SO_4 for 60 mins, (e) with anodising solution of 131 g/L H_2SO_4 for 40 mins and (f) with anodising solution of 131 g/L H_2SO_4 for 60 mins..... 127

Figure 5-14. 2D model representation surface roughness of aluminium substrates etched with a solution of 0.5 M HCl and 0.5 M H_2O_2 (a) treatment time 20 mins and temperature 40 °C, (b) treatment time 60 mins and temperature 40 °C, (c) treatment time 60 mins and temperature 30 °C and (d) treatment time 60 mins and temperature 60 °C..... 129

Figure 5-15. 2D model representation surface roughness of aluminium substrates etched with a solution of 2 M HCl and 0.1 M H_2O_2 (a) treatment time 20 mins and temperature 40 °C, (b) treatment time 60 mins and temperature 40 °C, (c) treatment time 60 mins and temperature 30 °C and (d) treatment time 60 mins and temperature 60 °C. 130

Figure 5-16. 2D model representation surface roughness of aluminium substrates etched with a solution of 2 M HCl and 0.5 M H_2O_2 (a) treatment time 20 mins and temperature

40 °C, (b) treatment time 60 mins and temperature 40 °C, (c) treatment time 60 mins and temperature 30 °C and (d) treatment time 60 mins and temperature 60 °C. 132

Figure 5-17. . 2D model representation surface roughness of aluminium substrates etched with a solution of 1 M HCl and 0.25 M H_2O_2 (a) treatment time 20 mins and temperature 40 °C, (b) treatment time 60 mins and temperature 40 °C, (c) treatment time 60 mins and temperature 30 °C and (d) treatment time 60 mins and temperature 60 °C..... 133

Figure 5-18. 2D model representation surface roughness of aluminium substrates etched with a solution of 2 M HCl and 0.25 M H_2O_2 (a) treatment time 20 mins and temperature 40 °C, (b) treatment time 60 mins and temperature 40 °C, (c) treatment time 60 mins and temperature 30 °C and (d) treatment time 60 mins and temperature 60 °C. 134

Figure 5-19. 3D model representation surface roughness of aluminium substrates deposited with Cu-nanoparticles in PFA 10.1 emulsion containing (a) 4 g/L Cu-nanoparticles and (b) 2 g/L Cu-nanoparticle solution. 136

Figure 5-20. Variation of PFA coating thickness with surface roughness for different surface modification processes (a) anodising, (b) chemical etching and (c) nanoparticle deposition, coated with PFA10.1 emulsion by spin coating process and cured at 80 °C. 140

Figure 5-21. Variation of water contact angle on anodised aluminium surface coated with polyfluoroacrylate emulsion containing various concentrations of fluorine after the water impinging test..... 141

Figure 5-22. Variation of water contact angle on chemically etched aluminium surface coated with polyfluoroacrylate emulsion containing various concentrations of fluorine after the water impinging test..... 142

Figure 5-23. Variation of water contact angle on Cu-nanoparticle deposited aluminium surface coated with polyfluoroacrylate emulsion containing various concentrations of fluorine after the water impinging test. 143

Figure 5-24. SEM image of surface morphology aluminium substrates (a) Anodised with a 175 g/L solution of H_2SO_4 with a current density of 15×10^{-4} Acm^{-2} under 10 °C for 40 mins and (b) Chemically etched with a 2 M HCl and 0.25 M H_2O_2 solution at 40 °C for 60 mins..... 145

Figure 5-25. SEM image of surface morphology of aluminium substrate anodised (a) with 175 g/L H_2SO_4 solution at 10 °C for 60 mins, (b) 175 g/L H_2SO_4 solution at 10 °C for 40 mins, (c) 300 g/L H_2SO_4 solution at 10 °C for 60 mins and (d) 300 g/L H_2SO_4 solution at 40 °C for 60 mins..... 146

Figure 5-26. Comparison of surface roughness for aluminium substrates treated with anodisation, chemical etching and Cu-nanoparticle deposition..... 148

Figure 5-27. Variation of average surface roughness with treatment temperature of chemically etched aluminium surfaces with with a 1 M solution of HCl and 0.5 M solution of H_2O_2 and at a constant etching time of 60 mins..... 149

Figure 5-28. Variation of surface roughness with etching duration of chemically etched aluminium surfaces with 1 M HCl and 0.5 M H_2O_2 at constant temperature of 40 °C. . 150

Figure 5-29. Variation of surface roughness of chemically etched aluminium surface with different concentration of HCl at constant 0.50 M concentration of H_2O_2 at 40 °C for 60 mins. 153

Figure 5-30. Variation of surface roughness of chemically etched aluminium surface with different concentration of H_2O_2 at constant 1 M concentration of HCl at 40 °C for 60 mins. 155

Figure 5-31. Variation of surface roughness of Cu-nanoparticle deposited aluminium surface with different concentration of Cu-nanoparticles deposited by spin coating process at a constant speed of 500 rpm for 1 min. 156

Figure 5-32. Surface roughness before and after PFA polymer coating on (a) anodised, (b) chemical etched and (c) nanoparticle deposited surfaces. 158

Figure 5-33. Decrease in weight percent of the coatings after the water impinging test for anodised, chemical etched and nanoparticle deposited substrates as a function of change in concentration of fluorine in the PFA emulsion. 159

Figure 6-1. Water contact angle with varied surface roughness for coating sample with a polyfluoroacrylate emulsion containing 1:1:1 molar ratio of styrene, acrylic acid and heptafluorobutyl acrylate on anodised aluminium. 164

Figure 6-2. Schemsatic diagram of water droplet on anodised aluminium surface coated with a thin layer of polyfluoroacrylate emulsion containing 1:1:1 molar ratio of styrene acrylic acid and heptafluorobutylacrlate and a surface roughness of (a) 1.5 to 3 μm and (b) 3.5 – 6 μm. 165

Figure 6-3. Average water contact angles with varied molar concentration of fluorine in polyfluoroacrylate emulsion coated on anodised aluminium surfaces with surface roughness ranging from 1.45 to 1.6 μm. 166

Figure 6-4. Average water contact angle on coating with polyfluoroacrylate emulsion containing 1:1:1 molar solution of styrene acrylic acid and heptafluorobutylacrylate on aluminium substrates etched with a solution containing HCl and H_2O_2. 167

Figure 6-5. Average water contact angle of polyfluoroacrylate coatings with various concentration of heptafluoroacrylate on aluminium substrates after etched with a solution containing 2 M HCl and 0.50 M H2O2 at 60 °C for 30 mins. 168

Figure 6-6. Average water contact angle on coating with polyfluoroacrylate emulsion containing 1:1:1 molar solution of styrene acrylic acid and heptafluorobutylacrylate on aluminium substrates and various wt % of Cu-nanoparticle solution. 169

Figure 6-7. Average water contact angle on coating with polyfluoroacrylate emulsion containing 1:1molar solution of styrene acrylic acid and various molar ratio of heptafluorobutylacrylate on aluminium substrates and 2 wt% of Cu-nanoparticle solution. 170

Figure 6-8. Variation of contact angle hysteresis of coating based on polyfluoroacrylate emulsion containing 1:1:1 molar ratio of styrene, acrylic acid and heptafluorobutyl acrylate on anodised aluminium substrates as a function of average surface roughness. 171

Figure 6-9. Variation of contact angle hysteresis of coating based on polyfluoroacrylate emulsion as a function of concentration of heptafluorobutyl acrylate with concentration of styrene and acrylic acid fixed at 1:1 molar ratio on anodised aluminium samples. 172

Figure 6-10. Variation of contact angle hysteresis of coating based on polyfluoroacrylate emulsion containing 1:1:1 molar ratio of styrene, acrylic acid and heptafluorobutyl acrylate on etched aluminium substrates as a function of average surface roughness. 173

Figure 6-11. Variation of contact angle hysteresis of PFA based coating on chemically etched aluminium substrates as a function of concentration of heptafluorobutyl acrylate. 175

Figure 6-12. Variation of contact angle hysteresis of coating based on polyfluoroacrylate emulsion containing 1:1:1 molar ratio of styrene, acrylic acid and heptafluorobutyl acrylate on nanoparticle deposited aluminium substrates as a function of average surface roughness. 176

Figure 6-13. Variation of contact angle hysteresis of PFA based coating on nanoparticle deposited aluminium substrates as a function of concentration of heptafluorobutyl acrylate. 177

Figure 6-14. Variation of ice adhesion strength and shear force on anodised aluminium surface coated with a PFA emulsion containing 1:1:1 molar ratio of styrene, acrylic acid and heptafluorobutyl acrylate as a function of surface roughness. 178

Figure 6-15. Variation of ice adhesion strength and shear force on anodised aluminium surface coated with a PFA emulsion containing various concentrations of fluorine and surface roughness ranging from 2 to 3.5 μm. 179

Figure 6-16. Variation of ice adhesion strength and shear force on chemically etched aluminium surface coated with a PFA emulsion containing 1:1:1 molar ratio of styrene, acrylic acid and heptafluorobutyl acrylate as a function of surface roughness. 180

Figure 6-17. Variation of ice adhesion strength and shear force on chemically etched aluminium surface coated with a PFA emulsion containing various concentrations of fluorine and surface roughness ranging from 1.8 to 1.85 μm. 181

Figure 6-18. Variation of ice adhesion strength on Cu-nanopaticle deposited aluminium surface coated with a PFA emulsion containing 1:1:1 molar ratio of styrene, acrylic acid and heptafluorobutyl acrylate as a function of surface roughness. 182

Figure 6-19. Variation of ice adhesion strength on Cu-nanoparticle deposited aluminium surface coated with a PFA emulsion containing various concentrations of fluorine and surface roughness ranging from 40-45 nm. 183

Figure 6-20. Variation of de-icing time for anodised aluminium substrates coated with a PFA emulsion containing 1:1:1 molar ratio of styrene, acrylic acid and heptafluorobutyl acrylate as a function of surface roughness. 184

Figure 6-21. Variation of de-icing time for anodised aluminium substrates coated with a PFA emulsion containing 1:1 molar ratio of styrene, acrylic acid and various concentrations of heptafluorobutyl acrylate with surface roughness ranging from 1.6 to 1.85 μm. 185

Figure 6-22. Variation of de-icing time for chemically etched aluminium substrates coated with a PFA emulsion containing 1:1:1 molar ratio of styrene, acrylic acid and heptafluorobutyl acrylate as a function of surface roughness. 186

Figure 6-23. Variation of de-icing time for chemically etched substrates coated with a PFA emulsion containing 1:1 molar ratio of styrene, acrylic acid and various concentrations of heptafluorobutyl acrylate with surface roughness ranging from 1.6 to 1.7 μm..... 187

Figure 6-24. Variation of de-icing time for nanoparticle deposited aluminium substrates coated with a PFA emulsion containing 1:1:1 molar ratio of styrene, acrylic acid and heptafluorobutyl acrylate as a function of surface roughness. 188

Figure 6-25. Variation of de-icing time for nanoparticle deposited samples coated with a PFA emulsion containing 1:1 molar ratio of styrene, acrylic acid and various concentrations of heptafluorobutyl acrylate with surface roughness ranging 40 to 50 nm. 189

Figure 6-26. Compared between spin, dip and spray coated aluminium substrates (a) static water contact angle and contact angle hysteresis measurement and (b) contact angle before and after water impinging test and loss in weight for the polymer coating. 191

Figure 6-27. Comparison of static water contact angle for anodised and chemically etched aluminium substrates (a) with variation of surface roughness and (b) with variation of concentration of fluorine in the deposited PFA emulsion. 194

Figure 6-28. Comparison of water contact angle hysteresis for anodised and chemical etched aluminium substrates (a) with variation of surface roughness and (b) with variation of concentration of fluorine in the deposited PFA emulsion. 196

Figure 6-29. Comparison of Ice adhesion strength for anodised and chemically etched aluminium substrates (a) with variation in surface roughness and (b) with variation in fluorine content in the PFA emulsion. 198

Figure 6-30. Comparison of de-icing time for anodised and chemically etched aluminium substrates (a) with variation in surface roughness and (b) with variation in fluorine content in the PFA emulsion. 200

Nomenclature

^{1}H Hydrogen

^{13}C carbon

^{19}F Fluorine

Al Aluminium

Al_2O_3 aluminium oxide

Ar Argon

CH_4 methane

C_2F_6 hexafluoroethane

C_2H_5OH ethanol

Cu Copper

$(COOH)_2$ oxalic acid

C_8H_8 styrene

$C_3H_4O_2$ acrylic acid

$C_7H_5F_7O_2$ heptafluorobutyl acrylate

Fe Iron

HBA heptafluorbutylacrylate

HCl Hydrocholric acid

HMDS hexamethyldisilazane

H_2CrO_4 chromoic acid

H_3PO_4 phosphoric acid

$HClO_4$ perchloric acid

H_2O_2 Hydrogen peroxide

H_2SO_4 sulfuric acid

KPS potassium persulfate

Mn Manganese

Mg Magnesium

OH hydroxy group

Pt platinum

POTS 1H,1H,2H,2H-perfluorooctyltriethoxysilane

PTFE polytetrafluoroethylene

PFPE polyfluoropolyether

Si Silicon

SDS sodium dodecyl sufate

TEOS Triethylorthosilicate

Ti Titanium

THF tetra hydrofuran

Zn Zinc

Abbreviations

γ_s^{disp} dispersion component of surface free energy

γ_s^{pol} polar component of solid surface free energy

τ shear stress

A ice/substrate contact area

F Force

K_a reaction rate constant for forward reaction

K_b reaction rate constant for backward reaction

K_c dissociation rate constant

m mass

R_a Surface roughness

r rotor length

w speed of rotation at detachment

ATR Attenuated total reflection

BSE Back scattered electrons

CAH Contact angle hysteresis

DSC Differential scanning calorimetry

EDX Energy dispersive X-ray

FTIR Fourier transform infrared spectroscopy

NMR Nuclear magnetic resonance

PFA Polyfluoroacrylate emulsion

SEM Scanning electron microscopy

SE Secondary electrons

WCA Water contact angle

XPS X-ray photo electron spectroscopy

1 Introduction

1.1 Background

Hydrophobic surfaces are widely employed in several industries including aerospace, automotive, powerlines, oil and gas, building industries due to their excellent anti-corrosion water repellence and self-cleaning properties [1-3]. Hydrophobicity is a natural phenomenon of a surface to repel water contact. The water contact angle ranges between 90° and 150°. It is generally recognised that the modification of surface profiles followed by deposition of low surface energy materials are effective in achieving hydrophobic surfaces [4, 5]. Superhydrophobic surface with water contact angle higher than 150° are of much interest as they inhibit phenomenon like sticking of water, contamination, oxidation and current conduction etc [6]. Hydrophobity and superhydrophobicity is a natural phenomenon and can be found in different plants and insects. Ramee leaf, chinese watermelon, taro plant leaf, leymus arenarius leaf shows superhydrophobicity and water contact angle ranging between 160-170° [7, 8]. Insects such as homoptera, water striders and diptera tabanus chrysurus also shows natural superhydrophobicity [9, 10].

Whereas icephobicity is relatively new phenomenon and analogous to the other "-phobicities" (hydrophobicity, oleophobicity, lipophobicity, omniphobicity etc). There are mainly three definitions of icephobicity. Firstly, icephobicity implies low adhesion force between ice and a solid surface with shear stress between 150 kPa and 500 kPa. It can go as low as 15.6 kPa [11, 12]. Secondly, icephobicity is also defined as the ability to prevent ice formation on the surface. Such ability depends on whether a droplet of supercooled water (below the normal freezing temperature of 0°C) freezes at the interface and characterized by time delay of heterogeneous ice nucleation [13, 14]. Thirdly, icephobic surface repels incoming small water

droplets at below freezing point temperatures [15]. It is very important especially for aviation industries as it leads to catastrophic aviation disasters [16, 17]. The ice protection systems currently used are based on electro-thermal systems that operate once the ice has been formed (de-icing): they melt the ice layer in contact with the solid surface and allow ice removal by aerodynamic forces. However, these methods present several drawbacks: for instance, such systems usually cover only the leading edge of the blade where ice accretes, leading to the potential formation of the so-called "runback ice", caused by liquid water flowing in the aft direction [18]. In addition, these systems operate cyclically (to avoid huge power consumption) allowing ice to accrete up to a thickness of several millimetres prior to removal. Finally, they require heavy devices, as well as high power inputs and generate large quantities of heat which is inappropriate for currently used polymer-based top coat materials [19].

So universal definition of icephobicity is a difficult task and debate always remained whether hydrophobic and superhydrophobic surfaces are best for anti-icing or de-icing applications. Many in depth studies have been conducted to establish the relation between the two [20-23]. Hydrophobic surfaces show higher resistance against icing as compare to hydrophilic surfaces . Again hydrophilic surface with low roughness (1.4-6 nm) shows greater freezing delay time as compared to high roughness hydrophobic surface. The performance of icephobicity degrades with icing and de-icing cycle [24]. Various aspects of anti-icing behavior of superhydrophobic coatings was investigated, including ice inhibition, ice adhesion, ice accumulation and frost formation. Inhibition of ice formation on superhydrophobic coatings was observed when supercooled water was poured onto a tilted surfaces [25]. It is found that superhydrophobic coatings greatly retard water freezing [26] on the surface. The ice adhesion strength of superhydrophobic coating surface is 3.5 times lower than that of an uncoated surface [27]. It is proved that superhydrophobic coatings could significantly restrain ice accumulation

on insulator strings [28] and retarded frost formation on the superhydrophobic isotactic polypropylene film is also observed [29]. A highly ordered superhydrophobic coating is also designed which can maintain ice-free down to −25 to −30 °C [30].

Aluminium and its alloys are most common structural materials due to low density, high strength and light weight as compared to other metal alloys [31]. To achieve the superhydrophobicity two main aspects are necessary : surface morphology and low surface energy. Anodisation is an effective method to modify the surface morphology for required surface profile but it is highly dependent on the temperature. Sulfuric acid anodisation also commonly known as hard anodisation is used for modifying the aluminium surface [32, 33]. Another way to produce surface morphology is chemical etching process. A mixture of hydrochloric acid (HCl) and hydrogen peroxide (H_2O_2) was used for the purpose. The deposition of nanoparticles on the substrate surface can produce desired surface morphology. Again low surface energy is another important factor to achieve surface hydrophobicity or icephobicity and the most common method is to deposit thin fluorinated polymer on substrate surface [34-36]. Polyurethane is one of the most commonly utilized polymer in different industrial applications, including coatings. [37, 38]. 1H,1H,2H,2H-perfluorooctyltriethoxysilane (POTS) is another widely used fluorinated polymer for low energy applications [39]. Polycarbonate coated superhydrophobic surface led to a significant decrease in ice-adhesion strength for aluminium samples as compared to the untreated reference [40]. A sol-gel coating of methyl triethoxysilane (MTEOS) and 3 –glycidyloxypropyl triethoxy silane (GLYMO) was reported to obtain a robust icephobic coating with water contact angle (WCA) as high as 163.5 ° and ice adhesion strength is lowered by 40% [41]. Self-assembling monolayers produced by varying hydrophobic components had also been used for icephobic application [42]. It was reported that the water contact angle on a micro-structured Poly(tetrafluoroethylene) (PTFE) coated

surface can be as high as 164° with contact angle hysteresis (CAH) of 2.5° [43]. And a polydimethylsiloxane (PDMS) based surface exhibited a water contact angle of 160° [44]. Besides, slippery liquid-infused porous surfaces were developed recently and have shown encouraging icephobic properties [40]. However, low mechanical properties of the coating materials, high processing temperature (e.g. 327 °C melting temperature of PTFE [45]) and usage of lubricating liquid on the surface are the key challenges for their applications. The combination of surface roughness and surface energy alters the hydrophobicity and icephobicity of the substrate.

1.2 Aims and objectives

1.2.1 Aims

The main aim of this project is to develop a new type of polymer coating that will be hydrophobic in nature and eventually can be applied for icephobic applications. The polymer can also be applied in coating form with proper surface morphology for superhydrophobic applications. For superhydrophobic and icephobic applications high water contact angle (WCA) is required as well as low contact angle hysteresis (CAH). The main factors affecting the WCA and CAH will be determined. The mechanical strength and water erosion resistance of the coating will also be evaluated. The synthesis mechanism of the low surface energy organic emulsion will be established. Ice adhesion strength of the coated substrate surface will also be determined. The icephobicty of the studied hydrophobic and superhydrophobic surface will be compared and discussed.

1.2.2 Objectives

The main objectives required to achieve the above goals are proposed as follows,

- Formation of micro and nanostructured roughness on the substrate surface. To obtain specific surface features, different processes are will be used like anodisation, chemical etching and deposition of nanoparticles etc. The parameters for these processes will also be optimised to obtain the desired result.
- Low surface energy polymer matrix will be synthesised. The structure, stability and other parameters of the polymer will also be evaluated. The properties of the polymer will be tailored by altering amount of the monomers. The synthesis mechanism of the polymer will be studied as well. The surface energy of the synthesised polymer will be evaluated.
- To deposit thin polymer coating on the substrate surface by various methods and to determine the most efficient method for the deposition. The physical and chemical properties of the coating will be studied.
- Microstructural characterisation of the surface is also very important to evaluate the surface morphology. Surface morphology will be analysed at different processing condition and the difference between different surface morphology will be compared.
- Erosion resistance of the polymer film will be determined and the effect of polymer film on the surface roughness will be discussed. The tensile strength of the polymer will be determined and also be compared with that of commonly used PTFE.
- The hydrophobicity will be measured by water contact angle (WCA) and contact angle hysteresis (CAH) data. The factors influencing the hydrophobicity of the surface will be analysed and optimised.
- The icephobicity of the surface will be measured and the influence of microstructure and surface energy on icephobicity will be discussed. The best condition of surface roughness and surface energy for icephobicity will also be determined.
- The comparison of hydrophobic and superhydrophobic surface and their suitability to be used as icephobic surface will be conducted in terms of ice adhesion strength and de-icing time tests.

2 Literature review

2.1 Hydrophobicity and Superhydrophobicity

2.1.1 Fundamentals of hydrophobic and superhydrophobic surface

Hydrophobicity or superhydrophobicity is a property of any surface to repel incoming water molecules. It is generally quantified by the water contact angle (WCA) and contact angle hysteresis (CAH) measurement. When a WCA is greater than 90 ° but less than 150 °, the surface is considered to be hydrophobic. Alternatively, if a WCA is greater than 150 ° and CAH is less than 10 °, the surface is considered as superhydrophobic [46].

WCA is defined as the angle at which the liquid vapour interface meets on a solid surface, when the liquid is water. It is determined by the interactions across the three phase line. The Young equation is the simplest way to describe the balance forces acting on a liquid droplet spreading on a surface [47].

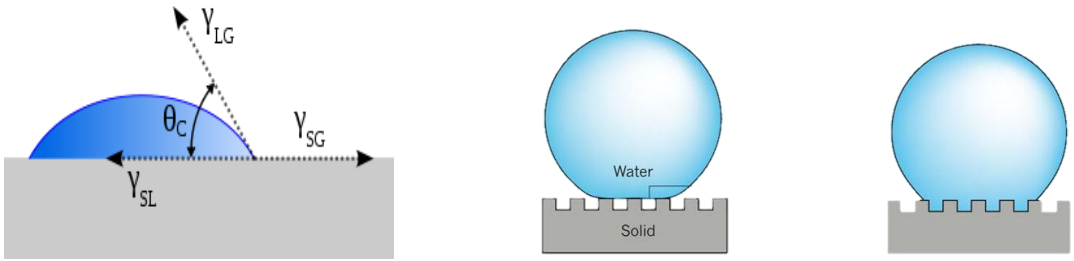


Figure 2-1. Schematic representation of (a) Young's model [48], (b) Cassie Baxter model [49] and (c) Wenzel model [50] for surface wetting.

Figure 2-1 (a) represents the Young's model of surface wetting. Where θ is the contact angle of the drop and is related to interfacial energies acting between solid-gas (γ_{SG}), liquid gas (γ_{LG}) and solid-liquid (γ_{SL}) interfaces [47].

$$\cos\theta = \frac{\gamma_{SG} - \gamma_{SL}}{\gamma_{LG}}$$ Equation 2-1

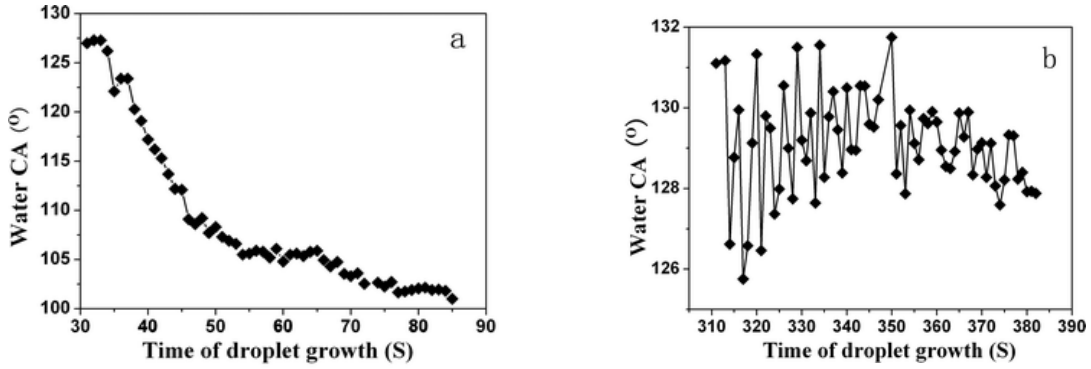
But Young Equation is only valid when the surface is smooth, chemically homogeneous and does not change by possible interactions with the probing liquid. For superhydrophobicity roughness is an essential requirement, so for rough surfaces Wenzel proposed a model with contact angle (θ') and the equation is given as follows [50]:

$$\cos(\theta') = \frac{r(\gamma_{SG} - \gamma_{SL})}{\gamma_{LG}} = r\cos\theta$$ Equation 2-2

Where r is the roughness factor and defined as the ratio of actual area of the rough surface to the geometric projected area. r is always greater than unity so it enhances hydrophilicity for a hydrophilic surface and hydrophobicity for a hydrophobic surface.

Frost formation was investigated on isopolypropylene (i-PP) deposited hydrophobic and superhydrophobic surfaces. It is also found frost formation is also retarded superhydrophobic i-PP surface as compared to hydrophobic surface. The main reason is wettability of superhydrophobic surface oscillates during the frost formation process while that for hydrophobic surface it steadily increases. The oscillation for superhydrophobic surface is due to the micro and nanostructures which prevents the movement of the three phase line (TPL). For hydrophobic surface TPL of condensed water droplet is unstable. The contact angle hysteresis (CAH) depends on TPL. TPL plays an important role in the stability of the water droplet and water contact angle [51, 52]. The solidification of the water droplet starts at the TPL. Higher the heat transfer rate at the TPL easier is the solidification.

If TPL is unstable then it can freeze easily. If the TPL is discontinuous for rough surface structure then it is metastable which is favourable for anti-freezing as compare to the unstable TPL [53].



(a) (b)

Figure 2-2. (a) Steady decrease of water contact angle on the hydrophobic i-PP films and (b) oscillatory water contact angle on the superhydrophobic i-PP film [53].

Figure 2-2 shows the variation of water contact angle with the time of droplet growth in seconds. It is clear from Figure 2-2 (a) that for hydrophobic surface the water contact angle decreases in a steady manner with the time of droplet growth while in the case of superhydrophobic surface the water contact angle oscillates with the increase in time of growth of the droplet as shown in Figure 2-2 (b).

Icephobic properties of a superhydrophobic surface decline as icing/deicing cycles process proceeds. The main reason is the loss of rough surface morphology which is essential for icephobicity [24]. But only rough surface structure is not sufficient for superhydrophobic property. The cavities on the surface could be wetted by moisture from the environment and upon freezing the condensed water in the cavities can turn into ice roots to anchor the ice layer into rough surface. Thus as a result ice-adhesion will increase with increasing surface roughness [54].

2.1.2 Applications of superhydrophobic surfaces

Superhydrophobic surfaces have many functional applications. It is used to improve the performance of conventional materials by surface modification, additionally superhydrophobic modifications can bring new functions which are not available to the material itself.

(I) Water corrosion prevention

The corrosion of metals is a significant problem and can be eliminated by fabrication of superhydrophobic coating. Layered double hydroxides (LDHs) with addition of a low surface energy material can be used for such preventative applications [55]. When polished copper surfaces are immersed into n-tetradecanoic acid ethanol solution a superhydrophoobic copper cluster surface can be obtained [56]. Again superhydrophobic corrosion resistant Magnesium (Mg) alloy surface can be fabricated by a combination of electrochemical machining process followed by covering with fluoroalkyl silane (FAS) layer [57] .

(II) Humidity proof coating of electronic devices

Excellent water repellency property of superhydrophobic coating can be used as waterproof coatings of some moisture-sensitive electronic devices. Commercially available paraffin wax-polyolefin thermoplastic blend with carbon nanofibers can produce thin superhydrophobic film on electronic devices [58]. Again when thin fluoropolymer superhydrophobic coating was fabricated on the surface of field effective transistor by violet photochemical process the surface discharge caused by the leakage current even at high relative humidity is eliminated [59].

(III) Textiles

Superhydrophobic textile fabrics can be prepared by a simple one step gas phase coating procedure in which a layer of polymethylsilsesquioxane nanofilaments was

grown onto the individual textile fibers. Because of the unique surface geometry generated by the nanoscopic fibrous coating on microscopic fibrous textiles the coated fabrics remains dry even after two months of complete immersion in water [60]. Modification of fibers with silver (Ag) nanoparticles followed by treatment with hexadecyltrimethoxysilane produces superhydrophobic coating that has antibacterial activity against gram-negative bacteria, escherichia coli [61].

(IV) Anti-biofouling

Bio-fouling indicates the undesirable adherence of microorganisms, plants, algae and animals on submerged surfaces. Bacterial biofilms on surfaces produce adverse impacts for pipeline corrosion, water contamination, and hospital associated infections etc [62-65]. Superhydrophobic surfaces can reduce bacterial adhesion significantly and hence can be used for anti-biofouling applications [66, 67]. These surfaces are effective for both, employing continuous flow of bacterial suspension over the superhydrophobic surface as well as when immersed in a static bacterial suspension for various periods of time [68-70]. For superhydrophobic surface air bubbles are physically entrapped when immersed in a bacterial suspension. The contact area between the superhydrophobic surface and bacteria decreases resulting significant decrease in number of adherent bacteria [71].

(V) Controlled transportation of fluids

Magnetic nanomaterials conjugating with biomolecules have been widely applied in biochemical separation, targeted drug delivery, immunoassay, biosensor and other fields. There is an increasing need for controlled transport of their small volumes of liquids. For microfluidic systems, delivered materials might be adsorbed on the solid walls due to the nature of the contact, leading to contamination or clogging of channels. Superhydrophobic surfaces with high adhesive force offer particular advantages to completely transport water microdroplets.

Superhydrophobic surfaces, with water contact angles (CAs) larger than 150°, can avoid the wetting problem [72, 73]. A microdroplet on this surface usually takes a quasi-spherical shape and dramatically lowers the contact area between droplet and solid surface, which would help to greatly reduce the possible deposition of liquid. Besides, the strong adhesive feature of the surface can make the microdroplet accurately hold in place without any sliding or rolling. Here, superhydrophobic surface was used for reversibly oriented transport of superparamagnetic microliter-sized liquid droplets with no lost volume in alternating magnetic fields, which is of great significance for the innovative design of open microfluidic devices [74, 75].

(VI) Transparent anti-reflective coating

The covering of a solar cell system is made of glass or plastic which have indices of refraction in the range of 1.45–1.7 [76, 77], so they reflect from 4% to over 6.5% of normally incident light on each air/substrate interface. The transmitted energy of a solar cell system will be lost considerably from multiple reflections. Accordingly, an antireflection (AR) coating on a covering is used to increase the efficiency of a solar cell system [78-81]. After some time, the surfaces of the coverings of a solar cell system in a natural environment become contaminated. Therefore, a self-cleaning coating on the covering helps to increase the efficiency of the solar cell system. Superhydrophobic surfaces with rough micro and nanostructures and low surface energy shows self-cleaning phenomenon. Since the microstructures of a superhydrophobic coating strongly scatter visible light, high transparency in the visible region and the superhydrophobic property are mutually exclusive in principle [82-84]. The transmittance of ZnO-based[85, 86], carbon nanotubes based [87, 88], or BN-based [89] transparent superhydrophobic films is about 80% or even lower. The transmittance of some superhydrophobic anti reflective films is close to that of untreated glass (90.6%) [90-92]. Anti-

reflective coatings with a transmittance of higher than 96% can be obtained on glass substrates by the Layer by layer deposition of polyelectrolytes. Superhydrophobic sol gel was prepared by hydrolyzing triethylorthosilicate (TEOS) and then adding the hydrolyzed TEOS with hexamethyldisilazane (HMDS) [93].

2.2 Icephobicity

2.2.1 Definition of icephobicity

Icephobicity is generally defined as a property of any surface repelling ice formation on it under icing conditions. Common strategy for minimizing ice formation and adhesion is application of chemical coatings which are classified as sacrificial coatings and permanent coatings [94]. These coatings reduce the ice adhesion and ice can shed more easily, with the help of existing forces such as wind, gravity and, vibrations [95]. The superhydrophobic surfaces are hypothesized to be successful in producing anti-icing property by repelling incoming water molecules. In addition the trapped air pockets forms a thermal barrier and hinders the heat transfer during icing and hence reducing ice adhesion strength [96, 97]. But the superhydrophobic surfaces fail at high humidity and ultralow temperature. When the temperature is too low the ice nucleation and propagation occurs on all areas of the surface and hence superhydrophobic property loses and ice adhesion increases [98, 99]. Again at high humid conditions moisture condenses in the cavities of the superhydrophobic surfaces and droplet grows and rapidly forms ice layer on the whole surface [100, 101].

2.2.2 Mechanism of ice formation

Ice formation on surface is a major problem in industries including transportation, power, buildings etc. Water gets adsorbed on the metal surfaces. The adsorbed water bound to the metal surface through the oxygen atom [102]. The binding

energy is slightly greater than that of the water on an ice surface. This adsorption results in an ordered structure based on the ice bilayer consisting of units of six water molecules bound in puckered hexagonal rings [103, 104]. The neighbouring bilayers are linked by hydrogen bonds between adjacent layers [105].

According to classical nucleation theory, the free energy barrier ΔG, the nucleation rate J, for heterogeneous ice nucleation depends on interfacial energies, lattice mismatch and radius of curvature [106]. The ΔG and J for a flat incoherent is expressed as,

$$\Delta G = \frac{\pi \sigma_{IV} r^2}{3}(2 - 3m + m^3);\ J = J_0 \exp(-\Delta G/kT), \tag{2-3}$$

Where $\sigma_{IV}$the ice vapour surface energy and r is the critical radius. The m is the ratio of the interfacial energies expressed as m = $(\sigma_{SV} - \sigma_{SI})/\sigma_{IV}$, σ_{SV} is the substrate vapour interfacial energy and σ_{SI} is the substrate ice interfacial energy. T is the flat ice surface temperature; k is the Boltzmann constant and J_0 is a kinetic constant [98].

Icing in the atmosphere occurs when a surface comes in contact with supercooled water. At first the surface wetted by supercooled water which determines the feasibility of icing and the surface-air interface is substituted by surface-water interface [107].

Hydrophobicity and icephobicity are parallaly related but there is no direct correlation between them [23, 108]. Icephobicity has different definitions which depend on different approaches for characterization of surface icephobicity. First approach implies icephobicity as a low adhesion force between ice and a solid surface which is quantified by critical shear stress and normal stress. The second

approach defines icephobicity as the ability of a surface to prevent ice formation on it. It depends on whether the droplet of supercooled water freezes at the interface and characterized by time delay of heterogeneous ice nucleation. The mechanism of droplet formation is quite complex and depends on the temperature level. Third approach encounters an impact test for incoming bouncing droplet and icephobic surfaces repel incoming small droplets [20].

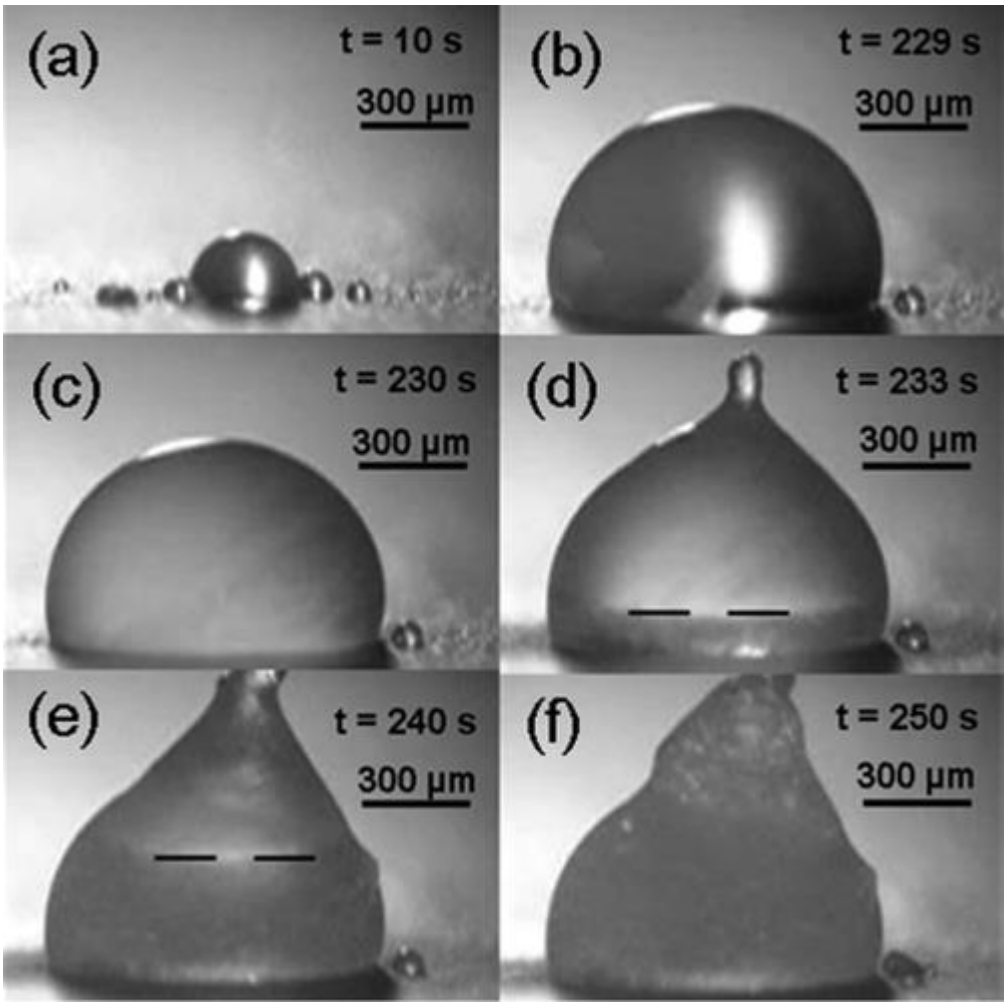


Figure 2-3. Drop-by-drop accumulation and freezing of a growing supercooled water volume on aluminium surface: The time from the onset of deposition is indicated on each frame. (a) First impacted supercooled droplets have merged together to form one major unit. (b) The main drop has grown by the sequential impaction of inkjetted droplets from above and remains all liquid. (c) Frozen drop shortly after the first freezing stage, which rapidly converts the supercooled liquid into a mushy liquid plus ice phase. (d, e) The crystallization front (horizontal dashed line) starts at the liquid−solid contact area and gradually advances upward. (f) Completely frozen drop [23].

Figure 2-3 shows stepwise freezing of a supercooled water droplet on aluminium surface. It is evident from Figure 2-3 (a) that the first impacted supercooled droplets have merged together to form one major droplet. The drop grows in size by sequential impaction of injected droplets as shown in Figure 2-3 (b) but still they remain liquid. Figure 2-3 (c) shows the first stage when the cooling starts and Figure 2-3 (d) when the crystallization of water droplet starts by the horizontal line as shown in figure. Finally Figure 2-3 (f) depicts the completely frozen water droplet. The time mentioned in each figure is the time after the injection of the first droplet of water.

As stated before hydrophobicity is not absolutely necessary for icephobic property of any surface, icephobicity can also be obtained on hydrophilic surface. It has been found that the surface ice nucleation on unmodified hydrophilic surface is lower in magnitude than on modified hydrophobic surface [99]. Based on the above literature investigations the study is limited for hydrophobic surfaces.

2.2.3 Anti-icing and de-icing

Anti-icing and de-icing systems are mainly used to solve the icing problem. Anti-icing prevents the formation of ice on the surface while de-icing removes the ice after it has been formed. Both strategies mainly divided into two methods: Passive and active. Passive methods take the advantage of the physical properties of the surface to eliminate or prevent ice while active methods use external systems and require an energy supply either thermal, chemical or pneumatic [109]. Most icing prevention methods are active heating systems that need a control strategy. Anti-icing requires much more energy than de-icing systems as it requires continuous heating. Moreover when the ice melts water can run back after the element and freeze again [90].

In theory icephobic coatings are more effective as it prevents ice formation on the surface due to its ice adherent properties. Superhydrophobic surfaces reduce the shear forces between ice and surface and also reduces sensitivity towards dirt and bugs [110].

For anti-icing applications mainly icephobic coatings are being used. On the icephobic surfaces the ice adhesion is very low [111]. Such coatings reduce the shear force needed to remove the ice from the surface. In an alternative approach superhydrophobic coating can be used for icephobic applications. This approach takes advantage of water repellency and low adhesion of water drops on the surface and reduces water accumulation on the surface. Ice and water adhesion depends on the intermolecular forces that interact at the ice-solid and water-solid interface [11].

2.2.4 Applications of icephobic surfaces

Ice, snow, glaze, rime or their mixtures formation, adhesion and accumulation can cause severe problems for solar panel, wind turbines, aircrafts, heat pumps, power lines, telecommunication equipment, submarines etc. It results in mechanical and electrical failure and decreases efficiency in power generation including safety hazard. Icephobic surfaces should prevent or delay of ice formation or formation rate of accumulation on the surface should be slowed down.

(I) Solar panel protection

Solar systems deliver energy all year and it can provide extremely high efficiency in cold climates as the snow on ground increases solar reflection. But it is also important that solar panels remain clear of snow and debris. When solar panel gets covered there is reduction in power output from snow cover and hence lose efficiency. Light snowfall does not cause much problem as the reflective nature of solar panels act as natural heaters and melt light snow. The heavier snowfall that

dump inches of snow causes the main problem. Anti-icing coating on the solar panels can reduce or eliminate the ice formation on the surface and also can easily remove accumulated ice on the surface [112].

(II) Aircraft surface protection

Aircraft icing refers to ice formation and accumulation on the windward surface of aircrafts. It is mainly caused by the striking of unstable supercooled water droplets suspended in clouds onto a solid surface. Aircraft icing poses an increasing threat to the safety of flight due to the damage of aerodynamic shape [113]. Once the ice is formed, the aerodynamic shape of aircraft is severely damaged; and the critical angle of attack also decreases. These changes lead to a series of serious flight problems, including the redistribution of airfoil pressure, reduction of lift factor, increase in resistance coefficient, and the rapid diminution of lift resistance ratio. Moreover, lift off speed and running distance increase significantly and make taking-off and climbing difficult under icing conditions [114].

(III) Wind turbine

Wind turbines in cold climate are exposed to icing issues over their service life. Ice accretion on wind turbines, particularly on the blades, can be detrimental to their performance, durability, and the safety of those in the vicinity of operating iced turbines. During icing events, ice accumulates on the rotor blades, thus reducing the aerodynamic efficiency and torque, leading to power losses [115]. Atmospheric ice is generally formed from supercooled water droplets that adhere strongly to the blade surface. Low-surface-energy materials have attracted attention as potential icephobic materials, or materials that allow the ice to detach itself under the effect of gravity or/and wind force [116]. Poly(tetrafluroethylene) or PFTE is a good example, due to its very low surface energy, and because it has the lowest ice-adhesion force among a wide variety of solid materials [117].

(IV) Powerlines

Combination of ice and wind on overhead electrical lines can cause serious damages, sometimes leading to power outages and dire socio-economic consequences. The January 1998 ice storm in North of America is a good example of such consequences. Electrical power network faces several problems under icy conditions. Since transmission lines are spread across long distances from generating stations to distribution grids. Such network runs through plane fields, high mountains, and small river crossings and covers long distances. During icing events, weight of ice puts an additional load and stress on the network and increases the possibility of power breakdown due to ice accretion. During ice storm ice accretion occurs on conductors, insulators and towers, which can lead to tripping of line, structure collapsing and additional load on conductors. Once the fault generates, it takes long time to normalize the network, since repair activities require fault pinpointing followed by mobilization of manpower, logistics, material, and check on adverse weather conditions etc [118].

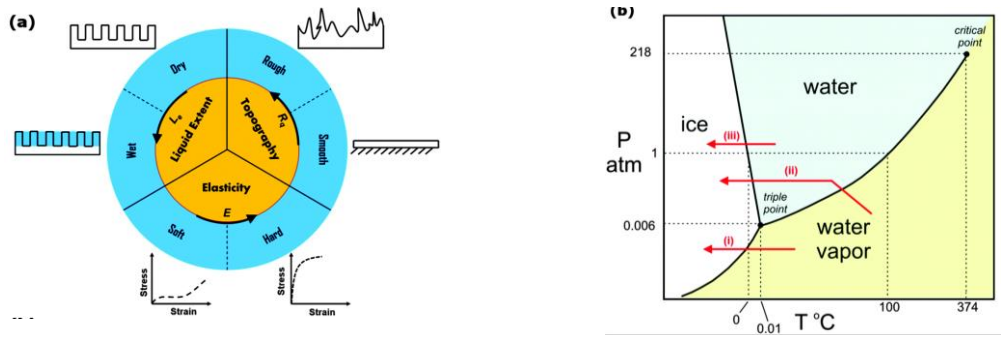
(V) Heat pumps

The problem of condensation and subsequent freezing of moisture on the surfaces of the heat exchange equipment cooled down to negative temperatures and using the low-potential heat of ambient air is one of the main technical obstacles on the way to wide application of air-source heat pumps in countries with cold climate. It decreases the coefficient of performance (COP) of the heat pump equipment [119]. To reduce the frost formation many anti frosting technologies are used including changing the characteristics (temperature, velocity, humidity, pressure and purified air) [120-122], changing the structure of air heat exchanger [123, 124], changing the interaction between air or frost layer and cold surface (electric field, magnetic field, ultrasonic wave)[125-127] etc. Surface treatment and the use of

anti-icing coating are promising solutions to overcome the frosting and increase the efficiency of heat pumps [128].

2.3 Relation of surface superhydrophobicity and icephobicity

To compare the icephobicity and superhydrophobicity the important consideration is relative humidity of the atmosphere. Under high humidity conditions the ice adhesion strength increases three-fold when water vapour condenses on a surface [24]. Surface topography, elasticity and liquid extent also influences the ice phobicity of a surface.



(a) (b)

Figure 2-4. (a) A framework for classifying recently developed icephobic coatings. (b) Phase diagram for water indicating three different pathways for formation of water-based solid by changes in temperature and/or pressure of water. (i) Vapor–solid desublimation deposition, (ii) vapor–liquid–solid or condensation followed by freezing, and (iii) liquid–solid or freezing [129].

Figure 2-4 (a) shows schematic of classification of icephobic coatings based on three distinctive surface attributes: elasticity (soft *vs.* hard), topography (smooth *vs.* rough), and liquid extent (dry *vs.* wet) and Figure 2-4 (b) shows phase diagram for water and how it can be changed from one form to another by changes in temperature and pressure. These characteristics are also related to differences in the formation mechanism of ice on smooth *vs.* rough, dry *vs.* wet, or soft *vs.* hard surfaces, which can lead to differences in their icephobic performance.

Surface roughness induced superhydrophobicity can widely be used to design icephobic and anti-icing coatings. The main assumption behind this suggestion is that the mechanism of ice and water adhesion are similar and hence when a surface with low surface energy is designed weak adhesion between surface and ice is also obtained [2, 130-132]. But in reality the mechanism of water and ice adhesion are different. Water can withstand pressure but it cannot support shear stress since shear stress tensor of liquid is spherical in the static limit [131, 133]. The mechanical force acting on a liquid droplet and on ice are different and adhesion of ice and water on substrate surface is also different [108]. When superhydrophobic surfaces are exposed to ambient atmosphere of high humidity, frost readily forms on the surface which subsequently becomes more ice friendly [98]. The formation of ice fundamentally changes the basic wettability of the surface: whereas the dry surface would typically cause impacting drops to bounce, with some frost, impacting droplets freeze on the surface [134].

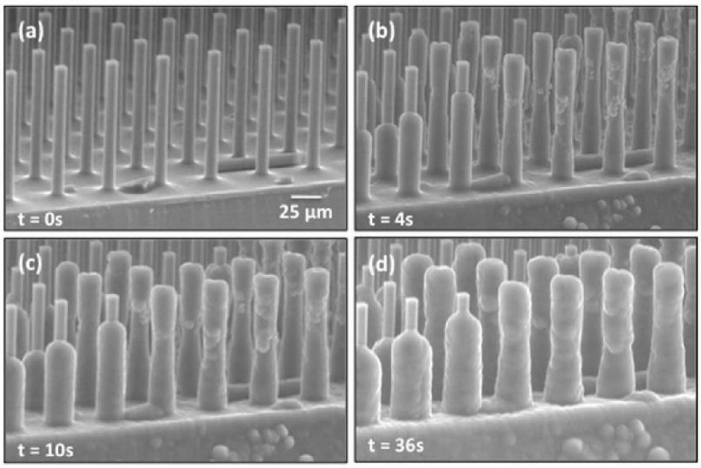


Figure 2-5. Frost formation on a microfabricated superhydrophobic surface. (a) Dry surface with a contact angle (for the flat material) of about 110°. The surface is maintained at −13 °C, and after the start of the experiment, the relative humidity is increased. (b–d) the time gradually increased from 4s to 10s to 36s. Frost formation is observed and occurs everywhere, including the top of the posts, the valleys, and the sides of the posts [98].

Figure 2-5 shows frost formation on a microfabricated superhydrophobic surface under high humidity conditions and at a temperature of -13 °C. It is observed that under high humidity and low temperature conditions with prolonged exposure time frost forms rapidly on rough superhydrophobic surface.

Again it is also reported that with fine control of surface microstructures, favorable anti-icing performance can be achieved. A robust icephobic coating based on superhydrophobicity was obtained via optimizing the coating's surface structure with the help of nanoparticles [41]. Colloidal surfaces with different content of fluorine polymers were also developed that shows superhydrophobic and icephobic properties [135]. The optimum coating demonstrated superhydrophobicity under freeze temperatures. A flexible superhydrophobic coating which could repel water and ice even at −20 °C with a relative humidity (RH) of 90% for more than three months was also reported [136]. Anti-icing properties of single nanostructured and micro-nanostructured superhydrophobic surfaces were also analysed. It was found that the single nanostructure surface demonstrated a reduced icing area and an icing mass than those of the micro-nanostructured surfaces [137].

2.4 Surface energy and low surface energy polymers

Low surface energy is essential for hydrophobicity of the surface. This low surface energy is obtained by the deposition of some hydrocarbon substances on the surface. The term hydrocarbon is used because they are inherently hydrophobic in nature. The organic molecules generally consist of hydrogen and carbon atoms. These atoms have low surface energy but not enough low energy to produce superhydrophobicity. So for superhydrophobicity the hydrogen atoms of the organic molecules are replaced by fluorine atoms. The fluorine atoms have much lower energy than corresponding hydrogen atoms and thus produce

superhydrophobicity on the surface effectively. There are also various other ways by which surface energy can be lowered and some of them are discussed below.

2.4.1 Low surface energy via surface treatment

(I) Organic acids

Possible method reported for surface energy reduction is deposition of stearic acid (SA). Before deposition of SA the surface roughening is essential. SA can be deposited ultrasonically as well as by normal immersion but ultrasonication leads to better result of superhydrophobicity than normal immersion. Different concentration of stearic acid can be used to find out the best result. After deposition of SA the substrates are cleaned properly with ethanol and finally dried at higher temperature [86, 138, 139].

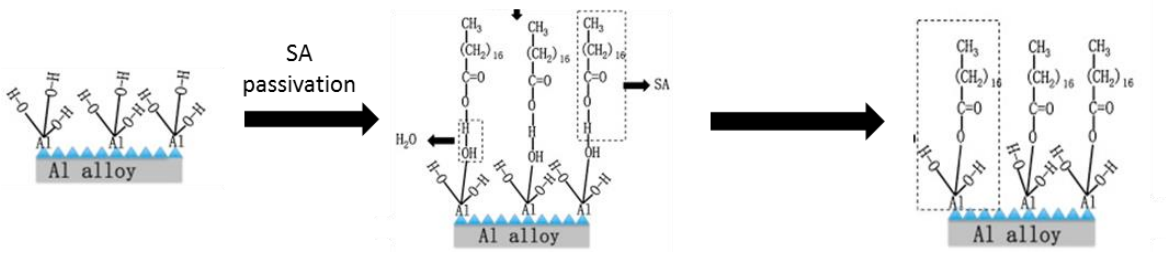
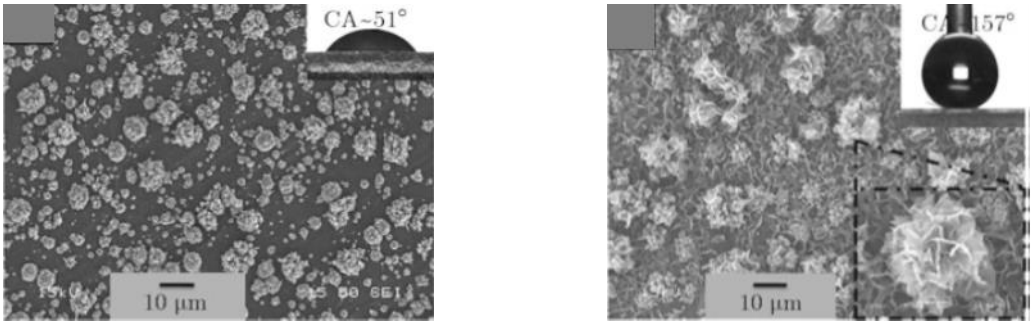


Figure 2-6. Schematic diagram of modification of sodium hydroxide (NaOH) etched aluminium surface after treatment with stearic acid [140].

Figure 2-6 depicts the schematic diagram of the modification of etched aluminium alloy sample surface with stearic acid. After etching the alloy surface got converted to $Al(OH)_3$. When stearic acid molecules are introduced the H atoms of stearic acid forms a weak H bonding with the O atom of Al-OH bond. Finally condensation takes place and it loses a water molecule and the stearic acid gets attached to Al atom via strong Al-O-CO bond. In another instance, the superhydrophobicity is obtained

on aluminium alloy surface by the deposition of copper followed by modification with ethanolic stearic acid [141].



(a) (b)

Figure 2-7. SEM image of the aluminium substrate (a) after deposition of copper films at 0.8 V for 10 minutes and (b) after electrochemical modification of the deposited copper films in ethanolic stearic acid solution at 30 V for 30 mins [127].

Figure 2-7 depicts the SEM image of the aluminium substrate after deposition of Cu film and after modification of the Cu- film with ethanolic stearic acid respectively. The Cu-film was deposited at a potential of 0.8 V and the deposition was continued for 10 mins. Rough surface was formed on aluminium substrate as evident from Figure 2-7 (a) and the water contact angle was measured to be 51 °, on the other hand after modification of the surface with stearic acid the contact angle increased to 157 ° which is depicted in Figure 2-7 (b).

Ethanolic lauric acid solution is also reported to produce superhydrophobicity on aluminium alloy surface. The surface was first modified with a mixture of 100 g/L sulfuric acid (H_2SO_4), 10 g/L oxalic acid ($C_2H_2O_4$) and 10 g/L glycerol ($C_3H_8O_3$). The treatment of the aluminium samples with this mixture of acids are varied between 10 to 120 mins and it drastically affects the final water contact angle of the lauric acid coated surface. The samples are treated with 5 wt% ethanol lauric acid solution for 1.5 h [96].

The contact angle obtained for superhydrophobic coating by different method is being listed in Table 2-1. For different process different time and different chemicals are used to produce the roughness on the surface but to produce low surface energy same chemicals are used under same condition for all the samples. It is clear that the best result for the water contact angle is obtained for a mixture of sulfuric acid, oxalic acid and glycerol with water contact angle around 167.9 °.

Table 2-1. The contact angle (CA) and total time used to fabricate superhydrophobic surface by different methods [96].

Method	Contact angle (CA/°)	Total time / min
two-step anodic oxidation method with H_2SO_4, $C_2H_2O_4$, $C_3H_8O_3$	167.9	150
two-step anodic oxidation method with H_3PO_4	159.6	150
two-step chemical etching method with $FeCl_3$, HCl	156.8	101
two-step chemical etching method with $FeCl_3$, HCl	159.1	23

(III) Aluminium acetylacetone

In another method a unique process for preparing transparent superhydrophobic coating has been reported by using sublimable pore-forming material. Aluminium acetylacetonate (AACA) is being used as the sublimable compound which sublimes at 193 °C and boehmite (AlOOH) is being used as the film material. AACA is mixed in ethanol and the weight ratio of boehmite and AACA to ethanol was 0.005 and 0.05. The mixture was sonicated for 20 mins. During the sonication AACA dissolves in ethanol. Then the sonicated mixture was deposited on the substrate surface by spin coating at 1000 rpm speed for 10 s. Then they are dried at room temperature and the substrate becomes opaque. Then the coated substrate was calcinated on a heated hot plate at 500 °C for 20 s. Now the substrate becomes transparent again [142].

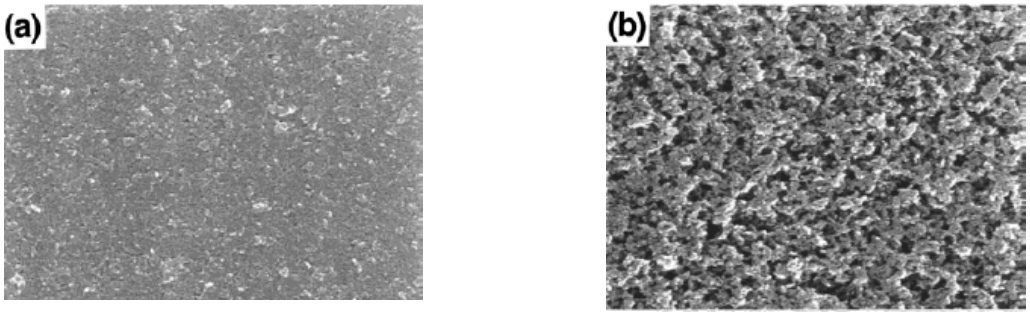


Figure 2-8. SEM micrograph of prepared films (a) Film prepared from suspension containing only boehmite and (b) Film prepared from a suspension containing boehmite and AACA [142].

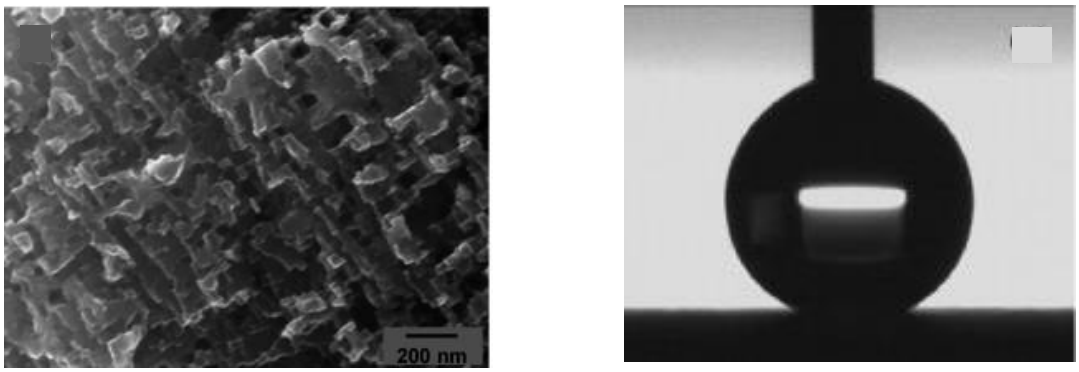
Figure 2-8 (a) and (b) depict SEM micrograph images of substrate after depositing on boehmite film and after depositing a composite film of boehmite and AACA respectively. It is evident that with the deposition of boehmite film, there is no significant change on the substrate surface morphology but after the deposition of the composite film, the surface morphology appears to be rougher.

(IV) Hydrocarbon and fluorinated hydrocarbon

In another process two compounds are used to produce stable superhydrophobicity. The aluminium alloys are treated with sodium hydroxide (NaOH). Then they are rinsed with deionized water and finally dried at 120 °C for 1 h. After that the aluminium alloy surface is first modified with perfluorononane (C_9F_{20}) and poly(dimethylsiloxane)vinyl terminated (PDMSVT) containing 1 wt% curing agent dimethyl methyl hydrogen siloxane was deposited on the surface. Both the films are obtained by spin coating at the speed of 3000 rpm for 30 s and then the samples are annealed at 80 °C for 2 h [143].

Hydrocarbon and fluorinated-hydrocarbon coatings can effectively produce superhydrophobicity on the aluminium alloy surface. They are deposited on the substrate surface by the process of plasma enhanced chemical vapour deposition

(PECVD). The RF source is used with a mixture of Ar and CH_4 for hydrophobic coating and Ar, CH_4 and C_2F_6 for fluorinated hydrocarbon coating at a power of 100 W [144]. The high vacuum chamber was maintained at a pressure of 20 mTorr and the base pressure was $2x10^{-6}$ Torr. And a voltage of 50 V applied on the substrate. Then the coating was deposited on an etched aluminium substrate [145].



(a) (b)

Figure 2-9. (a) SEM micrograph image of aluminium alloy substrate after etching and deposition of fluorinated hydrocarbon and (b)Image of a water drop suspended from a syringe needle during contact angle hysteresis measurement on fluorinated-hydrocarbon coated aluminium [145].

Figure 2-9 (a) shows surface morphology of the aluminium alloy substrate after being chemically etched and modified with fluorinated hydrocarbon and Figure 2-9 (b) is the image of a water drop suspended from a syringe needle while measuring water contact angle hysteresis.

2.4.2 Polymer coatings

Polymers containing fluorine atoms (Fluorocarbons) are unique as they can repel both oil and water. There has been great developmental work optimizing fluorocarbon polymers as ultra low adhesive materials. Comercially available fluorinated side chain acrylic and methacrylic polymers are typical low surface energy coating materials [146]. Amongst the numerous molecular structures investigated, a close-packed uniform CF_3 surface was found to possess the lowest surface tension ever measured [147]. In this section, different polymer coatings used as low surface energy polymer coatings will be discussed.

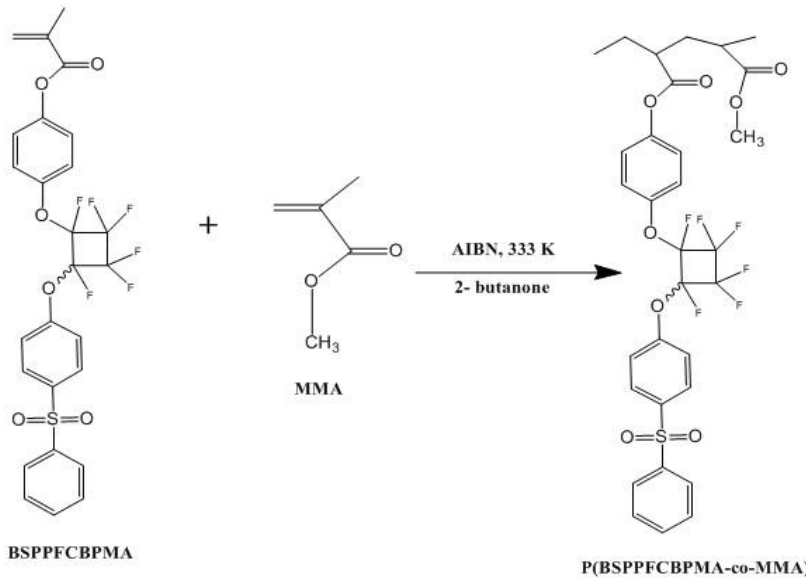
(I) Polyfluoroacrylate

Polyfluoroacrylate emulsion can produce low surface energy on the substrate surface. It generally consists of several organic components including a fluorinated organic compound, which could be synthesized by emulsion polymerization. One synthesis process of such polyfluoroacrylate emulsion consists of two stage process. In the first stage methyl methacrylate (MMA), butyl acrylate (BA), acrylic acid (AA), hydroxyl propyl acrylate (HPA) are mixed together with vigorous magnetic stirring. Then the mixture is added to a emulsifier solution and the mixture is stirred with a high dispersion homogenizer. Then the above prepared solution and potassium persulfate (KPS) solution added dropwise continuously to small volume of water with magnetic stirrer. It is refluxed with a refluxed condenser for 2 h at 80 °C under magnetic agitation. The solution was allowed to react to get the core PFA emulsion. In the next stage in another container MMA, BA and certain amount of dodecafluoroheptyl methyl acrylate are mixed together and homogenized as the first step. Then this fluorinated emulsion and KPS solution added to the core emulsion under agitation within 2 h at 80 °C. Finally

polymerization continued for another 1 h. The PFA emulsion was obtained after cooling to room temperature [148].

(II) Fluorinated polymethyl acrylate

Fluorinated poly(meth)acrylate can also be potentially used as a low surface energy material. These are used for wide specialty range and properties of transparency and resistance to detoriation by environmental effects. Most often used poly(meth)acrylate is poly(-methyl methacrylate) also known as PMMA. Poly(meth)acrylate copolymers containing fluorinated groups possess remarkably low surface energies, low friction co-efficients and incompatibility with strong polar solvents [149-151]. These are prepared by free radical random co-polymerization. Here azobisisobutyronitrile (AIBN) is being used as initiator. The random copolymerization of 1,1-dihydroperfluorooctyl acrylate with methyl methacrylate (MMA), styrene butyl acrylate (BA) and ethylene has been reported [149].



Reaction 2-1

Reaction 2-1 represents the schematic synthesis process of formation of random co-polymers of P(BSPPECBPMA-co-MMA) in the presence of 2-butanone at 60 °C. In the polymerization all the other groups remain unaffected except the C=C attached to CO group.

(III) Polytetrafluoroethylene

Polytetrafluoroethylene (PTFE) is a low surface energy material which can significantly lower the surface energy of roughened aluminium surface. This material is generally being used in anti-adhesion agents and chemical insulators coatings because of its very low surface energy. The hydrophobicity of PTFE is due to the fluorination of the carbon bonds. But it is very difficult to handle because of its insolubility, viscosity and melt strength. 20 wt % PTFE emulsion can be prepared by dispersing 2.0 g PTFE in 10 ml dimethylformamide (DMF). The solution is homogenized properly and then applied on the substrate surface as a composite coating with nanoparticles [152].

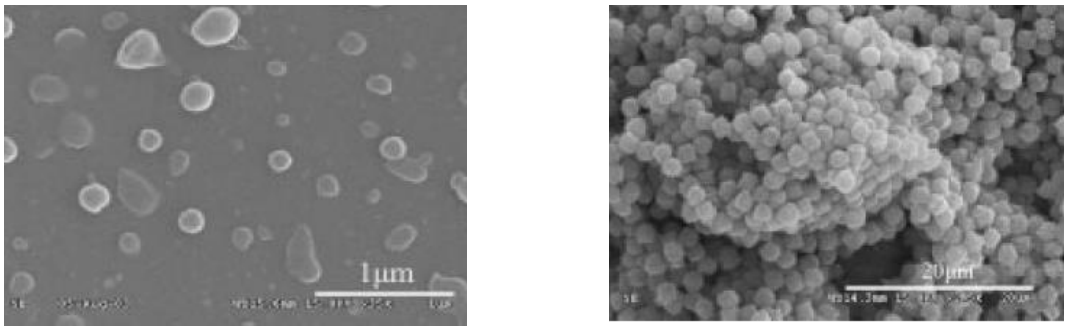
(IV) Polypropylene

Polypropylene is another polymer that may be used to generate hydrophobicity. The surface of the aluminium substrate is anodised first then polypropylene is deposited on the anodised substrate. Various concentration of polypropylene can be used for deposition and from the water contact angle measurement optimum concentration of polypropylene for superhydrophobicity can be determined [153].

(V) Block copolymers

Block co-polymers can also be deposited on the substrate surface to obtain superhydrophobicity. These block copolymers can form micelles. Depending on the concentration of the co-polymer they can form two types of micelle in selective solvent. When the concentration is very low ($< 10^{-6}$ gmL^{-1}) then monomolecular micelles are formed due to the length of the molecular chains. On the other hand at higher concentration ($>10^{-4}$ gL^{-1}) multimolecular micelles are formed. Superhydrophobic coating of block copolymer of polypropylene and poly(methyl methacrylate) (PP-PMMA) is dissolved in dimethylformamide (DMF) to form micelle

solution. The micelle is composed of insoluble core of PP chains and a soluble shell of PMMA chains. The mixture was casted on the substrate surface at room temperature with varying concentration to obtain the best result of superhydrophobicity [154].



(a) (b)

Figure 2-10. SEM images of PP-PMMA surface (a) Micelles deposited on a surface cast from DMF solution at a PP-PMMA concentration of $1x10^{-4}$ gmL^{-1} and (b) Micelles aggregates deposited on a surface cast from DMF solution at a PP-PMMA concentration of $5x10^{-2}$ gmL^{-1}[154].

Figure 2-10 represents the surface morphology of the substrate when PP-PMMA block co-polymer is deposited on the surface. Figure 2-10 (a) is the surface morphology when the concentration of the PP-PMMA copolymer is low i.e. $1x10^{-4}$ gmL^{-1} and Figure 2-10 (b) is the surface morphology at the high concentration of the copolymer i.e. $5x10^{-2}$ gmL^{-1}. It is clear that when the concentration of the co-polymer is high the aggregation of the co-polymer takes place.

(VI) Fluorinated polybutadiene

Plasma fluorinated polybutadiene can also be used for superhydrophobic coating on aluminium surface. So polybutadiene (Aldrich, Mw=420000, 36 % cis 1,4 addidtion, 55 % trans 1,4 addition, 9 % 1,2 addition) is dissolved in toluene at a concentration of 5 % (w/w). The mixture is spin coated on the substrate surface. Then the films were subsequently annealed at 90 °C under vacuum for 60 min in

order to remove excess solvent. These polybutadiene films are plasma fluorinated to achieve superhydrophobicity [155].

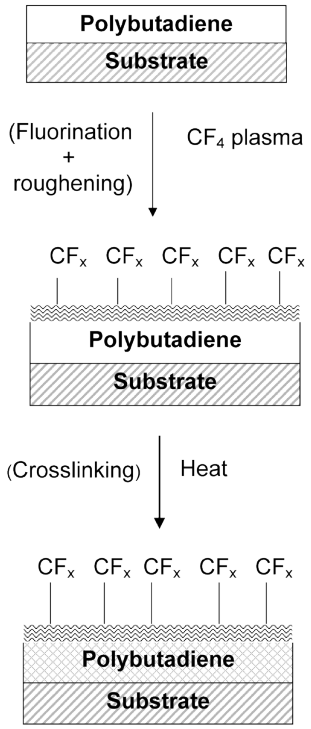


Figure 2-11. Schematic diagram of stepwise procedure of plasma fluorination of polybutadiene coated substrate[155].

Figure 2-11 shows schematic diagram of plasma fluorination of a polybutadiene coated substrate. After coating the substrate with polybutadiene it is being fluorinated with CF_4 plasma which also provides roughening. After that the system is heated and crosslinking occurs of the CF_x surface molecules.

(VII) Silane compounds

As described before the surface roughness on aluminium surface can be obtained by depositing nanoparticles. These nanoparticles can also be modified to get the low surface energy. Tridecafluoro-1,1,2,2-tetrahydrooctyltrichlorosilane ($C_8H_4Cl_3F_{13}Si$, FDTS) is used to produce a self-assembled monolayer on the nanoparticles. The alkoxy groups on the surface are hydrolysed to form silanol-

containing species. The monolayer is formed by a process of silanization. The silanization of nanoparticles with the $RSiCl_3$ particles starts with the hydrolysis of Si-Cl bond to Si-OH. The –OH groups on the surface can form hydrogen bond with each other. Then a condensation reaction occurs where the adjacent –OH groups react with each other and form Si-O-Si bridging bonds [156].

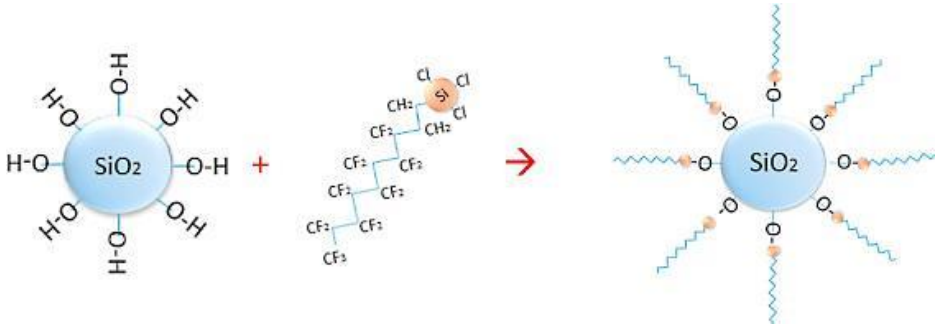


Figure 2-12. Schematic diagram of the salinization of silica nanoparticles using FDTS [156].

Figure 2-12 depicts the schematic diagram of the salinization of silica nanoparticles with FDTS. It is clear that the Si-Cl group of FDTS is hydrolysed and gets attached to the silica nanoparticles. Finally these Si atoms will get bonded with the neighbouring Si atom via Si-O-Si bond.

(VIII) Fluoroalkylsilane

Fluoroalkylsilanes (FAS) are mostly used for hydrophobic coating on the surface [53, 157, 158]. The tail end group of FAS molecules is the hydrophobic fluoroalkyl group. They can be deposited on the substrate surface by simple sol-gel processing method. FAS is being used as a precursor. Nanoparticles are functionalized using FAS molecules and then they are deposited on the substrate surface. (Heptadecafluoro-1,1,2,2-tetrahydrodecyl) trimethoxysilane (17FTMS) can be used for this process. 17FTMS in small amount is added to a mixture of deionized

water, ammonia and ethanol. Where ammonia is being used as a catalyst and water is used to promote hydrolysis. The functional methoxy group of 17FTMS undergoes hydrolysis and polycondensation reactions to form network structure with non-hydrolyzable fluorocarbon groups. This then mixed with nanoparticles and deposited on the substrate surface [157].

(IX) Hybrid coating

A hybrid material is defined as a combination of one or more dissimilar components to produce a single entity. For superhydrophobic coating again organic and inorganic hybrid coatings are also used. The hybrid material can enhance the hydrophobic property of the constituent materials or it can produce new hydrophobic property very different from that of the constituent materials. Hybrid superhydrophobic coating has been reported by a mixture of polymethylhydrosiloxane (PMHS), poly(vinyl chloride) (PVC), fluorinated methacrylate, mercapto functional monomers and various functional silane precursors [148].

Table 2-2 shows the surface energy values of some most commonly used polymer for low surface energy industrial applications. Polytetrafluoroethylene (PTFE) has the lowest surface energy of 20 mJ/m^2 of them all and hence widely used for hydrophobic applications. Polypropylene and polyethylene have low surface energy of 29.6 and 35.7 mJ/m^2 respectively.

Table 2-2. Surface energy values of some commonly used polymers (mJ/m^2) [159].

Polymer	Surface energy measured (γ / mJ/m^2)
PTFE	20
Polypropylene	29.6
Polyethylene	35.7
Polystyrene	40.7
PMMA	41.1
PVC	41.5
PET	44.6
Nylon 6	46.5

2.4.3 Polymer synthesis via chain growth and step growth process

Polymers are long chain giant organic molecules assembled from many smaller molecules called monomers. Polymers usually consist of a single repeating unit. Modern polymer chemistry allows the precise control over polymer architecture, molecular weight, functionality and other properties. Both chain growth (i.e. ionic or radical polymerization) and step growth (i.e. polycondensation and polyaddition) polymerization techniques are applied for the generation of a variety of soluble or cross-linked materials. This, in combination with postpolymerization modifications, such as crosslinking in emulsion or introduction of dyes, drugs or targeting moieties allow the design of desirable properties, e.g. biological recognition, degradability or other properties. As mentioned before the synthesis of polymers is broadly classified into two categories : step growth polymerization and chain growth polymerization.

2.4.3.1 Polymerization via chain growth polymerization

In chain growth polymerization, reaction consist of several steps: chain initiation, chain propagation, chain transfer, chain termination. The details of the reaction

mechanism will be discussed later in details. The chain growth polymerization can further be classified as radical, ionic, co-ordination, living, ring opening, reversible-deactivation polymerization etc. Self-condensing vinyl polymerization of 2-((2-bromopropionyl)oxy)ethyl acrylate results in the formation of hyperbranched polyacrylate and the process is atom transfer radical polymerization [160]. These hyperbranched polymers are very important and can provide intramolecular cavities, abundant functional groups, low viscosity and high solubility [161]. Vinyl polymers are usually synthesized by ionic polymerization as it can control the structure and architecture of the synthesized polymer and assure low polydispersity [162]. Co-ordination polymerization is usually catalysed by transition metal complexes [163]. The most common industrial co-ordination polymerization processes are Ziegler-Natta polymerization of 1-olefins and production of high density polyethene [164].

2.4.3.2 Polymerization via stepwise growth polymerization

Another main classification of polymerization is step growth polymerization. Step-growth polymerization, or condensation polymerization, is commonly employed to produce polyesters and nylons. The polymerization reaction occurs between the functional groups of molecules. Small molecules such as water are eliminated by the chemical reaction in step-growth polymerization. In step-growth polymerization, one or more types of monomers can be involved, and each monomer should have at least two sites for bonding. For polymerization with more than one type of monomers, for example, involving A and B monomers, A–B step-growth polymerization or A–A/B–B step-growth polymerization can occur [165]. Important polymers like polyester, polyamide, polysiloxane, polyurethane etc. are synthesized through step growth mechanism. The reactivity of the functional groups is unaffected by the length of molecular chain it is attached to [166].

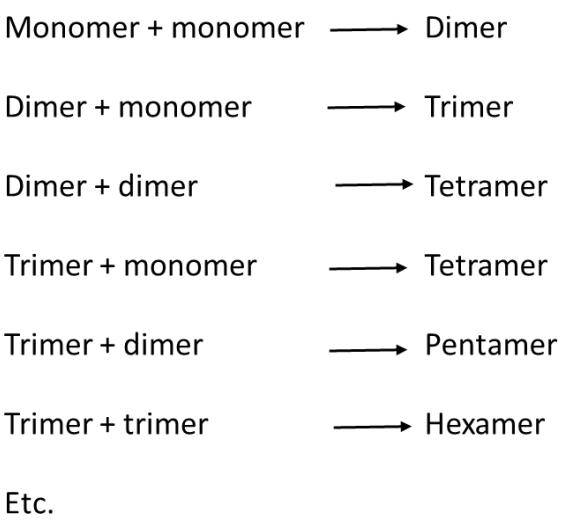


Figure 2-13. Illustration of steps leading to a polymer in step growth polymerization [166].

Figure 2-13 shows schematic illustrations of various steps in step growth polymerization reaction. The functional groups on two monomers react to form a dimer, the dimer reacts with another monomer to form a trimer, and these reactions lead to many monomeric units linked to form an intermediate molecular weight material, which is known as an oligomer, and eventually a polymer.

2.5 Surface morphology

High surface roughness can amplify the surface hydrophobicity. A physical structure of micro and nano-sized rough morphology can be obtained using various fabrication techniques, such as laser ablation, anodizing, sandblasting, nano/micro particle deposition and electrochemical etching [167]. Subsequently, the surface energy of the roughened surface could be reduced through chemical treatment. In this section, several surface modification processes will be reviewed.

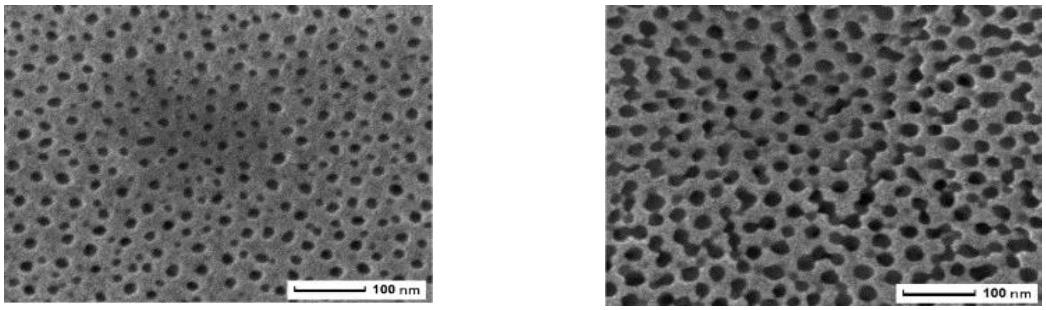
2.5.1 Anodisation

Anodisation is a common method for producing surface roughness but it is not applicable for all the substrates. Aluminium is the main substrate on which anodisation applied. The main principle is that the substrate aluminium is used as anode and for counter electrode (cathode) graphite or platinum may be used. The whole circuit is completed via an electrolyte solution. The whole process is carried out at a constant voltage or current for a particular time and a particular temperature. The voltage, current, time and temperature depends on the electrolyte used. This process is very popular and mostly used for colouring any aluminium substrate. Several electrolytes of different concentrations are used for the process. The anodisation process produces an oxide film on the substrate surface. The oxide films again may be of two types – dense barrier film, porous film. The mostly used anodisation electrolytes include sulfuric acid (H_2SO_4), oxalic acid ($H_2C_2O_4$), phosphoric acid (H_3PO_4) and chromic acid (H_2CrO_4). These electrolytes produce porous oxide films which are slightly soluble. The porous films can be controlled by anodising current density and anodising time. For dense barrier films boric acid, ammonium borate or ammonium tertraborate can be used. The thickness of the layer can be controlled by anodising voltage [168].

(I) Sulfuric acid anodisation

For sulfuric acid anodisation mainly low temperature is used 10 °C or less. The potential used is in the range of 20-40 V and the time of treatment is also varied. The concentration of sulfuric acid used is 16-25 wt%. The temperature of sulfuric acid anodisation should be very low because if the temperature is very high then no good surface morphology is obtained. The sulfuric acid anodisation at higher temperature results in formation of an oxide layer which is brittle in nature and thus will have no mechanical durability. It is being reported that when the anodisation temperature increased from 5 – 25 °C the microhardness gradually

decreased but the wear resistance remained constant but as the temperature increased further to 55 °C the wear resistance started to decrease and hence decreasing mechanical durability [169]. So the most important factor for sulfuric acid anodisation is that the temperature must be maintained low at all the time.



(a) (b)

Figure 2-14. SEM images of porous aluminium oxide film on substrate surface at electrolyte temperature of (a) 35 °C and (b) 55 °C [169].

The surface morphology of aluminium oxide film on substrate surface shows that it is porous in nature and highly dependent on electrolyte temperature as depicted in Figure 2-14 (a) and (b). It is also evident that with increase in electrolyte temperature the pore diameter gradually increases. When the anodisation was carried out at 35 °C electrolyte temperature shown in Figure 2-14 (a) then the pores formed are uniform on the surface. Again when the electrolyte temperature was 55 °C then the pore diameter increased and some of the pores joined together.

(II) Oxalic acid anodisation

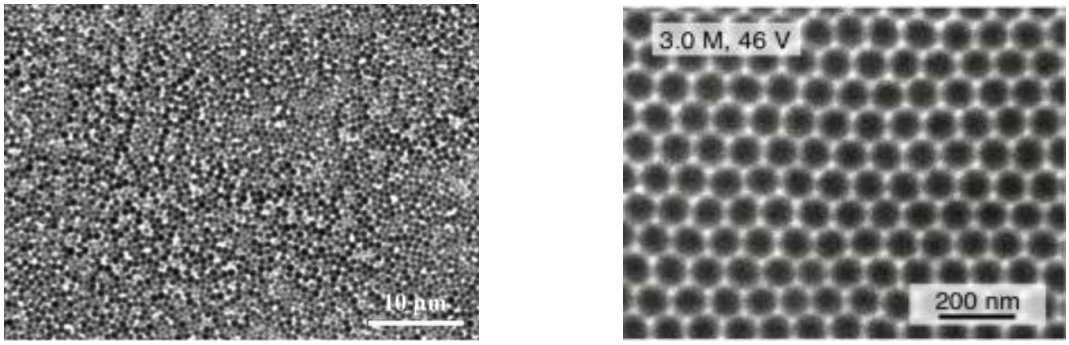
The next common anodisation is oxalic acid anodisation. It is named so as oxalic acid is being used as the electrolyte. The reaction can be performed at room temperature but the duration of the reaction is very long, around 10-13 h. The concentration of the oxalic acid used is 0.25-0.5 M. this is expected to produce a very uniform and rough microstructure on the surface [170].

(III) Organic acid anodisation

Some anodising uses organic acid as the electrolyte. The organic acids are as follows acetylenedicarboxylic acid, malic acid, a mixture of croconic and rhodizonic acid etc. The condition for anodisation changes is different from previous mentioned processes. When a mixture of croconic and rhodizonic acid is used as electrolyte the concentration of the acids are kept low 0.1 M of each. The anodisation was carried out for 60 mins and the current density is varied between 5-80 Am^{-2}. For counter electrode or cathode platinum is used [171].

Again when acetylenedicarboxylic acid is being used as electrolyte then 0.3 M solution of the acid is used. The time of anodisation is 180 mins but the voltage was kept very high 87.5-97.5 V range. Here also platinum is being used as counter electrode. The whole system is kept in a water bath to maintain the temperature and the solution is stirred using a magnetic stirrer [171].

Malic acid of 0.5 M can be used by anodisation of aluminium as well. The counter electrode is platinum and the anodisation was carried out for 48 hours. The reaction was carried out at constant but very high voltage of 200-350 V. The mixture was also stirred using a magnetic stirrer [172]. Other than these acids, selenic acid also used for anodisation. It is reported that by this process self-ordered porous aluminium films are obtained [171]. Malonic acid and tartaric acid were also used for anodisation [173].



(a) (b)

Figure 2-15. SEM images of aluminium surface after anodisation with (a) Malic acid [172] and (b) Selenic acid [171].

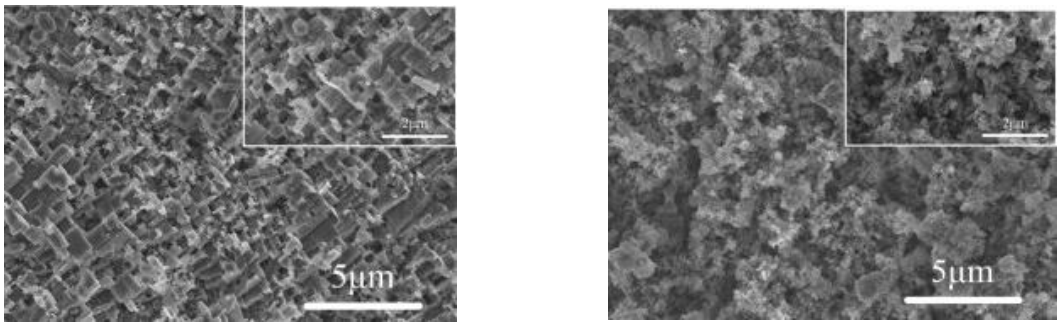
Figure 2-15 represents the morphology of aluminium oxide on aluminium surface when two different types of organic acids are used malic acid shown in Figure 2-15 (a) and selenic acid in Figure 2-15 (b). The advantage of selenic acid over malic acid is it has a self-ordering character of the pores formed.

Irrespective of the electrolyte and the other conditions the anodisation process requires some pre and post treatment. The pre-treatment includes the cleaning of the samples properly and electropolishing and the post-treatment requires removal of the produced oxide layer by chemical etching process and cleaning and drying of the samples. For the pre-cleaning of the samples, ultrasonication process is often used. Acetone and ethanol could be added during the ultrasonication. As for the electrochemical polishing 1:4 mixture of perchloric acid ($HClO_4$) and ethanol (C_2H_5OH) is being used at low temperature and for small interval of time. While the removal of oxide layer takes place in a mixture of phosphoric acid (H_3PO_4) and chromic acid (H_2CrO_4) at 60 °C.

2.5.2 Chemical Etching

2.5.2.1 Acid etching

This surface roughness can be obtained via several methods. One important method is acid etching. The main inorganic acids are corrosive in nature. So if they can be used in proper concentration then they can produce microstructured rough surface on aluminium. One of such solution is a mixture of hydrochloric acid (HCl, 37 wt% , 40 mL) and hydrofluoric acid (HF, 40 wt%, 2.5 mL)with distilled water (12.5 mL). The reaction can be performed at room temperature. The time of treatment is also very low 60 s -90 s [127]. The HF acid is very reactive in nature so it is being used in very small amount to avoid any explosion whereas HCl is corrosive but not very reactive so this is used in substantial amount and the rest volume is made up with distilled water. After this step the acid on the surface must be removed properly so that it cannot interfere in further processes.

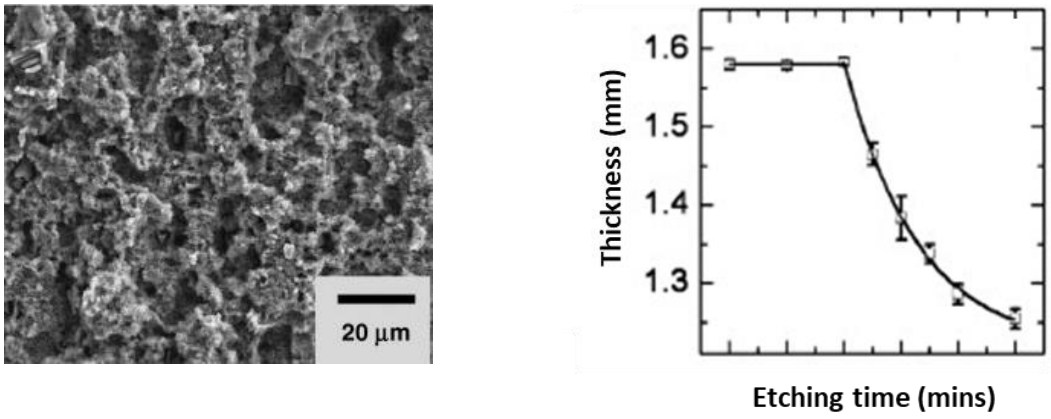


(a) (b)

Figure 2-16. SEM images of aluminium surfaces Polyfluoroalkyltryethoxysilane (PFO) coated and etched with mixed acid solution for (a) 10 s and (b) 20 s [127].

Figure 2-16 represents the SEM images of the aluminium substrate surface which are coated with PFO and etched with a mixed acid solution for various times. It is clear from the images that with the increase in the etching time the surface appearance changes and so does the surface roughness.

Instead of a mixture of acid only one acid can also be used for etching process. It is being reported for producing superhydrophobicity using Teflon coating. So before the application of Rf-sputtered Teflon coating the aluminium alloy samples are etched with 14.8 % HCl for different times ranging from 1 to 5 mins. It is also important that minimum of 2.5 min is necessary for sufficient roughness [144]. Compared to the previous step this process is relatively easy and less harmful as it doesn't include use of HF acid. But since HCl is less reactive than HF so more time is necessary to carry out the process to create sufficient roughness.



(a) (b)

Figure 2-17. (a) ESEM image of ultrathin rf-sputtered Teflon coated aluminium sample etched with 14.8 % HCl for 2.5 min and (b) Change in thickness of aluminium substrates with etching time [144].

Figure 2-17 (a) represents ESEM image of aluminium surface after being etched with 14.8 Wt% of HCl solution and subsequently coated with Teflon by RF-sputtering process. It is clear that the surface is considerably rough. Figure 2-17 (b) depicts the trend of change in thickness of the aluminium substrate with the etching time. It is evident that with high etching time the substrate thickness decreased significantly, but when the etching time is short, there is no significant change in thickness.

Peroxide mixed with acid can also be used for creating surface roughness on aluminium as well as on steel. Peroxide is used because of its high reactivity. The process reported uses a mixture of HNO_3 and H_2O_2 solutions in the ratio of (1:1 – 1:2, v:v) at room temperature. The time for etching is 20 mins for aluminium sample. After etching the samples are rinsed with deionized water followed by drying in flowing N_2 and then oven heated at 80 °C for 30 mins [86]. The H_2O_2 undergoes homogeneous fission reaction and produces OH radical. This produced OH radical is very reactive which helps in the etching process. The main concern in this method is the controlled use of H_2O_2. If there is excess peroxide it can seriously interfere in the further reaction so the complete removal of H_2O_2 is essential.

2.5.2.2 Alkali etching

Alkali etching is another simple method for producing rough surface. Generally NaOH or KOH can be used for the purpose. Alkalis are also corrosive in nature as acids. So the concentration of the alkali and the time of treatment should be maintained properly. The sodium hydroxide can be mixed with fluoroalkyl-silane and substrates can be immersed in it. So superhydrophobicity can be obtained in one step only. The sodium hydroxide used was 0.1 M in concentration and the fluoroalkyl-silane used was also in very low concentration 400 mM. The mixture was ultrasonicated with the substrate for 30 mins [145]. The substrates were then rinsed properly via ultrasonication to remove excess NaOH or fluoroalkyl-silane. Here the NaOH provides the required roughness to the surface while the fluoroalkylsilane provides the required low surface energy.

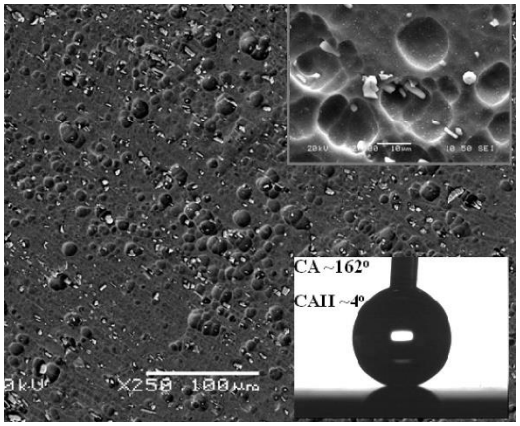


Figure 2-18. SEM image of aluminium surface treated with NaOH and fluoroalkyl silane (FAS-17) and inset shows a magnified image as well as a water drop image [145].

Figure 2-18 shows the SEM image of aluminium surface after treatment with NaOH and FAS-17 respectively and also the water drop on the surface and the corresponding water contact angle. The water contact angle is high 162° with low contact angle hysteresis (CAH). The surface is also sufficiently rough.

2.5.3 Growth of carbon nanotubes on substrate surface

Multiwalled carbon nanotubes (MWCNTs) can be also used to produce rough nanostructure on the substrate surface. The carbon nanotubes are used due to their high aspect ratio [64]. The nanocomposite coatings prepared using carbon nanotubes are expected to be ultrastable and healable. The MWCNTs are acid activated and by altering the temperature of acid activation and diameter of the carbon nanotubes, different microstructures can be obtained. To activate them MWCNTs (1.0 g) are treated in 100 ml of concentrated sulfuric acid (H_2SO_4) and nitric acid (HNO_3) in 3:1 (v/v) mixture at 60, 70, 80 and 90 °C respectively for 1 h [122]. The carbon nanotubes are used because it has very high strength and also low density. The diameter of the MWCNTs are in the range of 10-20 nm, 40-60 nm or 60-100 nm are used.

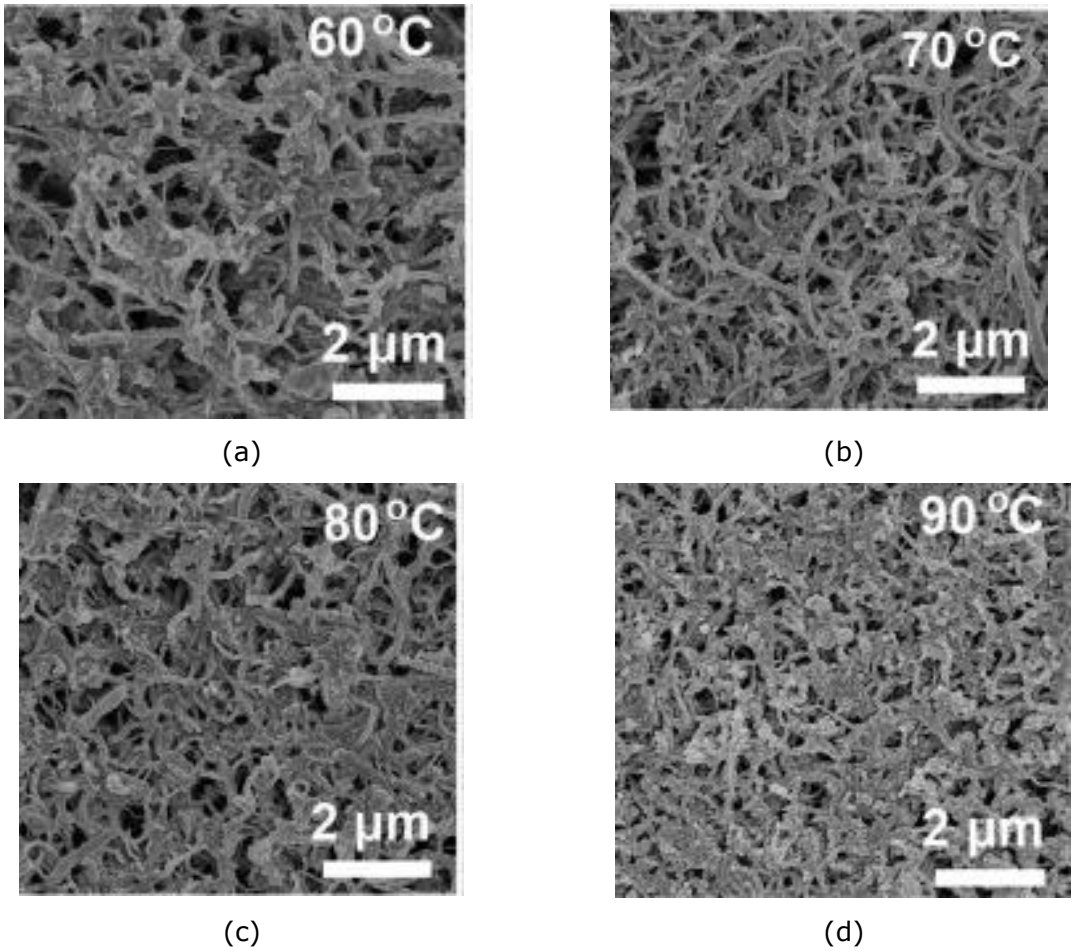


Figure 2-19 .SEM images of the Polysiloxanes (POS)/ MWCNTs surfaces annealed at (a) 60 °C, (b) 70 °C, (c) 80 °C and (d) 90 °C for 1 h with different MWCNT activation temperature [122].

Figure 2-19 (a-d) represents SEM images of POS/ MWCNT coating on aluminium substrate. The MWCNT was activated at 60 °C, 70 °C, 80 °C and 90 °C respectively. The surface microstructure changes with the activation temperature.

2.5.4 Surface modification using nanoparticles

(I) Different silica nanoparticles

Nanoparticles are also very popular for producing nanostructured surface roughness for hydrophobic applications. By controlling the rate of deposition of the nanoparticles the thickness of the layer may be controlled properly. There are

several nanoparticles which are in use, SiO_2, TiO_2, ZnO to name quite a few. SiO_2 particles are very useful as they can also be modified into hydrophobic particles. When it is deposited on the substrate surface, the SiO_2 particles condenses on the surface and produces -Si-O-Si- bridging bond on the substrate surface. This silicon atoms can get attached to hydrophobic molecules. The nanoparticles are not applied individually but they are mixed with hydrophobic particles and then the composite coating is applied on the substrate surface. The size and amount of the nanoparticles must be controlled very precisely. If they are not controlled properly then the surface properties may decrease instead of increase. In general the amount of nanoparticles is kept very low and their size is in narrow range. Thermally robust superhydrophobic coating is a mixture of thermoplastic polyurethane (TPU) and silica nanoparticles. The silica nanoparticles are deposited on a TPU coated substrate. The amount of nanoparticles used is 30, 100, 200 and 300 mg respectively. They are dispersed in toluene via vigorous stirring for 6 h. Afterwards again dispersed for 1 h via ultra-sonication [174].

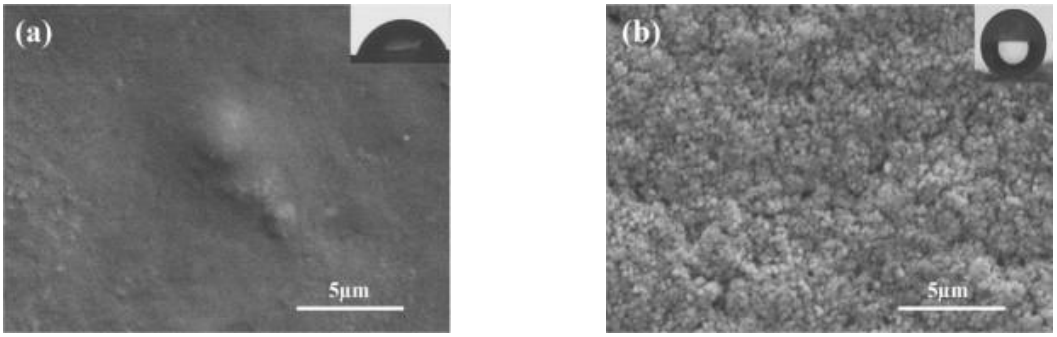


Figure 2-20 . SEM images of aluminium substrate surface (a) Poly urethane (TPU) coating only and (b) silica deposited coating only and the insets are corresponding water drop profile[174].

The surface morphology of aluminium surface after TPU coating only is shown in Figure 2-20 (a) and from the water drop profile it is clear that low water contact

angle is associated with that. In Figure 2-20 (b) surface morphology of silica coated aluminium substrate is shown and it is significantly rough. From the water drop profile it is also clear that high water contact angle is associated with that.

But instead of using only silica nanoparticles there is a much more use of hydrophobic silica nanoparticles. The normal silica nanoparticles can be converted to hydrophobic silica nanoparticles by treating them with hydrophobic material. There are several fabrication methods reported as well as hydrophobic silica nanoparticles are also commercially available. The hydrophobic silica nanoparticles with 7 nm mean diameter can be mixed with poly (methyl methacrylate) of 5 wt% and 7 wt% solution of polysiloxane. The mixture should be stirred vigorously and then can be sprayed on substrate surface. The poly (methyl methacrylate) can be prepared in toluene while the polysiloxane can be prepared in white spirit [175]. Again hydrophobically modified silica (HMS) particles are mixed with PTFE solution (20 wt%) in dimethylformamide (DMF) solution by ultrasonication and then applied on the substrate surface [152].

The fluorinated silica nanoparticles can be synthesized by the following process. In a hot plate and at temperature 50 °C ammonium hydroxide (NH_4OH) and ethanol (C_2H_5OH) are mixed together using magnetic stirrer. While stirring a solution, tetraethoxysilane (TEOS) is added dropwise into the mixture. When the transparent mixture turns opaque it confirms the formation of silica nanoparticles. Thus formed silica nanoparticles are further modified in an ethanolic solution of FAS-17 ($C_{19}H_{19}F_{17}O_3Si$). These nanoparticles are coated on the substrate surface and dried on a hot plate at 70 °C [5]. So the modification of silica nanoparticles can provide both surface roughness and low surface energy simultaneously. So no further treatment of the surface is required.

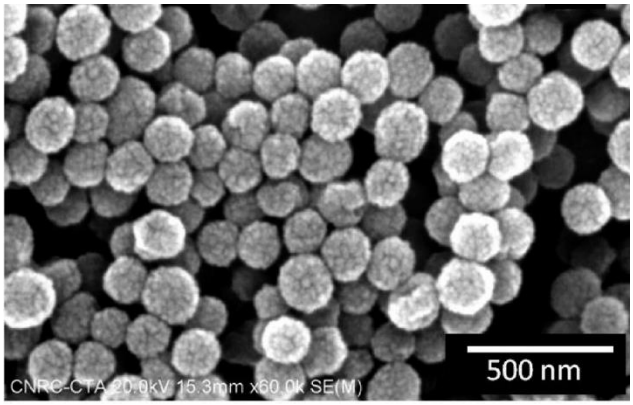


Figure 2-21. SEM images of fluorinated silica nanoparticles of sizes 169 ± 8 nm [5].

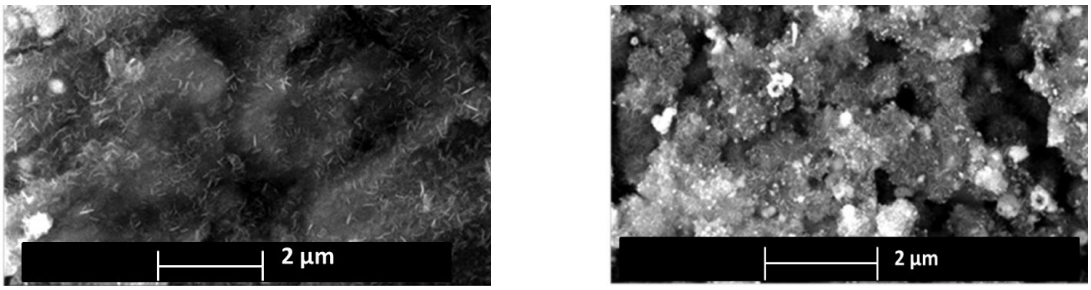
Figure 2-21 shows fluorinated silica nanoparticles of size 169 ± 8 nm. These silica nanoparticles are hydrophobic in nature. When these fluorinated silica nanoparticles are deposited on aluminium surface it produces hydrophobicity.

(II) TiO_2 nanoparticles

Titanium dioxide (TiO_2) is another nanoparticle that can be used to create surface roughness on substrate surface. The TiO_2 nanoparticles can be used in combination with a polysiloxane binder and can be applied on substrate surface. The coatings are stable at a wide range of temperature (-20-200 °C) and also durable within the entire pH range 1-14. The highest hydrophobicity was obtained at a TiO_2 content of 35 wt% [176]. The TiO_2 nanoparticles can also be prepared in the laboratory by reaction of solution of titanium (IV) in isopropylic alcohol (molar ratio 1:4) with water. The reaction was performed in an ultrasonic bath at room temperature. The gel obtained was aged overnight at room temperature for ensuring complete hydrolysis and then dried at a temperature 343 K. The dried material was again heated at 773 K in air for 2 h (heating rate 10 K/min) in order to get fully crystallized material and also to remove all the contaminants [177].

(III) ZnO nanoparticles

ZnO nanoparticles are also used to provide surface roughness on substrate surface. The surface roughness is obtained by simple immersion and ultrasonication. The substrates are immersed into a 50 mL aqueous solution containing 0.01 M Zincacetate [$Zn(Ac)_2$] and 0.1 M trimethylamine and stirred at 40 °C for different intervals. Then they are washed with distilled water and dried at 100 °C for 1 h [138].



(a) (b)

Figure 2-22. SEM images of ZnO coated aluminium (a) by classical dipping method and (b) by ultrasonication method [138].

SEM images of ZnO coated aluminium substrate surface is given in Figure 2-22 (a) and (b). While in the first case ZnO is deposited by classical dipping method and in the later the ZnO is deposited by ultrasonication method. It is evident that the surface roughness is better when ZnO is deposited by ultrasonication.

2.5.5 Surface modification using functionalised nanoparticles

(I) Nanoparticle composite

Nanoparticle-polymer composite can also be used to obtain superhydrophobicity. The nanoparticle-polymer composite preparation requires various steps which include synthesis of acrylic polymer resin, preparation of polymer binder and finally the particle-polymer composite. The acrylic polymer resin is the main low surface

energy material. The polymer binder mainly helps in binding the polymer with the substrate surface as well as the nanoparticles. Styrene, butyl methacrylate and glycidyl methacrylate mixture can be used to produce such polymer resin using azodiisobutyronitrile (AIBN) as an initiator. For the binder a mixture of toluene, silicone resin and acetone can be used and the mixture is cured at high temperature [25].

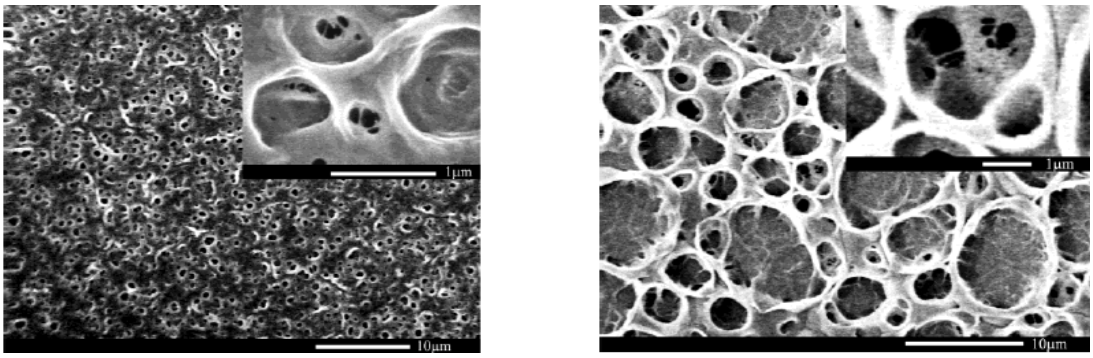
In addition to above silicon-polymers and palmitic acid can also be used to prepare hydrophobic surface. The silicon–polymer used in the form of room temperature vulcanization of silicon rubber. The samples are first chemically etched and then the etched samples are dip coated with the polymer and acid mixtre and finally it is cured at higher temperature [127].

Nanocomposite coating can also be prepared by modifying carbon nanotubes with a polysiloxane. The polysiloxane modified carbon nanotubes and free polysiloxane are highly dispersable in various alkenes and arenes. The mixture can be easily spray coated on the surface. The polysiloxane modified carbon nanotubes can be prepared by hydrolytic condensation of tetraethoxysilane (TEOS) and n-hexadecyltriethoxysilane (HDTES) in presence of acid activated carbon nanotubes. Then they are dispersed in solvent and applied on the surface [122].

(II) Nanoparticle consisting polyelectrolyte multilayer

Polyelectrolyte multilayer films can also produce superhydrophobicity on aluminium alloy surfaces. First it was reported via deposition of SiO_2 nanoparticle multilayer. Then heating the layer at 650 °C to remove the polyelectrolyte to produce required surface roughness [178]. Again dendritic gold clusters were electrochemically deposited on electrodes covered with polyelectrolyte multilayer film. The surface showed superhydrophobicity by deposition after deposition of n-dodecaethiol monolayer [75]. In another report superhydrophobic surface can be

obtained by using appropriate combination of acid treatment polyalkylamine hydrochloride (PAH) /polyacrylic acid (PAA) 8.5/3.5 (pH/pH). It can produce honeycomb like structure on the surface. But the main important thing that is to be kept in mind is that the film not to be rinsed by water after low pH treatment and staged pH treatment protocol is better than a single low pH treatment [179].



(a) (b)

Figure 2-23: SEM images of (PAH/PAA) films (a) After single acid treatment and (b) After a combined acid treatment [179].

Figure 2-23 shows SEM images of aluminium substrate surface coated with PAH/PAA films. In Figure 2-23 (a) the substrate undergoes single acid treatment at low pH. The surface is also rough in nature. In Figure 2-23 (b) it undergoes a high pH treatment and hence the surface roughness decreases dramatically.

3 Methodologies

3.1 Introduction

The main objective of the project is to synthesize a low temperature curing polymer with high adhesion on the substrate surface and to produce hydrophobicity and icephobicity on it. The research will include the following sequential; experimental process.

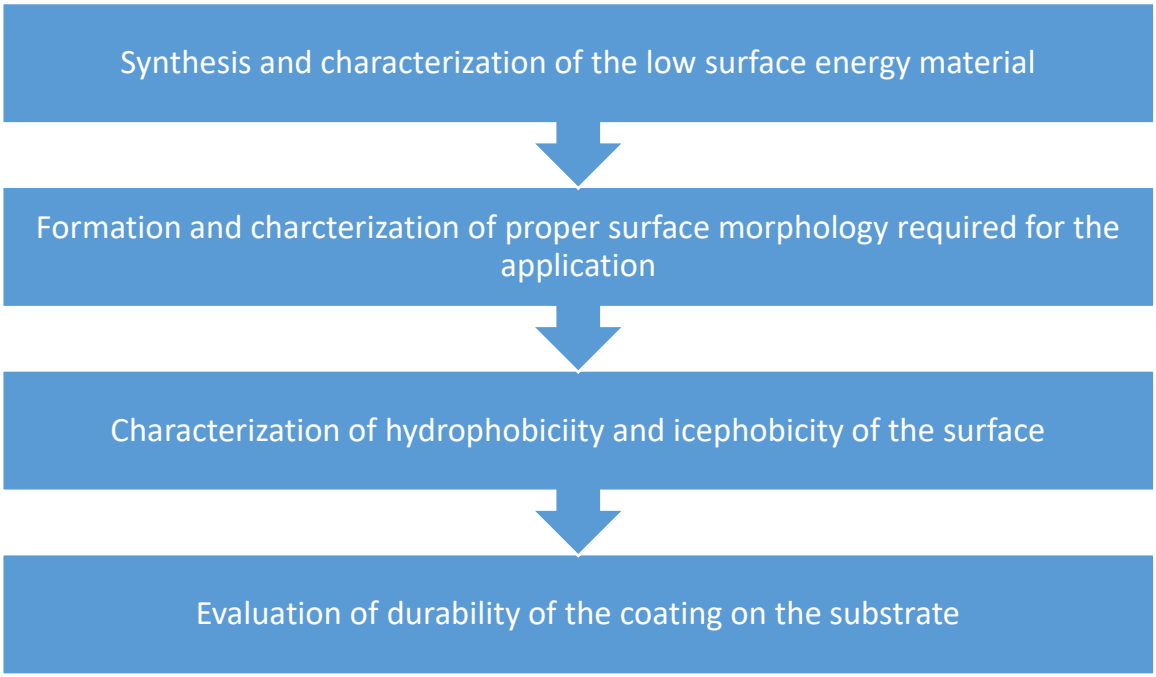


Figure 3-1. Schematic diagram of the experimental outline of the research.

Figure 3-1 represents schematic and sequential outline of the experimental methodology of the research. Firstly, a polyfluoroacrylate emulsion will be synthesized containing various concentration of fluorine. The synthesized PFA emulsion will be characterized and thermal property will be analysed. The reaction mechanism of the synthesized polymer will be established along with the confirmation of the structure of the polymer. The relative amount of elements incorporated in the polymer structure from the monomers will also be evaluated.

In the next step, the surface morphology of the substrate will be modified by electrochemical, chemical etching and deposition processes. The surface morphology will be analysed along with the surface roughness be measured. The process parameters will also be tailored to obtain micro or nano surface roughness.

Combining the above two, the surface morphology will be modified followed by deposition of the synthesized polymer on the modified surface by different coating methods. The surface hydrophobicity and icephobicity will be evaluated followed by the coating and ice adhesion strength on the substrate surface.

3.2 Raw materials, chemicals and substrates

There were different chemicals and substrates used for the experimental processes. The main processes involved anodisation, chemical etching, nanoparticle deposition and synthesis of polyfluoroacrylate emulsion.

3.2.1 Substrates

The main substrate used was aluminium AA1050 (RS components). Table 3-1 represents the chemical composition of the substrate material used for the experiments. For aluminium AA1050 the main alloying elements are iron (Fe), silicon (Si) and zinc (Zn) while manganese (Mn), copper (Cu), magnesium (Mg) and titanium (Ti) are present in small amount.

Table 3-1. Chemical composition of aluminium alloy AA1050 (wt %).

Element	Mn	Fe	Cu	Mg	Si	Zn	Ti	Al
Composition (wt%)	0.05	0.40	0.05	0.05	0.25	0.07	0.05	balanced

3.2.2 Chemicals for the synthesis of PFA emulsion

Styrene (C_8H_8, sigma Aldrich), acrylic acid ($C_3H_4O_2$, sigma Aldrich) and Heptafluorobutyl acrylate ($C_7H_5F_7O_2$, fluorochem) was being used as the starting monomers for the polymer synthesis. Potassium perdisulfate ($K_2S_2O_8$, fluorochem) was used as the initiator for the reaction and sodium dodecylsulfate ($NaC_{12}H_{25}SO_4$, sigma aldrich) was used as a surfactant and emulsifier.

3.2.3 Surface modification process

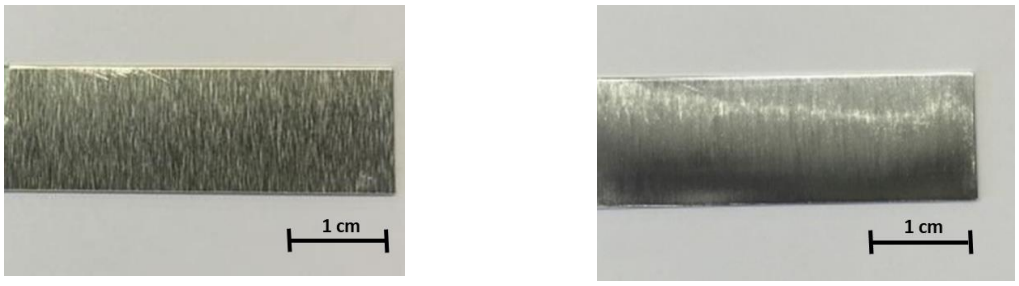
Mainly three processes were used for surface modification: anodising, chemical etching and deposition of micro and nanoparticles. Mainly sulphuric acid (H_2SO_4, sigma aldrich) was used for anodisation process, other chemicals used were oxalic acid [$(COOH)_2$, Sigma Aldrich], chromic acid (H_2CrO_4, Sigma Aldrich), phosphoric acid (H_3PO_4, Sigma Aldrich). For chemical etching hydrochloric acid (HCl, sigma Aldrich) and hydrogen peroxide (H_2O_2, sigma aldrich) was used. Copper microparticles and nanoparticles (sigma aldrich) were being used to deposit on substrate surface for surface modification.

3.3 Surface modification for aluminium substrates

3.3.1 Preparation of the substrates

Before any surface modification or surface treatment the aluminium substrates were first cleaned thoroughly. The substrates were ultrasonically degreased with acetone and ethanol respectively by immersing in for 10 mins each. Then the samples were thoroughly cleaned with distilled water and finally dried at 60 °C. Pre-treatment of the sample was absolutely necessary before surface modification processes and for that eletcrolpolishing was mostly used. The pre-treatment of the sample removes any manufacturing rolling lines on the aluminium substrate surface. Electropolishing was done with 1:4 mixtures of perchloric acid ($HClO_4$) and

ethanol (C_2H_5OH). The temperature of the system was kept 10 °C and the time of treatment was 5 mins. The current density used was 0.5 A/dm^2 and graphite being used as the counter electrode.



(a) (b)

Figure 3-2. Aluminium AA1050 plate samples (a) before electropolishing and (b) after electropolishing.

Figure 3-2 (a) and (b) represents the sample before and after electropolishing. It is clear that after electropolishing the surface of the substrate became shiny as it removed the natural oxide layer on the surface and also removed any manufacturing rolling lines.

3.3.2 Anodisation

Mainly an organic or inorganic acids can be used for the anodisation surface treatment. The main acids used for these experiments were sulfuric acid (H_2SO_4), oxalic acid [$(COOH)_2$], chromic acid (H_2CrO_4) and phosphoric acid (H_3PO_4). For this experiment mainly sulfuric acid was used. The setup of all the anodisation processes included some common equipments like electrodes, connecting wires, power supply, conducting salt etc. For the control of temperature, a polystat temperature controller (Cole Parmer polystat R6LP) was used which can control temperature upto -10 °C. The main important parameters for the anodisation process were current density, voltage, time of treatment, concentration of electrolyte and temperature.

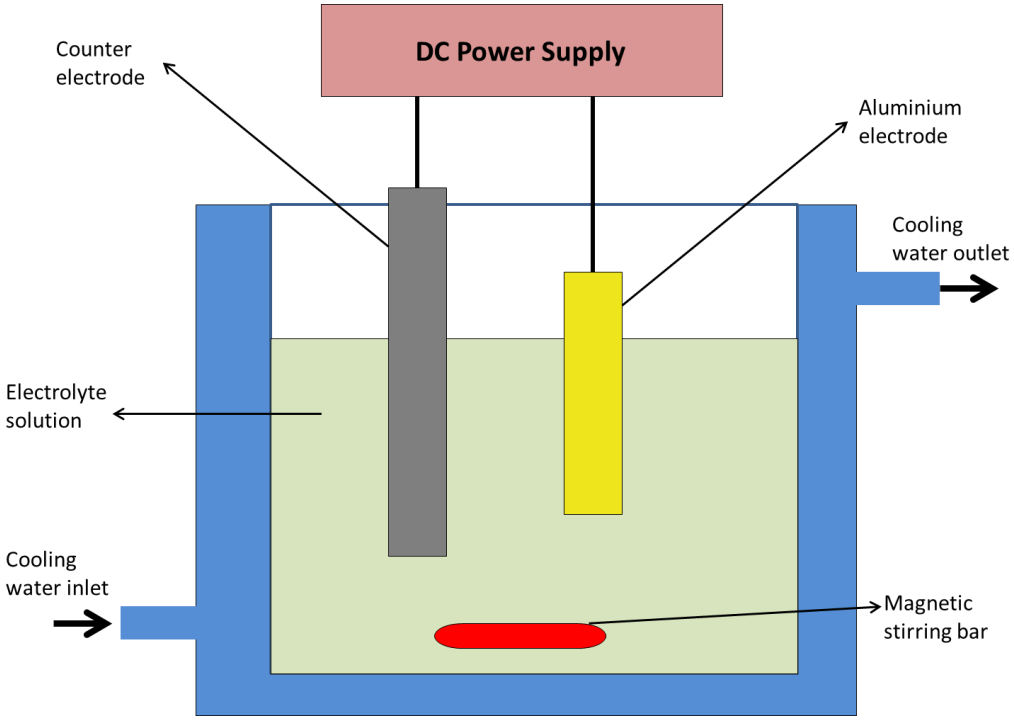


Figure 3-3. Schematic diagram of anodisation process and the equipments needed for the process.

Figure 3-3 represents the schematic diagram of anodisation process and the important parts for the assembly of the process. The counter electrode was cathode and generally an inert metal was used as cathode like platinum (Pt), graphite etc. The anode was aluminium. For constant stirring of the solution magnetic stirrer was used. Cooling water was used to keep a controlled temperature. The electrolyte solution in this case was sulphuric acid which produces H^+ ions.

Sulfuric acid anodisation is also known as hard anodisation process. Different concentration of sulfuric acid, current density, temperatures and treatment times were used for the process. The controlling of temperature is very important for the anodisation process.

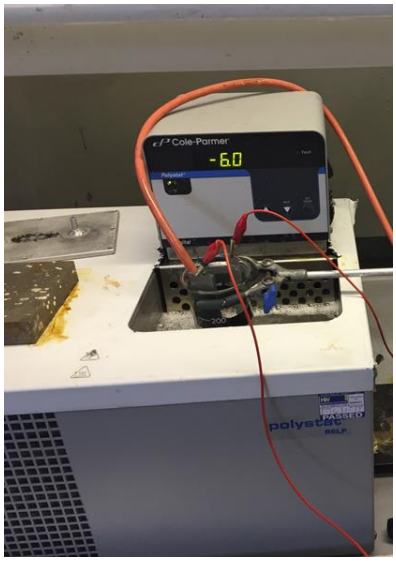


Figure 3-4. The temperature control instrument - Cole Parmer polystat R6LP for sulfuric acid anodisation.

Figure 3-4 shows the temperature control instrument Cole Parmer polystat R6LP which was necessary for sulfuric acid anodisation. This machine allowed decreasing and maintaining the temperature to a much lower extent. The temperature used for experiment was 10 ℃.

Anodisation processes were carried out with different process parameters to obtain the best set of conditions to obtain required surface roughness. Table 3-2 gives a set of anodisation process parameters in which the concentration of sulfuric acid was changed but all the other parameters were kept constant.

Table 3-2. Anodising condition for aluminium AA1050 by varying concentration of sulfuric acid and keeping the other parameters constant.

Sample name	Concentration of sulfuric acid (wt%)	Current (A/cm^2)	Time of treatment (minutes)	Temperature (°C)	Voltage (V)
SH 1	16.56	$9x10^{-4}$	45	31.4	4.0-5.8
SH 2	18.40	$9x10^{-4}$	45	30.6	7.4-12.2
SH 3	20.24	$9x10^{-4}$	45	31.4	9.5-13.1
SH 4	21.16	$9x10^{-4}$	45	30.6	8.1-11.9
SH 5	22.08	$9x10^{-4}$	45	31.4	5.6-10.7

In the next set of experiments given in Table 3-3 the current density was varied keeping the other parameters like concentration of sulfuric acid, time of treatment and temperature constant. The current density was varied from $6x10^{-4}$ A/cm^2 to $18x10^{-4}$ A/cm^2. The time of treatment was constant at 45 mins.

Table 3-3. Anodising condition for aluminium AA1050 by varying current density and keeping the other parameters constant.

Sample name	Concentration of sulfuric acid (wt%)	Current (A/cm^2)	Time of treatment (minutes)	Temperature (°C)	Voltage (V)
SH 6	20.24	$6x10^{-4}$	45	29.8	6.2-8.7
SH 7	20.24	$9x10^{-4}$	45	29.8	9.5-13.1
SH 8	20.24	$12x10^{-4}$	45	30.1	10.3-12.6
SH 9	20.24	$15x10^{-4}$	45	30.1	11.8-13.5
SH 10	20.24	$18x10^{-4}$	45	32.7	12.9-13.6

To observe the effect of time of treatment on the surface roughness the time of treatment was varied from 30 mins to a maximum of 90 mins and given in Table

3-4. The other parameters were kept constant to observe the sole effect of treatment time.

Table 3-4. Anodising condition for aluminium AA1050 by varying time of treatment and keeping the other parameters constant.

Sample name	Concentration of sulfuric acid (wt%)	Current (A/cm^2)	Time of treatment (minutes)	Temperature (°C)	Voltage (V)
SH 11	20.24	$9x10^{-4}$	30	30.5	5.6-10.2
SH 12	20.24	$9x10^{-4}$	45	29.8	9.5-13.1
SH 13	20.24	$9x10^{-4}$	60	31.0	10.3-12.6
SH 14	20.24	$9x10^{-4}$	75	31.0	11.8-13.5
SH 15	20.24	$9x10^{-4}$	90	32.0	12.9-13.6

Finally the effect of temperature on the surface roughness was observed by varying it from 10 °C to 50 °C as listed in Table 3-5.

Table 3-5. Anodising condition for aluminium AA1050 by varying temperature of treatment and keeping the other parameters constant.

Sample name	Concentration of sulfuric acid (wt%)	Current (A/cm^2)	Time of treatment (minutes)	Temperature (°C)	Voltage (V)
SH 16	20.24	$9x10^{-4}$	45	10	3.1-3.5
SH 17	20.24	$9x10^{-4}$	45	15	3.3-3.5
SH 18	20.24	$9x10^{-4}$	45	35	5.6-8.0
SH 19	20.24	$9x10^{-4}$	45	40	7.8-9.0
SH 20	20.24	$9x10^{-4}$	45	45	8.0-10.0
SH 21	20.24	$9x10^{-4}$	45	50	7.7-5.5

The surface roughness results and surface morphology obtained for the samples as listed in Table 3-2 to Table 3-5 are combined and the parameters are optimised. This is to obtain the best conditions for anodisation and the modified sulfuric acid anodisation parameters are listed in Table 3-6.

Table 3-6. Modified anodisation parameters for aluminium AA1050.

Sample name	Concentration of H_2SO_4 (g/L)	Current density (A/cm^2)	Voltage (V)	Time of treatment (mins)	Temperature (°C)
SH 22	300	$15x10^{-4}$	21.8-19.6	60	35~40
SH 23	175	$15x10^{-4}$	22.5-17.0	60	35~40
SH 24	131	$15x10^{-4}$	22.2-19.0	60	35~40
SH 25	300	$15x10^{-4}$	21.8-19.6	40	10
SH 26	175	$15x10^{-4}$	22.5-17.0	40	10
SH 27	131	$15x10^{-4}$	22.2-19.0	40	10
SH 28	300	$15x10^{-4}$	21.8-19.6	60	10
SH 29	175	$15x10^{-4}$	22.5-17.0	60	10
SH 30	131	$15x10^{-4}$	22.2-19.0	60	10

3.3.3 Chemical etching process

For the chemical etching process a solution containing various concentration of HCl and H_2O_2 was used. The temperature and treatment time was also varied to obtain varied surface roughness. The substrates were cleaned and electropolished as mentioned before. Then 20 ml of the prepared solution of HCl and H_2O_2 was taken in a beaker with constant magnetic stirring connected with a heat plate to maintain the temperature.

A beaker containing the etching solution and magnetic stirrer is set up on a hot plate to control the experimental temperature. The substrates are fully immersed in the etching solution and the volume of the etching solution was kept constant to 20 ml in each case. The temperature was maintained constant throughout the experiment. The magnetic stirrer was added for continuous homogenization of the solution. Like the anodisation, samples were prepared by chemical etching at different concentration of etching solution, treatment time and temperature.

Table 3-7 shows the chemical etching conditions for aluminium substrates with an etching solution containing various concentration of H_2O_2 and constant 1 M concentration of HCl. The treatment time and temperature is also kept constant at 60 mins and 40 °C respectively. The concentration of H_2O_2 is varied from 0.1 M to 2M.

Table 3-7. Chemical etching conditions with varying concentration of H_2O_2 and concentation of HCl constant at 1 M at 40 °C for 60 mins.

Sample Name	**Concentration of H_2O_2 (M)**	**Concentration of HCl (M)**	**Temperature of treatment (°C)**	**Treatment time (mins)**
Al 1	0.10	1	40	60
Al 2	0.25	1	40	60
Al 3	0.50	1	40	60
Al 4	1.00	1	40	60
Al 5	1.50	1	40	60
Al 6	2.00	1	40	60

The chemical etching parameters for aluminium substrates with an etching solution containing constant concentration of H_2O_2 and varying concentration of HCl is given in Table 3-8. The concentration of HCl is varied from 0.25 M to 2 M. The treatment time and temperature is also kept constant at 60 mins and 40 °C respectively for all the samples. The concentration of H_2O_2 kept constant at 0.5 M.

Table 3-8. Chemical etching conditions with varying concentration of HCl and concentation of H_2O_2 constant at 0.5 M at 40 °C for 60 mins.

Sample Name	**Concentration of H_2O_2 (M)**	**Concentration of HCl (M)**	**Temperature of treatment (°C)**	**Treatment time (mins)**
Al 7	0.5	0.25	40	60
Al 8	0.5	0.50	40	60
Al 9	0.5	1.00	40	60
Al 10	0.5	1.50	40	60
Al 11	0.5	2.00	40	60

The treatment temperature was varied for the chemical etching process from 10 °C to 60 °C and aluminium substrates were etched with a solution containing 1 M HCl and 0.5 M H_2O_2. The treatment time was kept constant at 60 mins. The details of the samples prepared are given in Table 3-9.

Table 3-9. Chemical etching conditions with varying etching temperature and constant concentration of HCl and H_2O_2 at 1 M and 0.5 M respectively for 60 mins.

Sample Name	Concentration of H_2O_2 (M)	Concentration of HCl (M)	Temperature of treatment (°C)	Treatment time (mins)
Al 12	0.5	1.00	10	60
Al 13	0.5	1.00	20	60
Al 14	0.5	1.00	30	60
Al 15	0.5	1.00	40	60
Al 16	0.5	1.00	50	60
Al 17	0.5	1.00	60	60

3.3.4 Surface modification of the nanoparticles before deposition

Cu- nanoparticles were used to deposit on the substrate surface. Before deposition the particles were modified by surface treatment. 1H,1H,2H,2H-perfluorooctyltriethoxysilane (POTS) was used to make the surface of the particles hydrophobic. 20 ml of ethanol was taken into a beaker and 0.3 ml of POTS was added into it. The mixture was stirred with a magnetic stirrer for 30 mins to ensure complete homogenization. 1 g of the Cu-nanoparticles when then added to the mixture solution and the mixture was then ultra-sonicated for 1hr. Finally the particles filtered and washed thoroughly with ethanol first and then with distilled water to remove any excess ethanol and POTS. Finally the particles were dried in a desiccator to remove the excess water.

3.3.5 Deposition of Cu nanoparticles on aluminium substrate

The modified Cu-nanoparticles were mixed with the synthesized polyfluoroacrylate (PFA) emulsion to prepare a composite mixture and then finally deposited on the aluminium substrate surface. 0.4 g modified dried Cu-nanoparticles were weighed and mixed with 20 ml of the PFA emulsion. The mixture is then stirred with a magnetic stirrer for an hour to ensure complete mixing. The composite mixture was spin coated on the substrate surface at a speed of 500 rpm, 1 ml of the mixture was taken each time and continued for 30 s. The process was repeated for 3 times. Finally the coating was dried at 80 °C for 2 hrs.

3.4 Synthesis and curing of Polyfluoroacrylate emulsion

3.4.1 Synthesis of polyfluoroacrylate emulsion

The preparation of polyfluoroacrylate (PFA) emulsion was a crucial step for the further experiment as this will provide the required low surface energy on the substrate. There was several preparation methods of polyfluoroacrylate emulsion found in literature [149, 180-184]. Generally PFA is a mixture of more than one monomer, one of which is an acrylate. It also contains a fluorinated monomer which is responsible for the low surface energy.

A styrene based polyfluoroacrylate emulsion had been synthesized. The emulsion polymerization was a one step process. It was a copolymer of styrene, acrylic acid and heptafluoro butyl acrylate. Sodium dodecyl sulfate was used as a surfactant and potassium persulfate was used as an emulsifier for the process. The detailed experimental process is described below:

Styrene , acrylic acid and heptafluorobutyl acrylate were mixed together at 1:1:1 ratio with constant stirring using a magnetic stirrer. A sodium dodecyl sulfate (SDS) solution was prepared by dissolving 0.31 g of SDS in 10 g distilled water.

Similarly 0.21 g potassium persulfate (KPS) dissolved in 5 g water. The mixture prepared by mixing styrene, acrylic acid and heptafluorobutyl acrylate was added to the prepared SDS solution and the mixture was homogenized with high speed magnetic stirring (around 1000 rpm) for 15 mins. Then in a round bottom flask 25 ml of water was taken and it was connected with a reflux condenser. Cold water kept running through the reflux condenser at a constant speed. The round bottom flask was placed in a water bath with magnetic stirring at 80 °C. The homogenized mixture prepared with SDS and other monomers and prepared KPS solution was added to the round bottom water flask dropwise slowly with constant magnetic stirring. The whole mixture was refluxed for 2 hrs at 80 °C and then it was allowed to cool completely and left overnight to complete polymerization.

The synthesised polyfluoroacrylate emulsions were classified according to the molar ratio of styrene, acrylic acid and heptafluorobutyl acrylate used during the synthesis process and listed in the Table 3-10 below.

Table 3-10. Synthesised polyfluoroacrylate emulsion with 1 :1 molar ratio of styrene/acrylic acid and different molar ratios of heptafluorobutyl acrylate.

Name	Molar ratio of styrene	Molar ratio of acrylic acid	Molar ratio of Heptafluorobutyl acrylate
PFA 0.1	1	1	0.1
PFA 0.25	1	1	0.25
PFA 0.75	1	1	0.75
PFA 10.1	1	1	1
PFA 10.2	1	1	2
PFA 10.3	1	1	3

3.4.2 Preparation of polyfluoroacrylate coatings

The synthesized polyfluoroacrylate emulsion was deposited on the substrate by different coating methods as described below :

3.4.2.1 Spray coating

In Spray coating an air spray gun Clarke air brush (Model: CAB3P) was used. The PFA emulsion was sprayed on the aluminium substrates from a constant distance of 10 cm. The time of spray was varied for the samples from 30 seconds to 120 seconds. Then the samples were heat treated at 80 °C for curing of the emulsion and to obtain strong adhesion of the coating on the substrate.

3.4.2.2 Dip coating

The modified aluminium substrates were inserted inside a beaker containing 20 ml of the synthesized PFA emulsion. The substrates were inserted at a constant speed, kept inside the emulsion for a certain time and finally taken out of the beaker using a dip coater. The process was repeated for 3 times. Then finally the samples were heat treated at 80 °C to ensure full curing of the polymer and cross-linking.

3.4.2.3 Spin coating

For spin coating spin coater (Chemat technology spin coater KW-4A) is used. The substrate surface was cleaned thoroughly to remove any residual chemical from surface treatment or any other impurity. The substrates were attached to the spin coater with the help of a both sided tape. Then 0.5 ml of the PFA emulsion was deposited on the substrate and the spin coater was switched on. The process was repeated 3-5 times. After each coating process substrate was heat treated for strong adhesion of the coating on the substrate surface. The spin coater was rotated at a speed of 500 rpm and process was continued for 30 seconds. After each coating process the samples were heated in a vacuum oven at 80-150 °C to ensure the complete curing of the polymer and finally cooled down to room temperature.

3.5 Thermogravimetric and Differential Scanning Calorimetric analysis

For the characterization of thermal behaviour of the prepared PFA emulsion differential scanning Calorimetry (DSC) and Thermo Gravimetric Analysis (TGA) processes were used. In the DSC process generally the difference in heat flow is measured. Heat was passed through both sample and reference and their temperature is increased. During the whole reaction the temperature was maintained same for both sample and reference. The change in heat flow was measured as a function of temperature. In TGA analysis, the change in physical and chemical properties were measured as a function of temperature. Both of this gave the information about the thermal behaviour of the sample.

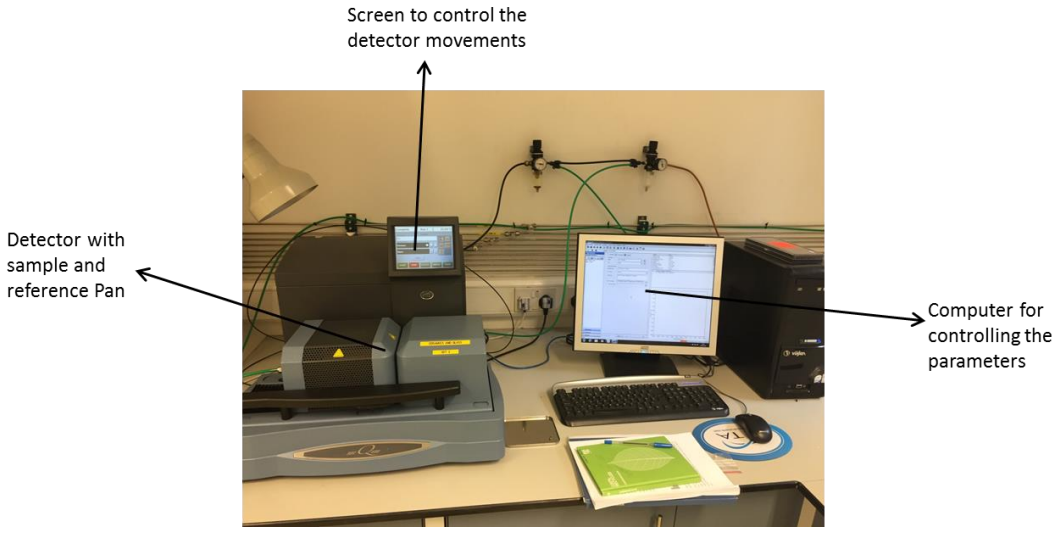


Figure 3-5. SDT machine which simultaneously perform TGA and DSC analysis.

The machine used for TGA and DSC analysis was SDT Q600 as shown in Figure 3-5. The testing method used was Ramp and the temperature used for the testing was from room temperature to 500 °C. The rate of heating was 20 °C/min. Air was used as the gas environment and the flow rate of air was high.

3.6 Microstructural characterization

3.6.1 Sample preparation for microstructural characterisation

The microstructural characterisation of the anodised sample was very important to see the difference between the surfaces before and after anodisation. After anodisation the surface of the aluminium did not remain anymore conductive due to the formation of a protective oxide layer (Al_2O_3) on the aluminium surface. But for microstructural analysis by the scanning electron microscope (SEM) the surface of the sample essentially needed to be conductive. So the sample produced after anodisation could not be directly used for SEM analysis. A conductive layer of Pt was formed on the anodised aluminium surface by sputter coating process. To deposit the platinum by sputter coating process of current was 15 mA and potential difference was 2.2 kV. It was treated for 90-120 secs in an argon gas atmosphere.

3.6.2 Measurement of surface roughness

The surface roughness measurement was conducted by 3D optical profilometer. The profilometer consists of two parts : a detector and a sample stage. The detector determines the point on the sample and the stage holds the sample. The stage moves to allow for measurement. Optical profilometer uses light instead of physical probe. The light is directed in a way that it can detect the surface in 3D.

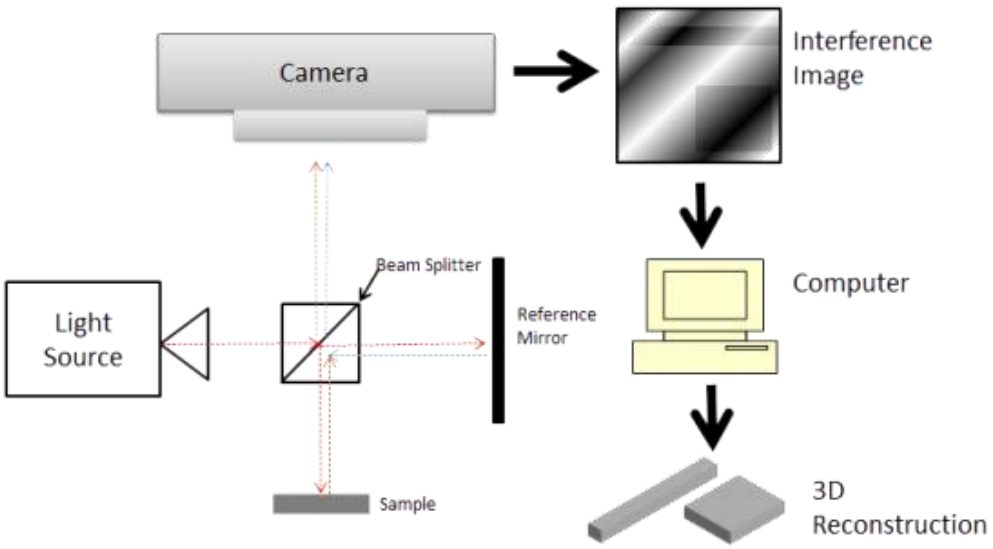


Figure 3-6. Schematic of an Interferometric profilometer.

Figure 3-6 shows schematic diagram of interferometric optical profilometer. It consists of several part. It uses wave properties of light to compare the optical path difference between a test surface and a reference surface. The light beam coming from the source is split inside the profilometer and reflects half the beam from the sample and another half is reflected from the reference mirror. When the distance between the beam splitter to the reference mirror and beam splitter to the sample is same, the split beams recombine to produce constructive and destructive interference. This creates light and dark bands known as interference fringes. This interference beam is focused into a digital camera. The light and dark bands are recorded in the image and finally produces 3D image of the surface.

3.6.3 Imaging and analysis

The microstructures of the Pt- coated aluminium were analysed using two different scanning electron microscope : environmental Scanning Electron Microscope

(ESEM, Philips XL30) and field emission scanning electron microscopy (Zeiss Sigma 500 VP, FESEM). The ESEM was equipped with backscattered electron (BSE) and secondary electron (SE) detector for imagining. It was also fitted with X-ray detector for energy dispersive X-ray (EDX) analysis.The images were taken using SE detector as it gave the surface morphology. Due to anodisation the surface of aluminium was roughened. The main objective was to observe the different surface roughness produced by difference in process parameters.The spot size 4 and accelerating voltage of 20 KV were set during the imagining of the Pt-coated samples. The substrate material used was aluminium AA1050. The difference of surface roughness of these samples at different process parameters were observed. Field emission scanning electron microscope (Zeiss Sigma 500 VP, FESEM) was operated at 3 kV with the working distance of 10 mm and the secondary electrons (SE) were used to form images.

3.6.4 NMR analysis

It gave the physical and chemical properties of atoms or molecules. This method of spectroscopy uses the magnetic properties of certain atomic nuclei. It relies on the phenomenon of nuclear magnetic resonance and it can provide detailed information of the structure. Nuclear magnetic moments are sensitive to their surroundings and interact very weakly with them. A magnetic nucleus placed in a magnetic field has small number of quantized energy levels. They differ in the orientation of the nuclear magnetic moment which can point in the same direction of the magnetic field or in the opposite direction. This interaction splits the energy levels within the nucleus. The value of ΔE depends on the extent of interaction [185]. Depending on the different types of interaction in different environment the signals change and we can identify the different groups present within the species.

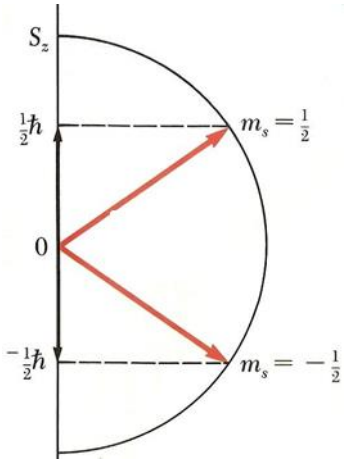


Figure 3-7. Spin quantization of the angular momentum of spin 1/2 nuclei [108].

Figure 3-7 depicts the example of a nuclei with overall spin $\frac{1}{2}$. After the interaction with the magnetic field the spin level again got split into two energy levels with an energy gap between them. This is also known as spin quantisation of angular momentum.

Mainly three types of NMR processes were performed ^{1}H, ^{13}C and ^{19}F NMR. They were to analyse hydrogen, carbon and fluorine nuclei respectively. For analysation of the sample Bruker Advance III spectrometer operating at a 19F Larmor frequency of 564.7 MHz was used. The probe was a 1.3 mm double resonance H(F)X probe spinning at 49.4 kHz.

3.6.5 X-ray photoelectron spectroscopy

X-ray photoelectron spectroscopy is a quantitative surface spectroscopic technique to measure the elemental composition. It can also measure the empirical formula, chemical state and electronic state of the element that exist within the material. XPS spectra are obtained by irradiating a material with X-rays beam while simultaneously measuring the kinetic energy and number of electrons that escape

from the top 0 to 10 nm of the material. XPS requires high vacuum ($P \sim 10^{-8}$millibar) or ultra-high vacuum (UHV; $P < 10^{-9}$ millibar) conditions.

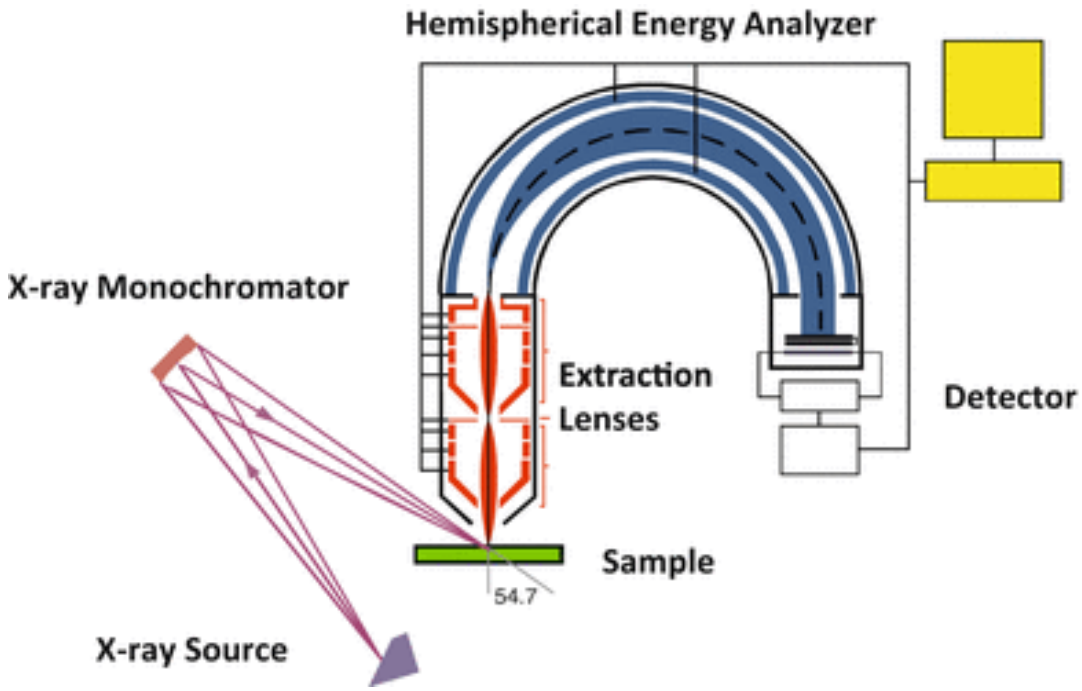


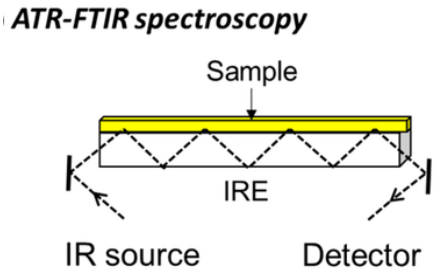
Figure 3-8. Schematic diagram of a X-ray photoelectron spectrometer [186].

Figure 3-8 shows schematic diagram of an X-ray photoelectron spectrometer. It consists of mainly a X-ray source, X-ray monochromator, extracting lenses, energy analyser and detector. The sample was irradiated with X-ray beam and kinetic energy and number of electron that escape from the material surface was measured simultaneously. The XPS also requires high vacuum (~ 10^{-8} milibar) or ultra high vacuum(< 10^{-9} milibar) conditions.An X-ray photoelectron spectroscopy (XPS, Kratos Axis Ultra Dld, Kratos Analytical Limited) was used to conduct the chemical analysis of the PFA films using Al Kα X-ray as the radiation source and the data was processed using CasaXPS software.

3.6.6 Fourier transform Infrared spectroscopy

This technique was used to obtain infrared spectrum of absorption or emission of a solid, liquid or gas. The raw data was transformed into signal by Fourier transformation. An attenuated total reflection FTIR machine operates by measuring the changes that occur in a totally internally reflected infrared beam when the beam comes in contact with the sample. An infrared beam was directed onto an optically dense crystal and the internal reflectance creates an evanescent wave that extends beyond the surface of the crystal into the sample held in contact with the crystal.





(a) (b)

Figure 3-9. (a) FTIR instrument and (b) schematic diagram of mechanism of FTIR machine on ATR mode [187].

Figure 3-9 (a) shows the FTIR instrument (Perkin Elmer, spectrum one) used for the analysis of the PFA emulsion and Figure 3-9 (b) depicts the working mechanism of the FTIR machine on attenuated total reflectance (ATR) mode.

3.6.7 X-ray Fluoroscence Spectrometer (XRF)

XRF spectrometer (Finder 100, Walopt) was used to measure the thickness of the deposited Polyfluoroacrylate coating. It can measure the thickness of the coating from 1 nm to 30 μm range. Accuracy of the instrument was ~ 3% with a measurement time of 1 min. The atomic composition of the substrate matrix and the measured layer must be known and it must have X-ray fluoroscenece characteristics.

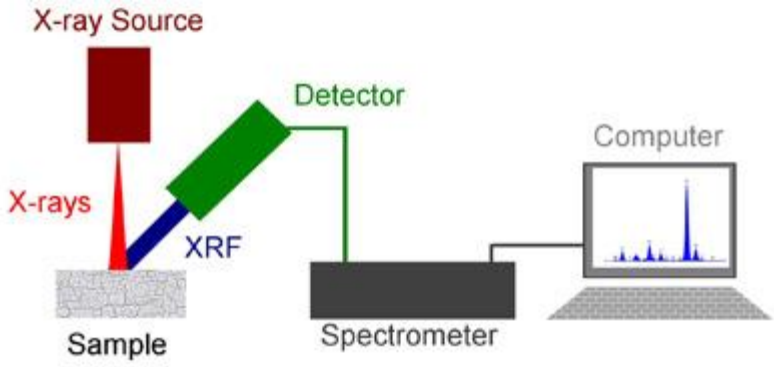


Figure 3-10. Schematic diagram of mechanism of X-ray Fluoroscence Spectroscopy [188].

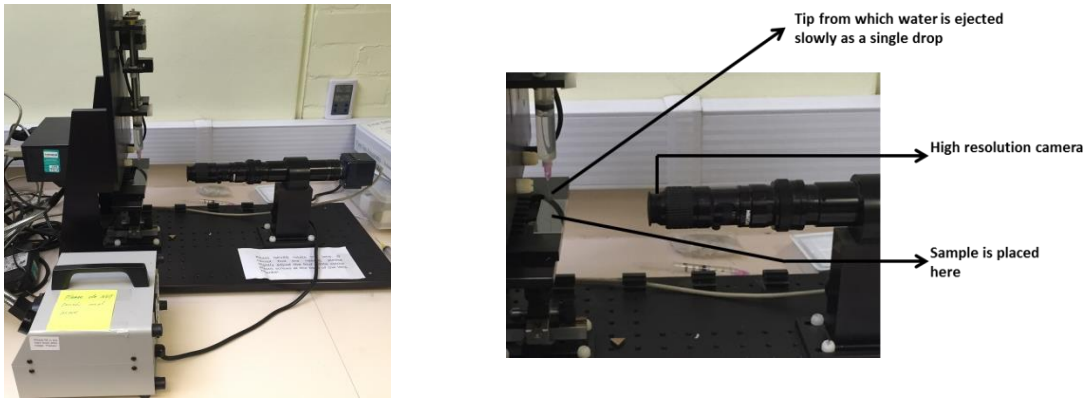
Figure 3-10 shows the schematic diagram of mechanism of XRF spectrometer An X-ray tube irradiates the sample and X-ray fluorescence occurs; a detector counts the incoming X-ray photons and measures their energies. The x-ray fluorescence spectrum is recoded and analysed.

3.7 Surface hydrophobicity measurement

3.7.1 Water contact angle and Contact angle hysteresis measurement

To test the hydrophobicity of the surface static water contact angle measurement and contact angle hysteresis measurement (First Ten Angstroms, Model: FTA200 dynamic contact angle system) were used. The basic principal was that water was ejected from a narrow tip so that only a single drop of water could form and it was dropped on the sample surface. The whole system was monitored by a high-resolution camera and with the image of the droplet on the surface and with the aid of computer program the water contact angle can be measured. For each contact angle measurement 5 times the experiment was repeated and their average value was recorded.

For water contact angle hysteresis (CAH) measurement advancing water contact angle and receding angle was measured. It measured the adhesion strength of the water droplet on the surface. A single water droplet was dropped on the substrate surface. The narrow tip of the water source was inserted inside the droplet and the water ran at a constant speed. With the increase in volume of water the droplet size increased and water contact angle changes. This gives the value of advancing water contact angle. Again the water is pumped in through the narrow tip and size of the water droplet decreases gradually as the volume decreases which in turn varies the water contact angle and that measures the receding water contact angle. The difference between the advancing and receding water contact angle gives the CAH value.



(a) (b)

Figure 3-11. (a) Water contact angle measurement instrument unit and (b) some important part of the instrument (ejecting tip, high resolution camera and sample bed).

Figure 3-11 (a) shows water contact angle measurement instrument and Figure 3-11 (b) shows the tip from which water was ejected slowly; high resolution camera was used to capture the image and the platform on which the sample was kept.

3.7.2 Surface energy measurement

Contact angle measurement technique is used to measure the surface energy and tension. Contact angle describes the shape of a liquid droplet resting on a solid surface. When drawing a tangent line from the droplet to the touch of the solid surface, water contact angle is the angle between the tangent line and the solid surface. If a liquid with well known properties is used, the resulting interfacial tension can be used to identify the nature of the solid. Table 3-11 shows the liquids used for the surface energy measurement and their corresponding surface tension values.

Table 3-11. The liquids employed and their known surface tension values, where γ_l is the liquid total surface tension, γ_l^d is dispersion component of liquid surface tension and γ_l^p is polar component of liquid surface tension.

Liquids	γ_l **(N/m)**	γ_l^d **(N/m)**	γ_l^p **(N/m)**
Distilled water	72.8	21.8	51
Formamide	58	39	19
Methilene Iodide	50.8	50.8	0

The surface free energy was calculated according to Owens-Wendt (OW) method. The principal assumption for the OW method is that the surface free energy is a sum of the two components : dispersion and polar components. The Owens-Wendt model is represented by the following mathematical formula [189] :

$$\frac{1}{2}(1+cos\theta)\gamma_l = (\gamma_s^d\gamma_l^d)^{\frac{1}{2}} + (\gamma_s^p\gamma_l^p)^{\frac{1}{2}} \qquad 3\text{-}1$$

Where:

θ = contact angle between the liquid droplet and surface

γ_l = liquid total surface tension

γ_l^d = dispersion component of liquid surface tension

γ_l^p = polar component of liquid surface tension

γ_s^d = dispersion component of solid surface free energy (unknown)

γ_s^p = polar component of solid surface free energy (unknown)

The value of total surface free energy of the solid is obtained by

$$\gamma_s = \gamma_s^d + \gamma_s^p \qquad 3\text{-}2$$

Dividing both sides of equation 3-1 by $(\gamma_l^p)^{\frac{1}{2}}$, it can be rewritten as :

$$\frac{\frac{1}{2}(1+cos\theta)\gamma_l}{(\gamma_l^p)^{\frac{1}{2}}} = (\frac{\gamma_l^p}{\gamma_l^p})^{\frac{1}{2}}(\gamma_s^d)^{\frac{1}{2}} + (\gamma_s^p)^{\frac{1}{2}} \qquad 3\text{-}3$$

The left hand side of the equation 3-3 contains quatities that are measured experimentally (θ) and available from the literature. So the plot of left hand side of equation 3-3 vs $(\frac{\gamma_l^p}{\gamma_l^p})^{\frac{1}{2}}$ gives a straight line with slope of $(\gamma_s^d)^{\frac{1}{2}}$ and intercept $(\gamma_s^p)^{\frac{1}{2}}$.

3.8 Evaluation of material and coating performance

3.8.1 Water impinging tests

Water impinging test measures the erosion resistance of the coating. To evaluate the durability, erosion tests under pressurized water impinging using an atomiser with a gas pressure of 15 psi, the velocity of 35–37 m/s and liquid flow rate of 72 mL/min were performed. Pressurized water with the droplet size of 12.7 μm (Sauter Mean Diameter) was sprayed onto the coated samples using a stainless nozzle (PNR UK Ltd) for the duration of 90 min. The distance between the tip of the nozzle and the substrate surface was also kept constant to 3 cm. The

substrate was weighed before and after the tests to measure any weight loss and the change in water contact angle.

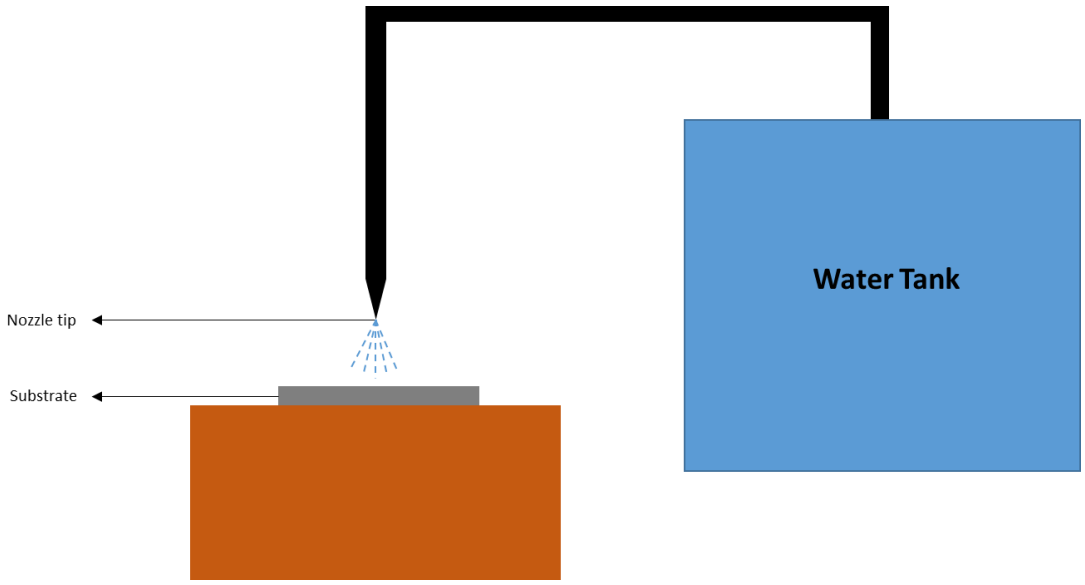


Figure 3-12. Schematic diagram of water impinging test setup.

Figure 3-12 shows a schematic diagram of water impinging test setup. The nozzle is connected to the water tank containing constant volume of water. Before the test samples were weighed and water contact angle (WCA) was measured. The water is ejected with high speed through the nozzle on the substrate surface. After the test, the samples were dried to remove any excess water. Finally water contact angle and weight were measured again to identify the changes.

3.8.2 Tensile test

The mechanical property of PFA polymer was determined by performing tensile test. During the experiment, a dog-bone shaped specimen with 10 mm length and 0.5 mm thickness was gripped at its two ends and was pulled to elongate at a determined rate of 0.1 mm/min to its breakpoint. A force of 20 N was applied by the machine.

For analytical purposes, a plot of stress (σ) versus strain (ε) was constructed during a tensile test experiment, which was done automatically on the software provided by the instrument manufacturer. Stress, in metric system, was measured in N/m^2 or Pa, such that 1 N/m^2 = 1 Pa. From the experiment, the value of stress was calculated by dividing the amount of force (F) applied by the machine in the axial direction by its cross-sectional area (A), which is measured prior to running the experiment. Mathematically, it was expressed in Equation 3-4. The strain values, which have no units, was calculated using Equation 3-5. In the equation, L is the instantaneous length of the specimen and L_0 is the initial length.

$$\sigma = \frac{F}{A} \tag{3-4}$$

$$\varepsilon = \frac{L - L_0}{L_0} \tag{3-5}$$

3.9 Ice adhesion tests

Ice adhesion tests measure the adhesion energy of the ice on the substrate surface. The tests were performed by centrifuge adhesion test method. A rotor holding the ice/substrate sample on one end and exact same weight on the other end was rotated at an increasing rotation speed. When the centripetal acceleration on the on the substrate induced by the rotation overcomes the ice adhesion strength it detaches from the substrate surface. Thus, the adhesion strength of ice to the substrate can be estimated as $F = mr\omega^2$ where m is the mass of ice, r is the rotor length and ω is the speed of rotation at detachment in rad/s. As a shear stress, the adhesion stress is $\tau = F/A$, where A is the ice/substrate contact area.

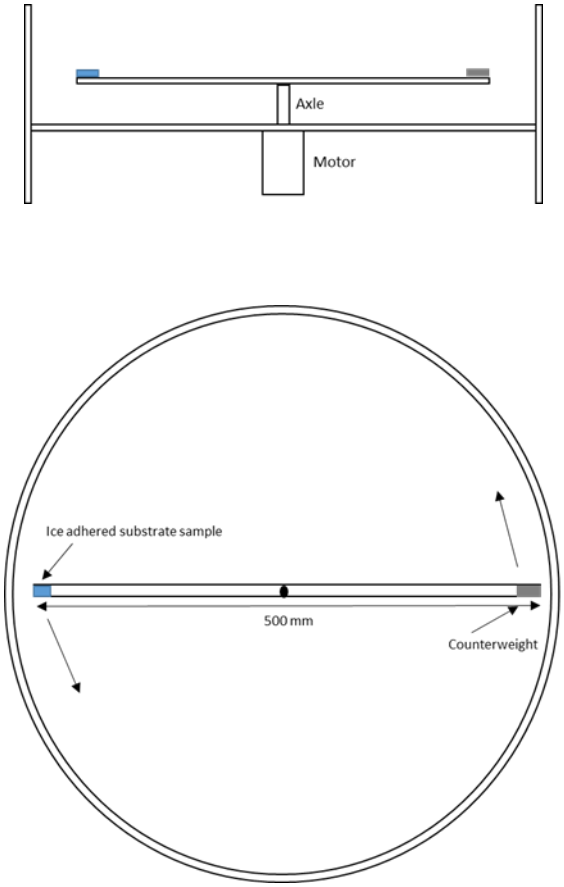


Figure 3-13. Schematic diagram of centrifuge ice adhesion test device with rotor driven by a motor in a stainless steel casing. The ice/substrate sample on one end and counterweight on the other end. The rotor was spun at increasing rate until detachment of ice [190].

Figure 3-13 shows a schematic diagram of ice adhesion test setup. The length of the rotor blade is 500 mm. The volume and shape of the ice was kept constant so the area of contact between the ice and substrate was constant throughout. The whole system was maintained at a temperature of -10 °C.

3.10 De-icing energy efficiency test

The de-icing tests are also important to measure the time required to remove the ice attached on the substrate surface. The main concept is that electrical energy is provided to the substrate which in turn converts into heat energy, it heats the

substrate and the ice detaches from the substrate surface. The time of detachment of the ice is noted and compared with uncoated substrate. Thus efficiency of the coating is measured.

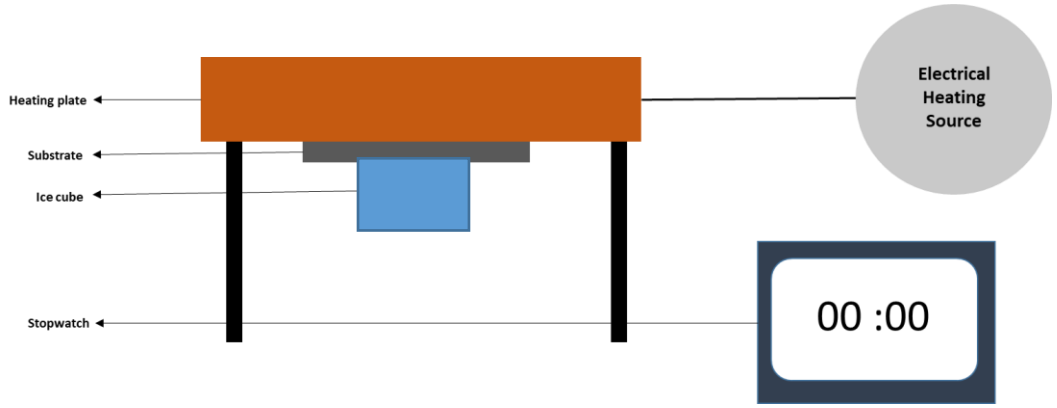


Figure 3-14. Schematic diagram of de-icing test set-up.

For the de-icing tests the substrates were attached with the heating plate as shown in Figure 3-14. The volume and shape of the ice cube was kept constant in each case so the contact area remains same. The whole system was monitored with a camera to record the detachment time. The electro-thermal heating tests were performed using a home-made testing facility on a cold plate with a setting temperature of −30 °C. The distance between the sample and cold plate was 5.5 cm. The ice blocks with the weight of 8 g were frozen on the samples. A heating element driven by a power supply with a voltage of 15 V and a current of 0.09 A started to heat once the temperature reached −5 °C. The ice blocks would drop when the ice melted at the interface.

3.11 Statistical analysis

The experiments were repeated 10 times or more in each case. The experimental conditions of each of these sets were kept constant including temperature,

pressure, concentration and surrounding gas environment. Standard deviation (SD) for each of these sets were calculated and added to the graphical reprentation where appropriate.

4 Synthesis, mechanism of polymerization and characterization of polymer properties of PFA emulsion

4.1 Introduction

Polymers are widely used for coating purposes as the property of the polymers can easily be altered and it is a cost effective solution. In addition polymer coatings have several other advantages as compared to metal coatings. Polymers are more resistant to chemicals than their metal counterparts, as metal coatings also require post-treatment finishing unlike polymers. It is lightweight than metal and hence can be used for lightweight applications. One of the main applications of polymeric coating is for superhydrophobic and icephobic applications including corrosion protection, anti-biofouling, transparent coatings etc. Nanocomposite coating of acrylic polymer resin and organosilane modified silica can produce effective superhydrophobic property [25]. Another commercially used polymer coating for superhydrophobic applications is polytetrafluoro ethylene (PTFE) [191]. The present coating systems are not cost-effective and curing temperature of the coatings are usually very high. In this work polyfluoroacrylate emulsion was synthesized which has substantially low curing temperature and can easily be synthesized with a low-temperature polymerization process. The polymer has hydrophobic properties and also can be used for anti-icing applications.

In this chapter synthesis process of polyfluoroacrylate emulsion will be discussed followed by a possible reaction mechanism for the process. The possible structures of the synthesized polymer will also be predicted. Thermal stability of the polymer will be established along with the curing temperature. Later in this chapter the polymer will be analysed and different elements present in the polymer will be

determined and their relative amount will also be investigated. The mechanical property of the polymer will also be evaluated. Finally, the effect of different process parameters for the synthesis of the polymer will be discussed along with the reaction mechanism. The polymer will be characterized and effect of concentration of the reactant will also be discussed leading to the determination of the structure of the polymer.

4.2 Design of the polymer structure

Polyfluoracrylates have ultralow surface tension and related hydrophobicity, it has very good antichemical property and thermostability as well as excellent mechanical behaviour [173, 181, 192, 193]. For the synthesis of polyfluoroacrylate emulsion, several approaches can be taken. Mainly the synthesis of polymers can be classified in many categories like step-growth polymerization, condensation polymerization and chain-growth polymerization [194]. Hexamethylene diisocyanate functional groups of polyfluoropolyether (PFPE) monofunctional macromonomers have been grafted on a poly(butyl methacrylate-*co*-hydroxyethyl acrylate-*co*-ethyl acrylate) random terpolymer. The synthesis process is a radical solution polymerization in tetrahydrofuran (THF) using an initiator [181]. Again paraxylene bisdialkyl suldonium salts can be polymerized via condensation as well as additional polymerization methods leading to various polymers including poly(p-xylylene), poly(p-xylylidine), poly(xylylene sulphide)s, poly(xylylene oxide)s etc [195]. Also depending on the degree of crosslinking and polymerization mechanism the polymer can be thermoplastic or thermoset and hence a wide variety of properties.

Synthesis processes of the polymer are highly dependent on temperature, the initial concentration of the reactants, initiator concentration, pressure and other surrounding conditions. This will be discussed later in this chapter. Depending on

the conditions different polymers and oligomers can be formed. The size of the molecular chain also depends on the polymerization synthesis method. For the synthesis of styrene-based polyfluroacrylate emulsion, the detailed process is discussed in the previous methodology section. It is a co-polymer and formed via theradical co-polymerization method.

4.3 Possible Structure and Reaction Mechanism of Polyfluoroacrylate Polymers

4.3.1 Possible structures of the polymers

Styrene, acrylic acid and heptafluorobutyl acrylate are being used as starting material. With different reaction mechanism and respect to the different starting materials, a range of different products can be formed. In reality for any polymerization process always more than one product is formed but the relative amount of the products dictates the main product and the by-products. The following co-polymers can be formed apart from the homopolymers of styrene, acrylic acid and heptafluorobutyl acrylate:

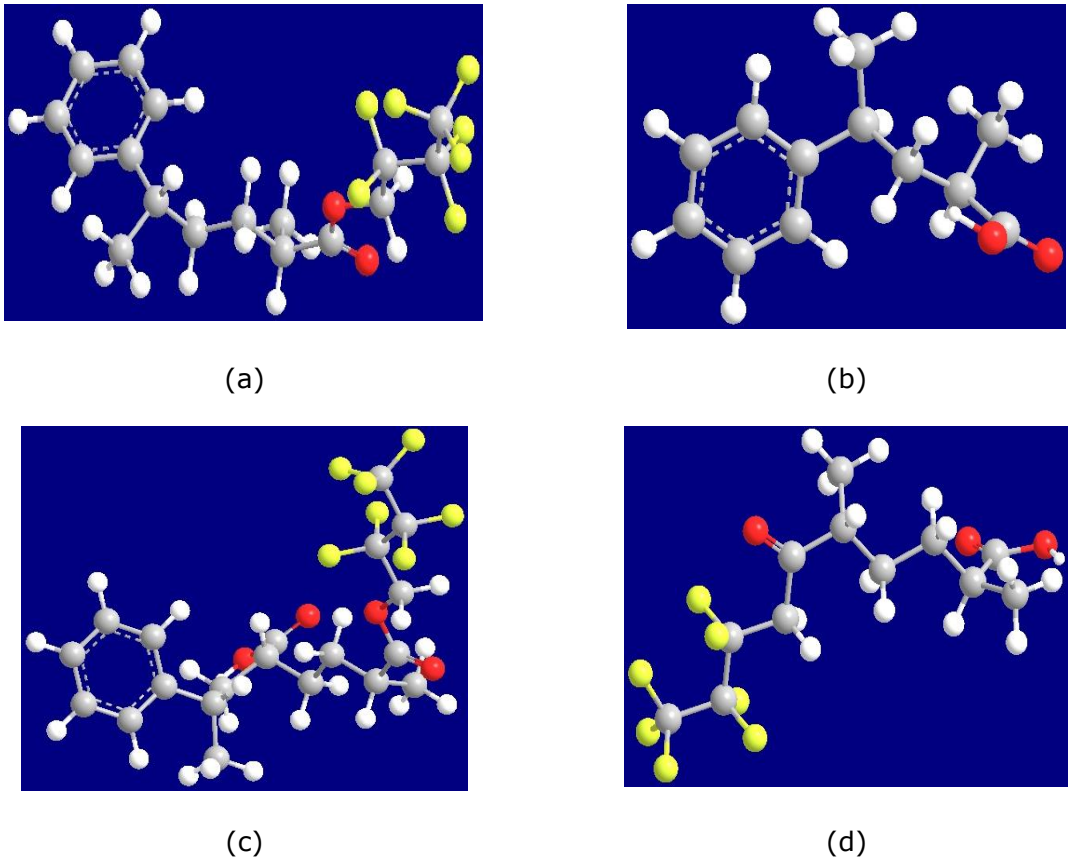


Figure 4-1. Possible polymer structures combining styrene, acrylic acid and heptafluorobutyl acrylate (a) co-polymer of Styrene and heptafluoro butyl acrylate, (b) co-polymer of styrene and acrylic acid, (c) co-polymer of styrene acrylic acid and heptafluorobutyl acrylate and (d) co-polymer of acrylic acid and heptafluorobutyl acrylate. The red atoms are oxygen atoms, the yellow is fluorine, the white atom corresponds to the hydrogen atoms while the grey atoms are carbon.

Figure 4-1 (a-d) shows the possible co-polymer structures that can be formed by a combination of styrene, acrylic acid and heptafluorobutyl acrylate as monomer. The actual structure of the polymer can be concluded only after the compositional analysis of the emulsion. These are the co-polymers of styrene and heptafluoro butyl acrylate, co-polymer of styrene and acrylic acid, co-polymer of styrene acrylic acid and heptafluorobutyl acrylate and co-polymer of acrylic acid and heptafluorobutyl acrylate respectively. In addition to the above co-polymers there is also probability of formation of homopolymers of styrene, acrylic acid and heptafluorobutyl acrylate. For any polymerization reaction it is very likely to form

more than one product. Always several polymers with a range of molecular weight are formed [196].

4.4 Characterization of the polymers

4.4.1 Thermal Analysis

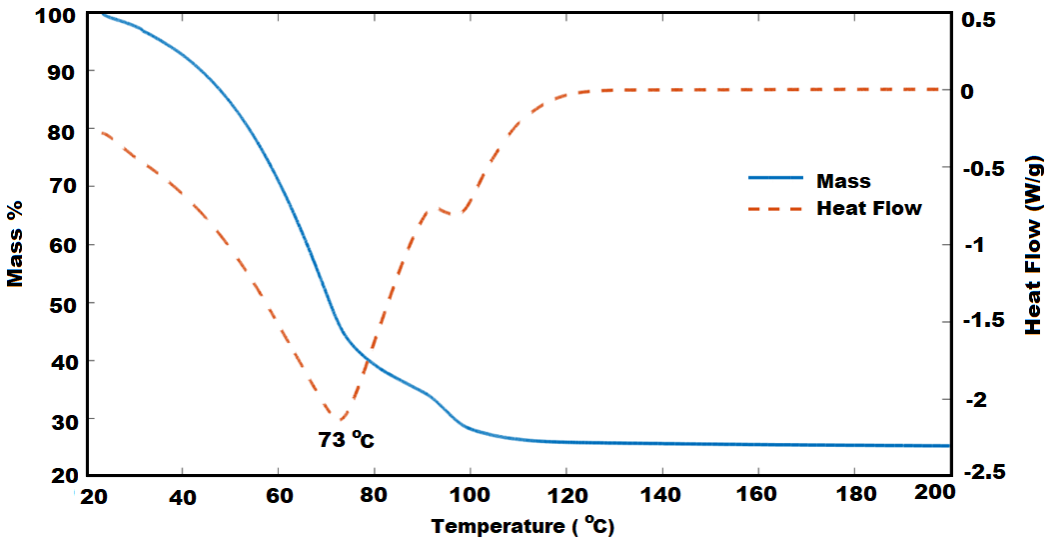


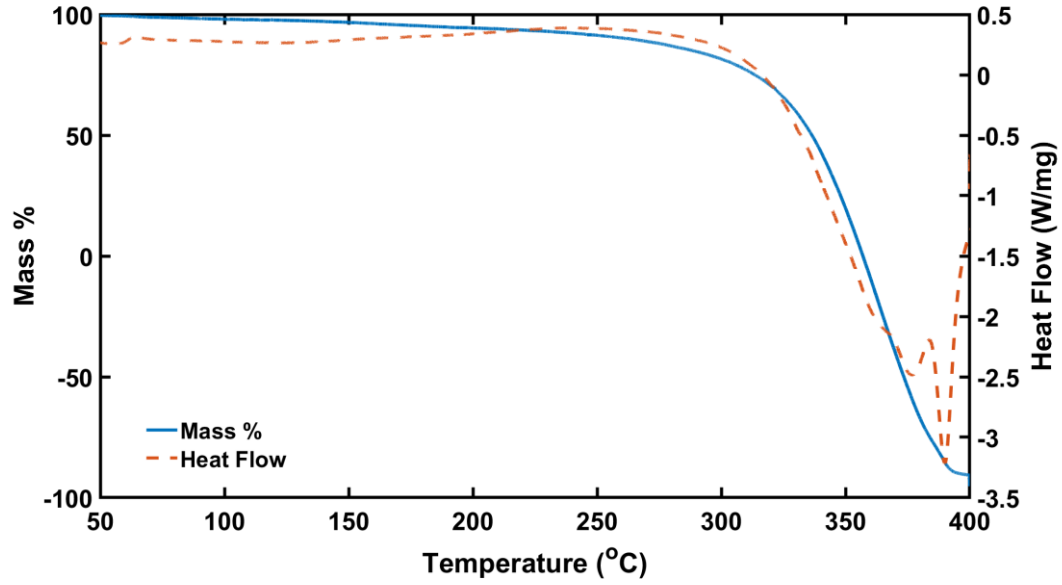
Figure 4-2 Variation of mass change (wt%) and heat flow of PFA emulsion (PFA 10.1) with increasing temperature.

Figure 4-2 shows the variation of Mass % and Heat flow% through PFA 10.1 sample when the temperature was increased at a rate of 2 °C/ min. The temperature was varied from room temperature till 200 °C. Initially, both the heat flow and the mass decrease rapidly as the temperature increases to 73 °C, attributing to the evaporation of the solvent (e.g. water). After 73 °C, the heat flow of the sample gradually increases, indicating the start of curing of the sample, while the mass continues to decrease and becomes stable after 100 °C. The heat flow of the sample increases until 120 °C and then keeps at 0, indicating that no more reaction occurs after 120 °C. It is suggested that the curing temperature of the polymer

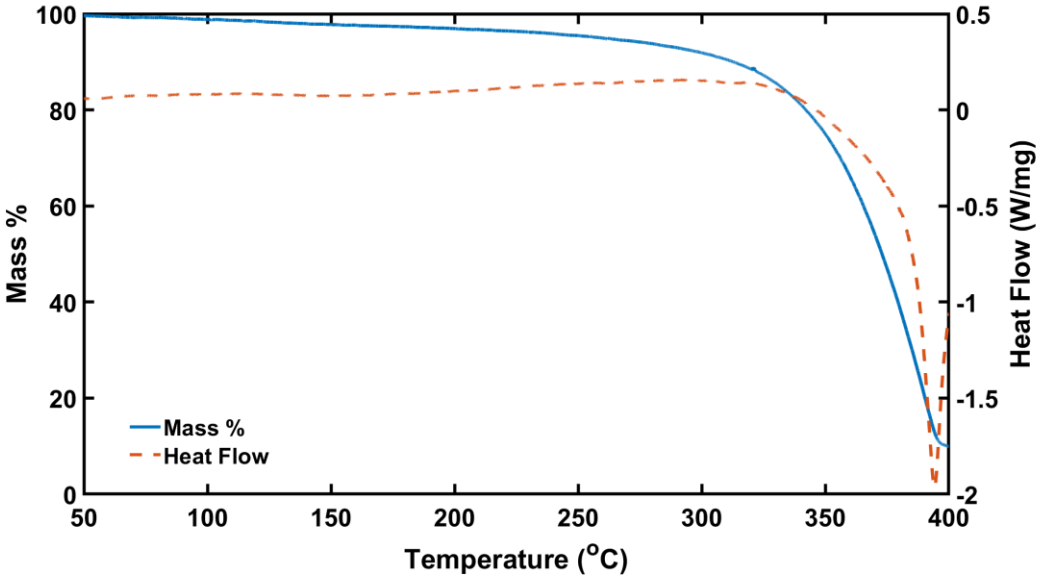
ranges from 73 to 120 °C. The tested polymer cannot be re-melted and maintains a stable state at a high temperature, reflecting a thermosetting nature.

The thermal stability analysis of the polymer and the curing temperature determination was done by thermogravimetric (TGA) and differential scanning calorimetric (DSC) method.

The thermal stability of the polymer is determined by TGA and DSC analysis. Figure 4-3 (a) represents the change in mass% and heat flow with temperature. With increasing temperature initially there is little or no loss in weight percentage as indicated by the blue line, meaning there is no major change in the PFA emulsion at that temperature range. With the higher temperature around 300 °C there is a gradual start of decrease in mass percentage followed by drastically drop in mass percentage at around 317 °C indicating a major change in the polymer composition. The initial small decrease in mass may be attributed to the evaporation of some left water. Again the red line represents the variation of heat flow of the sample with temperature and time. Up to 300 °C there is no significant difference in heat flow between the reference and the sample but after that the heat flow through the sample gradually increased indicating that heat is consumed by the sample and hence may be some bond breaking or bond making is taking place and finally leading to dissociation. For polytetrafluoroethylene (PTFE) the physical transformation starts at 327 °C, but does not undergo rapid thermal decomposition below 450 °C [197]. So for high-temperature application PTFE is a more desirable choice and hence used for non-stick coatings for pans and cook wares [198].



(a)



(b)

Figure 4-3.TGA and DSC analysis data for PFA emulsion containing styrene, acrylic acid and heptafluorobutyl acrylate in the molar ratio of (a) 1:1:1 and (b) 1:1:2 respectively.

In Figure 4-3 (b) the green curve depicts the change in mass percentage with the reaction temperature. Like Figure 4-3 (a) here also the curve initially shows a little or no loss until temperature 300 °C. After 300 °C there is a gradual decrease in mass % indicating a change in the compound and hence the compound is thermally

stable till 300 °C. Beyond 310 °C there is a sudden drop indicating a decomposition of the compound and hence the polymer composition.

In both the cases the polymer is stable up to temperature of 300 °C as evident by the change in weight percentage and heat flow. Hence it can be used for moderately high- temperature operations. The decrease in weight percentage may be contributed to the decomposition of the polymer into smaller fragment and it is also supported by the decrease in heat flow data. As with the decrease in fragment size the heat flow value decreases as well.

Several other samples with different fluorine content were also analysed by TGA and DSC analysis. But in all the cases no substantial difference in temperature is being observed indicating that the thermal behaviour of the polymer is independent of the fluorine content of the polymer.

4.4.2 Characterization of different bonds

The different bonds in the polymer sample and the raw materials are characterized by FTIR analysis technique.

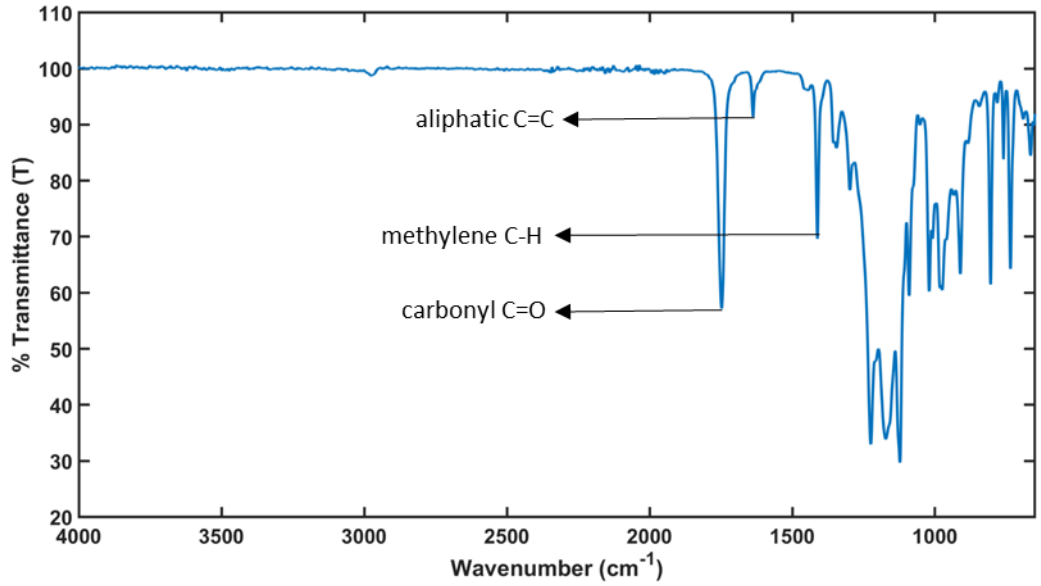


Figure 4-4. FTIR spectrum of heptafluorobutyl acrylate used as one of the raw materials for the synthesis of PFA emulsion.

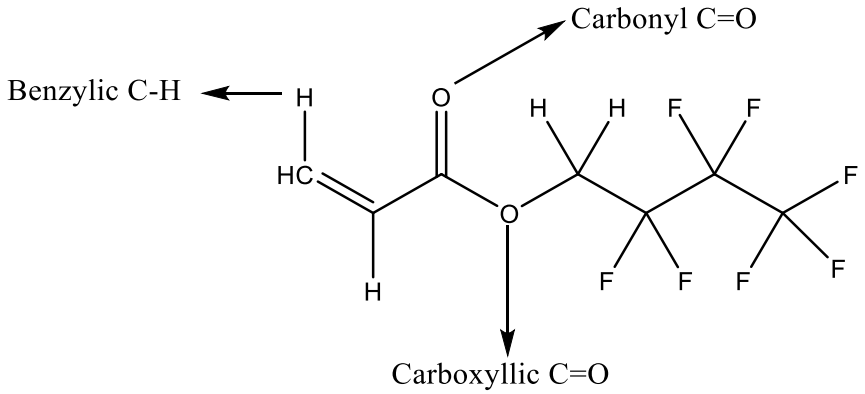


Figure 4-5. Chemical Structure of 1H,1H- Heptafluorobutyl acrylic acid with all different bonds.

Figure 4-4 represents the absorbance spectrum for pure heptafluorobutyl acrylate and Figure 4-5 shows the chemical structure of heptafluorobutyl acrylate with all different bonds present in it. The aliphatic C=C bond frequency is observed around 1625 cm^{-1} as a sharp peak. At around 1420 cm^{-1} the methylene C-H frequency is also observed. The peak around 1750 cm^{-1} with a shoulder is associated with the carbonyl C=O bonds followed by C-O of the ester group. The absorbence peaks of $-CF_3$ and $-CF_2$ groups are observed between 1300-700 cm^{-1} range [199].

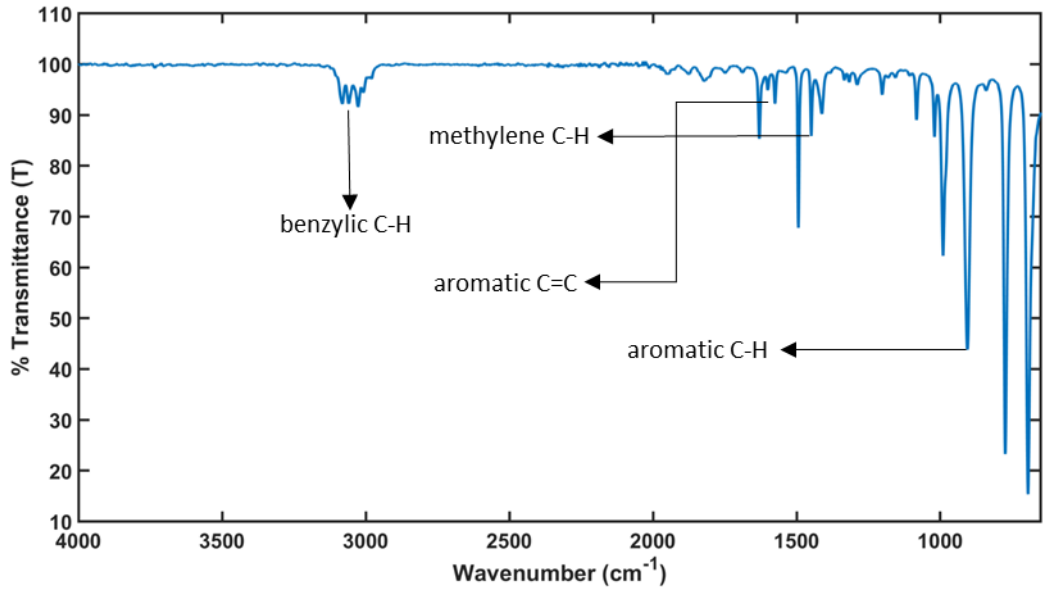


Figure 4-6. FTIR spectrum of styrene used as one of the raw materials for the synthesis of PFA emulsion.

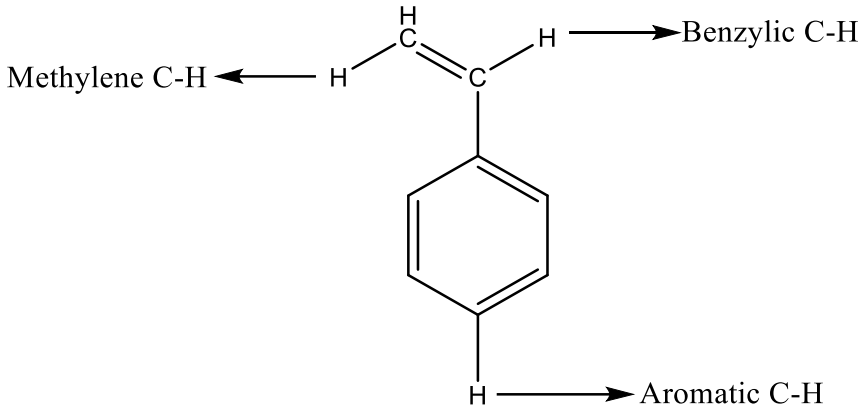


Figure 4-7. Chemical structure of styrene with all different bonds.

Figure 4-7 shows the chemical structure of styrene with all different bonds present in the structure. The spectrum in Figure 4-6 represents the absorbance peaks for pure styrene. The peak around 1460 cm^{-1} corresponds to the methylene group of styrene. The range of absorptions between 1900-1600 cm^{-1} is associated with the C-C double bond of the aromatic ring. The small peaks beyond 3000 cm^{-1} are due to the benzylic C-H bond frequency. The peaks on or below 1000 cm^{-1} correspond to the aromatic C-H bond frequencies of ortho meta and para positions [200].

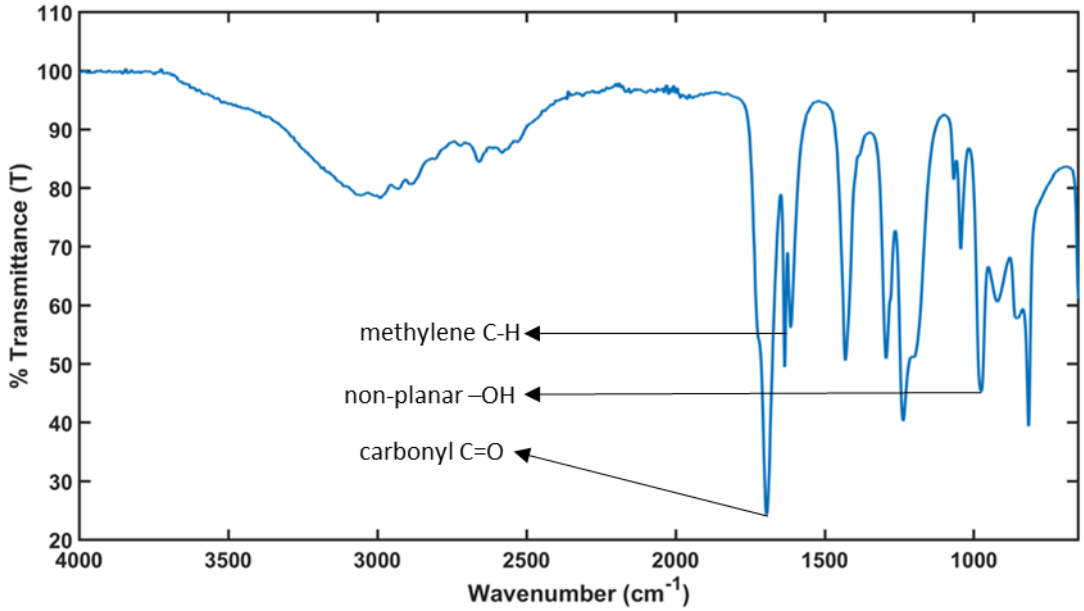


Figure 4-8. FTIR spectrum of acrylic acid used as one of the raw materials for the synthesis of PFA emulsion.

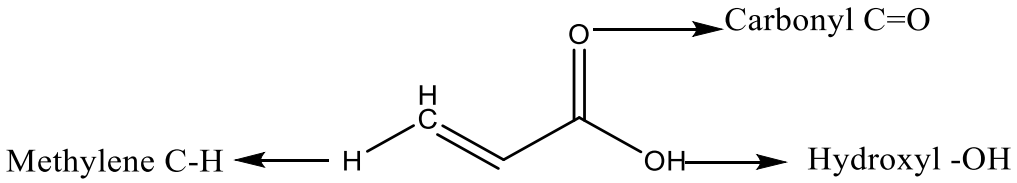


Figure 4-9. Chemical Structure of acrylic acid with all the different bonds present.

Figure 4-8 shows the FTIR spectrum for Acrylic acid. The chemical structure of acrylic is acid is relatively simple with all the bonds is shown Figure 4-9. Again a peak observed around 1620 cm^{-1} indicating the presence of methylene C-H group. For the carbonyl C=O, a sharp peak is observed at 1750 cm^{-1}. The stretching frequencies around 950 cm^{-1} are associated with the non-planar –OH stretching frequencies [201].

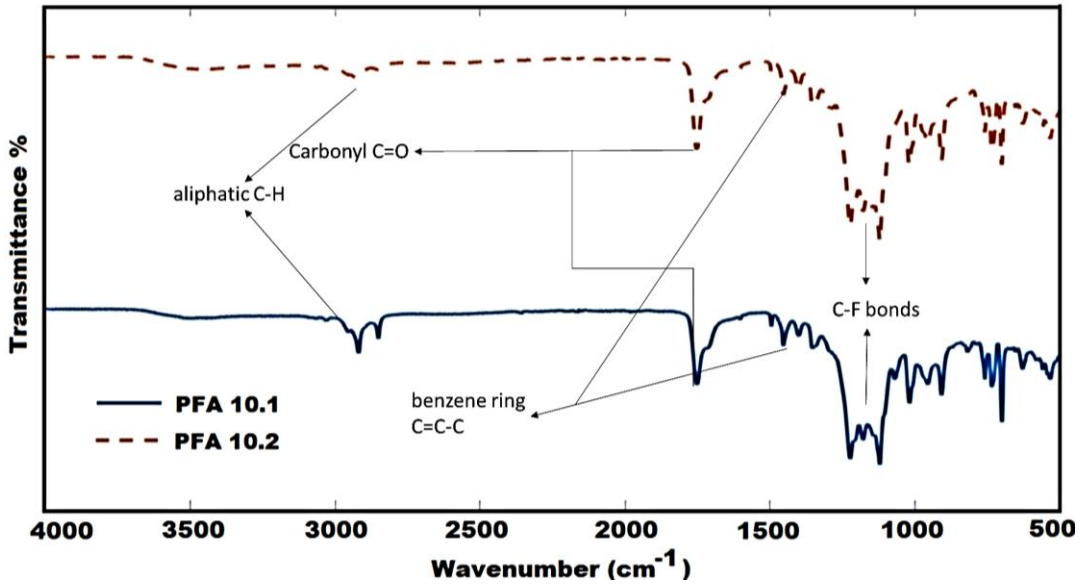


Figure 4-10.FTIR spectra of PFA emulsion synthesized from 1:1:1 and 1:1:2 molar ratio of styrene, acrylic acid, and heptafluorobutyl acrylate PFA10.1 and PFA 10.2 respectively.

Figure 4-10 shows the FTIR analysis of a PFA emulsion containing molar ratio of styrene, acrylic acid and heptafluorobutylacrylate as 1:1:1 and 1:1:2 respectively. As compared to PFA 10.1 the amount of fluorine is doubled in PFA 10.2. The spectra are similar in the appearance of the peaks for these two PFAs, as are their structures. But the spectra are different in the variability in the intensity of the peaks for these two PFA emulsions.

It can be seen from Figure 4-10 that no C=C characteristic peak is observed between 1660-1630 cm^{-1} [202], indicating that polymerization of the monomer occurred. The small peaks obtained at 2852 cm^{-1}, 2920 cm^{-1} and 3030 cm^{-1} frequency correspond to aliphatic C-H stretching bonds [203]. Several peaks (1604cm^{-1}, 1496cm^{-1} and 1456cm^{-1}) are obtained between 1450-1610 cm^{-1} and that matches with the benzene ring C=C-C stretches confirming there is a benzene ring present in the result PFA products. The two strong peaks at 700 and 758 cm^{-1} relate to the monosubstituted benzene ring and hence presence of styrene units in the result products [204]. The absorption at 2852 and 2920 cm^{-1} shows aliphatic

(saturated) C-H groups. A sharp peak is obtained at 1750 cm^{-1} which corresponds to the presence of carbonyl, C=O, in ester group and the shoulder at 1716 cm^{-1} corresponds to the presence of carbonyl in carboxylic acid group. A wide peak around 3400-3500 cm^{-1} relates to the O-H stretching vibration and the other peak at 909 cm^{-1} corresponds to the non-planar angular vibration of O-H group in carboxylic acids [202]. The FTIR indicates the presence of acrylic acid structural unit acid in the result products. The $-CF_3$ group absorbs at 1350 cm^{-1}. Several complex absorption peaks between 1280-1120 cm^{-1} are attributed to the $-CF_2$ group. $CF-CF_3$ group absorbs strongly at 735 cm^{-1}. Since the intense carbonyl peak at 1750 cm^{-1} belongs to the ester group, there is heptafluorobutylactrylate structural unit in the result products [205].

The amount of monomer units in the PFA emulsion is determined by calculating the relative absorbance of absorption bands as A/A_0 using the baseline method, where A_0 is the internal standard. In this study, the benzene ring C=C-C stretching vibration peak of styrene unit at 1604 cm^{-1} is taken as the internal standard [202]. The calculation results show that the amount of acrylic acid unit in the PFA10.2 is slightly more than that in the PFA10.1 and the amount of the heptafluorobutylactrylate unit in the PFA10.2 is significantly more than that in the PFA10.1.

By comparing the above the FTIR data it is observed that irrespective of the fluorine content each time the same type of peaks are obtained with indicating that each time same type of compound is being formed with no additional different types of bond. So reaction mechanism and products remain unaltered. So amount of heptafluorobutylactrylate doesn’t affect the mechanism of the reaction.

4.4.3 Detection of elements in Polyfluoroacrylate emulsion

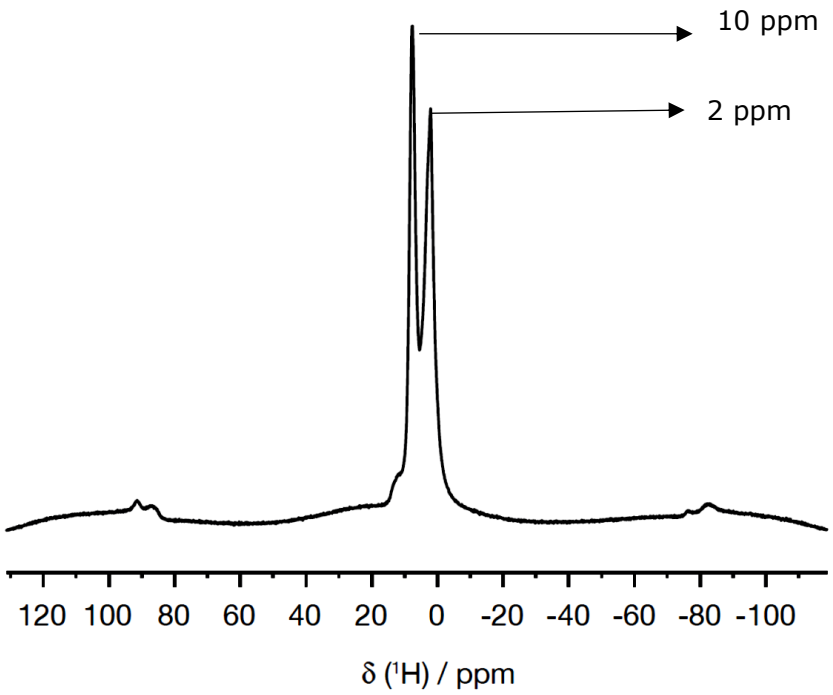


Figure 4-11. 1H NMR analysis data for PFA emulsion containing 16.6 wt% of fluorine.

Three types of NMR analysis are done ^{1}H, ^{13}C and ^{19}F NMR to determine the groups that are present in the synthesized PFA emulsion. Figure 4-11 ^{1}H spectrum shows two peaks which means that in the compound there are two types of hydrogens present and both of them are in totally different environment. Both of the signals are sharp and intensity is high indicating they are quite different from each other. Two peaks are obtained at 2 ppm and 10 ppm respectively. The starting materials were styrene, acrylic acid and heptafluorobutyl acrylate and hence two types of hydrogen present: aromatic hydrogen of the benzene ring and aliphatic hydrogen atom from the other two monomers. The existence of two peaks in the final product indicates that the aromatic ring of styrene remains in the final product and no ring opening reaction has taken place. The peak with high chemical shift from zero (10ppm) is for the aromatic hydrogen coming from the styrene. The chemical shift for aromatic hydrogens is usually in the range of 5-7 ppm [206] but here the

chemical shift is higher as the aromatic ring is substituted by a large aliphatic chain. Other peak with relatively lower chemical shift value (2 ppm) is for the aliphatic hydrogens.

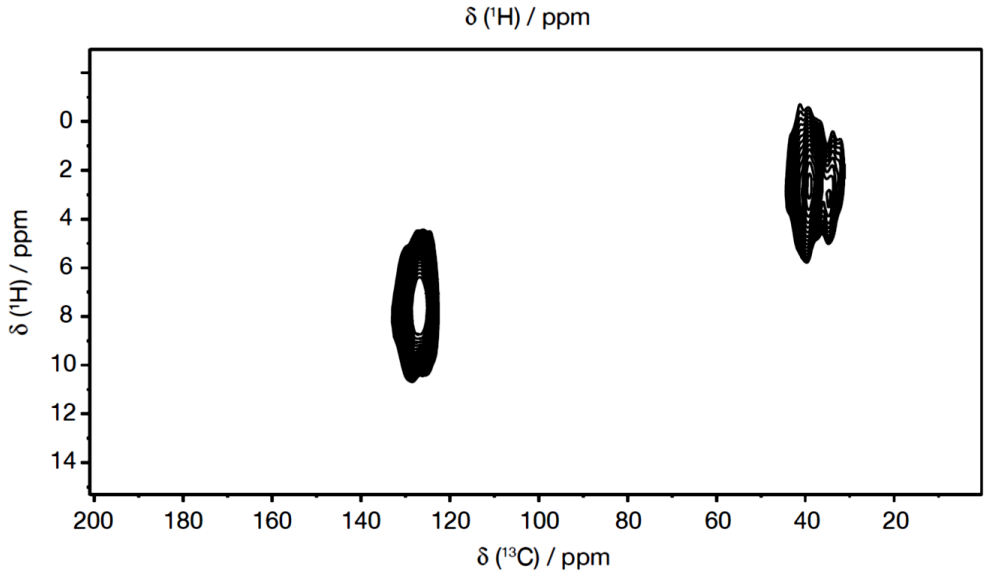


Figure 4-12. ^{13}C NMR analysis data for PFA emulsion containing 16.6 wt% of fluorine.

To support the result obtained from ^{1}H NMR analysis further ^{13}C NMR is being done. Figure 4-12 depicts the ^{13}C NMR peaks for the same PFA emulsion. It also shows two peaks supporting the result obtained by the ^{1}H NMR and concluding that there are two different types of C atoms in the compound. Similarly, the peak with high chemical shift in the region of 120-140 ppm [207] corresponds to the carbon atom in an aromatic ring coming from styrene. The greater chemical shift for aromatic carbon atom is due to the high electron density on the aromatic ring. The chemical shift region of 20-40 ppm corresponds to aliphatic carbon atom. The ^{13}C NMR also supports the result obtained for ^{1}H NMR in Figure 4-11.

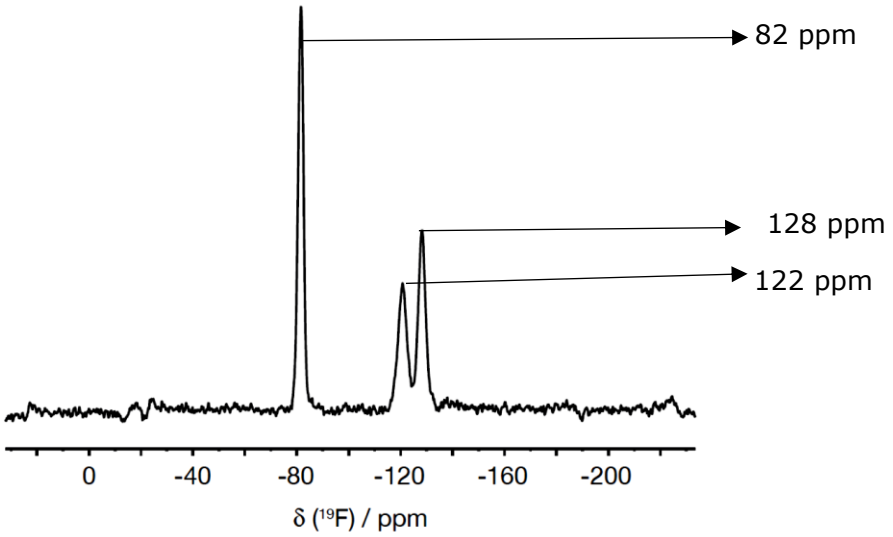
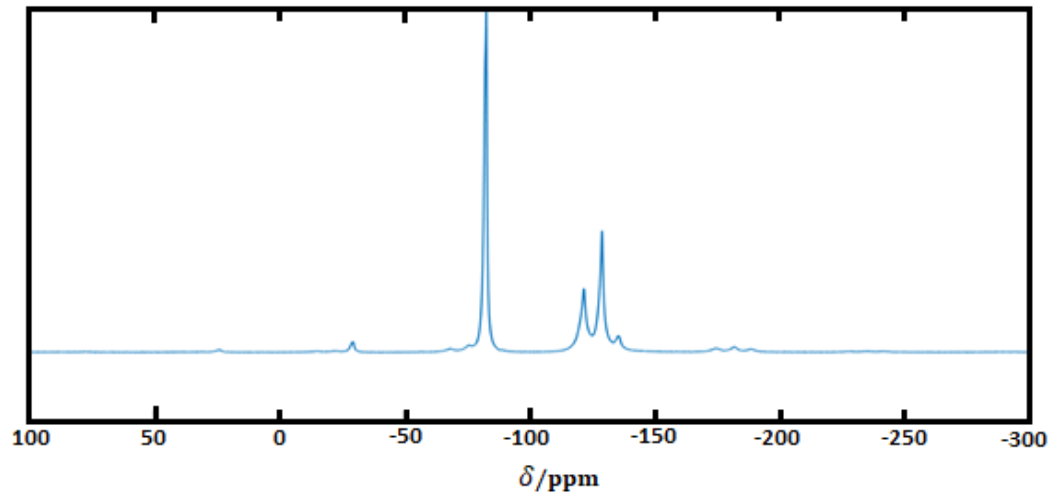


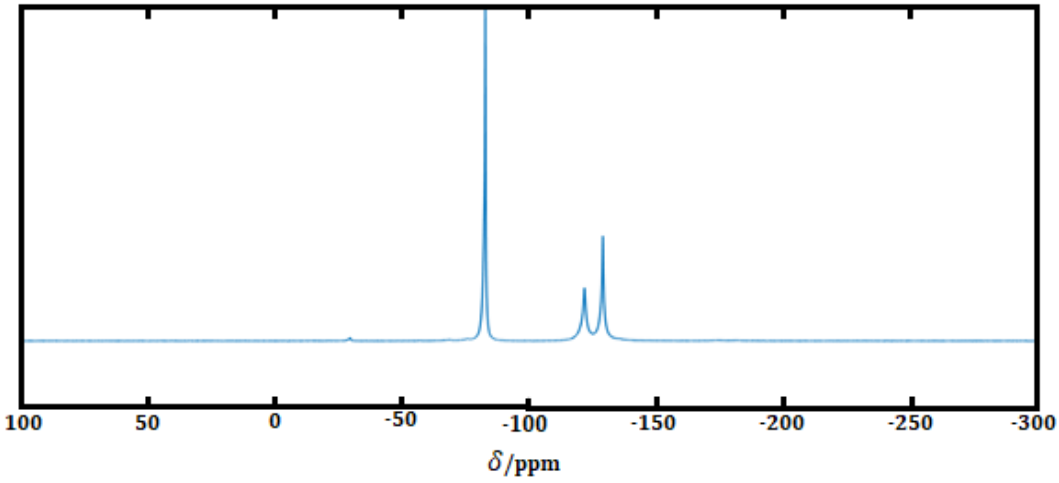
Figure 4-13. ^{19}F NMR analysis data for PFA emulsion containing 16.6 Wt% of fluorine.

Finally, ^{19}F NMR in Figure 4-13 shows three peaks at 82 ppm, 122 ppm and 128 ppm. This peaks corresponds to $-CF_3$, $-CF_2$ and $-CF_2$ respectively of heptafluorobutylacrylate. So the group present is CF_3-CF_2-CF_2- [208]. The two $-CF_2$ group will give different peaks as their surroundings are different. The peak at 128 ppm corresponds to the $-CF_2$ group that is directly attached to the CF_3 group as it is expected due to the higher interaction with greater number of fluorine atoms. The peak at 122 ppm corresponds to the other $-CF_2$ group and ultimately the peak at 82 ppm corresponds to the $-CF_3$ group fluorine atoms. These peaks also integrate to 3:2:2 respectively for CF_3:CF_2:CF_2 indicating that no other fluorine groups are present.

4.4.4 Comparison of fluorine content in the polyfluoroacrylate emulsion



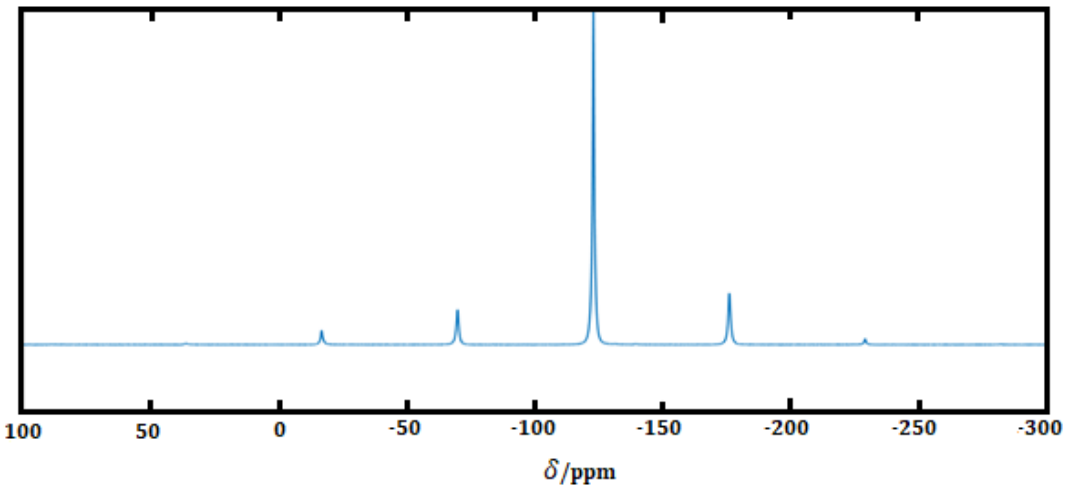
(a)



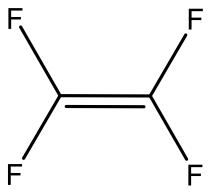
(b)

Figure 4-14. ^{19}F NMR analysis of (a) PFA10.1 and (b) PFA 10.2.

Figure 4-14 (a) and (b) shows 19 F NMR peaks of PFA 10.1 and PFA 10.2 respectively. In both cases, peaks are obtained at 83 ppm, 122 ppm and 129 ppm. It indicates in both cases the $-CF_2-CF_2-CF_3$ group got incorporated in the polymer structure.



(a)



(b)

Figure 4-15. (a) ^{19} F NMR analysis of reference polytetrafluoroethylene (PTFE) and chemical structure of tertrafluoroethylene.

When the 19 F NMR of reference PTFE is done a single peak is obtained -123 ppm chemical shift as shown in Figure 4-15 (a). This result supports the chemical structure of PTFE depicted in Figure 4-15 (b). Though there are four fluorine atoms in the structure, all the fluorine atoms are in exact same chemical environment. So chemical shift values for all the fluorine should be same and hence only single high-intensity peak is obtained.

4.4.5 Elemental Analysis of the synthesised PFA emulsion

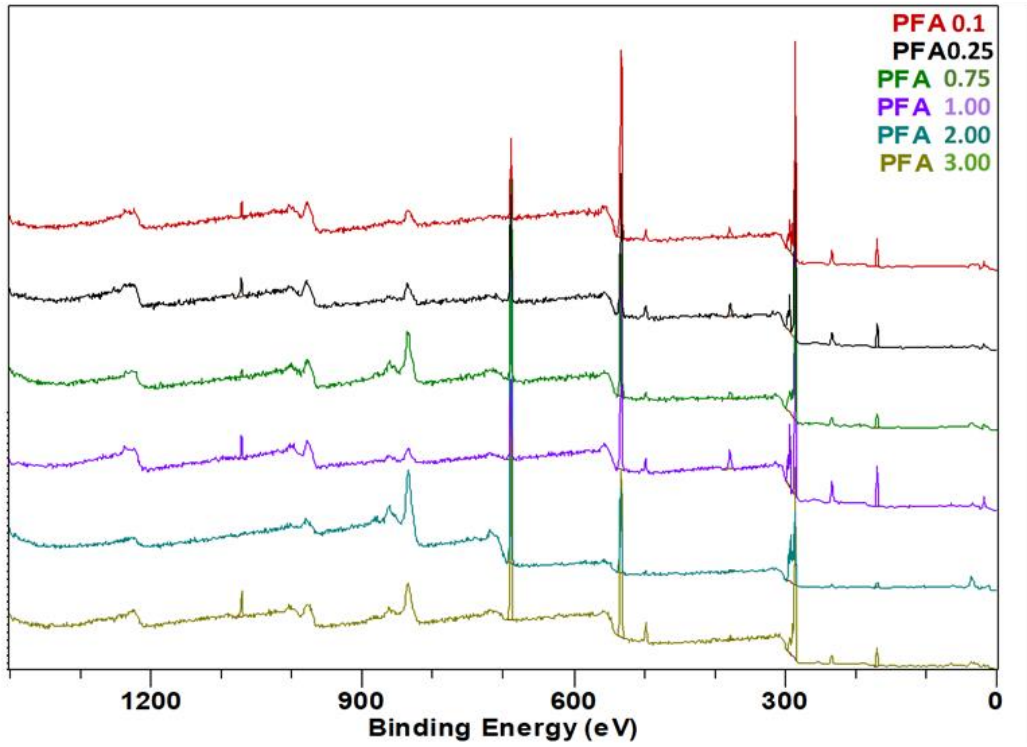


Figure 4-16. XPS spectra from one area on each sample, showing that all samples are similarly dominated by fluorine (F), oxygen (O), carbon (C) and sulphur (S) peaks.

Figure 4-16 shows XPS spectra of PFA samples containing a constant amount of styrene and acrylic acid and various amount of heptafluorobutylacrylate. The molar ratio of styrene and acrylic acid was kept constant at 1:1. The molar ratio of heptafluorobutylacrylate was varied from 0.1 to 3.

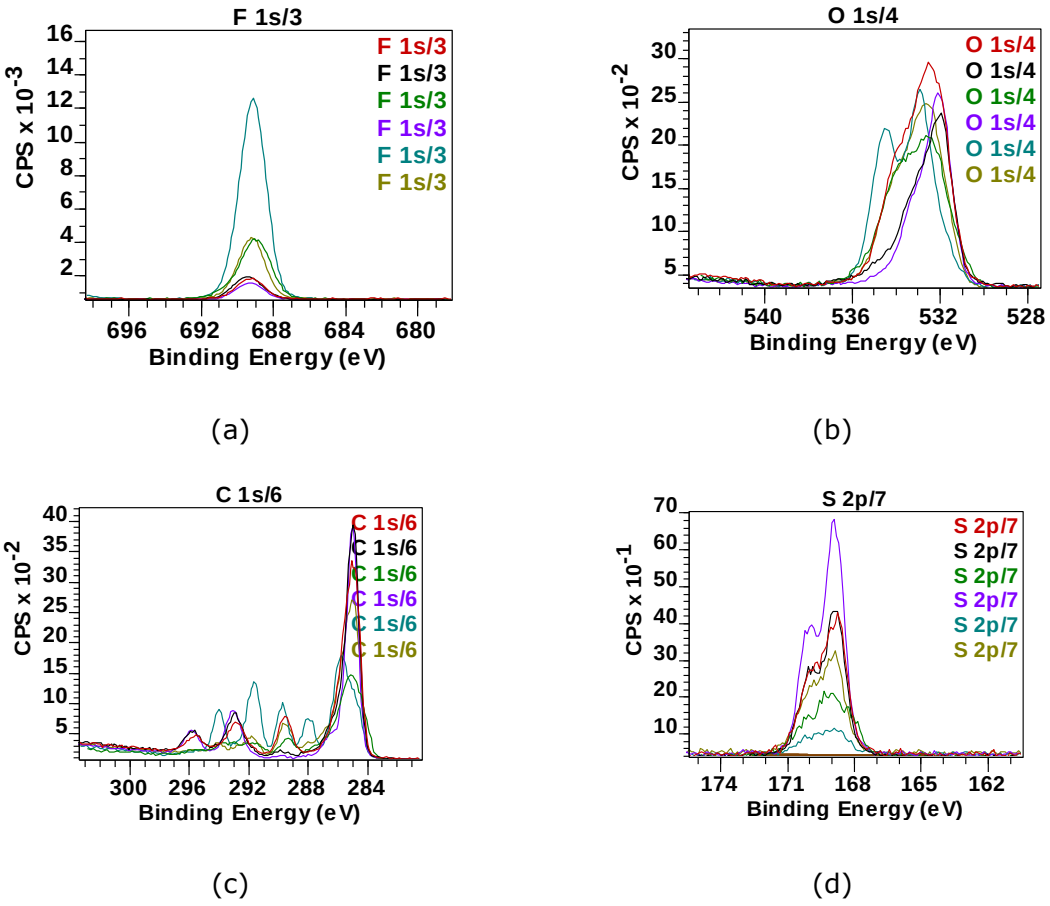
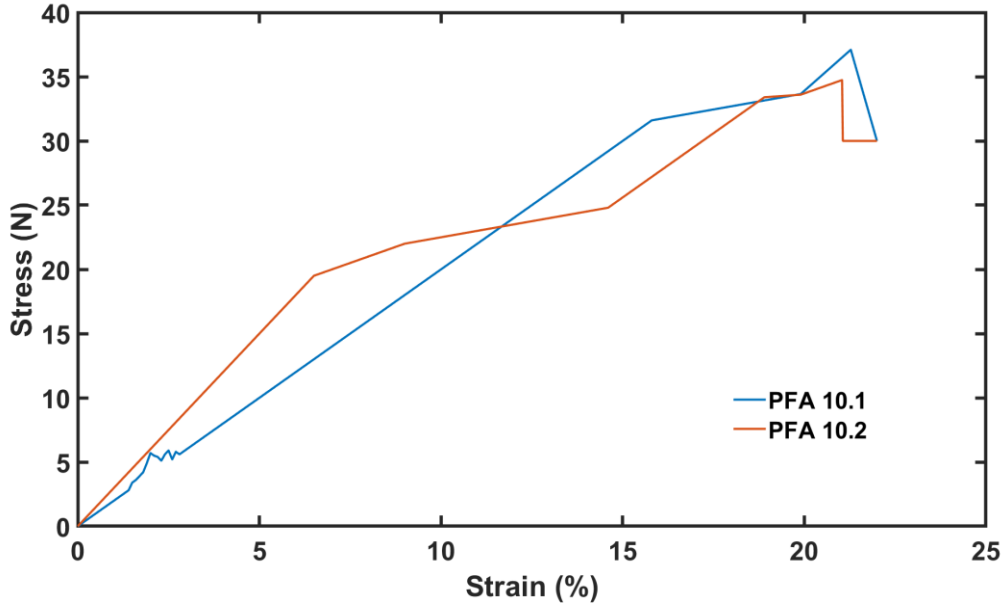


Figure 4-17. High-resolution spectra for all PFA samples, key as wide scan in Figure 4-16.

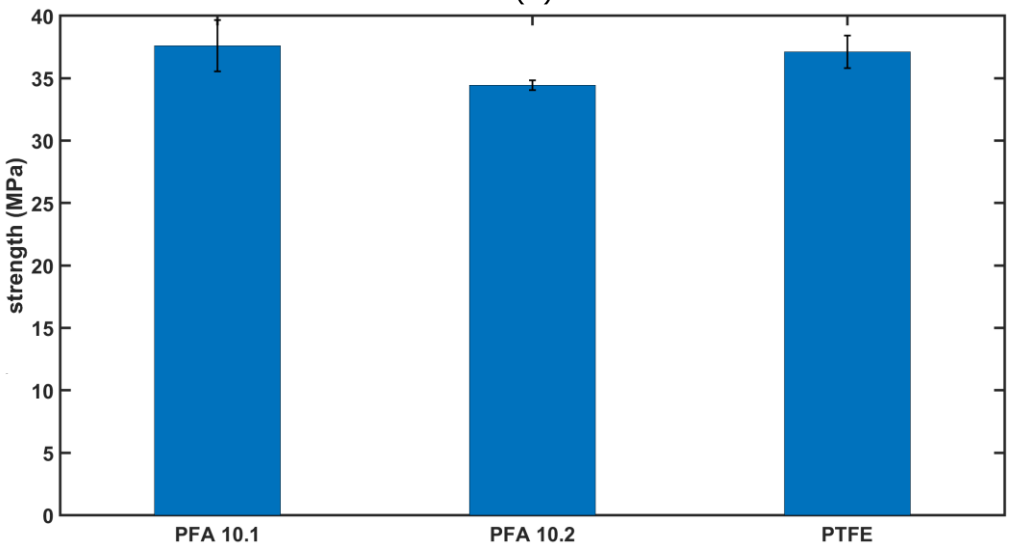
The wide scan of PFA sample spectra shown in Figure 4-16 is given in Figure 4-17(a-d). The dominant fluorine (F), carbon (C) and oxygen (O) signals are attributed to the monomers styrene, acrylic acid and heptafluorobutyl acrylate. The sulphur (S) signal is from the initiator potassium perdisulfate. The binding energy of organic fluorine F1s ranges between 688-689 eV which matches with the experimental data. This fluorine solely comes from heptafluorobutyl acrylate (HBA) monomer. Again the binding energy for oxygen comes at 533 eV characteristic for carbonyl C=O oxygen coming from acrylic acid. The binding energy for carbon C1s ranges from 286-296 eV. The sharp peak at 286 eV is for the C-C, again the peak near 290 eV is standard for O-C=O.

4.5 Mechanical testing for the polymer

Ultimate tensile strength



(a)



(b)

Figure 4-18.(a) stress vs strain graph for PFA 10.1 and PFA 10.2 and (b)comparison of average ultimate tensile strength of PFA 10.1, PFA10.2 and PTFE.

Figure 4-18 (a) shows the stress strain curve for the polyfluoroacrylate emulsion PFA10.1 and PFA10.2. The ultimate tensile stress (UTS) of PFA10.2 is slightly lower than that of PFA10.1 Tensile strength of the polyfluoroacrylate polymer was measured and compared with that of poly tetrafluoroethyle (PTFE). Figure 4-18

(b) shows the average ultimate tensile strength values for PFA 10.1, PFA 10.2 and PTFE respectively. The tensile strength of PFA is comparable to that of standard PTFE which is above 35 MPa. The value is also comparable to that of mostly used polymeric material like polystyrene, polypropylene etc [209]. When moved from PFA 10.1 to PFA 10.2 the fluorine content doubles as mentioned before but there is also a slight decrease in tensile strength as evident from the graph. With the increase in fluorine content the polymer structure changes and more heptafluorobutylacrylate group gets incorporated in the main polymer chain framework.

4.6 Surface energy

Table 4-1 shows the comparison of surface energy of synthesized PFA emulsions with respect to polytetrafluoroethylene (PTFE). The surface energy is calculated using Owens-wendt model, water , methyl iodide and formamide was used as testing liquid. All the tests were performed at room temperature. The total surface free energy is measured as a sum of dispersion component of surface free energy (γ_s^{disp}) and polar component of solid surface free energy (γ_s^{pol}) . It is observed that the surface free energy of synthesized PFA emulsions are slightly lower than the PTFE film. Thus making it desirable for low surface enrgy applications. When the concentration of fluorine doubled in the PFA emulsion the surface energy reduced from 19.66 to 19.15 (N/m), with further increase in fluorine content in the PFA emulsion, the surface free energy further changes to 19.17 (N/m).

Table 4-1. Comparison of surface free energy of synthesized polyfluoroacrylate emulsions with standard poly tetrafluoro ethylene.

Sample Name	Total Surface Free Energy (γ_s^{tot})(N/m)	Dispersion component of solid surface free energy (γ_s^{disp}) (N/m)	Polar component of solid surface free energy (γ_s^{pol}) (N/m)
PTFE	21.35	20.31	1.04
PFA 10.1	19.66	19.58	0.08
PFA 10.2	19.15	18.97	0.18
PFA 10.3	19.17	19.04	0.13

4.7 Discussion

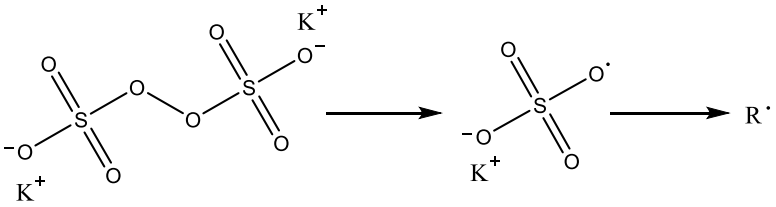
4.7.1 Effect of different fluorine content on the polymer composition

From the reaction kinetics the reaction is a co-polymerization of styrene, acrylic acid and heptafluorobutyl acrylic acid. Now for a A-B-C type of polymerization the molar concentration of the monomers should ideally be 1:1:1. But concentration of heptafluorobutyl acrylate is varied to get different polymer as mentioned in the earlier chapter. The molar ratio of heptafluorobutyl acrylate is varied from 1 to 2 and the corresponding 19F NMR data shown in Figure 4-14. It shows that the CF_2-CF_2-CF_3 groups are in same chemical environment otherwise some change for chemical shift in the position is expected. So irrespective of the fluorine content the reaction product remains same.

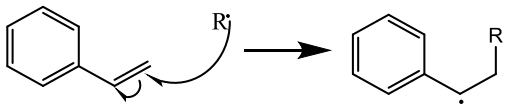
Comparing the ^{19}F NMR results of PFA 10.1 and 10.2 with that of PTFE as shown in Figure 4-14 and Figure 4-15 it can be concluded that there are three different environment fluorine atoms present in the synthesized PFA emulsion and hence three distinguished peaks with substantial chemical shift difference are obtained.

4.7.2 Reaction mechanism of the polymer

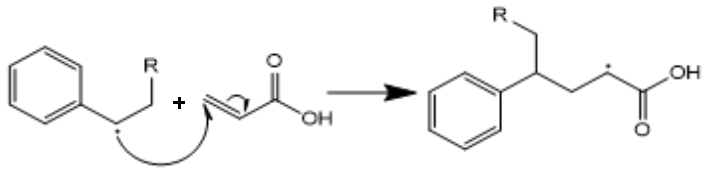
The reaction goes via radical random polymerization reaction. Potassium perdisulfate dissociates and acts as an initiator for the polymerization reaction. The reaction occurs at 80 °C in a reflux condenser and the final crosslinking occurs at 80 °C for 2hrs. For simplification only one unit of each monomer is used to show the polymerization reaction. In reality for a random co-polymerization reaction the number of units of monomer cannot be controlled. Stepwise reaction mechanism for the synthesis of PFA emulsion is given below.



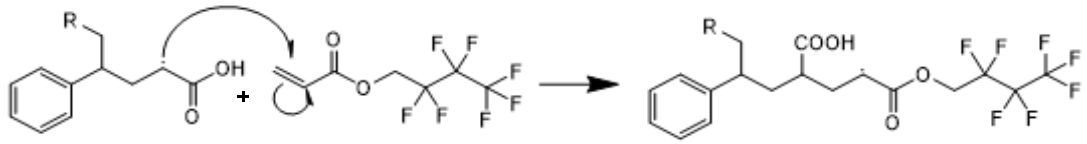
Reaction 4-1

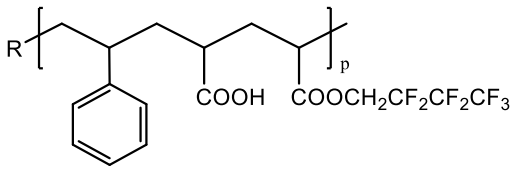


Reaction 4-2

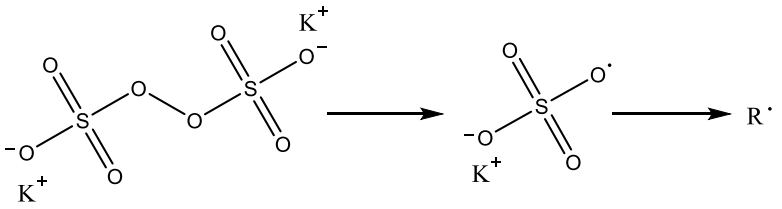


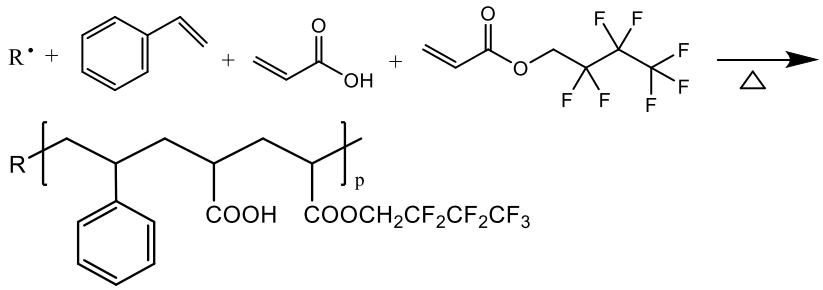
Reaction 4-3





Reaction 4-1 and Reaction 4-2 can be combined and written as follows





Reaction 4-4

The above reaction mechanism shows radical polymerization reaction of styrene, acrylic acid and heptafluorobutyl acrylate. Potassium persulfate (KPS) in this reaction acts as an initiator. It dissociates along the –O-O- bond and forms the initiator as shown in Reaction 4-1. The initiator concentration is important as the rate of the reaction for radical initiated polymerization reactions are directly dependent on it [210]. The rate of decomposition of KPS also follows the first-order reaction kinetics and the rate of reaction increases at elevated temperature [211]. Also the presence of free monomolecular dispersed sodium dodecylsulfate (SDS) promotes the decomposition of KPS whereas some SDS molecules form micelle and get adsorbed on the polystyrene particles and hence do not contribute to the decomposition of KPS [212]. The free radical formed by the decomposition of KPS attacks the $-C_2H_3$ group of styrene and forms another radical as shown in Reaction 4-2. It attacks the outer carbon atom of $-C_2H_3$ group due to less steric hindrance.

The activated styrene then reacts with the outer carbon atom of C=C of acrylic acid and forms an oligomer of radical of styrene and acrylic acid depicted in Reaction 4-3. The reaction further continues as the radical produced in Reaction 4-3 reacts with the C=C of heptafluorobutyl acrylate and forms an A-B-C type of building block of the polymer. The reaction further continues unless all the monomers are completely converted into polymers. The monomers are mixed in 1:1:1 molar ratio and stirred vigorously before the start of the polymerization process to ensure all the monomers are mixed uniformly and the reaction occurs uniformly as well. The reaction continues at elevated temperature and when it is cooled the initiator again recombines and the final polymer is formed.

4.7.3 Role of concentration of fluorine in the polymerization process

Several PFA polymers were prepared with different fluorine content and keeping all the other process parameters the same as mentioned in the previous chapter. Now the concentration of fluorine is most important as it directly influences the hydrophobic property of the polymer.

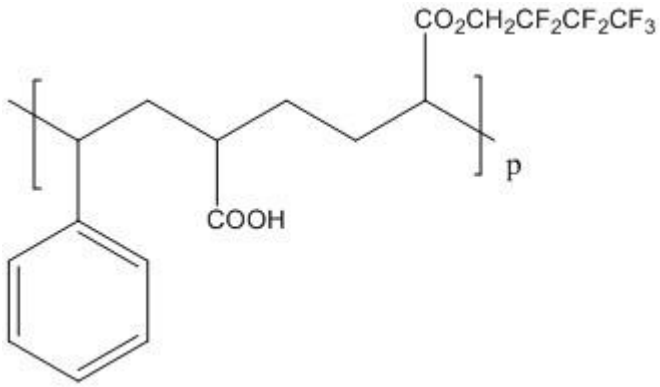
As evident from the FTIR spectra, there is no difference in spectral data and relative amount of fluorine also cannot be predicted from the FTIR spectrum data. So to determine relative amount of fluorine X-ray photoelectron spectroscopy technique is used shown in Figure 4-16 and Figure 4-17.

The atomic percentage of carbon (C), oxygen (O) and fluorine (F) of key samples containing a various concentration of heptafluorobutyl acrylate (HBA) is given in Table 4-2. It is observed that with the increase in molar ratio of HBA the atomic percentage of fluorine increases in the sample and a maximum of 34 atomic % of fluorine reached when the molar ratio of heptafluorobutyl acrylate and with further increase in concentration of heptafluorobutyl acrylate the atomic % of fluorine does not increase by any significant amount .

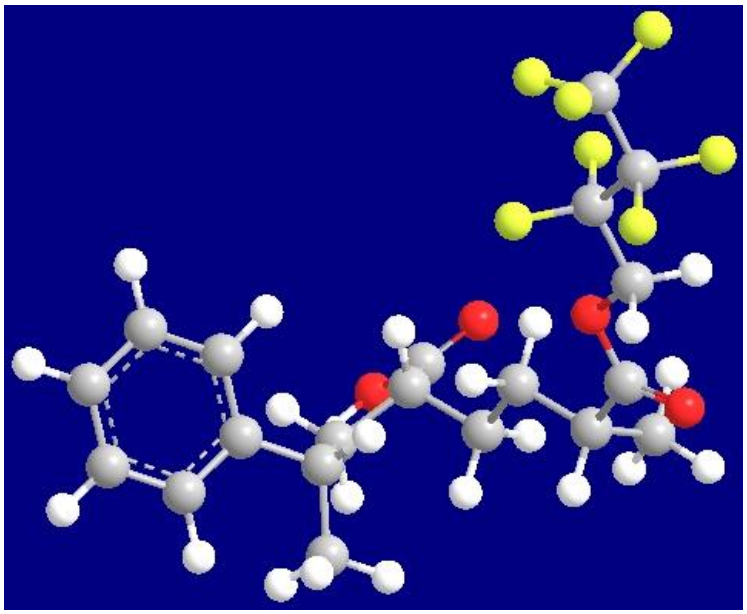
Table 4-2. Atomic contents of major elements of PFA films produced from different HBA/styrene molar ratios.

HBA/styrene ratio	C 1s %	F 1s %	O 1s %
0.75	54.4	26.0	19.5
1.00	54.0	28.9	17.0
2.00	48.5	34.0	18.6
3.00	47.8	34.2	18.0

4.7.4 Structure of the PFA polymer



(a)



(b)

Figure 4-19.(a) 2D and (b) 3D structures of probable co-polymer of styrene acrylic acid and heptafluorobutyl acrylate containing 1 unit of each. The red atoms are oxygen atoms, the yellow are fluorine, the white atom corresponds to the hydrogen atoms while the grey atoms are carbon.

After the FTIR and NMR analysis results the most convincing structure is co-polymer structure containing styrene, acrylic acid and heptafluorobutylacrylate. So the most probable structure of the polymer is proposed in Figure 4-19 consisting

of each monomer unit. The number of monomers in each unit is not fixed as expected from a random co-polymerization reaction. The fluorine groups are towards the surface and can provide good hydrophobicity when deposited on substrate surface. The presence of all the groups and bonds are confirmed from the FTIR and NMR analysis data as shown in previous sections. This is the most probable structure of the polymer formed before crosslinking. The other products as discussed in section 4.3.1 may also be formed in small amounts as the reaction is not very selective but the amount of other product is very small as compared to the main product.

4.8 Summary

Polyfluoroacrylate emulsion was synthesized via random radical co-polymerization reaction of styrene, acrylic acid and heptafluorobutyl acrylate. The polymer will be used as a coating on aluminium substrates for low surface energy applications. The polymer was synthesized and cured at a low temperature of 80 °C. The polymer was characterized by FTIR, NMR and XPS analysis. Thermal properties of the polymer were evaluated with TGA and DSC analysis. The yield tensile strength of the polymer was also determined and compared to that of commercially available PTFE as a reference. The key findings of the chapter were summarised as follows

The curing temperature of the PFA was 80 °C which is relatively low and the polymer is thermally stable till 300 °C as indicated from the TGA and DSC analysis. The surface energy calculation shows that for polyfluoroacrylate emulsion the average surface energy is 19 N/m which is comparable to that of commercially available PTFE (21 N/m). It is due to the incorporation of the fluorine group in the branched polymer chain.

FTIR and NMR analysis proves the incorporation of all the monomers (styrene, acrylic acid and heptafluorobutyl acrylate) in the PFA unit. The specific number of

monomer units in the polymer cannot be predicted as it was a random polymerization. The schematic atomic structure of the polymer has been predicted. XPS analysis reveals atomic percentage of fluorine in the PFA. It was observed that with the increase in molar concentration of heptafluorobutyl acrylate, the fluorine content increases in the final PFA. When the molar ratio of styrene, acrylic acid and heptafluorobutyl acrylic acid was 1:1:2, the concentration of fluorine went upto 34 % in the polymer.

The ultimate tensile strength of the synthesized polymer PFA 10.1 and PFA 10.2 were 37 MPa and 35.5 MPa which are comparable to that of PTFE 36.7 MPa which is widely used for commercial purposes. The polymer is also found to be thermoset in nature and hence cannot be melted once cured.

5 Surface treatment of aluminium substrate and the deposition of polymer coating on the treated substrate

5.1 Introduction

As mentioned earlier, one of the main requirement for a super hydrophobic surface is the surface morphology. The synthesized polymer is deposited on the modified aluminium substrate surface. Mainly three processes are used for this purpose: anodisation, chemical etching and deposition of nano and micro particles. The detailed experimental process is described in section 3.3. Two different techniques: Spin coating and spray coating are also used to deposit the synthesized polyfluoroacrylate emulsion on aluminium substrate surface. Spin coating is a relatively easy process and the uniformity of the coating depends on the competition between centrifugally driven drainage of the liquid film and concentration-based evaporation of the solvents. The coating process is more suitable for volatile solvent [213]. Thin film transistor of high molecular weight poly(3-hexylthiophene) has been fabricated by depositing by spin coating process [214]. On the other hand the spray coatings can be uniformly applied for a range of coating materials.

In this chapter the surface morphology of the aluminium substrate surface will be modified and characterized after different surface modification process. The surface roughness will also be characterized. The PFA polymer will be deposited on the modified surface and change in surface roughness will be studied. The erosion resistance properties of the coating is also measured with water impinging test. Finally the surface morphology of the coating substrates will be compared by different surface treatment process along with surface roughness variation. The role of concentration of etching agent, treatment time and treatment temperature will be discussed for chemical etching process, and the effects of concentration of

anodising agent and nanoparticles for surface modification will also be studied. Finally the erosion resistance will be compared on the substrate surface.

5.2 Surface modification of aluminium substrate

Mainly three approaches were used for surface modification: anodisation, chemical etching and nanoparticle deposition. All the process parameters were altered to achieve micro/nanoscale surface roughness and morphology.

5.2.1 Anodisation

Alminium substrates were cleaned, dried and electropolished before anodisation process. The detailed menthod of anodisation is given in section 3.3.2. The effect of reaction temperature, current density, treatment time and concentration of the electrolyte on the surface morphology is compared.

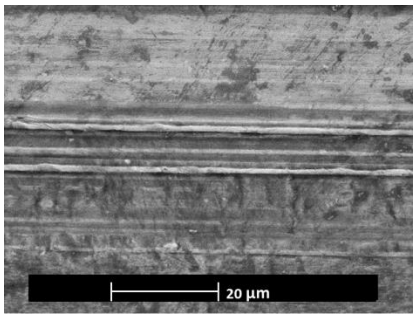
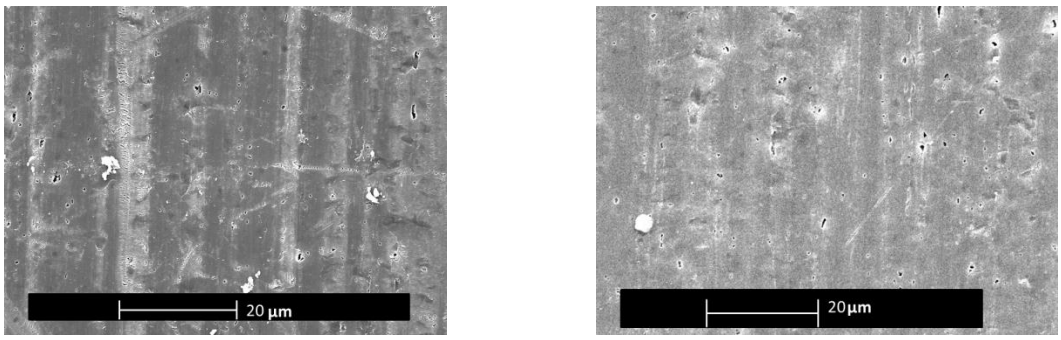
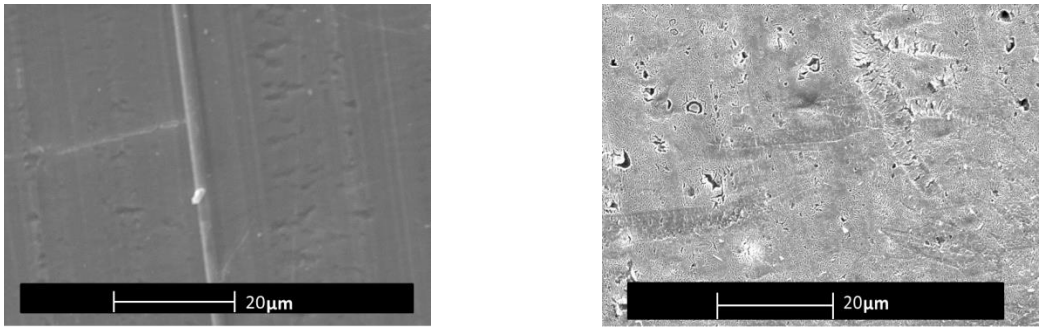


Figure 5-1. ESEM image of surface morphology of untreated aluminium AA1050 sample at 2000x magnification with working distance (WD) 10 spot size 4 and accelerating voltage 20 KV.



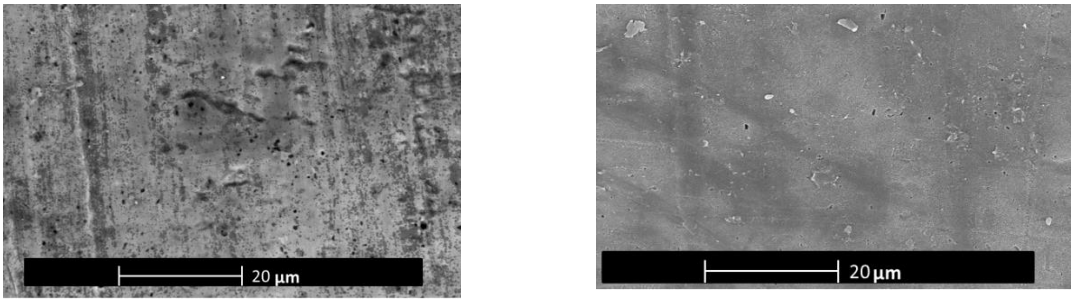
(a) (b)

Figure 5-2. ESEM image of surface morphology of anodised aluminium sample treated with 20.24 wt% sulphuric acid for 45 mins at a temperature of 30 °C(a) current density of 6 x 10^{-4} Acm^{-2} and (b)) current density of 18 x 10^{-4} A/cm^2 at 2000x magnification with working distance (WD) 10 spot size 4 and accelerating voltage 20 KV.



(a) (b)

Figure 5-3. ESEM image of surface morphology of anodised aluminium sample treated at a current density of 9x10-4 A/cm^2 for 45 mins at ~30 °C (a) with 16.56 wt% sulfuric acidand (b) with 20.24 wt% sulfuric acid at 2000x magnification with working distance (WD) 10 spot size 4 and accelerating voltage 20 KV.



(a) (b)

Figure 5-4. ESEM image of surface morphology of aluminium samples treated with 20.24 wt % sulfuric acid at a current density 9 x 10^{-4} A/cm^2 for 45 mins(a) at 15 °C and (b) at 50 °C at 2000x magnification with working distance (WD) 10 spot size 4 and accelerating voltage 20 KV.

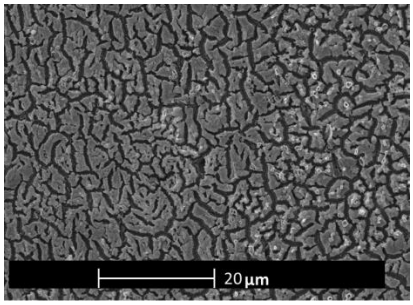


Figure 5-5. ESEM-SE image of surface morphology of aluminium sample treated with 20.24 wt % sulfuric acid at a current density 9 x 10^{-4} A/cm^2 for 90 mins at room temperature.

Figure 5-1 represents surface morphology of aluminium AA1050 without any treatment and under various anodising conditions from Figure 5-2 to Figure 5-5. It is clear that current density, concentration and anodisation temperature has significant effect on surface morphology. The anodisation time has no significant effect on surface morphology unless the anodisation time is too high then the surface gets damaged as shown in Figure 5-5, for this the treatment time was 90 mins. So for sulfuric acid anodisation the anodisation time is kept between 45-60 mins.

It is clear with increasing current density the surface morphology changes as shown in Figure 5-2 (a) and (b). The current density increased from 6x10^{-4} A/cm^2 to 18x10^{-4} A/cm^2 , this is expected as with increase in current density the rate of anodisation increases. Similarly when concentration of sulfuric acid increased from 16.56 to 20.24 wt% the nanostructured surface morphology also changed as evident from Figure 5-3 (a) and (b). With higher concentration of sulfuric acid the electrolyte concentration increases and hence the rate of anodisation increases. The sulfuric acid reacts with aluminium substrate and produces aluminium sulfate which gets into the electrolyte solution and liberates hydrogen gas. This process produces micrometer roughness on the aluminium surface. But the temperature has opposite effect on surface morphology i.e lower the temperature better is the

anodisation process and more rough surface morphology. When the temperature is 15 °C the surface morphology is more rough than when the temperature is 50 °C as shown in Figure 5-4 (a) and (b) respectively. It is observed that with increase in temperature the rate of anodisation should increase as the electrolyte molecules becomes more mobile but in real situation with increase in temperature the surface of aluminium inherently gets covered with an oxide layer and hence the anodisation process can no longer occur effectively.

Optimisation of anodisation parameters

The results obtained from the above ESEM images were studied properly and sulfuric acid anodisation parameters were modified. The modified conditions for sulfuric acid anodisation were given in Table 5-1.

Table 5-1. Optimised sulfuric acid anodisation parameters for aluminium AA1050 to obtain desirable surface morphology.

Sample name	Concentration of H_2SO_4 (g/L)	Current density (A/cm^2)	Voltage (V)	Treatment time (mins)	Temperature (°C)
SH300	300	$15x10^{-4}$	21.8-19.6	60	35~40
SH175	175	$15x10^{-4}$	22.5-17.0	60	35~40
SH131	131	$15x10^{-4}$	22.2-19.0	60	35~40
SH410	300	$15x10^{-4}$	21.8-19.6	40	10
SH415	175	$15x10^{-4}$	22.5-17.0	40	10
SH411	131	$15x10^{-4}$	22.2-19.0	40	10
SH610	300	$15x10^{-4}$	21.8-19.6	60	10
SH615	175	$15x10^{-4}$	22.5-17.0	60	10
SH611	131	$15x10^{-4}$	22.2-19.0	60	10

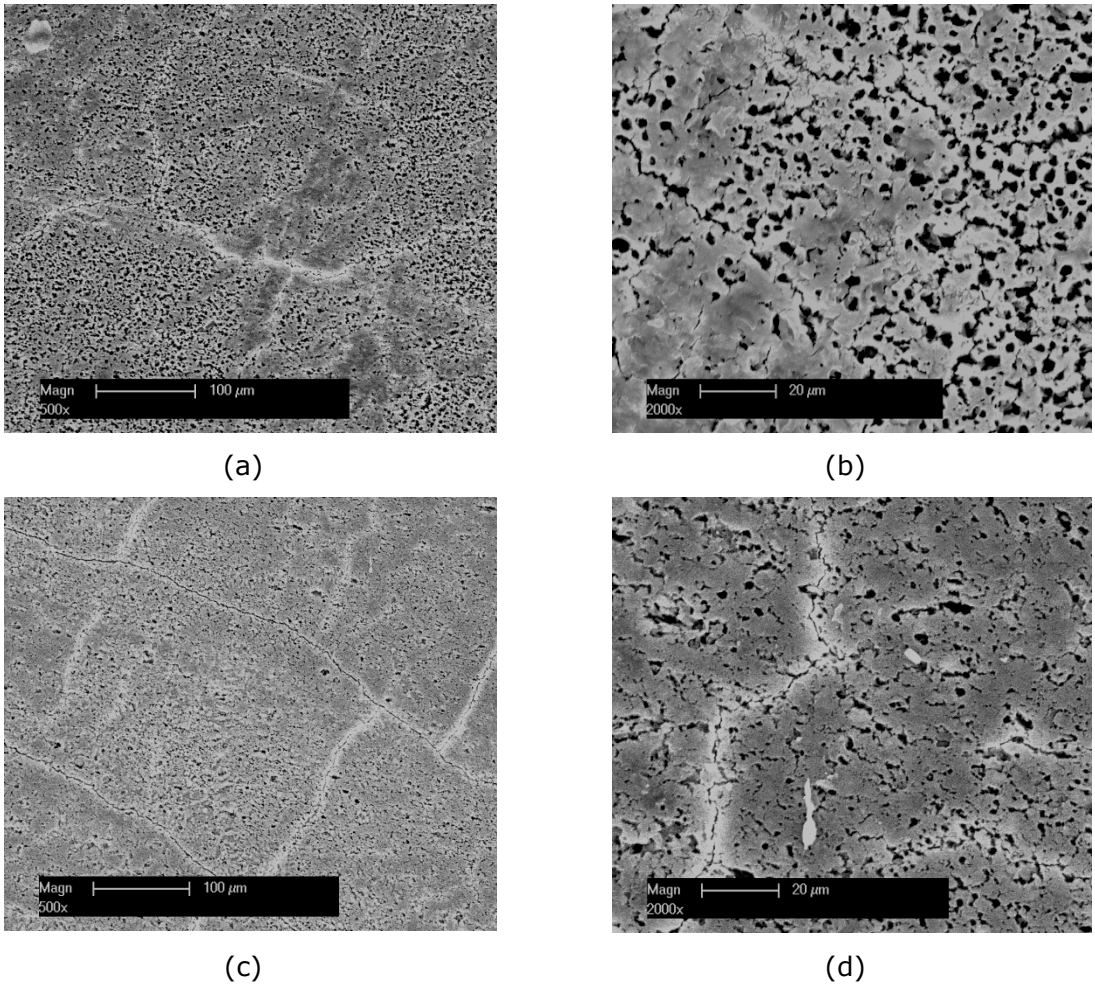
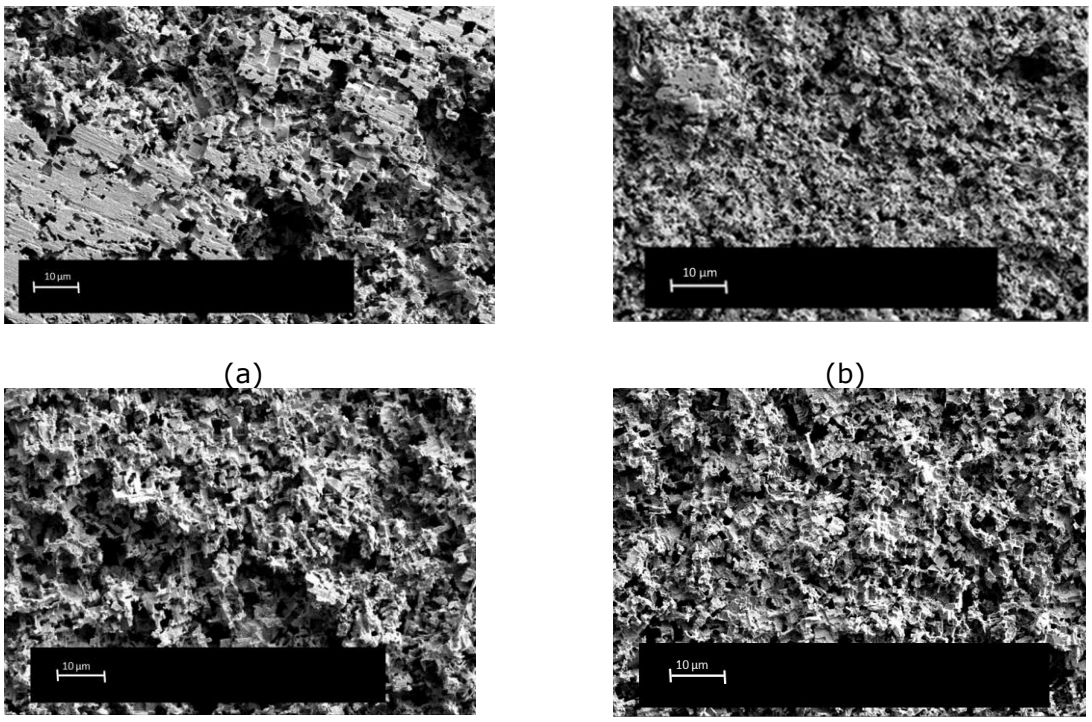


Figure 5-6. ESEM image of surface morphology of aluminium AA1050 samples (a) SH610 at 500x magnification, (b) SH610 at 2000x magnification, (c) SH410 at 500x magnification and (d) SH410 at 200x magnification. In all the cases the accelerating voltage is 20 kV and spot size 4.

After modifications of anodisation conditions some tests were performed at higher temperature 35-40 °C but the surface morphology was not improved but when the tests were performed at a controlled temperature of 10 °C the surface morphology improved as depicted in Figure 5-6 (a-d). The experiments were performed in two different time parameters: 60 mins and 40 mins respectively. The concentration, temperature and all the other experimental conditions were kept constant. It is observed the surface morphology improved with a longer anodisation time. In all the cases, the concentration of sulfuric acid was 300 g/L. It is clear that in the first case the surface morphology is more uniform than the later.

5.2.2 Chemical etching

The chemical etching was performed by a mixture of hydrochloric acid (HCl) and hydrogen peroxide (H_2O_2). The detailed experimental conditions are given in section 3.3.3. The etching temperature, etching time and conc of the etching solution were modified to obtain uniform surface morphology.



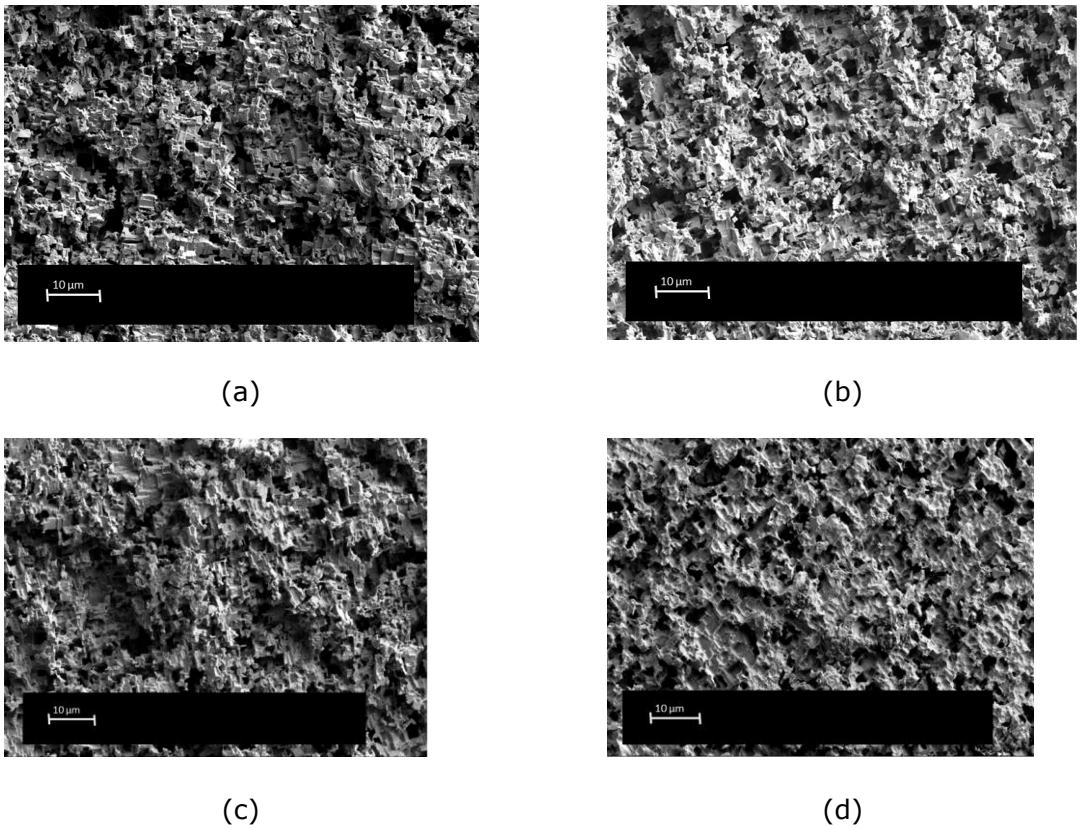
(a) (b)

(c) (d)

Figure 5-7. ESEM image of aluminium substrates etched with a mixture of 0.5 M HCl and 0.5 M H_2O_2 (a) Al.50.50.40.20, (b) Al.50.50.40.60, (c) Al.50.50.30.60 and (d) Al.50.50.60.60 with accelerating voltage of 20 kV and spot size 4.

Figure 5-7 shows the surface morphology of aluminium substrate samples chemically etched with a mixture of 0.5 M HCl and 0.5 M H_2O_2. The etching duration and etching temperature is varied to analyse the difference in morphology. The average pore size on the substrate surface was measured from the ESEM images using digital scale. In Figure 5-7 (a) and (b) the etching was done at a constant temperature of 40 °C and the etching time is varied, 20 mins for the former and 60 mins for the later. It is observed when treatment time was 20 mins no

significant pores on the substrate surface, while when etching time was increased to 60 mins an average pore size on the surface is 5.73 µm. Again the etching time is kept constant for 60 mins and the etching temperature is increased from 30 °C to 60 °C as shown in Figure 5-7 (c) and (d). With increasing temperature the pore size increases drastically from 2.43 µm to 6.03 µm.



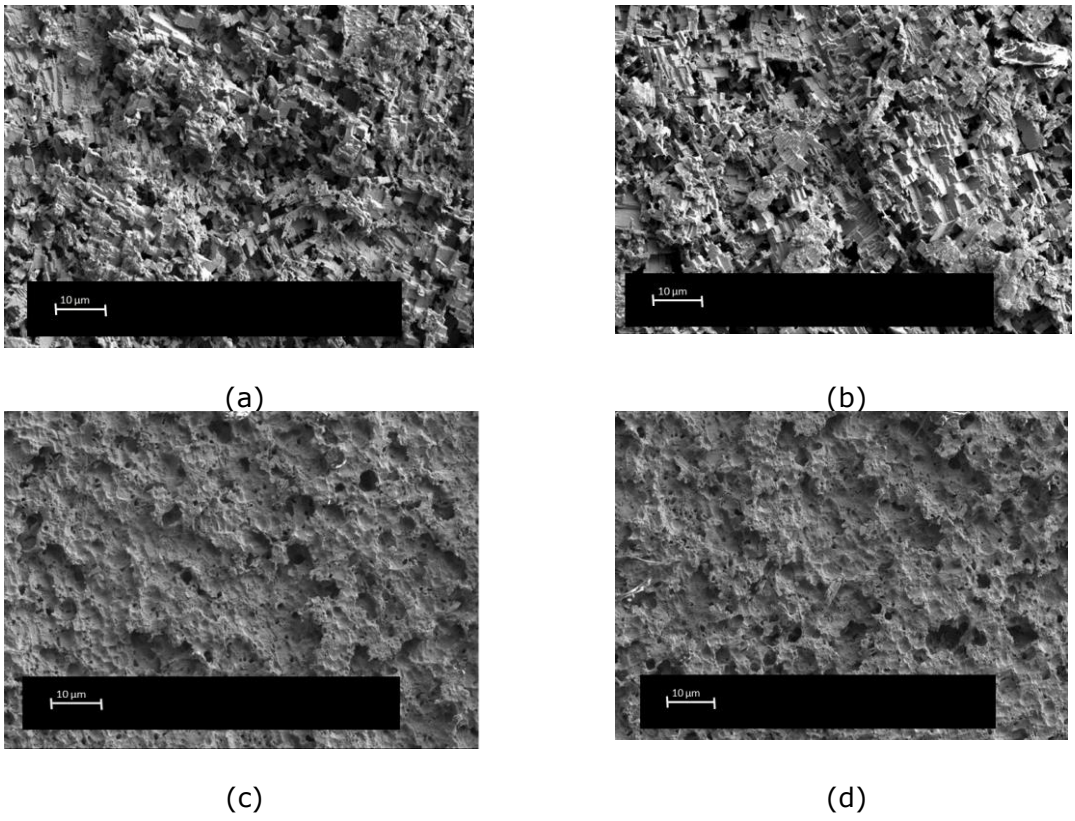
(a) (b)

(c) (d)

Figure 5-8. ESEM image of aluminium substrates etched with a mixture of 1 M HCl and 0.25 M H_2O_2 (a) Al.1.25.40.20, (b) Al.1.25.40.60, (c) Al.1.25.30.60 and (d) Al.1.25.60.60 60 with accelerating voltage of 20 kV and spot size 4.

Figure 5-8 depicts ESEM SE image of aluminium substrate surface after chemical etching with a mixture solution of 1 (M) HCl and 0.25 (M) H_2O_2. The etching time is varied from 20 mins to 60 mins at a constant temperature of 40 °C and the surface morphology alters as shown in Figure 5-8 (a) and (b). With the increase in concentration of HCl the pore size increases. When the etching time increased from 20 mins to 60 mins the pore size also increased from 1.47 to 5.93 µm. Again

as shown in Figure 5-8 (c) and (d) the etching time is kept constant for 60 mins and the etching temperature is increased from 30 °C to 60 °C. It is observed that with increase in temperature the pore size increases by 2.5 times from 2.70 to 6.67 µm. As compared to aluminium samples as shown in Figure 5-7 the concentration of HCl is increased two fold and the concentration of H_2O_2 is decreased two fold and a significant change in surface morphology and pore size is observed which will be discussed in later sections.



(a) (b)

(c) (d)

Figure 5-9. . ESEM-SE image of aluminium substrates etched with a mixture of 2 M HCl and 0.1 M H_2O_2 (a) Al.2.10.40.20, (b) Al.1.25.40.60, (c) Al.1.25.30.60 and (d) Al.2.10.60.60 60 with accelerating voltage of 20 kV and spot size 4.

The ESEM-SE image of aluminium substrates when treated with an etching solution of 2 (M) HCl and 0.1 (M) H_2O_2 is given in Figure 5-9 (a-d). The etching temperature and time was varied under the same conditions as shown in Figure 5-7 and Figure 5-8 . In this case the concentration of H_2O_2 is very low of 0.1 (M) and hence small pores on the surface is observed even when the etching temperature was kept high at 60 °C and the etching was continued for 60 mins as shown in Figure 5-9

(d). The pore size is 3.47 µm and is almost 1.5 times lower as observed under the same conditions of temperature and etching time but the concentration of H_2O_2 is high as 0.5 M and 0.25 M as shown in previous two cases.

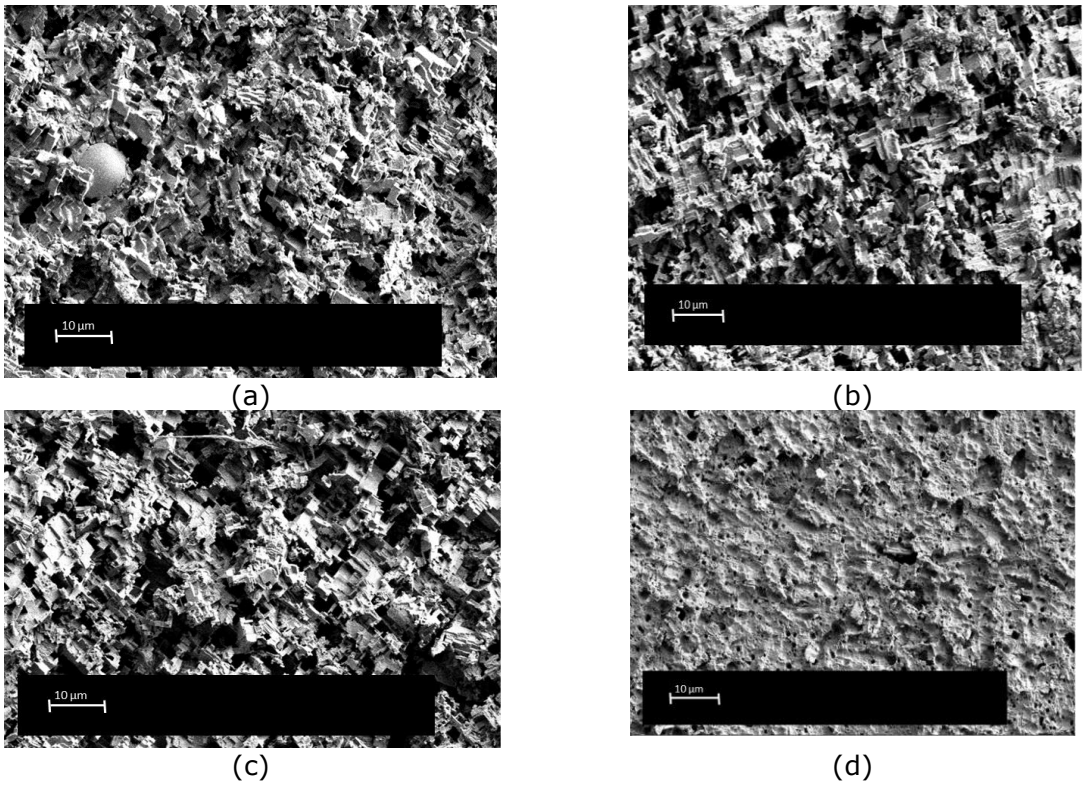
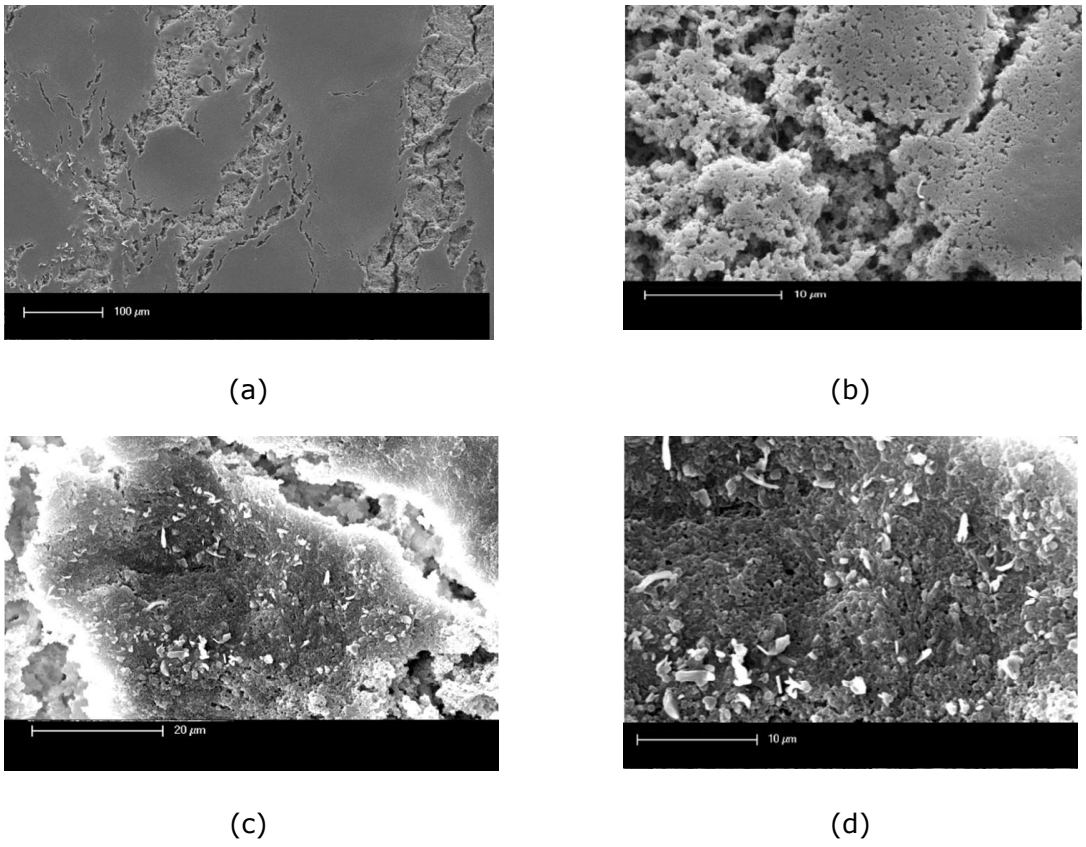


Figure 5-10. ESEM-SE image of aluminium substrates etched with a mixture of 2 M HCl and 0.25 M H_2O_2 (a) Al.2.25.40.20, (b) Al.2.25.40.60, (c) Al.2.25.30.60 and (d) Al.2.25.60.60 60 with accelerating voltage of 20 kV and spot size 4.

Figure 5-10 (a to d) shows the ESEM-SE image of chemically etched aluminium samples with a mixture of 2 M HCl and 0.25 M H_2O_2. The substrates were treated at 40 °C for 20 mins and 60 mins respectively as shown in Figure 5-10 (a) and (b). The pore size changes from 1.73 µm to 4.47 µm respectively. Again for Figure 5-10 (c) and (d) the substrates were treated for 60 mins at 30 °C and 60 °C. When the temperature is doubled the pore size decreases from, 2.53 µm to 1.20 µm. With the increased temperature the pore size should increase as the electrolyte becomes more mobile and hence pore size should increase, but in this case the pore size decreases.

5.2.3 Deposition of Nanoparticles

The Cu nanoparticles were deposited on the aluminium surface by spin coating process. For the process mainly two approaches were used. Firstly, the nanoparticles were dispersed in a solution of ethanol and the dispersion was deposited on the aluminium surface followed by a thin layer of PFA emulsion. Secondly, Cu-nanoparticles were functionalised with the PFA emulsion and then the particles along with excess PFA emulsion were deposited on the aluminium surface.



(a) (b)

(c) (d)

Figure 5-11. ESEM image of aluminium substrates coated with a composite mixture of2 g/L Cu-nanoparticles and synthesized PFA 10.1 emulsion (a) 500x magnification cured at room temperature, (b) 8000x magnification cured at room temperature, (c) 4000x magnification cured at 80 °C and (d) 8000x magnification cured at 80 °C.

Figure 5-11 (a – d) shows ESEM SE image of aluminium substrate coated with a 2 g/L solution of Cu-nanoparticle in PFA 10.1 emulsion solution. The polymer was cured at room temperature as shown in Figure 5-11 (a) and (b) and at 80 °C as shown in Figure 5-11 (c) and (d). The images were captured at different magnification and the uniformity of the coating is dependent on the curing temperature.

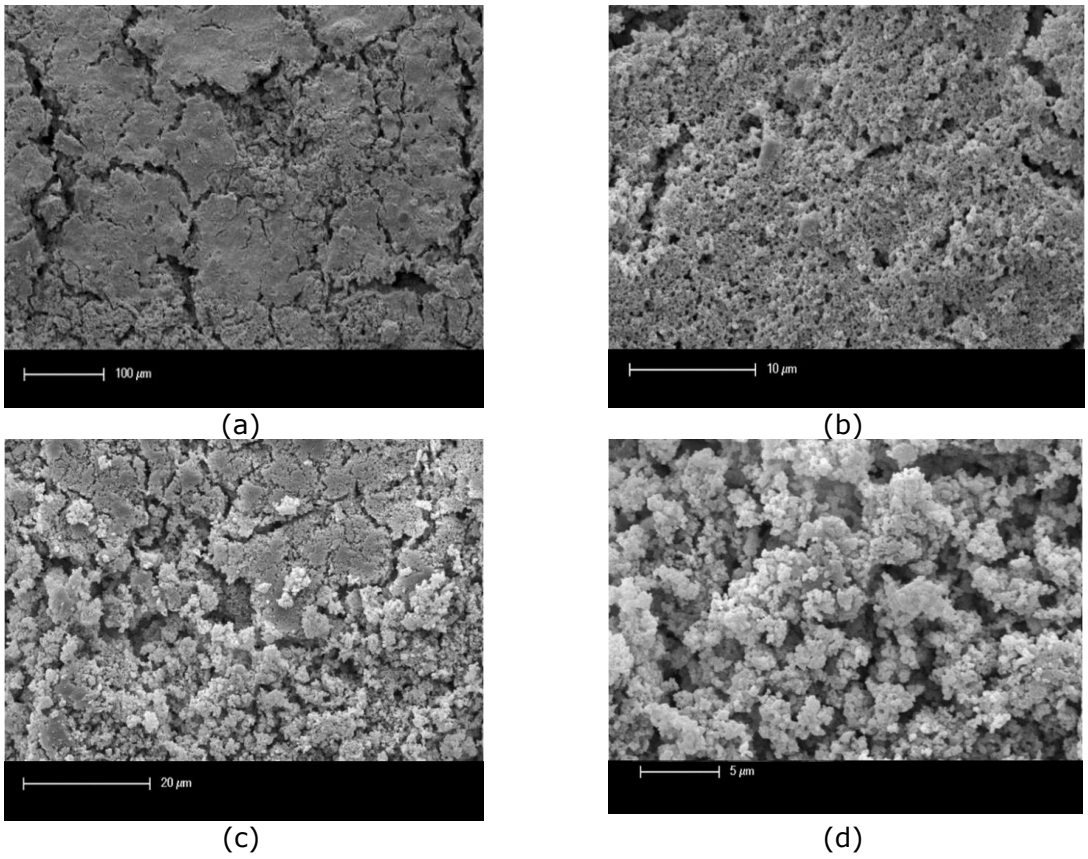


Figure 5-12. ESEM image of aluminium substrates coated with a composite mixture of 2 g/L Cu-nanopartcles with 0.1 M POTS in synthesized PFA 10.1 emulsion (a) 500x magnification cured at 80 °C, (b) 8000x magnification cured at 80 °C, (c) 4000x magnification cured at 120 °C and (d) 10000x magnification cured at 120 °C.

Figure 5-12 (a-d) shows ESEM SE image of aluminium substrates coated with a composite coating of 2g/L solution of Cu-nanoparticles in PFA10.1 emulsion solution. The only difference with the samples shown in Figure 5-11 is that here the Cu-nanoparticles were first modified with a 0.1 M POTS solution and then

dispersed in PFA 10.1 solution. The detailed synthesis and modification process of PFA emulsion is given in chapter 4. After modification of Cu-nanoparticles with the POTS solution the surface hydrophobicity increases substantially and will be discussed in details in next chapter. The icephobic property of the surface also changes due to the modification. The surface morphology does not change significantly with the modification of Cu nanoparticles with POTS.

5.3 Surface roughness study

5.3.1 Anodisation

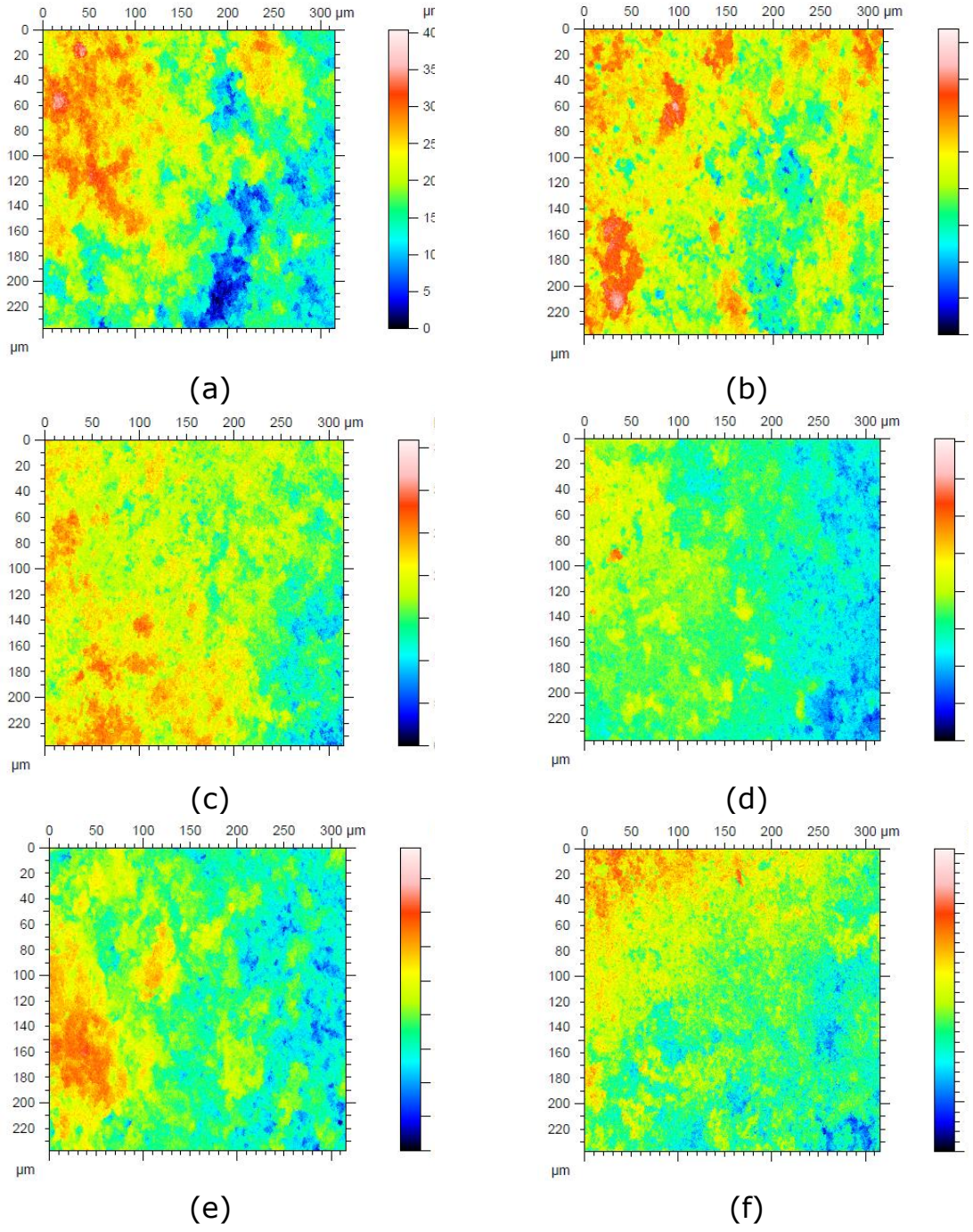


Figure 5-13. 2D model representation of aluminium substrates anodised under optimised conditions with controlled temperature at 10 °C and constant current density of $15x10^{-4}$ A/cm^2 (a) with anodising solution of 300 g/L H_2SO_4 for 40 mins, (b)with anodising solution of 300 g/L H_2SO_4 for 60 mins, (c) with anodising solution of 175 g/L H_2SO_4 for 40 mins, (d) with anodising solution of 175 g/L H_2SO_4 for 60 mins, (e) with anodising solution of 131 g/L H_2SO_4 for 40 mins and (f) with anodising solution of 131 g/L H_2SO_4 for 60 mins.

Figure 5-13 (a to f) shows surface roughness variation of aluminium substrates after anodising under optimised conditions as stated in section 5.2.1. The temperature for anodisation is kept under 10 °C in each case and the current density is maintained at 15 x 10^{-4} A/cm^2 throughout the anodisation process. The concentration of H_2SO_4 is varied from 300 g/L to 131 g/L and the time of treatment is varied from 40 mins to 60 mins. It is observed that when the electrolyte concentration is 300 g/L the concentration of H^+ ions increases in the solution and hence the rate of anodisation increases with high surface roughness of 3.65 µm as shown in Figure 5-13 (a). The treatment time is 60 mins in this case. When the treatment time is decreased to 40 mins the surface roughness value also decreases to 2.44 µm shown in Figure 5-13 (b). Again the concentration of electrolyte is lowered from 175 g/L to 131 g/L , with constant treatment time of 60 mins the surface roughness value decreases gradually from 2.98 µm to 2.12 µm as shown in Figure 5-13 (c) and (e) respectively.

Alternatively when time of treatment is decreased from 60 mins to 40 mins the surface roughness value decreases significantly. For the same set of concentration as mentioned above when the treatment time was decreased to 40 mins the surface roughness becomes 2.15 µm and 1.59 µm respectively, i.e; 25-30 % decrease in surface roughness is observed.

Table 5-2 shows the average surface roughness of the anodised aluminium substrates. The details of the anodising conditions are given in section 3.3.2.

Table 5-2. Average Surface roughness of anodised aluminium samples.

Sample Name	Average surface roughness (Ra, µm)
SH 25	2.44
SH 28	3.65
SH 26	2.15
SH 29	2.98
SH 27	1.59
SH 30	2.12

5.3.2 Chemical Etching

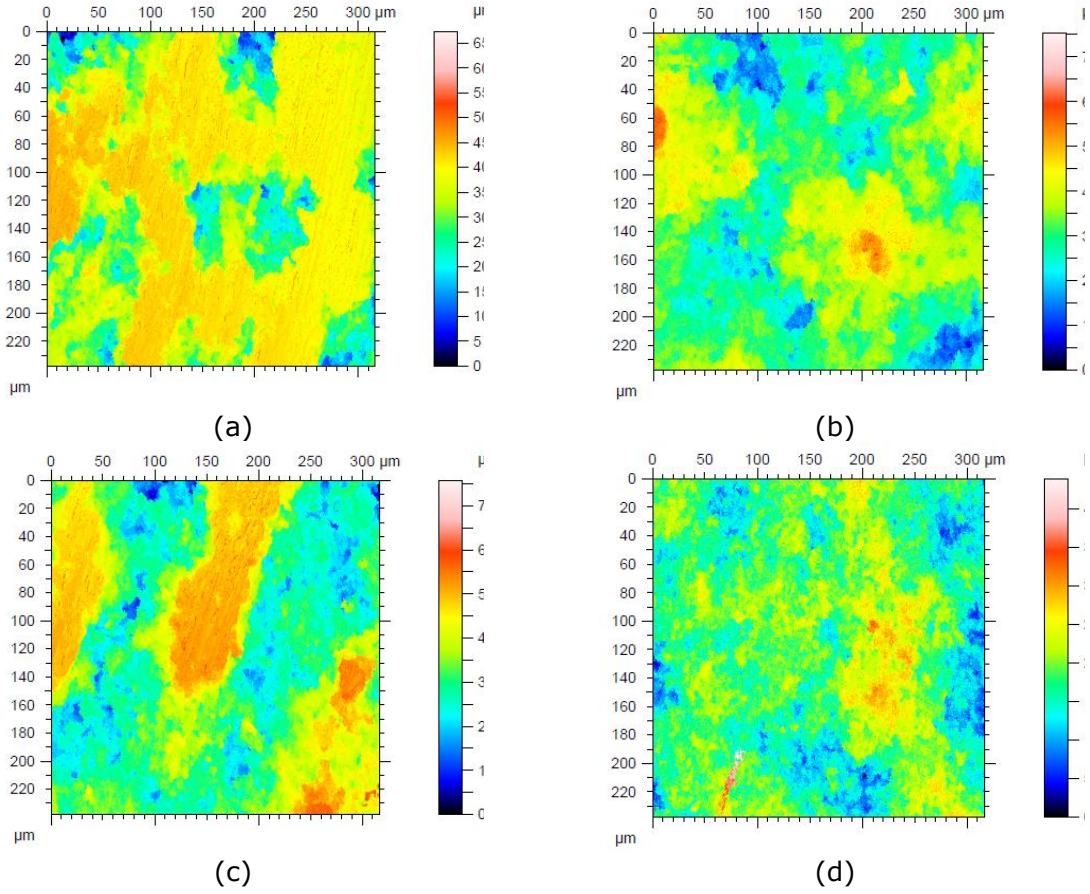


Figure 5-14. 2D model representation surface roughness of aluminium substrates etched with a solution of 0.5 M HCl and 0.5 M H_2O_2 (a) treatment time 20 mins and temperature 40 °C, (b) treatment time 60 mins and temperature 40 °C, (c) treatment time 60 mins and temperature 30 °C and (d) treatment time 60 mins and temperature 60 °C.

Figure 5-14 (a to d) shows the 2D image of surface roughness of aluminium substrates etched with a solution of 0.5 M HCl and 0.5 M H_2O_2. Different colours represent different height on the surface with blue is the lowest surface roughness and light red is the highest surface roughness. Figure 5-14 (a) and (b) shows sample etched at 40 °C for 20 mins and 60 mins respectively. With increase in treatment time the surface roughness R_a value varies from 2.13 µm to 2.22 µm. Again when the temperature is increased from 30 °C to 60 °C and treatment time is kept constant at 60 mins, surface roughness R_a value decreases from 2.52 µm to 1.82 µm as represented in Figure 5-14 (c) and (d).

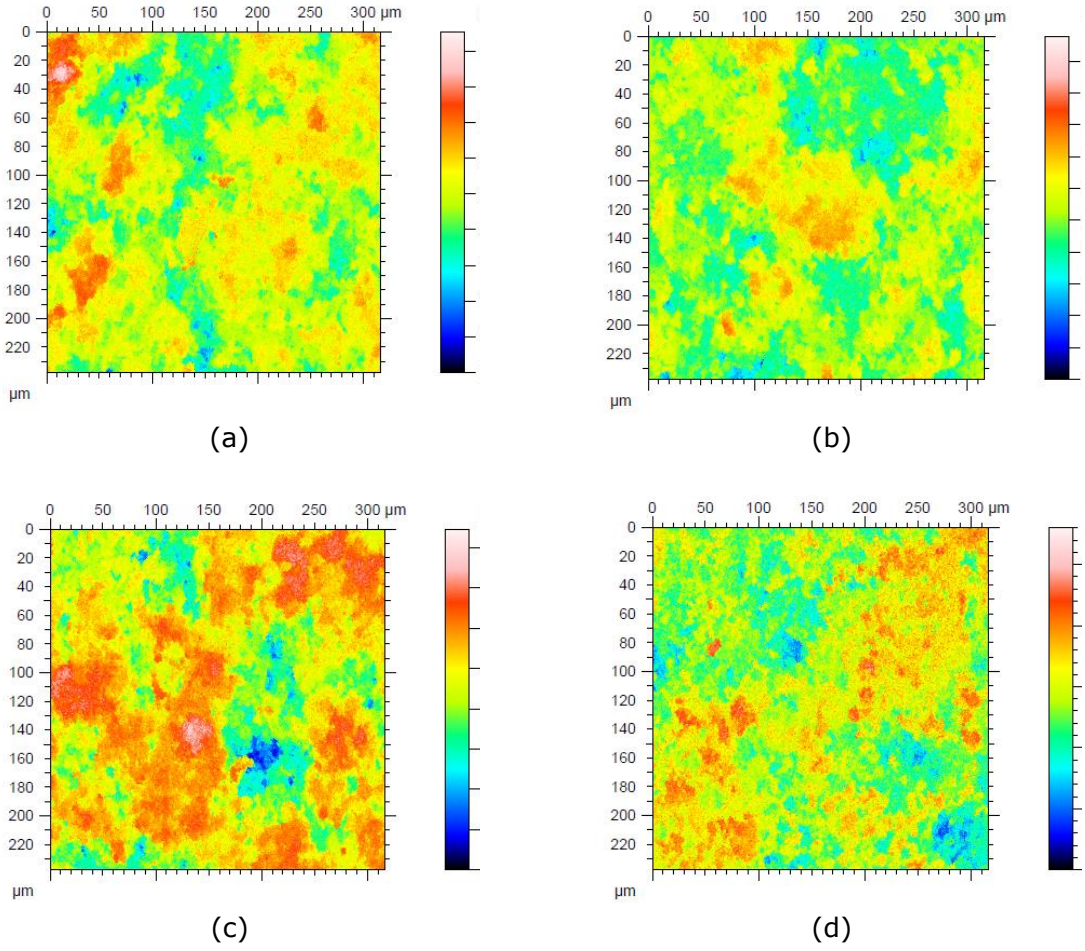


Figure 5-15. 2D model representation surface roughness of aluminium substrates etched with a solution of 2 M HCl and 0.1 M H_2O_2 (a) treatment time 20 mins and temperature 40 °C, (b) treatment time 60 mins and temperature 40 °C, (c) treatment time 60 mins and temperature 30 °C and (d) treatment time 60 mins and temperature 60 °C.

The surface roughness variation of aluminium substrates are shown in Figure 5-15 (a to d), chemically etched with a solution of 2 M HCl and 0.1 M H_2O_2 at different temperatures and etching times. Distribution of different colours on the image shows a variation of surface roughness and it is more uniform as compared to that shown in Figure 5-14 (a to d). With an increase in treatment time at a constant temperature of 40 °C, there is a significant change in surface roughness R_a value. When the etching time increases from 20 to 60 mins, the roughness changes from 2.17 to 1.96 μm as shown in Figure 5-15 (a) and (b). Similarly, there is also a drop in surface roughness 2.23 μm to 1.5 μm when the temperature is increased from 30 °C to 60 °C and treatment time is kept constant at 60 mins depicted in Figure 5-15 (c) and (d).

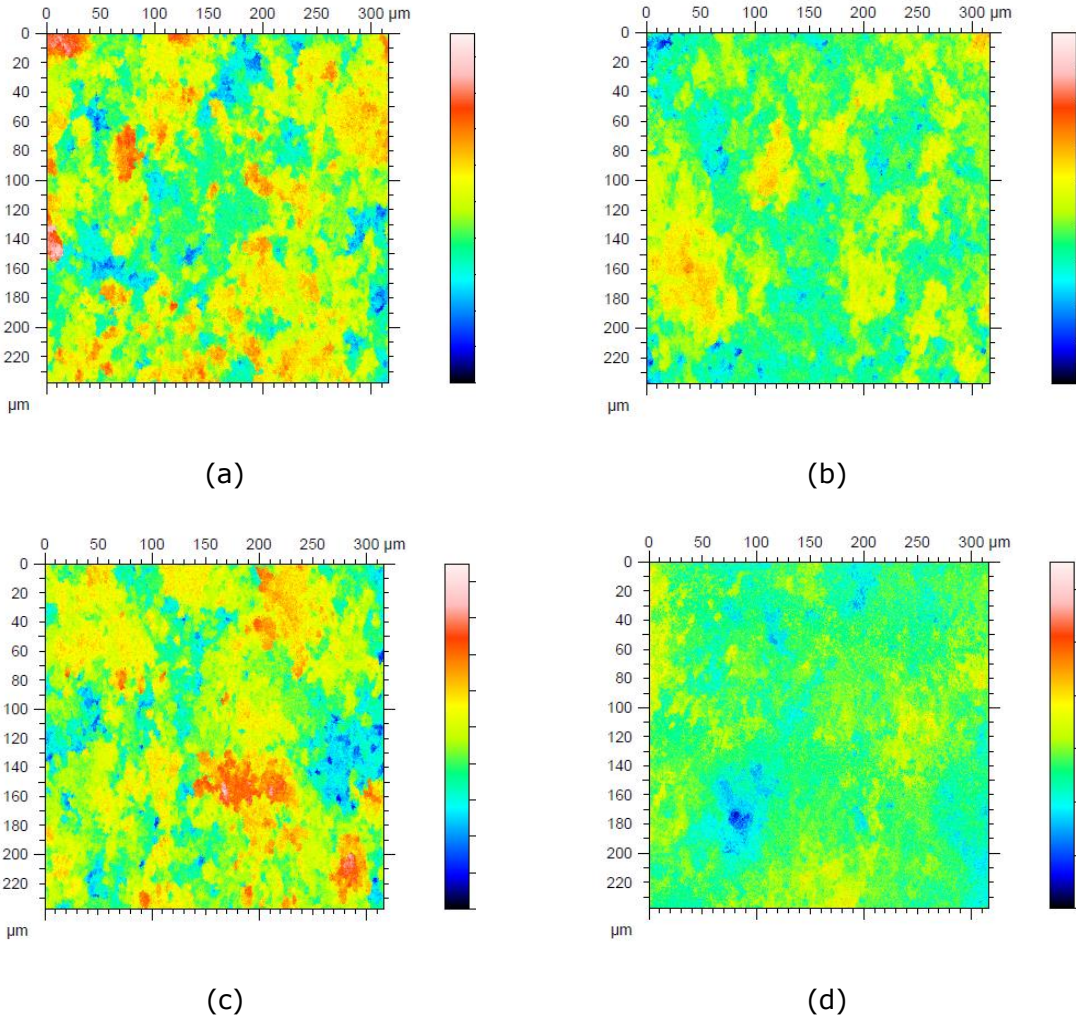


Figure 5-16. 2D model representation surface roughness of aluminium substrates etched with a solution of 2 M HCl and 0.5 M H_2O_2 (a) treatment time 20 mins and temperature 40 °C, (b) treatment time 60 mins and temperature 40 °C, (c) treatment time 60 mins and temperature 30 °C and (d) treatment time 60 mins and temperature 60 °C.

Figure 5-16 (a to d) shows chemically etched aluminium surface with a solution of 2 M HCl and 0.5 M H_2O_2. The concentration of H_2O_2 is kept the same and concentration of HCl increased 4 times as compared to aluminium samples as shown in Figure 5-14. The surface roughness R_a decreases by 3.2 µm to 2.3 µm when treatment time increased from 20 mins to 60 mins at 40 °C, the thickness of the substrate decreases by 0.27 µm as well as shown in Figure 5-16 (a) and

(b). Alternatively, the surface roughness R_a value decreases from 2.4 µm to 1.2 µm when treatment temperature increased from 30 °C to 60 °C and treatment time was kept constant for 60 mins as shown in Figure 5-16 (c) and (d).

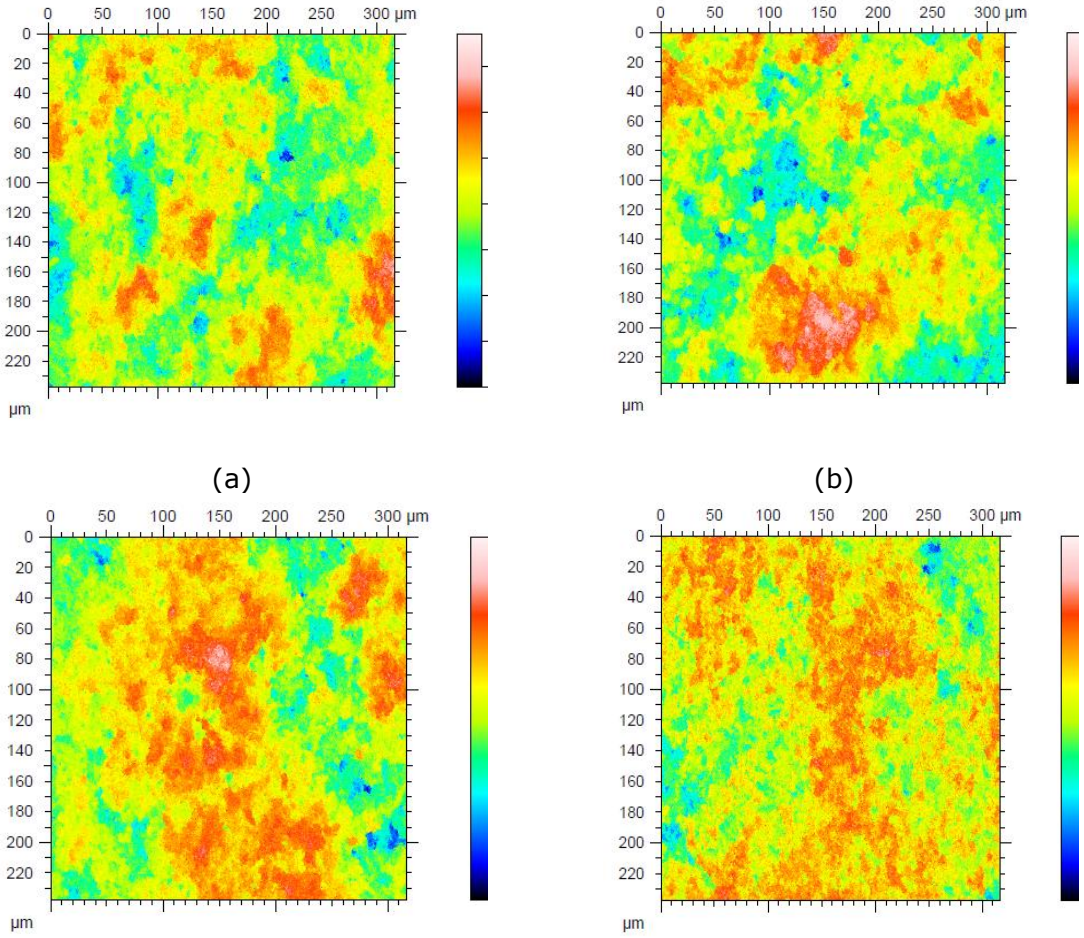


Figure 5-17. . 2D model representation surface roughness of aluminium substrates etched with a solution of 1 M HCl and 0.25 M H_2O_2 (a) treatment time 20 mins and temperature 40 °C, (b) treatment time 60 mins and temperature 40 °C, (c) treatment time 60 mins and temperature 30 °C and (d) treatment time 60 mins and temperature 60 °C.

Aluminium substrates are chemically etched with a solution of 1 M HCl and 0.25 M H_2O_2 and the surface morphologies are given in Figure 5-17 (a to d). When the etching time is increased from 20 mins to 60 mins the surface roughness R_a value increases from 1.88 µm to 2.26 µm, the temperature is kept constant at 40 °C

shown in Figure 5-17 (a) and (b). Again, as shown in Figure 5-17 (c) and (d) when the temperature is increased from 30 °C to 60 °C and the etching time is kept constant for 60 mins, the surface roughness R_a value changes from 1.86 µm to 1.6 µm.

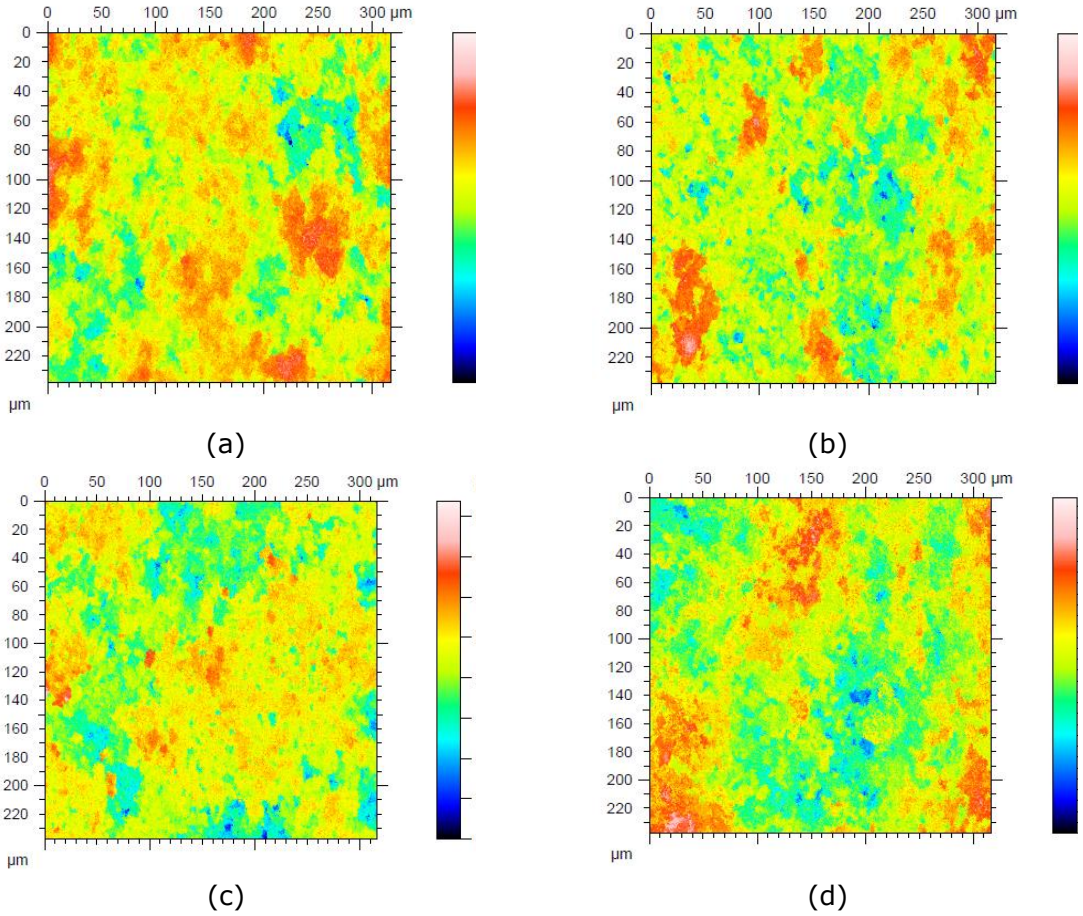


Figure 5-18. 2D model representation surface roughness of aluminium substrates etched with a solution of 2 M HCl and 0.25 M H_2O_2 (a) treatment time 20 mins and temperature 40 °C, (b) treatment time 60 mins and temperature 40 °C, (c) treatment time 60 mins and temperature 30 °C and (d) treatment time 60 mins and temperature 60 °C.

Figure 5-18 (a to d) shows the variation of surface roughness of aluminium substrates when chemically etched with a solution of 2 M HCl and 0.25 M H_2O_2. Figure 5-18 (a) and (b) shows the substrate surface when the treatment time is increased from 20 mins to 60 mins and the temperature is kept constant at 40 °C. The surface roughness R_a value increases from 1.78 µm to 2.82 µm. Again the

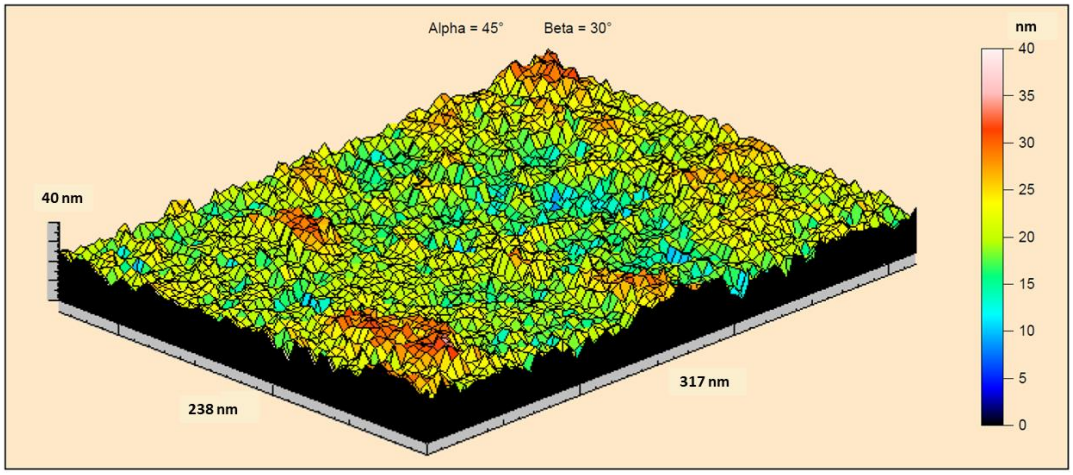
time of treatment is kept constant for 60 mins and the treatment temperature is doubled from 30 °C to 60 °C, the surface roughness decreases from 2.54 μm to 1.77 μm as shown in Figure 5-18 (c) and (d).

Table 5-3 shows the average surface roughness of chemically etched aluminium surfaces. The etching conditions including the concentration of HCl and H_2O_2, treatment time, and etching temperature are also listed.

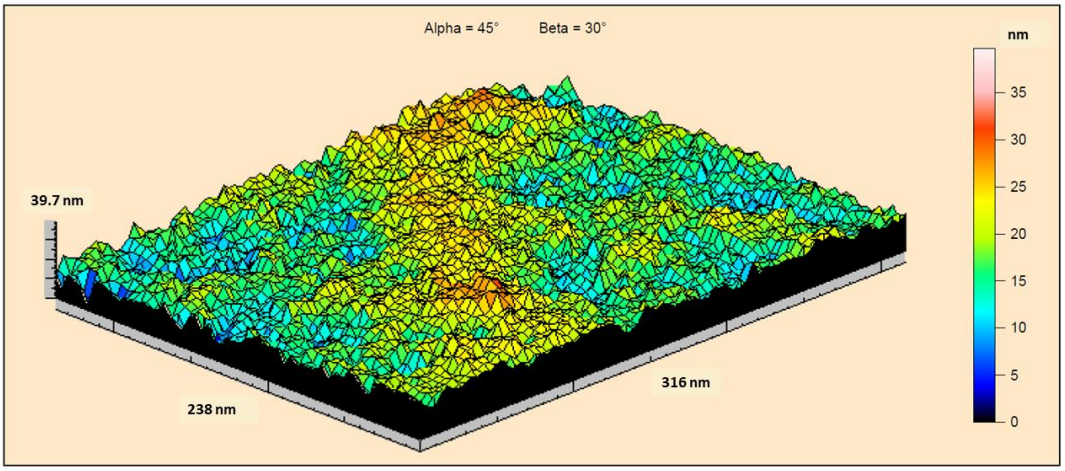
Table 5-3. Average surface roughness values of chemical etched aluminium substrates with etching conditions.

Sample Name	**Conc. Of HCl (M)**	**Conc. Of H_2O_2 (M)**	**Treatment time (mins)**	**Treatment temperature (°C)**	**Average Surface Roughness (Ra, μm)**
Al 18	0.5	0.5	20	40	2.13
Al 19	0.5	0.5	60	40	2.22
Al 20	0.5	0.5	60	30	2.52
Al 21	0.5	0.5	60	60	1.82
Al 22	2.0	0.1	20	40	2.17
Al 23	2.0	0.1	60	40	1.96
Al 24	2.0	0.1	60	30	2.23
Al 25	2.0	0.1	60	60	1.50
Al 26	2.0	0.5	20	40	3.20
Al 27	2.0	0.5	60	40	2.30
Al 28	2.0	0.5	60	30	2.40
Al 29	2.0	0.5	60	60	1.20
Al 30	1.0	0.25	20	40	1.88
Al 31	1.0	0.25	60	40	2.26
Al 32	1.0	0.25	60	30	1.86
Al 33	1.0	0.25	60	60	1.60
Al 34	2.0	0.25	20	40	1.78
Al 35	2.0	0.25	60	40	2.82
Al 36	2.0	0.25	60	30	2.54
Al 37	2.0	0.25	60	60	1.77

5.3.3 Deposition of nanoparticles



(a)



(b)

Figure 5-19. 3D model representation surface roughness of aluminium substrates deposited with Cu-nanoparticles in PFA 10.1 emulsion containing (a) 4 g/L Cu-nanoparticles and (b) 2 g/L Cu-nanoparticle solution.

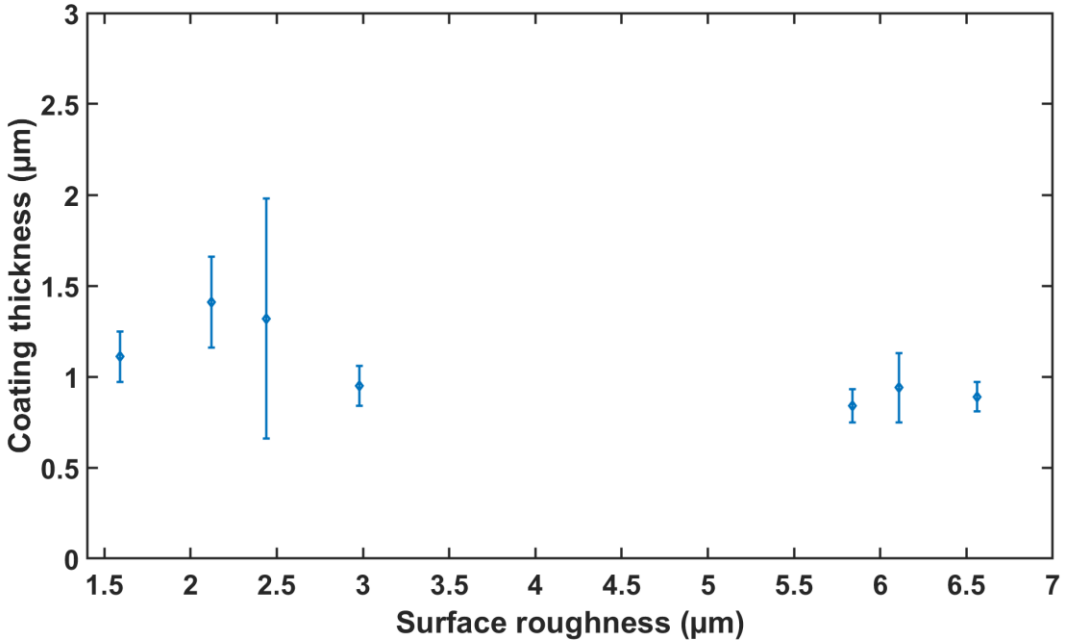
Different concentration of Cu-nanoparticles were dispersed in PFA 10.1 emulsion solution and then the mixture was deposited on the substrate surface. Figure 5-19 (a) and (b) shows variation of surface roughness when 4 g/L Cu-nanoparticle and 2 g/L Cu-nnaoparticle solution is used. It is observed that with the increase in concentration of Cu- nanoparticle the surface roughness increases. Unlike the anodised samples and chemically etched samples as discussed in section 5.2.1 and 5.2.2 the surface roughness is in the nanometer range. When the 4 g/L Cu

nanoparticle was deposited average R_a value of 23.6 nm was obtained and when the concentration was reduced to 2 g/L the average R_a value decreases slightly to 20.1 nm.

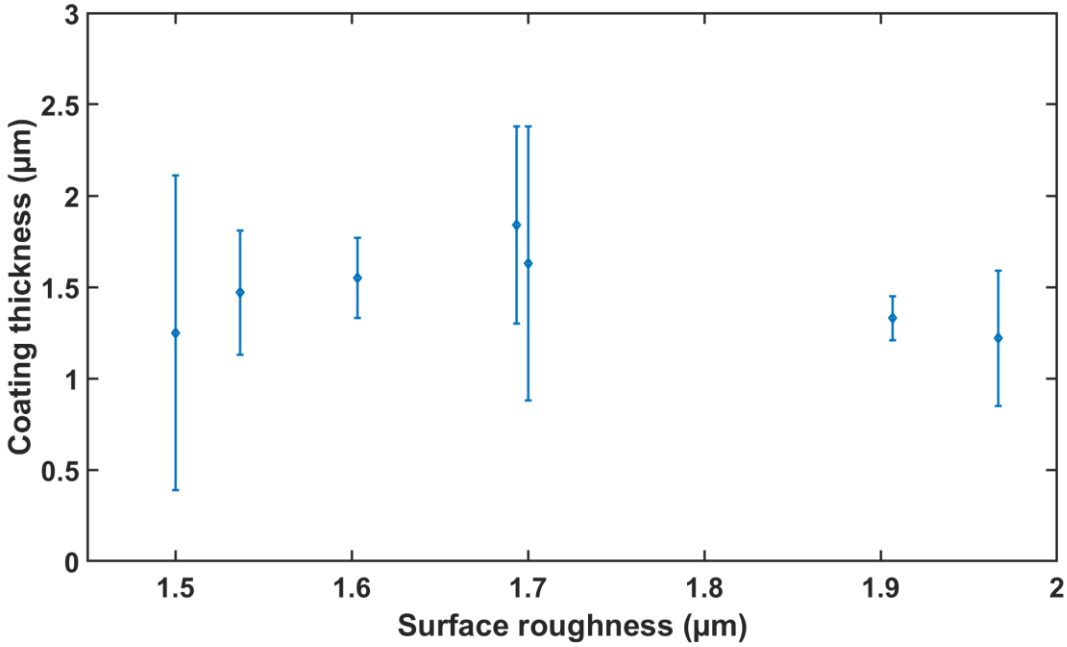
5.4 Effect of deposition of polyfluoroacrylate polymer coating on the modified surfaces

Thickenss of the polymer coating

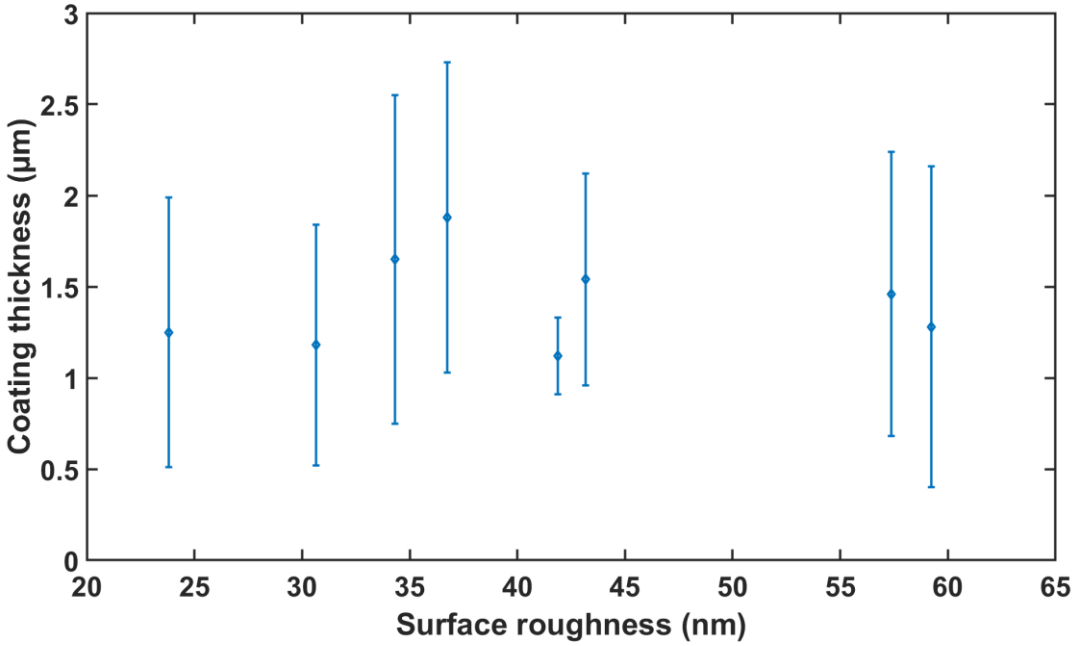
The synthesized polyfluoroacrylate emulsion is deposited on the anodised, chemically etched and nanoparticle deposited substrates by spin coating method. In each case 0.5 ml volume of PFA emulsion is used and the curing temperature was kept at 80 °C and duration also kept at 120 mins in all the cases.


Coating thickness (µm)
Surface roughness (µm)
0
0.5
1
1.5
2
2.5
3
1.5
2
2.5
3
3.5
4
4.5
5
5.5
6
6.5
7

(a)


Coating thickness (µm)
Surface roughness (µm)
0
0.5
1
1.5
2
2.5
3
1.5
1.6
1.7
1.8
1.9
2

(b)



(c)

Figure 5-20. Variation of PFA coating thickness with surface roughness for different surface modification processes (a) anodising, (b) chemical etching and (c) nanoparticle deposition, coated with PFA10.1 emulsion by spin coating process and cured at 80 °C.

Figure 5-20 (a-c) shows variation of coating thickness for PFA deposited on anodised, chemical etched and nanoparticle deposited substrates. It is observed that coating thickness is very low in all the cases and hence will have very small effect on altering the surface roughness. The average coating thickness of PFA coating in all the cases for chemical etched and nanoparticle deposited surfaces were above 1 µm as shown in Figure 5-20 (b) and (c). For anodised samples with the increase in surface roughness beyond 3 µm the PFA coating thickness decreases below 1 µm as found in Figure 5-20 (a).

5.5 Evaluation of coating water erosion resistance

The coating erosion resistance of the synthesized polymer on the aluminium substrate is evaluated by water impinging test. The details of the experimental process is given in section 3.8.1. The substrates are coated with the polymer before

and after surface treatment by anodization, chemical etching and nanoparticle deposition. The rate of flow of water is kept constant throughout the experiment and the decrease in thickness of the coating layer is measured.

The anodised, chemically etched and Cu-nanoparticle deposited substrates were coated with synthesized polyfluoroacrylate emulsion and subjected to water impinging test to analyse the coating adhesion strength and erosion resistance on the modified surfaces. The conditions and details of the impinging tests were given in section 3.8.1 and kept uniform throughout.

5.5.1 PFA coating on anodised aluminium substrate

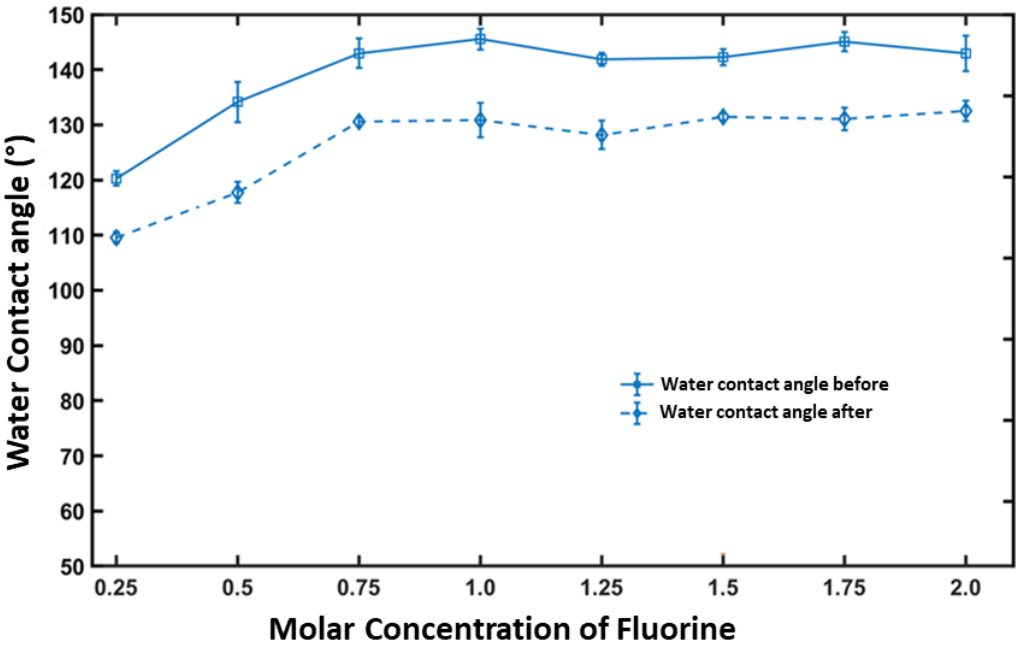


Figure 5-21. Variation of water contact angle on anodised aluminium surface coated with polyfluoroacrylate emulsion containing various concentrations of fluorine after the water impinging test.

The erosion resistance of the polymer coating on the anodised surface is shown in Figure 5-21, as a change in water contact angle before and after the impinging

tests. Polymers with various concentration of heptafluorobutyl acrylate is being used. The hydrophobicity of the samples are also evaluated before and after the impinging test. It is clear from the water contact angle data before and after the water impinging that surface hydrophobicity is maintained for all the samples though there is a slight decrease in hydrophobicity indicating some loss of the polymer. This is supported by the measured weight difference of the same samples before and after the impinging tests. The weight of the samples decreases in the range of 17 to 24 mg, indicating a loss in the polymer coating material. Highest water contact angle obtained for the anodised sample when the polymer containing 1 molar ratio of heptafluorobutyl acrylate is being used. After the water impinging test the WCA value decreases from 145 ° to 131 °.

5.5.2 Coatings on chemically etched substrate

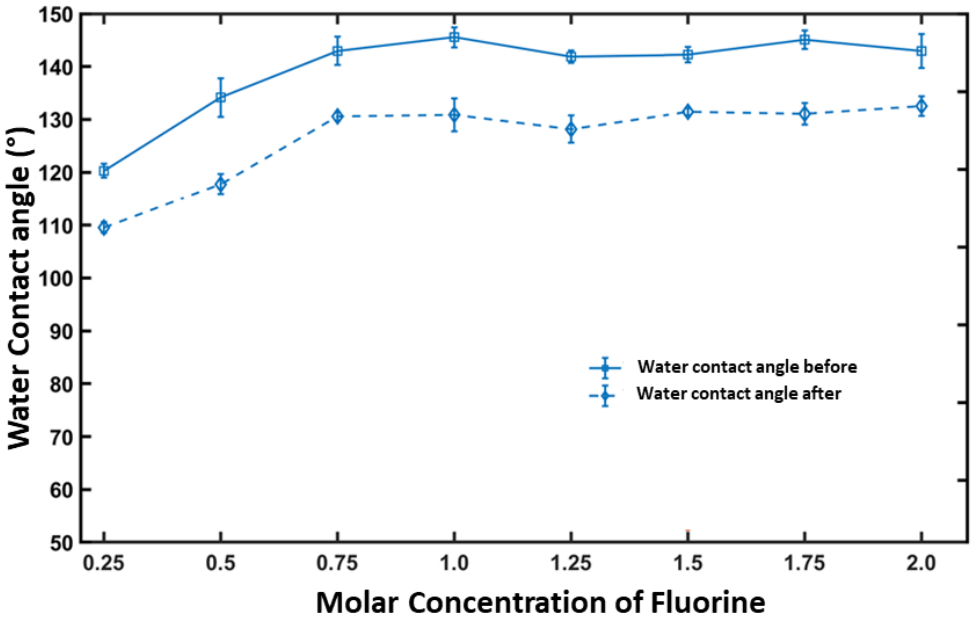


Figure 5-22. Variation of water contact angle on chemically etched aluminium surface coated with polyfluoroacrylate emulsion containing various concentrations of fluorine after the water impinging test.

Figure 5-22 shows change in weight of the polymer coating and variation of surface hydrophobicity of the polymer coated chemically etched aluminium substrate as a function of fluorine content of the coated polymer emulsion. Similar to the anodised samples, the chemically etched samples also retain their hydrophobicity after water impinging test. Average water contact angle after water impinging tests range between 110 ° to 131 ° depending on the fluorine content. The average decrease in water contact angle before and after the water impinging test is 11 °. The weight loss of the polymer coating also ranges between 5 to 35 mg. This indicates that after the water impinging test some polymer is lost from the substrate surface and hence change in water contact angle. The condition for water impinging tests were kept constant for all the samples and detailed conditions are given in chapter 3.

5.5.3 Coatings on nanoparticle deposited surface

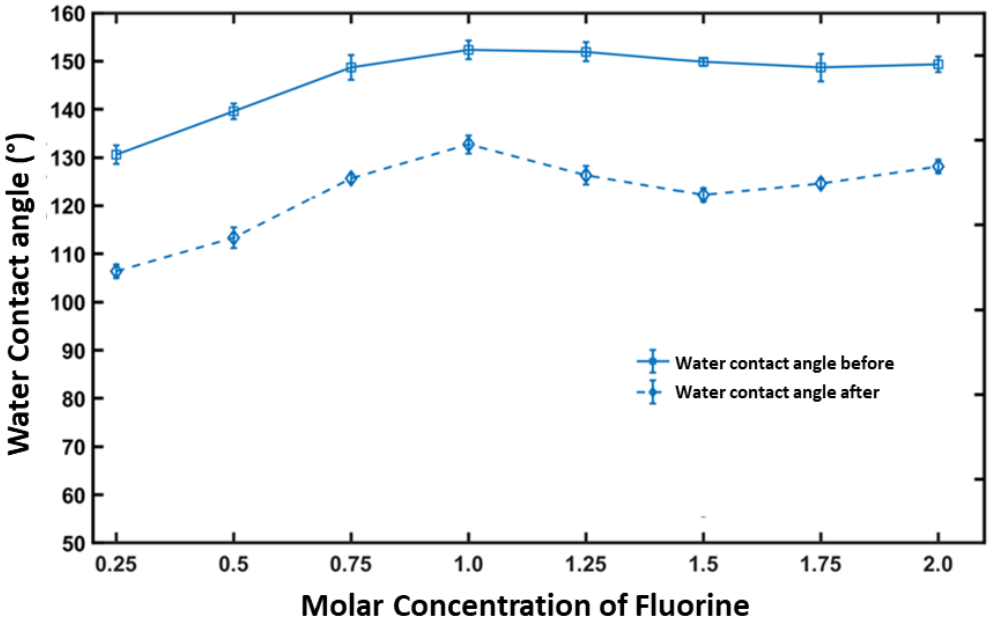


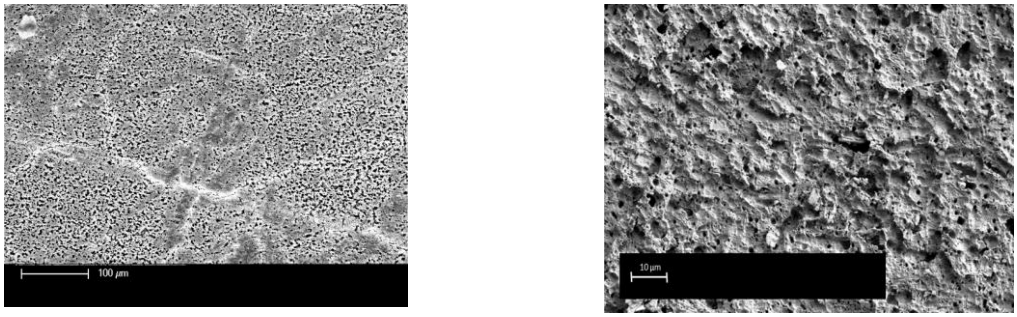
Figure 5-23. Variation of water contact angle on Cu-nanoparticle deposited aluminium surface coated with polyfluoroacrylate emulsion containing various concentrations of fluorine after the water impinging test.

A composite coating of Cu-nanoparticle and polyfluoroacrylate emulsion was deposited on aluminium substrate surface and then the substrates were subjected to water impinging test. Figure 5-23 shows the variation of water contact angle on the coated substrates before and after the impinging tests due to erosion. 1 wt % of Cu-nanoparticles were used in all the cases, the concentration of fluorine was varied from 0.25 to 2 M. It is observed that similar to anodised and chemically etched substrates, the water contact angle decreases for all the cases after the erosion test but the extend of decrease is higher than the former two as shown in Figure 5-21 and Figure 5-22.

5.6 Discussion

5.6.1 Comparison of Anodisation and Chemical etching for surface modification

As presented earlier mainly three processes are used to produce surface roughness anodisation, chemical etching and deposition of nanoparticles. The former two processes are highly dependent on the temperature, treatment time and concentration of the electrolyte and etching agent respectively. The effect of all the process parameters on the surface morphology and surface roughness will be discussed in details in the later sections. But from the surface morphology and roughness value obtained for different processes in section 5.2 and 5.3 it is observed a uniform surface morphology is obtained for both chemical etching process and anodisation but for nanoparticle deposition the surface is not uniform as compared to the former two. Also for chemical etching the process parameters are easy to control as compared to anodisation process, where it is hard to maintain the temperature below 10 °C.



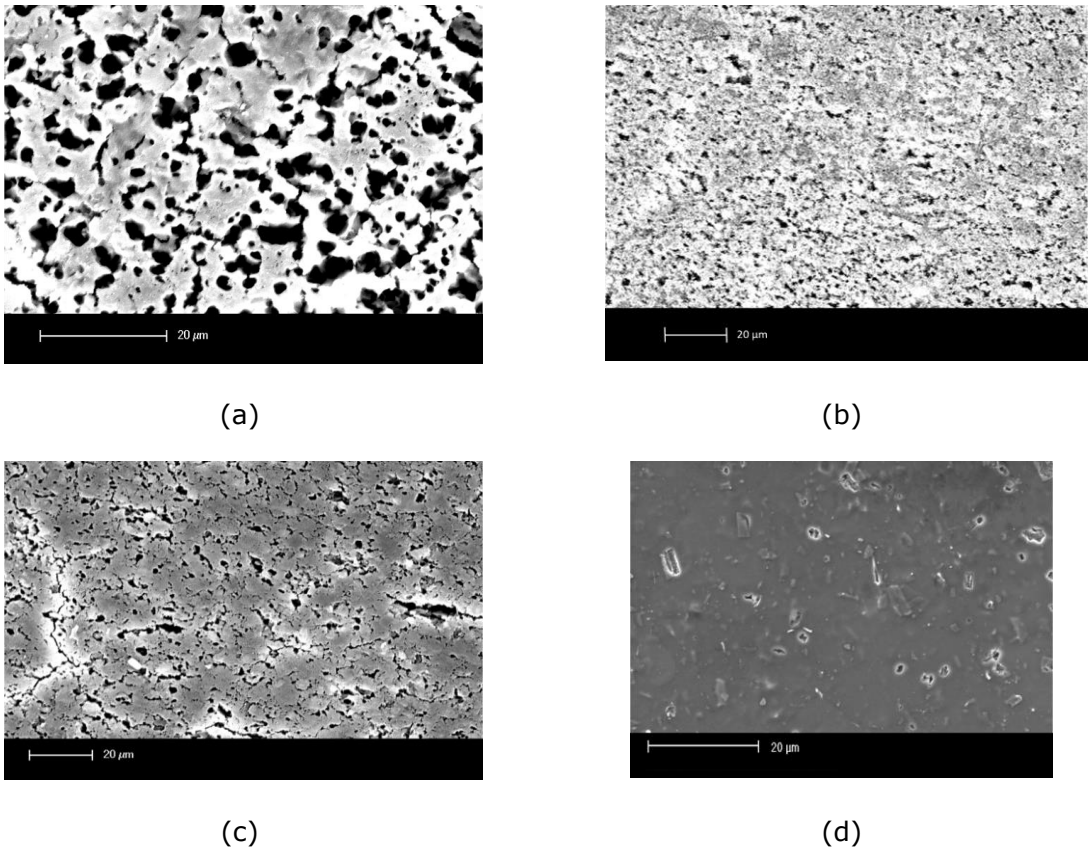
(a) (b)

Figure 5-24. SEM image of surface morphology aluminium substrates (a) Anodised with a 175 g/L solution of H_2SO_4 with a current density of 15 x 10^{-4} Acm^{-2} under 10 °C for 40 mins and (b) Chemically etched with a 2 M HCl and 0.25 M H_2O_2 solution at 40 °C for 60 mins.

Figure 5-24 (a) and (b) shows the aluminium substrate surface after anodisation and chemical etching respectively. For anodisation, 175 g/L H_2SO_4 solution was used as an electrolyte with a current density of 15 x 10^{-4} Acm^{-2} at 10 °C for 40 mins. Again for chemical etching, a mixture solution of 2 M HCl and 0.25 M H_2O_2 were used at 40 °C for 60 mins. In both cases the average surface roughness values obtained are 2.12 µm and 2.09 µm respectively. But the average pore size for anodisation processed samples is 1.9 µm which is much higher than pore size (0.98 µm) of the samples obtained by chemical etching method H_2SO_4 is a strong acid and the H^+ ions are more reactive resulting wider pore. Alternatively in the case of chemical etching the reaction of H_2O_2 and HCl produces reactive OH radical but since there is no electrodes or potential difference in the solution the process is slow and hence smaller pores were obtained.

The concentration of electrolyte in anodisation process also has significant influence on the surface morphology and roughness of the aluminium substrates. The surface roughness can go up to 4 µm when the temperature is low as 10 °C and the concentration of H_2SO_4 is high (300 g/L).The concentration of etching

solution also alters the surface morphology and surface roughness but the variation is not as high compared to anodisation process.



(a) (b)

(c) (d)

Figure 5-25. SEM image of surface morphology of aluminium substrate anodised (a) with 175 g/L H_2SO_4 solution at 10 °C for 60 mins, (b) 175 g/L H_2SO_4 solution at 10 °C for 40 mins, (c) 300 g/L H_2SO_4 solution at 10 °C for 60 mins and (d) 300 g/L H_2SO_4 solution at 40 °C for 60 mins.

The effects of anodisation time on surface morphology of the substrates are shown in Figure 5-25 (a) and (b). In both the cases the concentration of sulphuric acid and temperature is kept same at 175g/L and 10 °C. The anodisation time varies from 60 mins (Figure 5-25 (a)) to 40 mins (Figure 5-25 (b)). It is clear that surface morphology is highly affected by the anodisation time. Wider pore with diameter of 3.42 µm was obtained as compared to 2.86 µm when the anodisation time increased from 40 mins to 60 mins. The average surface roughness R_a value also changes from 2.15 µm to 2.98 µm with increase of treatment duration. The

substrate surfaces were exposed to the H_2SO_4 solution longer, leading to larger pore diameter and higher surface roughness with the increase of treatment duration.

When the anodisation temperature was increased from 10 °C to 40 °C, the surface morphology and surface roughness changes significantly. Figure 5-25 (c) and (d) shows the SEM surface morphology of anodised aluminium substrates at 10 °C and 40 °C respectively. The concentration of sulphuric acid was 300 g/L and anodisation time of 60 mins was kept constant in both the cases. When the temperature was 10 °C, the surface morphology is uniform and average surface roughness R_a is 2.12 µm. However, when the temperature was higher at 40 °C, there is no visible surface feature observed and the average surface roughness value is 0.96 µm. This indicates that the surface is no longer rough when the temperature is high. One of the possibility is that when the temperature is higher the anodisation is too fast leading to polishing effect on the surface and also a layer of Al_2O_3 gets formed. This concludes that controlling temperature and treatment time is very crucial for anodisation process as the variation in surface morphology and surface roughness is significantly high.

5.6.2 Surface morphology of aluminium substrate deposited with Cu-nanoparticles

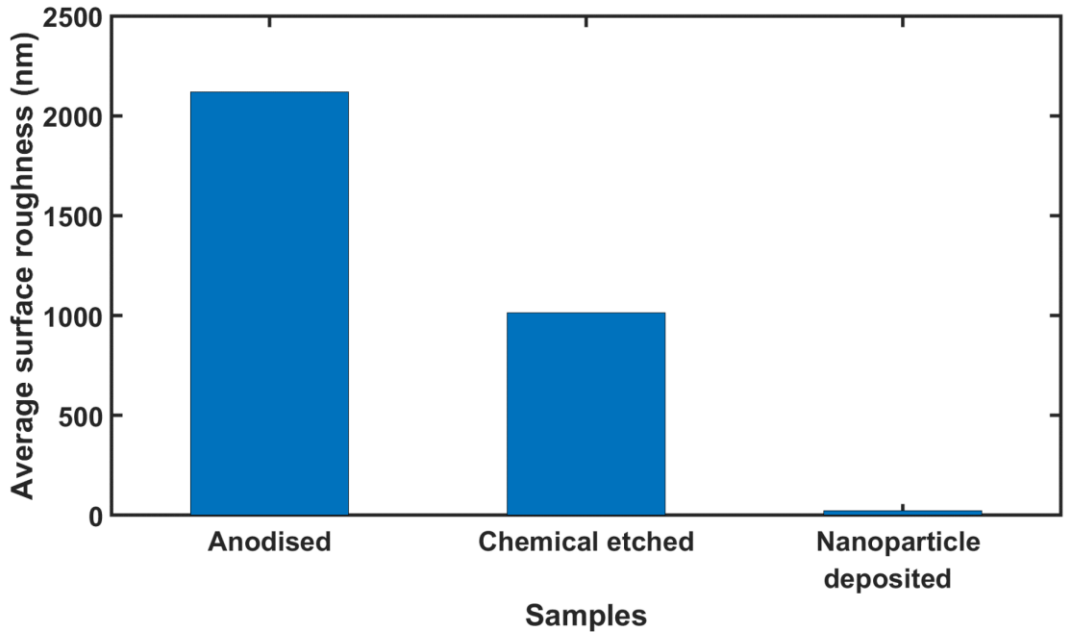


Figure 5-26. Comparison of surface roughness for aluminium substrates treated with anodisation, chemical etching and Cu-nanoparticle deposition.

Cu-nanoparticle deposition provides surface roughness in nanometer range unlike for anodised or chemically etched samples for which the surface roughness is in micrometer range. Figure 5-26 shows the comparison of surface roughness values for aluminium substrates by different surface modification techniques. It is observed that highest average surface roughness values are obtained for anodised substrates when anodised with a 300 g/L H_2SO_4 solution with a current density of 15 A/cm^2 for 60 mins and the temperature was maintained at 10 ºC. Again when the samples were chemically etched with a mixture of HCl and H_2O_2 solution containing 1 M HCl and 0.5 H_2O_2, the average surface roughness value decreases to 1.66 µm as compared to 2.12 µm for anodised samples. The average surface roughness drastically decreases to 23.6 nm when 2 g/L Cu-nanoparticles were deposited on the substrate surface.

5.6.3 Effect of temperature in chemical etching process

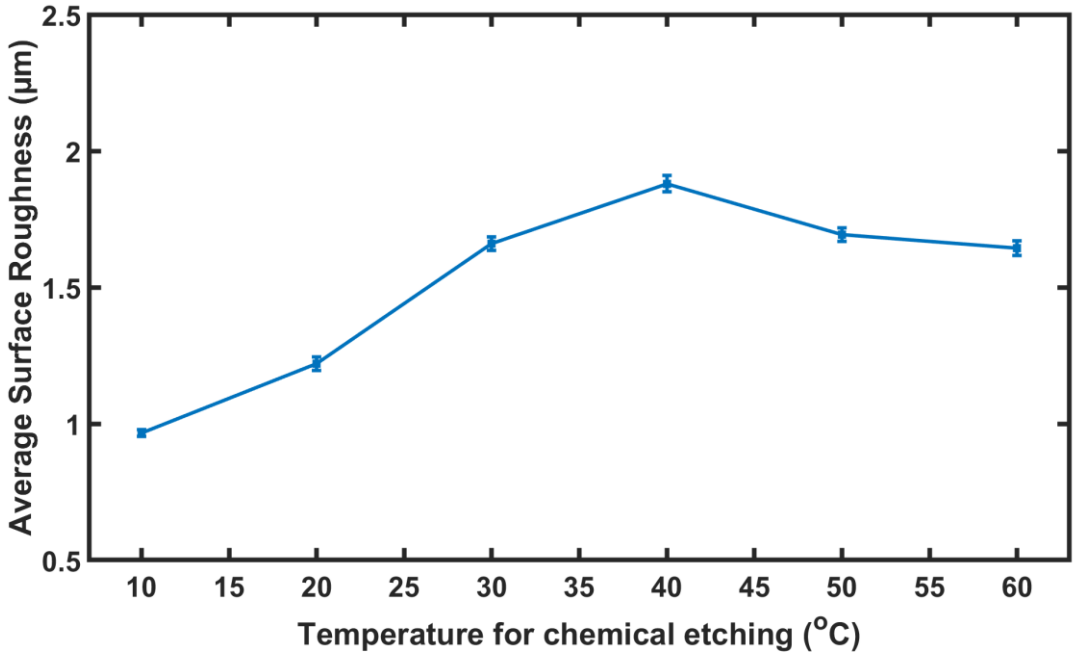


Figure 5-27. Variation of average surface roughness with treatment temperature of chemically etched aluminium surfaces with with a 1 M solution of HCl and 0.5 M solution of H_2O_2 and at a constant etching time of 60 mins.

Temperature also have significant effect on the surface roughness during the chemical etching process. Figure 5-27 shows the variation of average surface roughness of chemically etched aluminium substrates. The temperature of etching was varied from 10 °C to 60 °C. The concentration of etching solution was kept constant at 1 M HCl and 0.5 M H_2O_2. The etching time was also kept constant for 60 mins. It is observed that the average surface roughness value ranges between 0.9 to 1.9 μm. When the temperature is increased from 10 to 40 °C the average surface roughness also increases from 0.95 μm to 1.89 μm. With the increasing temperature, the surface roughness increases gradually as the ions become more mobile and the oxidation of Cl^- to Cl_2 is also increased due to chemical etching. With further increase in temperature the average surface roughness decreases to

a small extent but the thickness of the substrate decreases to a 20 % of original value. The significant decrease in thickness is due to the very high rate of chemical etching, resulting in polishing effect and hence sometimes lower surface roughness is obtained. The trend of variation of surface roughness with variation of concentration is more or less same for the other concentration chemical etching processes as well.

5.6.4 Role of treatment time in chemical etching process

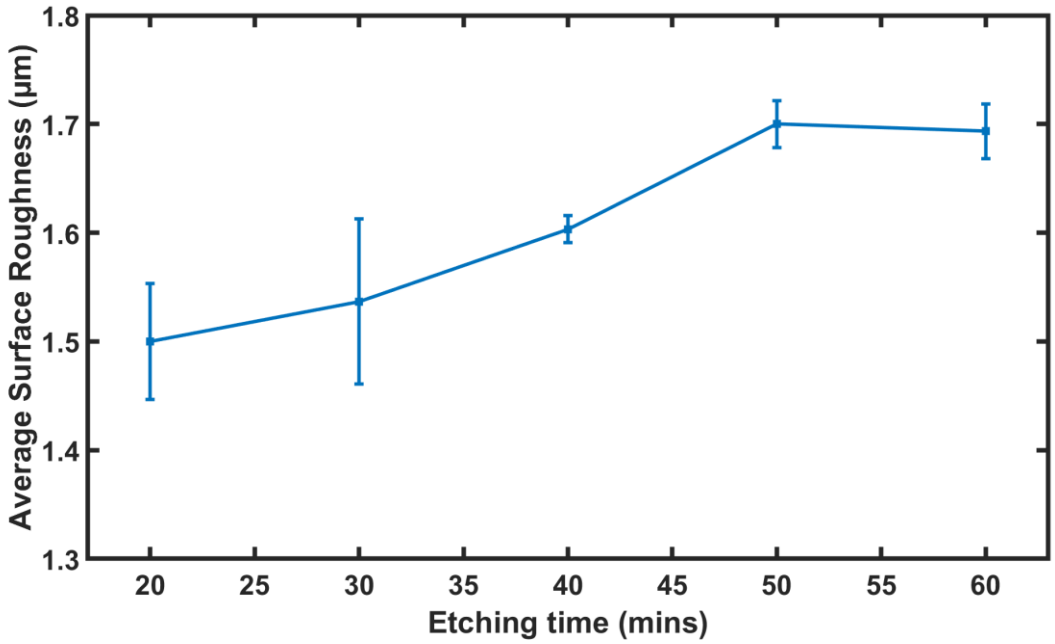


Figure 5-28. Variation of surface roughness with etching duration of chemically etched aluminium surfaces with 1 M HCl and 0.5 M H_2O_2 at constant temperature of 40 °C.

Figure 5-28 shows the variation of average surface roughness of chemically etched aluminium substrate surfaces with increasing etching time. The etching was carried out at a 10 min interval from 20 mins to 60 mins. The etching temperature in all the cases was maintained at 40 °C. The concentration of HCl and H_2O_2 was kept constant for 1 M and 0.5 M respectively. The average surface roughness value obtained is in the range of 1.45 to 1.7 μm. It is observed that initially with increase

in etching time from 20 to 40 mins the surface roughness value gradually increases from 1.49 μm to 1.60 μm. With further increase in etching time fom 40 to 60 mins the surface roughness becomes almost constant at 1.70 μm indicating no further effect of etching time on surface roughness. This can be explained as with increase in etching time the chemical etching gradually increases but when certain time duration is reached there are no more free ions in the solution for further etching process and hence the no change in surface roughness.

5.6.5 Influence of concentration of the etching agent

The concentration of HCl and H_2O_2 is an important determining factor for the chemical etching process as it determines the rate of the chemical etching. The concentration of HCl was varied from 0.25 M to 2 M and the concentration of H_2O_2 is varied from 0.1 M to 1 M. The concentration of HCl influences the rate of the overall reaction and hence the reaction rate.

In a solution of HCl and H_2O_2 , the HCl dissociates rapidly into H^+ and Cl^- ions. Now comparing the reduction potential of H_2O_2 and Cl^- the later gets oxidised to the Cl_2 gas. This Cl_2 gas is in constant equilibrium with the Cl^- ions in the solution. The H_2O_2 also gets reduced to H_2O.

$$H_2O_2 + Cl_2 \rightleftharpoons O_2 + 2H^+ + 2Cl^- \qquad \text{Reaction 5-1}$$

The rate law of the reaction when the concentration of HCl is more than 1 M can be represented as reference in [215],

$$-\frac{d(H_2O_2)}{dt} = -\frac{d(Cl_2)}{dt} = k\frac{[H_2O_2][Cl_2]}{[H^+][Cl^-]} \qquad 5\text{-}1$$

Where $-\frac{d(H_2O_2)}{dt}$ is the rate of dissociation of H_2O_2 and $-\frac{d(Cl_2)}{dt}$ is the rate of dissociation of chlorine. $[H_2O_2]$, $[Cl_2]$, $[H^+]$ and $[Cl^-]$ is the concentration at equilibrium for hydrogen peroxide, chlorine gas, hydrogen ion and chloride ion respectively. 'k' is the equilibrium constant for the reaction. The rate determining step of the reaction is between hydrogen peroxide and hypochlorous acid as written below,

$$H_2O + Cl_2 = H^+ + Cl^- + HOCl$$ Reaction 5-2

$$HOCl + H_2O_2 \longrightarrow H_2O + O_2 + H^+ + Cl^-$$ Reaction 5-3

When the hydrochloric acid concentration is lesser than 1 M the rate of the reaction is less than that expected by the above equations. At lower concentration of HCl the reaction mechanism changes to the following,

$$H_2O_2 + Cl_2 \underset{k_b}{\overset{k_a}{\rightleftharpoons}} H^+ + Cl^- + HOOCl$$ Reaction 5-4

$$HOOCl \xrightarrow{k_c} O_2 + H^+ + Cl^-$$ Reaction 5-5

Where k_a is the rate constant for forward reaction and k_b is the rate constant for backward reaction as shown in Reaction 5-4. The rate constant for dissociation HOOCl is k_c as given in Reaction 5-5. The resulting rate law is described as :

$$-\frac{d(H_2O_2)}{dt} = \frac{k_c k_a [H_2O_2][Cl_2]}{k_b[H^+][Cl^-] + k_c}$$ 5-2

When the concentration of hydrogen ions and chloride ions are high the rate law reduces according to equation 5-2 . At lower concentration of H^+ and Cl^- ions the k_c value becomes significant and hence the rate of the reaction decreases. And at further low concentration of H^+ and Cl^- the rate law changes to the following equation 5-3 where K is the hydrolysis constant for chlorine.

$$-\frac{d(H_2O_2)}{dt} = k_a [H_2O_2][Cl_2] = \frac{k_a}{K}[H_2O_2][HOCl][H^+][Cl^-] \quad 5\text{-}3$$

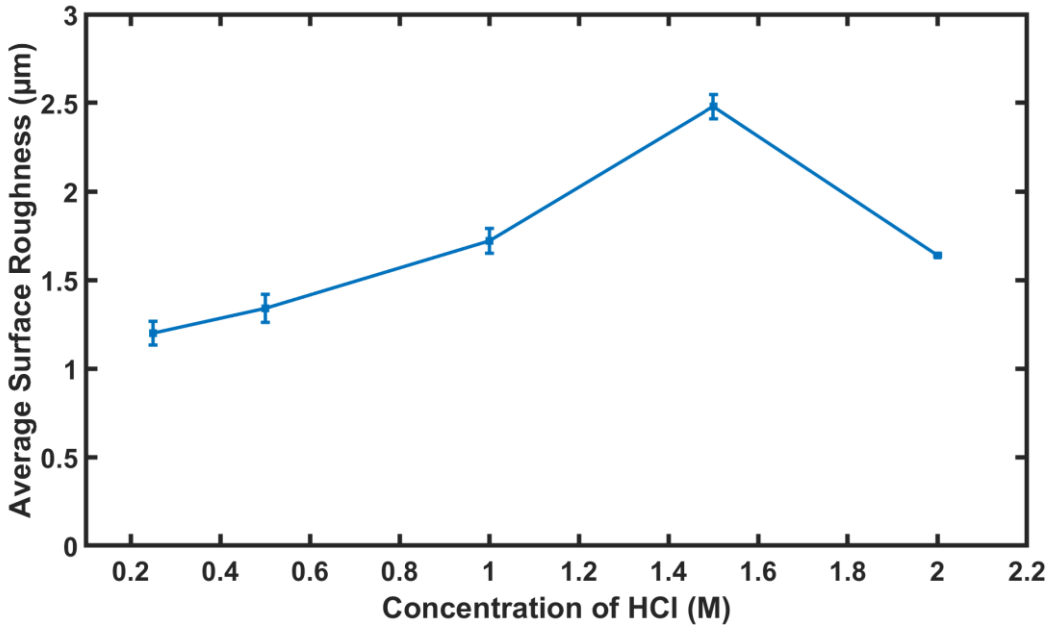


Figure 5-29. Variation of surface roughness of chemically etched aluminium surface with different concentration of HCl at constant 0.50 M concentration of H_2O_2 at 40 °C for 60 mins.

Figure 5-29 shows the surface roughness variation of aluminium substrates when etched with a solutions of constant concentration of H_2O_2 and different concentration of HCl. The treatment temperature and treatment time was also kept constant at 40 °C and 60 mins. The concentration of HCl was varied from 0.25 M to 2 M. The volume of etching solution is also kept constant in each case. It is

evident that with increase in concentration of HCl from 0.25 M to 1.5 M, the average surface roughness increases indicating increase in etching rate. But when the concentration increased from 1.5 to 2 M, the average surface roughness value decreases drastically. The rate of change in surface roughness is not uniform throughout as depicted above. When the concentration of HCl is increased from 0.25 M to 0.50 M, there is a very small increase in surface roughness which supports the theory that rate of the reaction is slow at less than 1M concentration of HCl and the rate equation is given in equation 5-3 . Again when the concentration is increased from 0.50 M to 1 M, the average surface roughness increases from 1.34 to 1.72 μm; and when the concentration increased from 1 M to 1.5 M, the average surface roughness increases significantly from 1.72 to 2.48 μm, indicating that the rate of the reaction increases abruptly as given in equation 5-1. With the increase in reaction rate between HCl and H_2O_2, the etching rate increases as well. But with further increase in concentration from 1.5 to 2 M of HCl, the surface roughness decreases drastically from 2.48 to 1.64 μm, and the thickness of aluminium substrate decreases by 27 %, as compared to original substrate due to polishing effect by HCl at very high concentration.

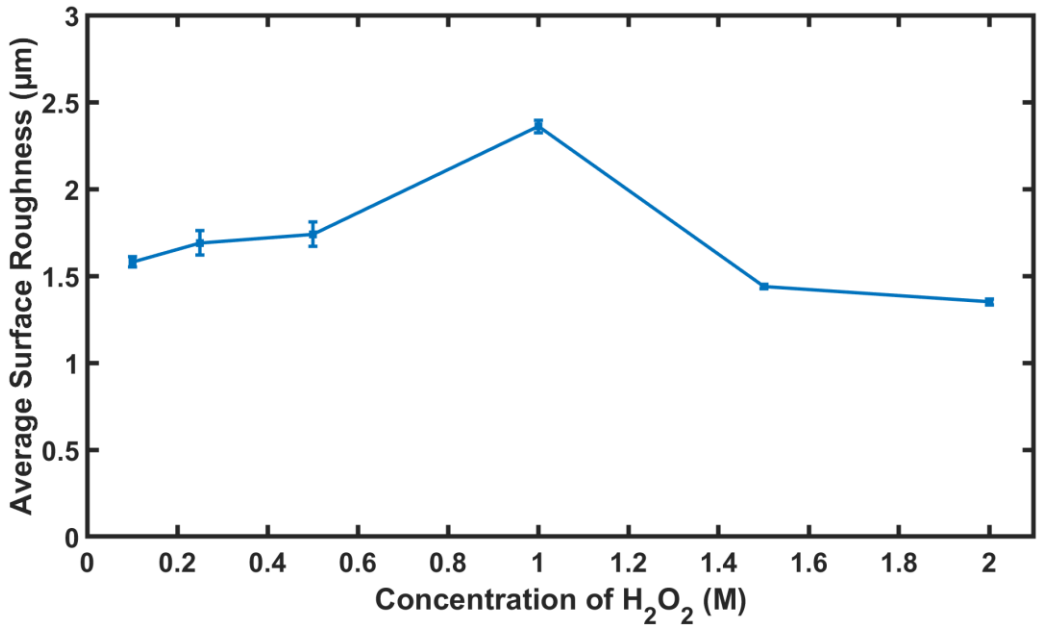


Figure 5-30. Variation of surface roughness of chemically etched aluminium surface with different concentration of H_2O_2 at constant 1 M concentration of HCl at 40 °C for 60 mins.

Figure 5-30 shows variation of average surface roughness on aluminium substrates with varying concentration of H_2O_2 ranging from 0.1 M to 2M when chemically etched with solutions of HCl and H_2O_2 containing constant 1 M concentration of HCl. All the other experimental parameters are kept constant including constant volume of etching solution. The etching was also conducted at a constant temperature of 40 °C for 60 mins. It is clear from the data initially with the increase in concentration of H_2O_2 from 0.10 M to 0.25 M to 0.5 M, the surface roughness gradually increases from 1.58 μm to 1.69 μm to 1.74 μm. with further increase in concentration of H_2O_2 to 1 M the surface roughness increases abruptly to 2.43 μm. This increase is supported by the rate law equation given in equation **5-1**. With increase in concentration of H_2O_2 the rate of chemical etching increases and hence the surface roughness increases. But when the concentration of H_2O_2 increased further the surface roughness decreased drastically. This is due to the fact with increase in concentration of H_2O_2 from 1M to 1.5 M the concentration of H_2O_2

becomes higher than HCl hence the concentration of H^+ ion remaining in the solution at equilibrium decreases and the solution no longer remains acidic enough for efficient chemical etching process. When the concentration of H_2O_2 above 1 M the decrease in thickness of the substrate surface is around 2 % concluding that there was not enough chemical etching.

5.6.6 Effect of concentration of Cu-nanoparticles on surface roughness

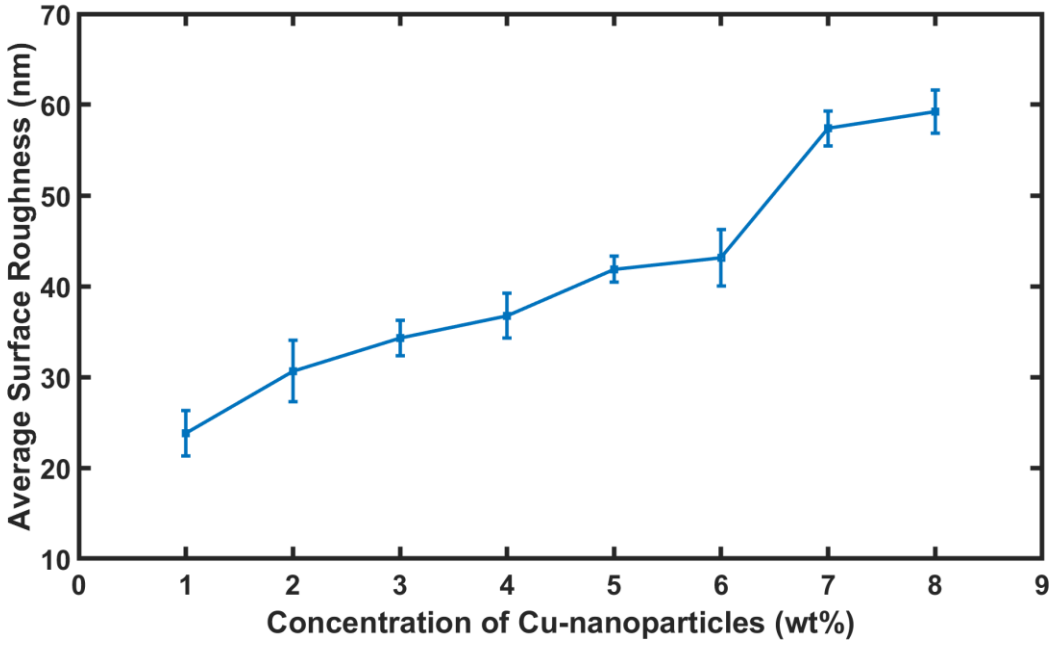


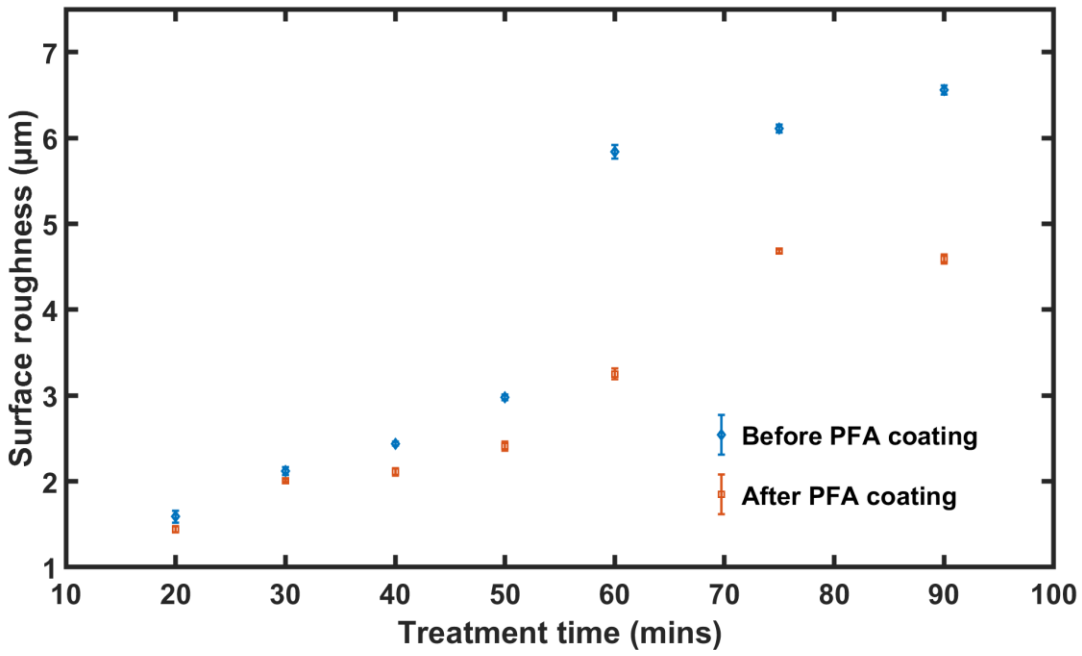
Figure 5-31. Variation of surface roughness of Cu-nanoparticle deposited aluminium surface with different concentration of Cu-nanoparticles deposited by spin coating process at a constant speed of 500 rpm for 1 min.

Figure 5-31 shows variation of surface roughness of Cu-nanoparticle deposited aluminium substrates when different conc of Cu-nanoparticles were deposited on the surface. The concentration of Cu-nanoparticle was varied from 1 to 8 wt %, all the other experimental conditions like temperature, pressure were kept room temperature and atmospheric pressure respectively. The Cu-nanoparticles were deposited via spin coating method. 1 ml of the solution was used each time and the coater was roatated at a speed of 500 rpm for 1 min. the process was repeated

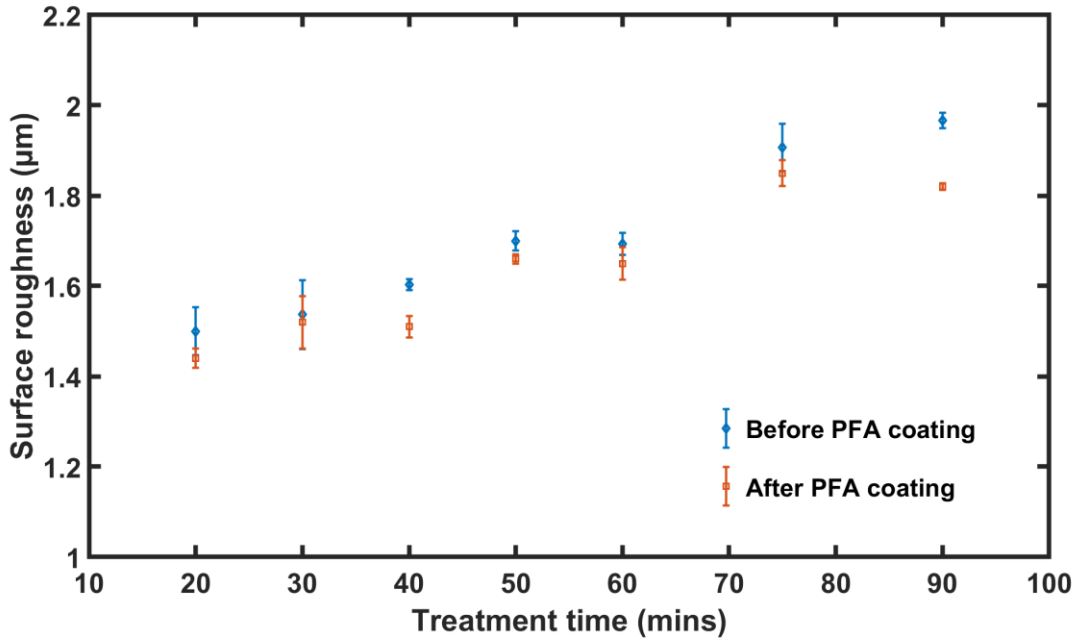
for three times. It is observed with the increase in concentration of Cu-nanoparticles the surface roughness gradually increases. As the amount of nanoparticle in the solution increases more nanoparticles gets deposited on the substrate surface and since the nanoparticles were directly responsible for surface roughness, so the roughness value gradually increases.

5.6.7 Effect of PFA coating on the surface roughness

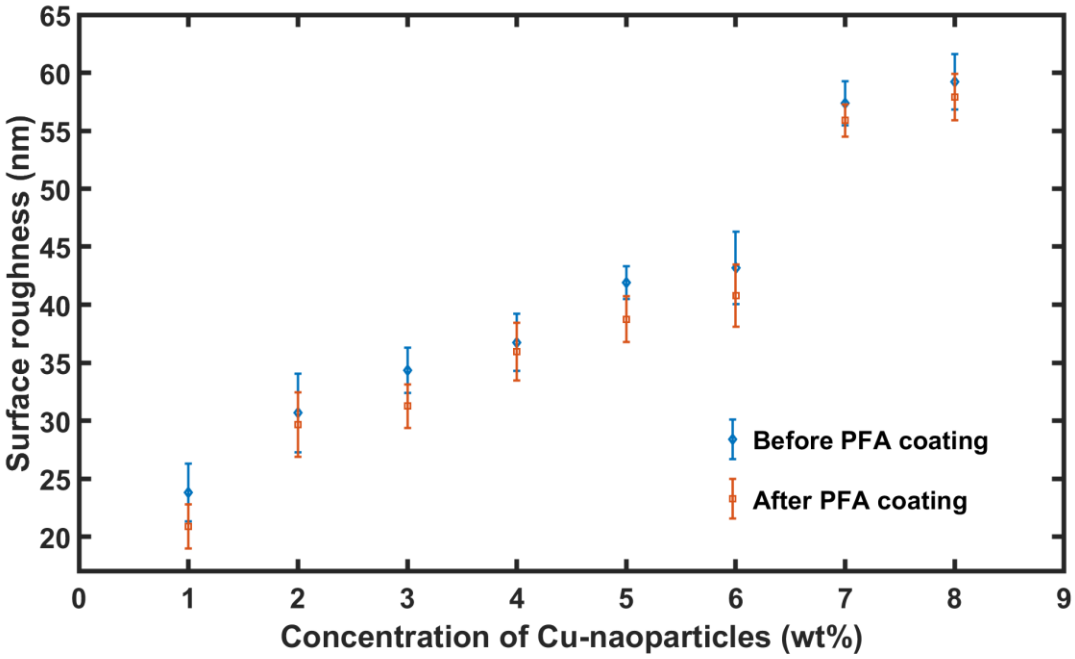
After the substrate surface were modified via anodisation, chemical etching and Cu-nanoparticle deposition separately, PFA emulsion was deposited on the substrate surface and cured. Finally the surface roughness of the substrate is measured and compared with that of the substrate without the polymer film.



(a)



(b)



(c)

Figure 5-32. Surface roughness before and after PFA polymer coating on (a) anodised, (b) chemical etched and (c) nanoparticle deposited surfaces.

Figure 5-32 shows effect of polymer coating on the surface roughness of the substrates treated via anodisation, chemical etching and nanoparticle deposition

separately. It is seen in section 5.4 in each case only a thin layer of polymer film was formed. In each case the surface roughness is slightly decreased with the deposition of PFA polymer. The overall surface roughness trend remains same for chemically etched and nanoparticle deposited surfaces as shown in Figure 5-32 (b) and (c). For the anodised surface when surface roughness is high as shown in Figure 5-32 (a) the surface roughness decreases to higher extent as compared to the mean roughness range. It may be attributed to, at higher surface roughness the cavities on the anodised surface are large and hence the deposited PFA fills up the cavity thus decreasing the average surface roughness value.

5.6.8 Coating erosion resistance

Coating erosion resistance of anodised, chemical etched and nanoparticle deposited substrates were evaluated in section 5.5 by measuring water contact angle before and after the water impinging test indicating change in surface property and also the weight loss due to the impinging test.

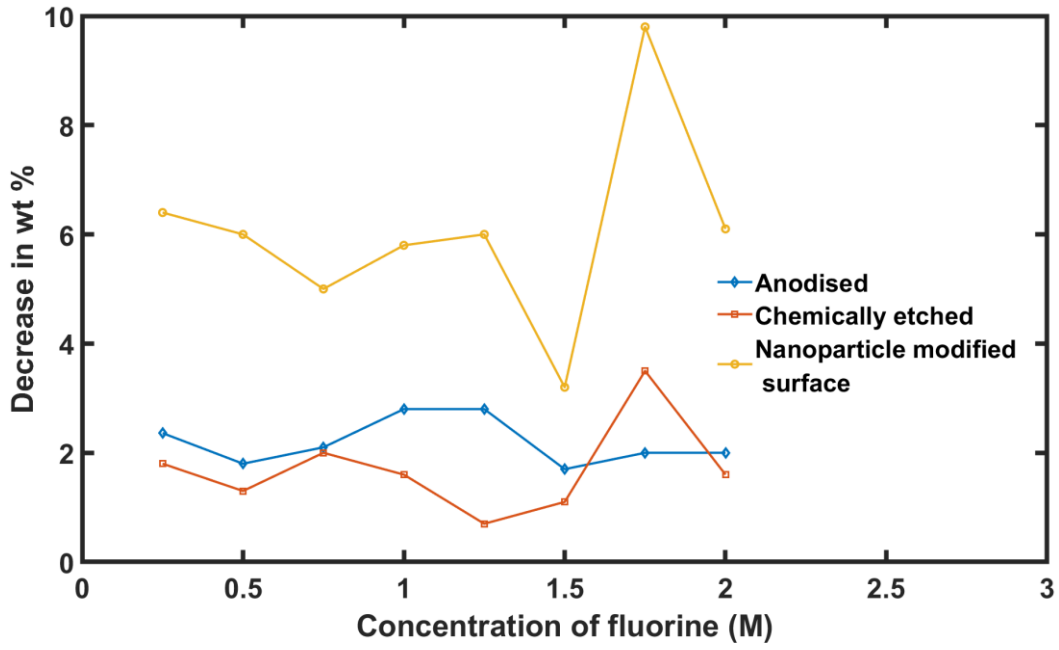


Figure 5-33. Decrease in weight percent of the coatings after the water impinging test for anodised, chemical etched and nanoparticle deposited substrates as a function of change in concentration of fluorine in the PFA emulsion.

Section 5.5 shows the water contact angle before and after the water impinging tests for anodised, chemical etched and nanoparticle deposited surfaces as a function of fluorine content in the PFA emulsion. It is observed that the change in water contact angle before and after the impinging test for nanoparticle deposited surface is much higher as compared to that of anodised or chemically etched surface implying the erosion resistance for composite nanoparticle emulsion is much lower as compared to PFA emulsion coating on anodised or etched surface. The observation is also supported by the drcease in weight percent of the coatings, as shown in Figure 5-33 . For substrates coated with PFA emulsion containing 1 M fluorine the average decrease in weight % after the impinging test is around 6 wt% while that for anodised sample is slightly higher than 2 wt% and least for the chemically etched surface below 2 wt%. Impinging tests condition were kept constant and same for all the samples. The main reason for higher weight loss % for the nanoparticle deposited samples is due to the loose bonding force for the nanoparticles on the substrate surface and hence after water impinging test significant amount of nanoparticle is lost from the substrate along with the PFA emulsion resulting greater loss in water contact angle and wt%. On the contray for anodised and chemical etched surfaces after water impinging test only deposited PFA emulsion is lost, the surface morphology may get altered but in a very insignificant amount and hence lesser decrease in wt%.

5.7 Summary

Anodisation, chemical etching and nanoparticle modifed processes were employed to obtain micro and nano range surface morphology on the substrate. The surface morphology was observed by scanning electron microscopy (SEM) and surface roughness is measured by 3D profilometer. The coating erosion resistance was

evaluated by water impinging tests in which water contact angles before and after the impinging test were measured.

It is observed that uniform surface morphology is obtained on chemically etched surface and the nanoparticle modified surface is most random. Anodisation produces fairly uniform surface morphology but the process is highly dependent on temperature. When the anodisation was conducted at 10 °C or below, 1-2 μm surface roughness is obtained. During chemical etching process the substrates were completely immersed in the etching solution and hence uniform environment was created for the etching process and uniform surface morphology was obtained. For the anodisation process the substrates were also completely immersed in the H_2SO_4 solution but the tempearature of the solution fluctuates during the anodisation process and hence some inconsistency in surface morphology. The H_2SO_4 is a strong acid and when it dissociates it produces energy in the form of heat. With increase in temperature the anodisation process becomes vigorous and hence thickness of the original sample decreases. The nanoparticles are deposited via spin coating process and hence the surface morphology is not uniform throughout. When the nanoparticles were dispersed in the solution they tend to agglomerate and hence their distribution is not uniform throughout.

The surface roughness of anodised samples and chemically etched samples were in micrometer range and that of Cu-nanoparticle modified surface was in nanometer range. The surface roughnesses of anodised and chemically etched surfaces were highly dependent on treatment time, temperature and concentration of the electrolyte solution etc and the processes were vigorous and hence micrometer range surface roughness was obtained in both the cases. But for nanoparticle modified surface, only the concentration of the nanoparticle mainly determines the surface roughness value and since the size of the Cu particles are in nanometer range so nano surface roughness obtained. As the Cu-nanoparticles

tends to agglomerate so that non-uniform surface roughness is obtained throughout.

The thickness of the deposited PFA coating was measured on anodised, chemical etched and nanoparticle deposited surfaces and in each case thickness was in the range of 0.5 -2 μm. The change in surface roughness is also measured before and after the deposition of the PFA coating. It is observed that in each case there is a slight decrease in surface roughness as expected due to the thin layer of PFA coating. But for anodised sample at higher surface roughness above 5 μm range the surface roughness value decreases significantly after the deposition of the PFA coating. This is due to the deposition of the PFA polymer in the large cavities on the surface and thus affecting the surface roughness value significantly.

The water impinging test on the PFA coated anodised, chemically etched and Cu-nanoparticle deposited sample surface indicated the coating erosion resistance. Cu-nanoparticle deposited surface showed lower erosion resistance than anodised or chemically etched surfaces. The main reason for that is attributed to the fact that Cu-nanoparticles were deposited via spin coating process and then heat treated to attach to the substarte surface, so they are loosely bound to the substrate surface as compared to anodised and chemically etched surface. So when water impinging tests were performed the Cu- nanoparticles modified surfaces would be more weak as compared to the other two types of coating samples.

6 Hydrophobicity and Icephobicity of PFA coatings

6.1 Introduction

After surface modification the substrates were coated with the synthesized polymer as discussed in chapter 4. Mainly two different coating process methods were used: spin coating and spray coating. The experimental details of the coating process was given in previous chapter. After deposition of the polymer on the aluminium substrate, the polymer was cured at different temperatures. The curing temperature and fluorine content in the polymer significantly influences the hydrophobicity and icephobicity of the coated samples [216]. Fluorine functional groups in the coating material have very low surface energy. Depending on the concentration of fluorine and surface morphology, the surface becomes hydrophobic or superhydrophobic. The surface icephobicity was also evaluated, including the ice adhesion strength and the evaluation of de-icing energy.

In this chapter, the hydrophobicity of the surface was investigated by water contact angle (WCA) and contact angle hysteresis (CAH) measurement. The variation of hydrophobicity with different coating processes are also compared. The icephobicity of the surface was measured and compared with hydrophilic, hydrophobic and superhydrophobic surfaces and mechanism of reduced ice adhesion was studied. The hydrophobicity and icephobicity of nanocomposite coated substrate surfaces are also evaluated. The influence of surface roughness and concentration of fluorine on icephobicity and hydrophobicity is also discussed.

6.2 Characterization of hydrophobicity of the PFA coatings

6.2.1 Water contact angle analysis

The average water contact angle was obtained for all the aluminium substrate surface before and after the modification. The substrates were coated with synthesized polymer containing different concentration fluorine, cured at different temperature and different curing time etc.

6.2.1.1 Hydrophobicity of coatings on anodised aluminium

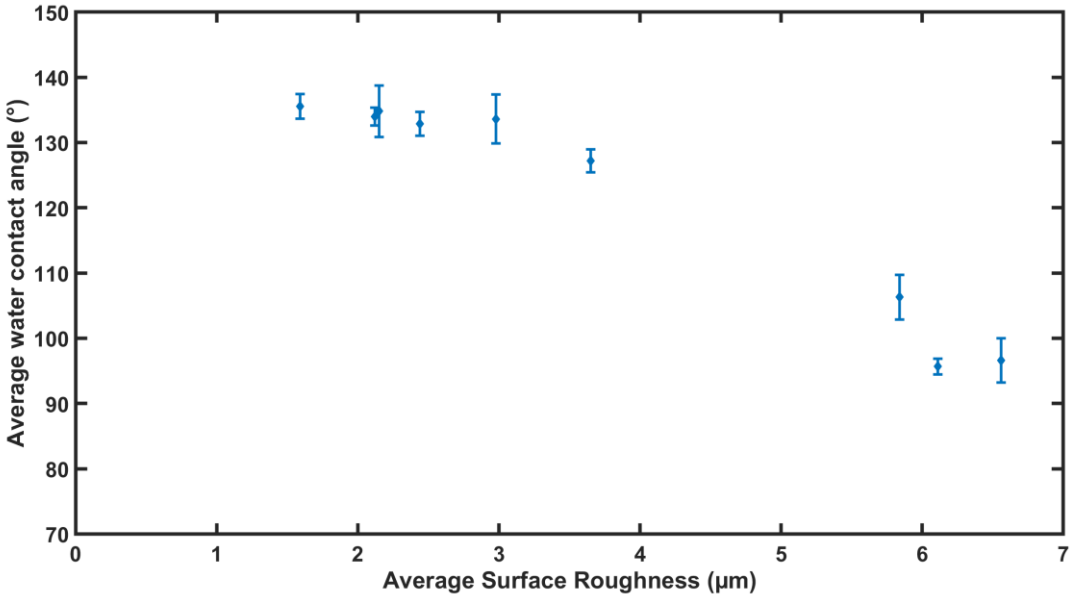
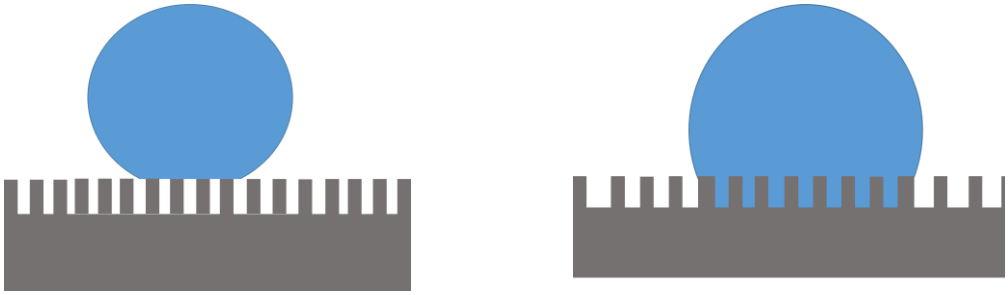


Figure 6-1. Water contact angle with varied surface roughness for coating sample with a polyfluoroacrylate emulsion containing 1:1:1 molar ratio of styrene, acrylic acid and heptafluorobutyl acrylate on anodised aluminium.

Figure 6-1 shows influence of surface roughness on the water contact angle for coating based on polyfluoroacrylate emulsion containing 1:1:1 molar ratio of styrene acrylic acid and heptafluorobutyl acrylate on anodised aluminium surface. The aluminium substrates were anodised at various condition given in previous section 5.2.1. It is clear that with increase in surface roughness the water contact

angle decreases. When the average surface roughness between 1.5 to 3 μm the water contact angles are above 125° indicating lower surface energy and lesser area of contact between the water droplet and the substrate surface. But when the surface roughness is further increased from 3 to 5 to 6 μm the water contact angle decreases drastically to 110 to 105 to 96°. This indicates that the surface roughness is too large and the water droplet no longer sits on the troughs of the rough surface but go inside the cavities and hence increasing the contact area between the water droplet and surface.



(a) (b)

Figure 6-2. Schemsatic diagram of water droplet on anodised aluminium surface coated with a thin layer of polyfluoroacrylate emulsion containing 1:1:1 molar ratio of styrene acrylic acid and heptafluorobutylacrlate and a surface roughness of (a) 1.5 to 3 μm and (b) 3.5 – 6 μm.

Figure 6-2 shows the contact area of water droplets on anodised aluminium surface coated with a thin layer of polyfluoroacrylate emulsion containing 1:1:1 molar ratio of styrene acrylic acid and heptafluorobutylacrlate. The contact area of the water droplet changes with the surface roughness. When the surface roughness is low in the range of 1.5 to 3 μm the water droplet makes less contact on the substrate surface. This is explained by Cassie model according to that air can be trapped below the water drop forming air pockets thus water contact angle increases and hydrophobicity increases. Again when the surface roughness increases beyond 3.5 μm the water droplet enters inside the cavity and hence contact angle decreases which is supported by Wenzel theory [217-220].

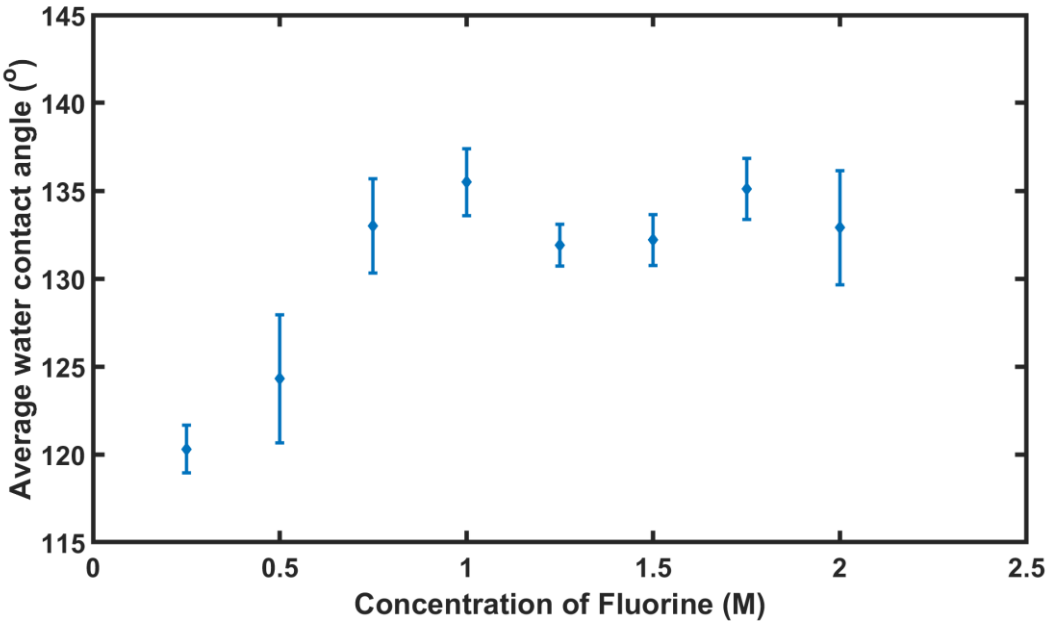


Figure 6-3. Average water contact angles with varied molar concentration of fluorine in polyfluoroacrylate emulsion coated on anodised aluminium surfaces with surface roughness ranging from 1.45 to 1.6 µm.

The variation of average water contact angle of coating based on polyfluoroacrylate emulsion containing different concentration heptafluoroacrylate emulsion on anodised aluminium surface is shown in Figure 6-3. The anodisation condition was kept constant for all the aluminium substrates. The concentration of H_2SO_4 was 131 g/L with current density of 15 x 10^{-4} Acm^{-2}, the treatment time was for 60 mins and the treatment temperature was controlled below 10 °C. The average surface roughness for all the samples is ranging between 1.45 to 1.6 µm. The concentration of heptafluorobutylacrylate (HBA) is increased at an equal interval of 0.25 M. In all the cases, the surfaces are hydrophobic in nature. It is observed initially when the concentration of HBA is increased from 0.25 to 1 M there is a gradual increase in water contact angle indicating decrease in surface energy. When the concentration of HBA is further increased from 1 M to 2 M gradually with 0.25 M interval the average water contact angle almost remains same with a slight decrease in value which is negligible. This indicates that the hydrophobicity is

optimised with 1 M HBA and the hydrophobicity will not be improved with higher concentration of more than 1 M.

6.2.1.2 Hydrophobicity of polymer coating on chemically etched aluminium

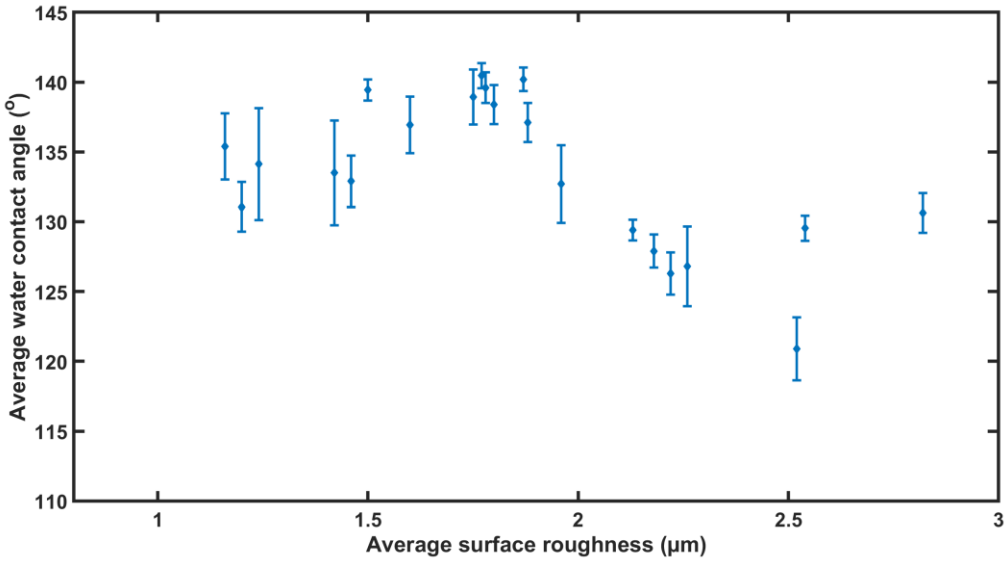


Figure 6-4. Average water contact angle on coating with polyfluoroacrylate emulsion containing 1:1:1 molar solution of styrene acrylic acid and heptafluorobutylacrylate on aluminium substrates etched with a solution containing HCl and H_2O_2.

Figure 6-4 shows the variation of average water contact angle of coating based on polyfluoroacrylate emulsion on chemically etched aluminium substrates. The substrates were etched with a solution of HCl and H_2O_2 containing various concentration, etching duration and temperature to obtain different roughness from 1 to 3 μm. The modified substrates were then coated a thin layer of polyfluoroacrylate emulsion containing 1:1:1 molar ratio of styrene acrylic acid and heptafluorobutylacrylate by spin coating method. Then the coated surfaces were cured at 120 °C for 1 hr. The average water contact angle on the coated surface ranges from 118 to 145° indicating all the surfaces are hydrophobic in nature. The highest water contact angle of 141° obtained when the surface roughness ranges from 1.85 to 1.88 μm. With the increase in surface roughness beyond 2 μm the

water contact angle decreases according to Wenzel model as described in section 6.2.1.1.

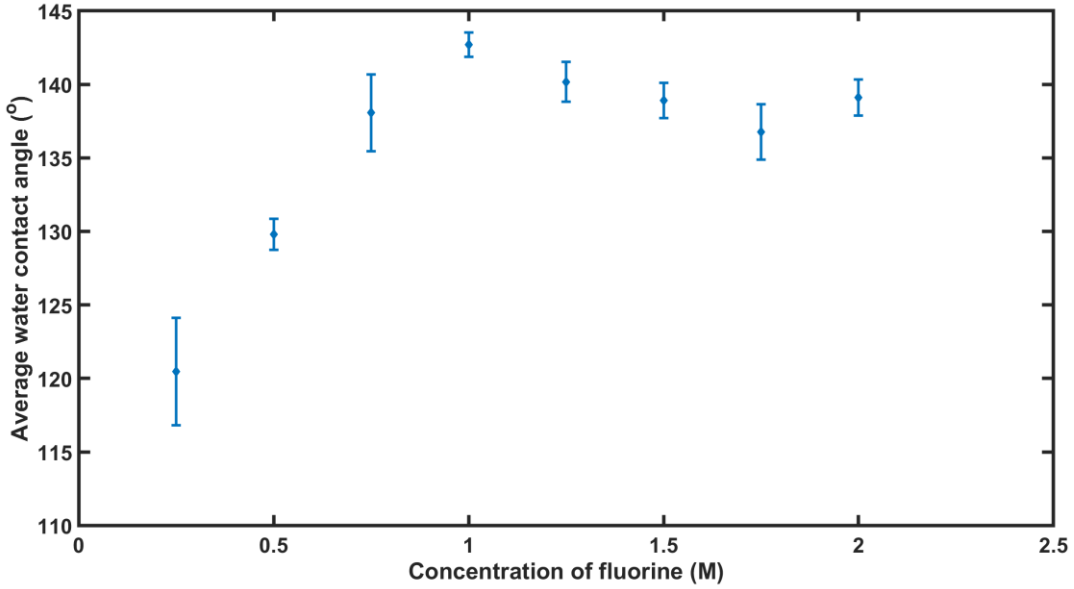


Figure 6-5. Average water contact angle of polyfluoroacrylate coatings with various concentration of heptafluoroacrylate on aluminium substrates after etched with a solution containing 2 M HCl and 0.50 M H2O2 at 60 °C for 30 mins.

Figure 6-5 shows variation of water contact angle of coatings with polyfluoroacrylate emulsion containing various molar concentration of heptafluorobutyl acrylate and 1:1 molar ratio of styrene and acrylic acid on chemically etched aluminium surface. The chemical etching was performed with a solution containing 2 M HCl and 0.50 M H_2O_2 at 60 °C for 30 mins. The surface roughness varies from 1.7 to 1.9 µm. The average water contact angle value varies from 120 to 145° when the molar concentration of heptafluorobutyl acrylate varied from 0.25 M to 2 M with 0.25 M interval. In all the cases, the surfaces are hydrophobic in nature. Initially with increase in concentration of heptafluorobutyl acrylate from 0.25 to 0.5 to 0.75 M the contact angle changes from 120° to 139°. When the concentration is increased further the contact angle increased to a small extend to 142° and then it almost remains unchanged with small variation

indicating no more heptafluorobutyl acrylate can be incorporated in the main polymer chain.

6.2.1.3 Hydrophobicity of polymer coating on aluminium with Cu-nanoparticle deposit

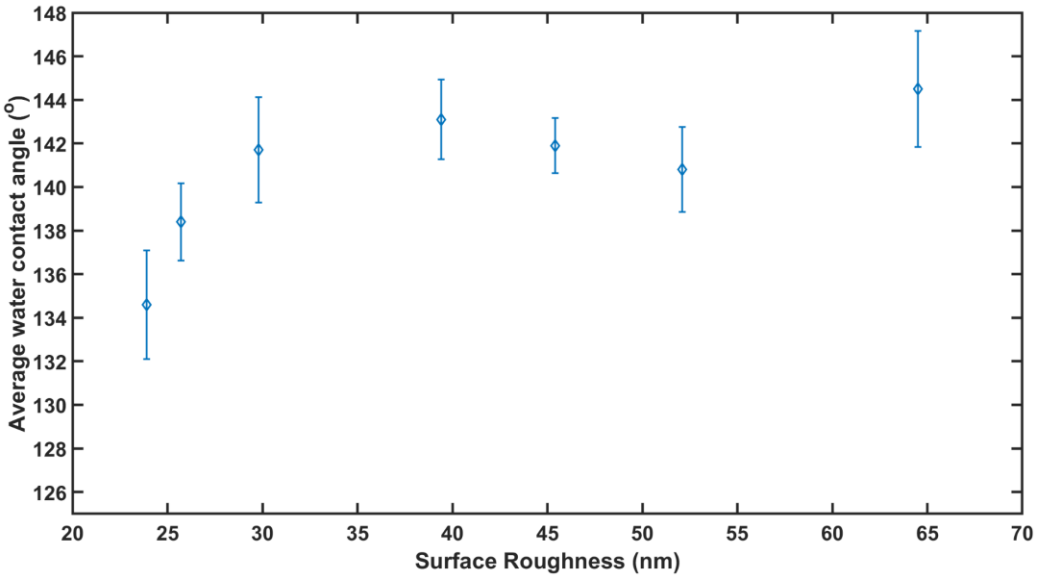


Figure 6-6. Average water contact angle on coating with polyfluoroacrylate emulsion containing 1:1:1 molar solution of styrene acrylic acid and heptafluorobutylacrylate on aluminium substrates and various wt % of Cu-nanoparticle solution.

When different concentration of Cu-nanoparticle is mixed with the PFA emulsion and deposited on the substrate surface various surface roughness is obtained as shown in Figure 6-6. The surface roughness varies between 23 to 65 nm. A PFA emulsion containing 1:1:1 molar ratio of styrene, acrylic acid and heptafluorobutyl acrylate was used in all the cases. It is observed that initially with the increase in surface roughness from 20 to 30 nm the water contact angle gradually increases from 135 to 141°. With further increase in surface roughness beyond 30 nm the water contact angle (WCA) varies insignificantly with highest WCA of ~144° is obtained when surface roughness was 65 nm. As mentioned in the previous cases the surface hydrophobicity is a combination of surface roughness and surface

energy. Since the polymer is same is all the cases so the surface enrgy factor remains constant and the only variable affecting the hydrophobicity is surface roughness.

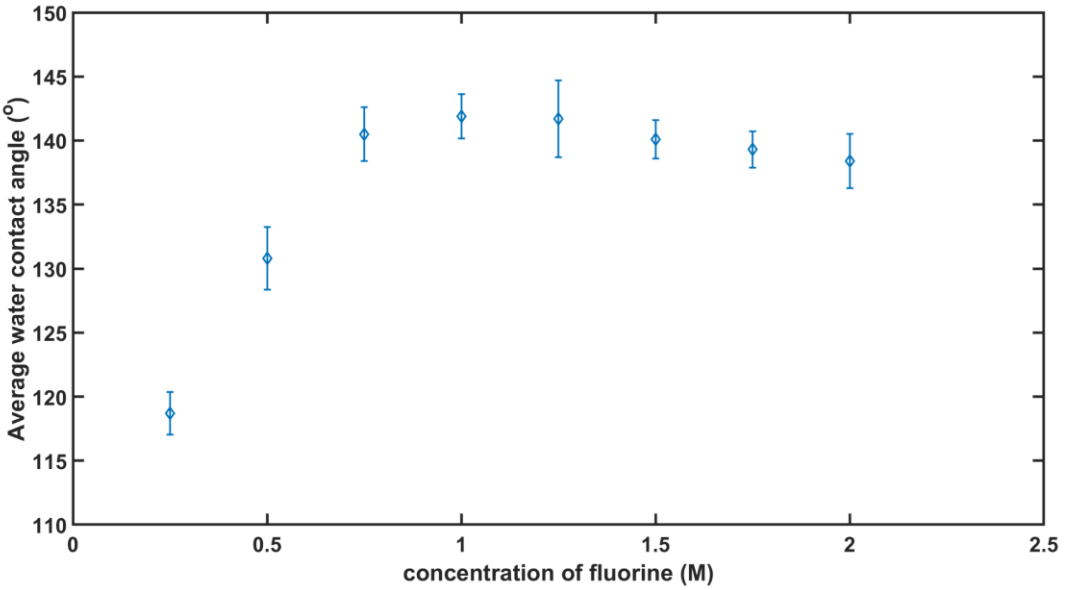


Figure 6-7. Average water contact angle on coating with polyfluoroacrylate emulsion containing 1:1molar solution of styrene acrylic acid and various molar ratio of heptafluorobutylacrylate on aluminium substrates and 2 wt% of Cu-nanoparticle solution.

Figure 6-7 shows variation of water contact angle on aluminium substrate as a function of concetration of fluorine in the PFA emulsion. The average surface roughness in all the cases was between 50-60 nm. The concentration of fluorine varied from 0.25 M to 2 M and corresponding water contact angle is measured. Initially when the concentration of fluorine increased from 0.25 to 0.5 to 0.75 M the water contact angle gradually increases from 118 to 140° indicating increase in surface hydrophobicity. In all the cases the surface roughness is considered same so the variable here affecting surface hydrophobicity is surface energy. With the increase in fluorine content in the polymer the surface energy gradually decreases as fluorine is the most electronegative and lowest surface energy material so the surface hydrophobicity in turn increases increasing the WCA value.

When the concentration of fluorine increased beyond 0.75 M the contact angle remains almost constant indicating no further decrease in surface energy.

6.2.2 Contact angle hysteresis study

6.2.2.1 Contact angle hysteresis of PFA coatings on anodised aluminium

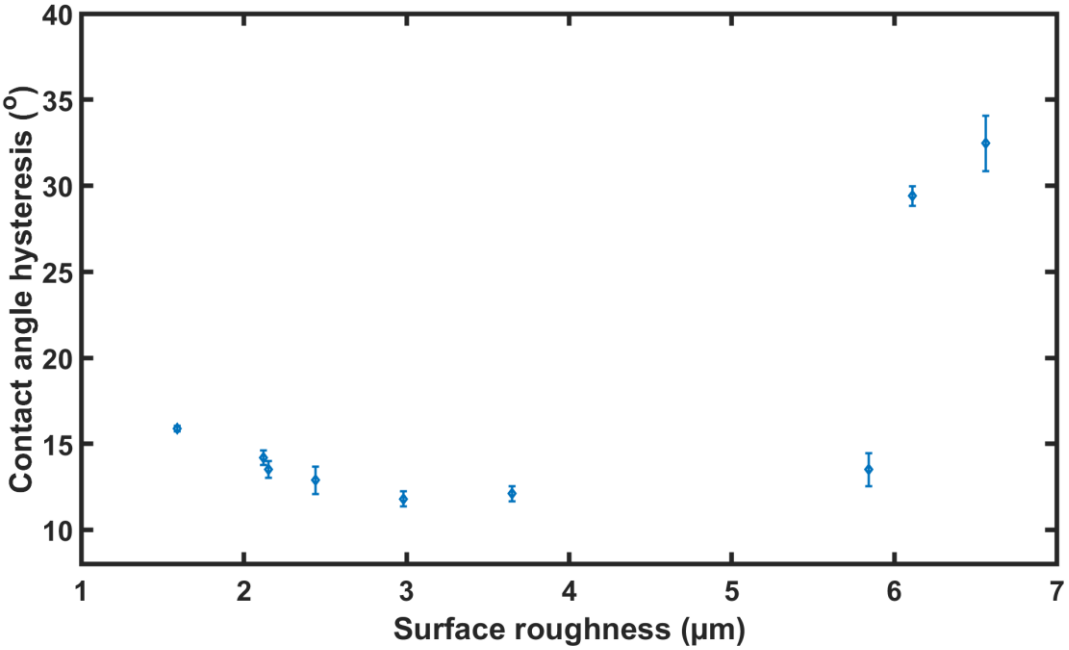


Figure 6-8. Variation of contact angle hysteresis of coating based on polyfluoroacrylate emulsion containing 1:1:1 molar ratio of styrene, acrylic acid and heptafluorobutyl acrylate on anodised aluminium substrates as a function of average surface roughness.

In addition to water contact angle measurement, the contact angle hysteresis (CAH) value defines whether the water droplet can easily roll off form the surface. When the CAH value is high i.e, the difference between the advancing angle and receding angle is high, then the droplet is more attached on the substrate surface. Figure 6-8 shows the variation of average water contact angle hysteresis of coating based on polyfluoroacrylate emulsion on anodised aluminium surface as a function of surface roughness. The detailed anodisation conditions are given in previous chapter. All the anodised samples were coated with a layer of polyfluoroacrylate emulsion containing 1:1:1 molar ratio of styrene, acrylic acid and heptafluorobutyl

acrylate. The surface roughness varies from 1.5 to 7 μm depending on anodisation conditions. The average contact angle hysteresis also varies from 10 to 33°. It is observed that the contact angle hysteresis increases with increase in surface roughness. When the surface roughness is below 3 μm, the CAH value also remains below 12° and hence the water droplet can easily roll off from the surface. As the surface roughness increases beyond 3 μm, the CAH increases above 15° and with a surface roughness of 6.5 μm, the CAH reaches as high as 32.5°. This high CAH indicates that the water droplet cannot easily roll off from the surface supporting the theory given in chapter 2. When the surface roughness is high, the water droplets can no longer sit on the air pockets of the rough surface and it goes inside the cavities to form a mechanical interlock resulting higher adhesion of water droplet on the substrate with a higher CAH value [221].

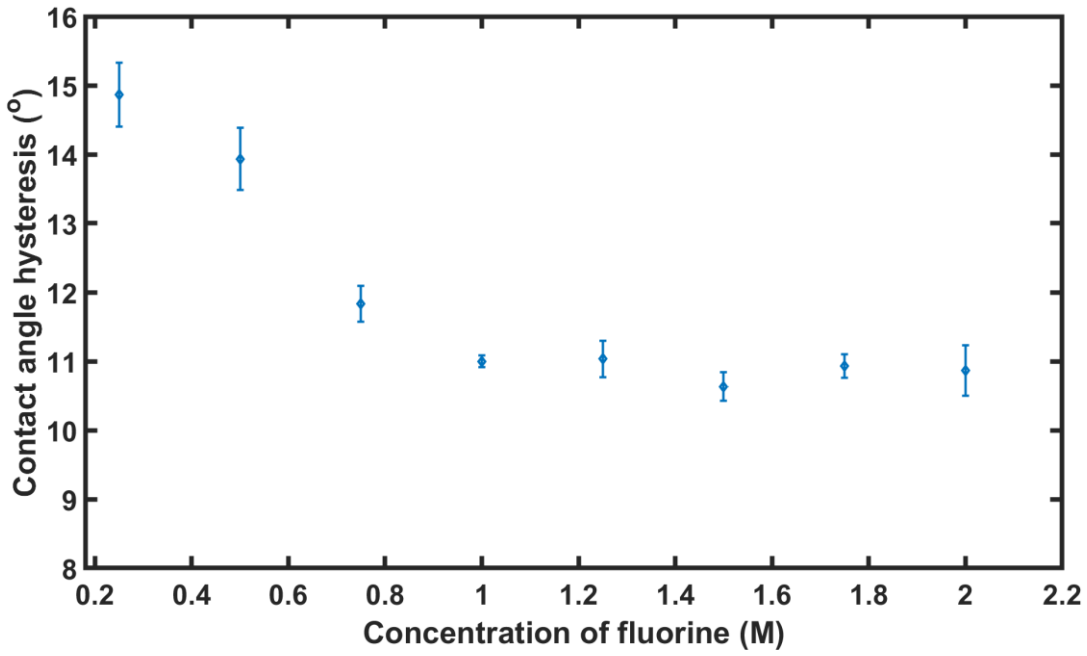


Figure 6-9. Variation of contact angle hysteresis of coating based on polyfluoroacrylate emulsion as a function of concentration of heptafluorobutyl acrylate with concentration of styrene and acrylic acid fixed at 1:1 molar ratio on anodised aluminium samples.

Figure 6-9 shows variation of contact angle hysteresis on coating based on polyfluororacrylate emulsion as a function of concentration of heptafluorobutyl

acrylate on anodised aluminium surface. The substrates were anodised at a constant temperature of 10 °C for 40 mins with a 131 g/L H_2SO_4 solution. The PFA emulsion was deposited on the substrate surface via spin coating process. The molar ratio of styrene and acrylic acid was kept at 1:1 as constant for all the samples. In all the cases the surfaces are hydrophobic and contact angle hysteresis is more than 10°. With the increase in molar concentration of heptafluorobutyl acrylate, the average CAH gradually decreases indicating that a water droplet can easily roll off from the surface. Beyond 1 molar ratio of heptafluorobutyl acrylate, the CAH value almost remains similar, which can be inferred that change in surface energy and hydrophobicity is negligible.

6.2.2.2 Contact angle hysteresis of PFA coatings on chemically etched aluminium

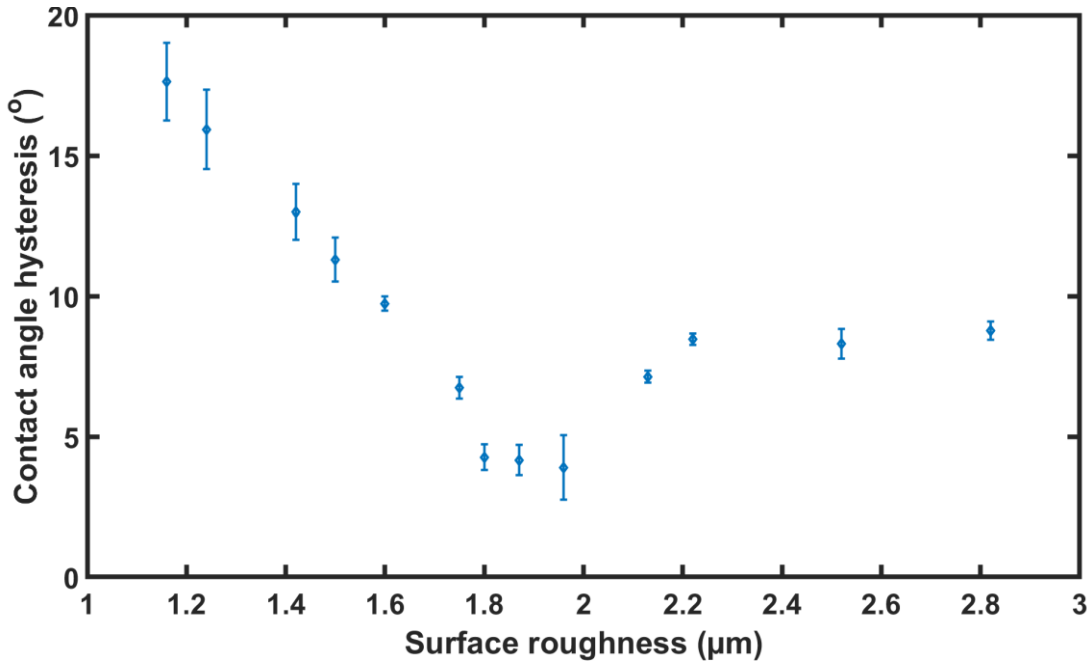


Figure 6-10. Variation of contact angle hysteresis of coating based on polyfluoroacrylate emulsion containing 1:1:1 molar ratio of styrene, acrylic acid and heptafluorobutyl acrylate on etched aluminium substrates as a function of average surface roughness.

Figure 6-10 shows the variation of water contact angle hysteresis of PFA coatings containing 1:1:1 molar ratio of styrene, acrylic acid and heptafluorobutyl acrylate

on chemically etched aluminium surface etched with a solution of HCl and H_2O_2 containing various concentration as a function of average surface roughness. It is observed that the surface roughness of chemically etched samples range from 1 to 3 μm. The CAH value never exceeds 20° as compared to the anodised samples as shown in Figure 6-9, where the CAH value exceeds 30° with increasing surface roughness. Initially when the surface roughness is low, high CAH value is observed indicating high adhesion of water droplet on the substrate surface. When the average surface roughness value increases beyond 1.5 μm, the CAH value also decreases below 10° and attains a lowest CAH with a surface roughness of 1.88 μm. With further increase in surface roughness to 3 μm the CAH increases a bit but remains below 10°. With the increase in surface roughness, a Cassie state is reached, as shown in Figure 6-2 (a), because the contact area of the water droplet on the surface decreases and rolling off of water droplet is easier resulting lower CAH. With further increase in surface roughness, the water droplet starts to enter into the cavities shown in Figure 6-2 (b) and adhesion strength increases. It is more difficult to roll off the water droplet resulting increased CAH.

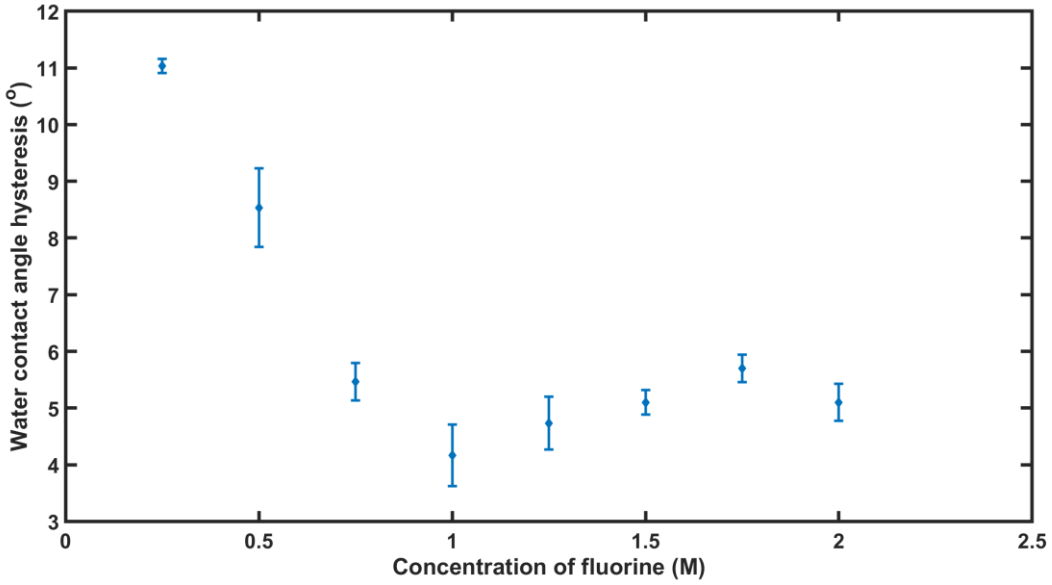


Figure 6-11. Variation of contact angle hysteresis of PFA based coating on chemically etched aluminium substrates as a function of concentration of heptafluorobutyl acrylate.

The contact angle hysteresis of PFA coating on etched aluminium substrates depends on the molar ratio of heptafluorobutyl acrylate (HBA) as given in Figure 6-11. The substrates were etched with a solution containing 2 M HCl and 0.50 M H_2O_2 at 60 °C for 60 mins. The PFA emulsions contain different molar ratio of heptafluorobutyl acrylate (HBA) with molar ratio of styrene and acrylic acid remaining as 1:1. The surface roughness of all the substrates is almost same with average value of 1.80 µm. The molar concentration of HBA was also varied from 0.25 M to 2 M. It is observed that with increase in molar ratio from 0.25 to 1 M, the contact angle hysteresis gradually decreases indicating that the water droplet is easier to roll off from the surface. It is supported by the fact that with increase in molar ratio of HBA the concentration of fluorine increases in the polymer composition. The fluorine provides low surface energy on the substrate and hence the adhesion of water droplet on the surface decreases, decreasing the CAH value. When the molar ratio of HBA is further increases beyond 1 M, the CAH value almost remain same around 4 to 5° indicating the concentration of 1 M reaches the

optimum value in the polymer with further increase in the molar concentration no more HBA gets incorporated in the polymer structure.

6.2.2.3 Contact angle hysteresis of PFA coatings on nanoparticle deposited surface

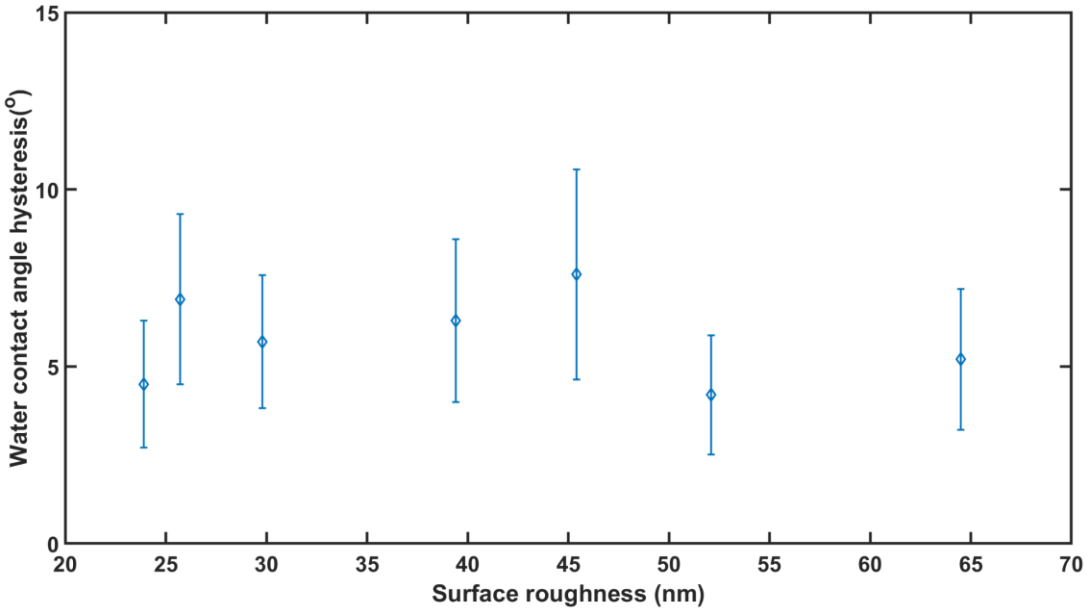


Figure 6-12. Variation of contact angle hysteresis of coating based on polyfluoroacrylate emulsion containing 1:1:1 molar ratio of styrene, acrylic acid and heptafluorobutyl acrylate on nanoparticle deposited aluminium substrates as a function of average surface roughness.

Figure 6-12 shows variation of water contact angle hysteresis of aluminium substrate coated with a composite coating of Cu-nanoparticles in polyfluoroacrylate emulsion containing 1:1:1 molar ratio of styrene, acrylic acid and heptafluorobutyl acrylate. The amount of nanoparticles varied and hence variation in surface roughness is obtained. The surface roughness varies from 23 to 65 nm range unlike the anodised and chemical etched samples in which case the surface roughness is in μm range. In all the cases the average water contact angle hysteresis is below 10 ° indicating low wetting of the surface by incident water droplet. Since the surface roughness is in nanometer range so it doesn't affect the wettability to a significant amount. The average contact angle hysteresis value ranges between 4

to 8 ° with lowest value of 4 ° was obtained when the surface roughness was 53 nm.

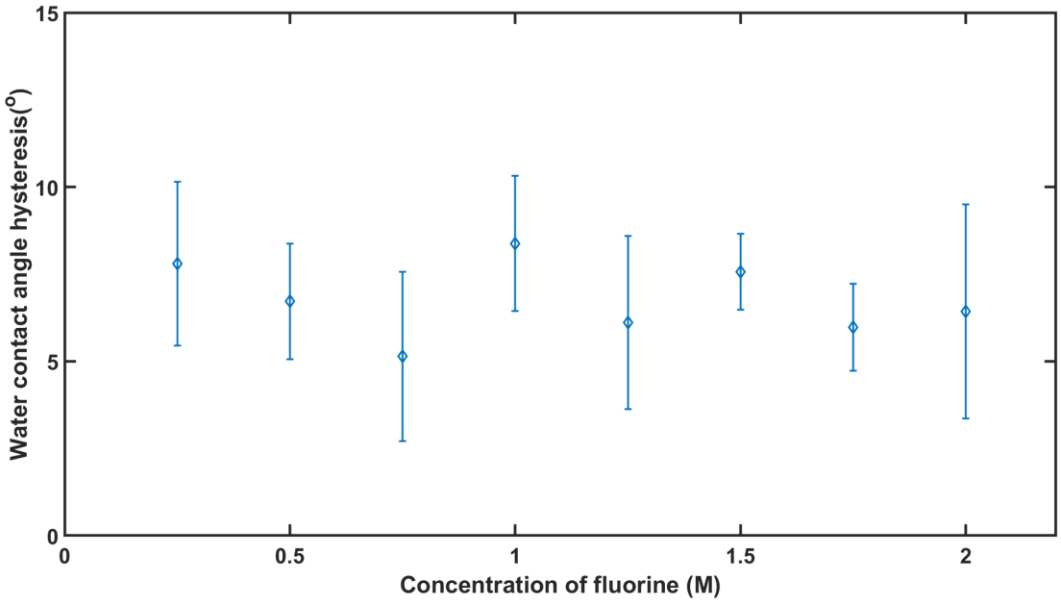


Figure 6-13. Variation of contact angle hysteresis of PFA based coating on nanoparticle deposited aluminium substrates as a function of concentration of heptafluorobutyl acrylate.

Similarly like surface roughness the fluorine content also do not have significant effect on surface wettability as shown in Figure 6-13. The fluorine content varied from 0.25 M to 2 M and corresponding water contact angle hysteresis value was measured. Here also the average contact angle hysteresis value is below 10° indicating lower wetting by the incident water droplet on the substrate surface. The surface roughness in all these cases were ranged between 40 to 50 nm. The lowest water contact hysteresis value of 5° obtained when the concentration of fluorine was kept at 0.75 M. Both the above cases suggest that in the case of nanoparticle deposited surfaces both surface roughness and concentration of fluorine has insignificant effect on the wetting property of the surface.

6.3 Characterization of icephobicity of the surface

To characterize the icephobicity of the substrate surfaces ice adhesion strength analysis and de-icing energy evaluation have been performed. The details of the experimental details and process parameters are given in section 3.9 and 3.10.

6.3.1 Ice adhesion strength analysis

6.3.1.1 Ice adhesion strength for anodised samples

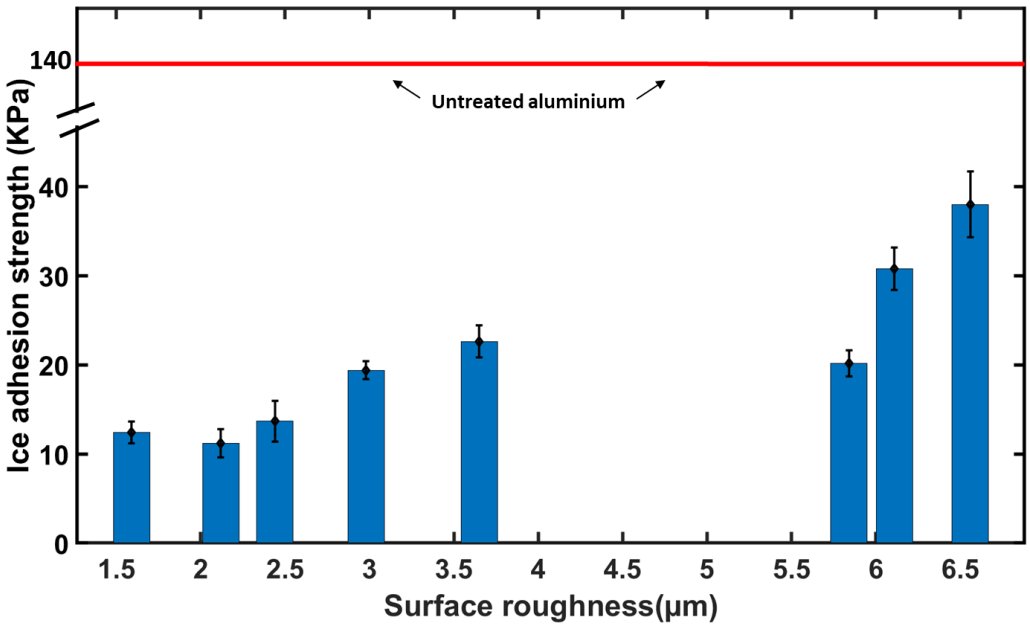


Figure 6-14. Variation of ice adhesion strength and shear force on anodised aluminium surface coated with a PFA emulsion containing 1:1:1 molar ratio of styrene, acrylic acid and heptafluorobutyl acrylate as a function of surface roughness.

Ice adhesion strength on anodised aluminium surface coated with PFA emulsion varies with surface roughness as shown in Figure 6-14. The PFA emulsion used was containing 1:1:1 molar ratio of styrene acrylic acid and heptafluorobutyl acrylate in all the cases. It is observed for anodised samples the ice adhesion strength is above 1O KPa which is quite high with the lowest value obtained ~11 KPa when the surface roughness is around 2.25 μm. The general trend is seen that with increase in surface roughness the ice adhesion strength gradually increases

with highest ice adhesion strength of 38 KPa was obtained when the surface roughness was 6.5 µm. The shear force also follows the same trend as ice adhesion strength. Highest shear force of 11.85 N was obtained when surface roughness was 6.5 µm. The conditions for the ice adhesion tests are discussed in chapter 3. With the increase in surface roughness the size of the cavities on the surface increases and when the water droplet freezes on the surface it anchors on the surface with strong mechanical interlocking system and hence cannot be removed easily from the surface hence lower higher ice adhesion strength.

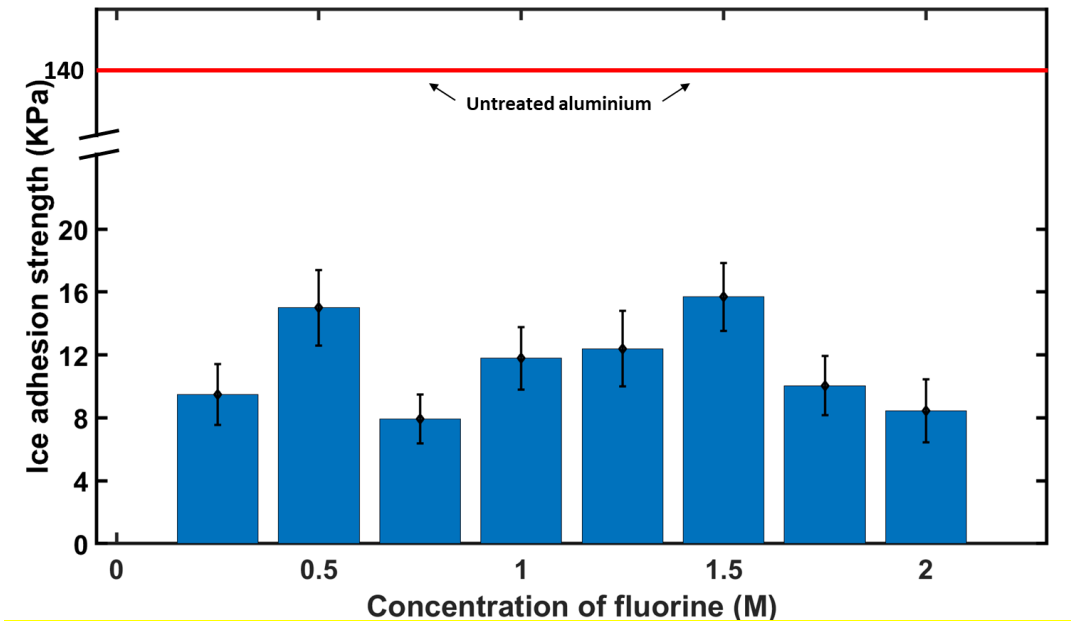


Figure 6-15. Variation of ice adhesion strength and shear force on anodised aluminium surface coated with a PFA emulsion containing various concentrations of fluorine and surface roughness ranging from 2 to 3.5 µm.

Figure 6-15 shows variation of ice adhesion strength and shear force on anodised aluminium substrate coated with PFA emulsion containing 1:1 molar ratio of styrene, acrylic acid and various molar ratio of heptafluorobutyl acrylate (HBA). The concentration of HBA varied from 0.25 to 2 M. The surface roughness of the aluminium surface ranged between 2 to 3.5 µm. The process of anodisation is highly affected by temperature and very hard to control and hence the range of

surface roughness obtained for same condition of anodisation is wide. Hence the ice adhesion strength here also have some influence for surface roughness not only concentration of fluorine. In all the cases the ice adhesion strength is lower than 16 KPa with lowest ice adhesion strength of ~ 7 KPa is obtained when the concentration of fluorine is 0.75 M. The shear force follows the same trend as ice adhesion strength as discussed in the previous case with highest shear force of 4.5 N was obtained when the concentration of fluorine was 1.5 M. The ice adhesion strength or shear force doesn't follow a proper trend with concentration of fluorine as seen in Figure 6-15, as surface roughness also affects here as it is not uniform throughout.

6.3.1.2 Ice adhesion strength for chemical etched samples

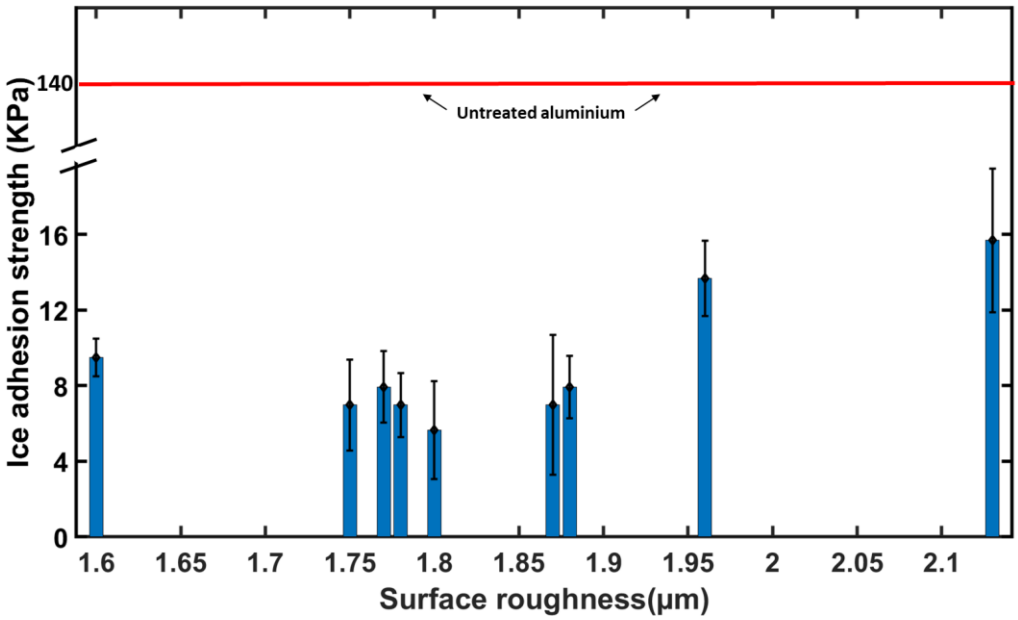


Figure 6-16. Variation of ice adhesion strength and shear force on chemically etched aluminium surface coated with a PFA emulsion containing 1:1:1 molar ratio of styrene, acrylic acid and heptafluorobutyl acrylate as a function of surface roughness.

For chemical etching process the process parameters can be controlled easily and hence the range of surface roughness obtained is narrow. The surface roughness ranges between 1.5 to 2.5 μm. The ice adhesion strength is below 16 KPa in all

cases. When the surface roughness is in the range of 1.6 to 1.9 μm the average ice adhesion strength below 10 KPa with lowest value of ~ 6 KPa is obtained when the surface roughness is 1.8 μm. With increase in surface roughness beyond 1.9 μm the ice adhesion strength increases beyond 10 KPa which highest value of 15.8 KPa was obtained when surface roughness was ~ 2.2 μm. The shear force value also lower as compared to anodised samples and increases as ice adhesion strength increases. The lowest and highest shear force values obtained were 1.8 and 4.7 N respectively.

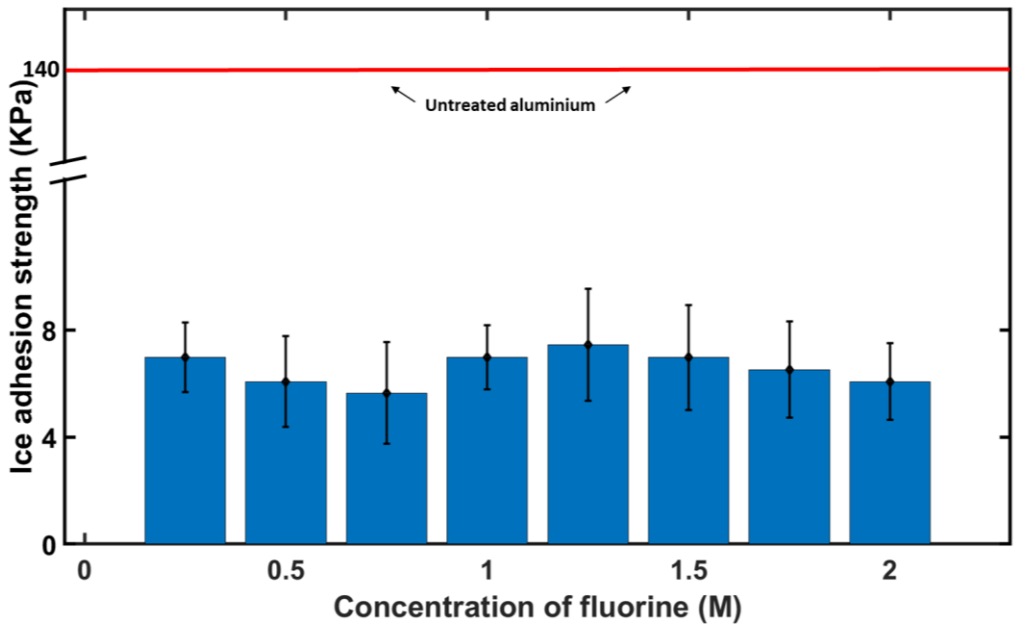


Figure 6-17. Variation of ice adhesion strength and shear force on chemically etched aluminium surface coated with a PFA emulsion containing various concentrations of fluorine and surface roughness ranging from 1.8 to 1.85 μm.

For chemically etched aluminium substrates the surface roughness can be controlled very easily and the surface roughness was maintained in the range of 1.8 to 1.85 μm. The concentration of fluorine varied between 0.25 to 2 M. The ice adhesion strength and shear force shows a relatively lower value as compared to anodised samples. The ice adhesion strength in all the cases is below 8 KPa with lowest value of 5.8 KPa is obtained when the concentration of fluorine is 0.75 M.

The average ice adhesion strength value ranges between 5.8 to 7.5 KPa hence it can be concluded that the ice adhesion strength doesn't alter massively as a result of change in fluorine content in the PFA emulsion. The average shear force is also below 2.2 N, the shear force value ranges between 1.65 to 2.2 N.

6.3.1.3 Ice adhesion strength for nanoparticle deposited samples

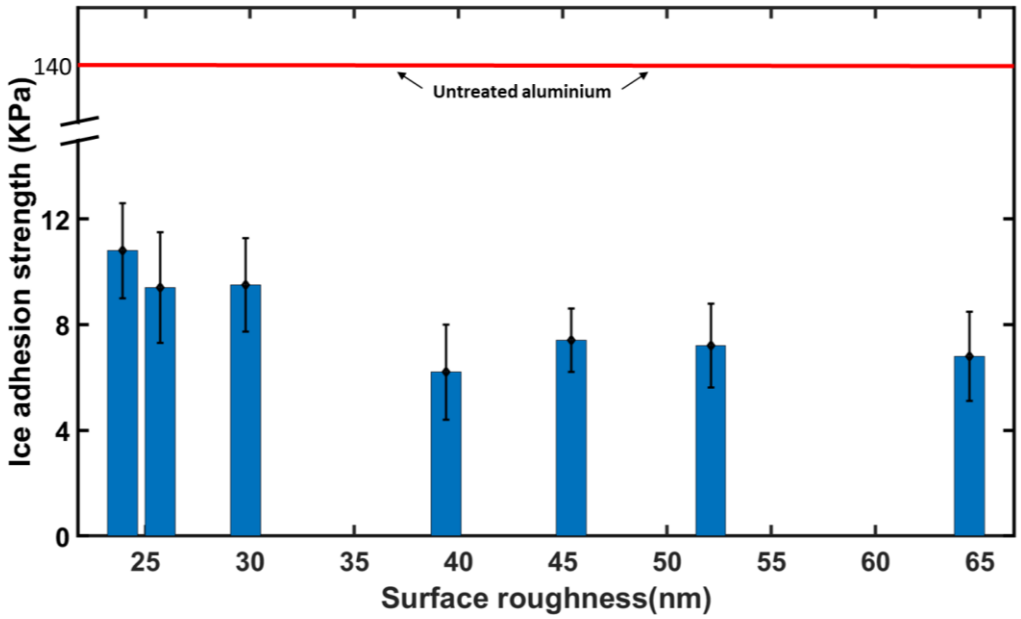


Figure 6-18. Variation of ice adhesion strength on Cu-nanopaticle deposited aluminium surface coated with a PFA emulsion containing 1:1:1 molar ratio of styrene, acrylic acid and heptafluorobutyl acrylate as a function of surface roughness.

Figure 6-18 shows variation of ice adhesion strength on aluminium surface coated with a PFA emulsion containing 1:1:1 molar ratio of styrene, acrylic acid and heptafluorobutyl acrylate and various concentration of Cu-nanoparticles. Due to the various concentration of Cu-nanoparticles the average surface roughness varies from 20 to 70 nm. The ice adhesion strength is below 10 KPa in most of the cases except when the surface roughness was below 25 nm the ice adhesion strength beyond 10 KPa. Lowest value of 6 KPa for ice adhesion strength is obtained when surface roughness is 40 nm. The average ice adhesion strength is lower than anodised or chemically etched substrates. The surface roughness value

does not alter the ice adhesion strength significantly for Cu-nanoparticle deposited aluminium substrates as the surface roughness is very low (nanometer range).

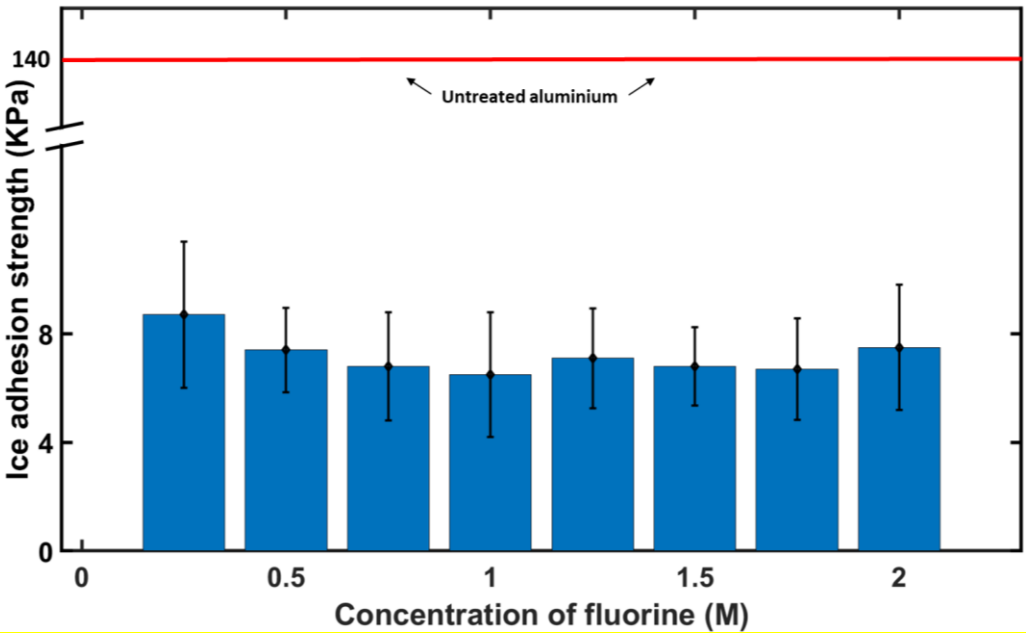


Figure 6-19. Variation of ice adhesion strength on Cu-nanoparticle deposited aluminium surface coated with a PFA emulsion containing various concentrations of fluorine and surface roughness ranging from 40-45 nm.

Similarly like surface roughness fluorine content in the PFA emulsion has least effect on the ice adhesion strength for Cu-particle deposited aluminium substrates as shown in Figure 6-19. The concentration of fluorine varied from 0.25 M to 2 M. The average ice adhesion strength in all the cases is below 9 KPa. The surface roughness is also maintained between 40 to 45 nm. Initially when the concentration of fluorine is 0.25 M the ice adhesion strength is above 8 KPa , with the increase in concentration of the fluorine to 0.5 to 0.75 M the ice adhesion strength gradually decreases to 7.5 to 7 KPa. The ice adhesion strength reaches a minimum of 6.5 KPa when the concentration of fluorine reaches to 1 M. When the concentration of fluorine is further increased the ice adhesion strength does not alter significantly.

6.3.2 De-icing energy evaluation

6.3.2.1 De-icing test for anodised samples

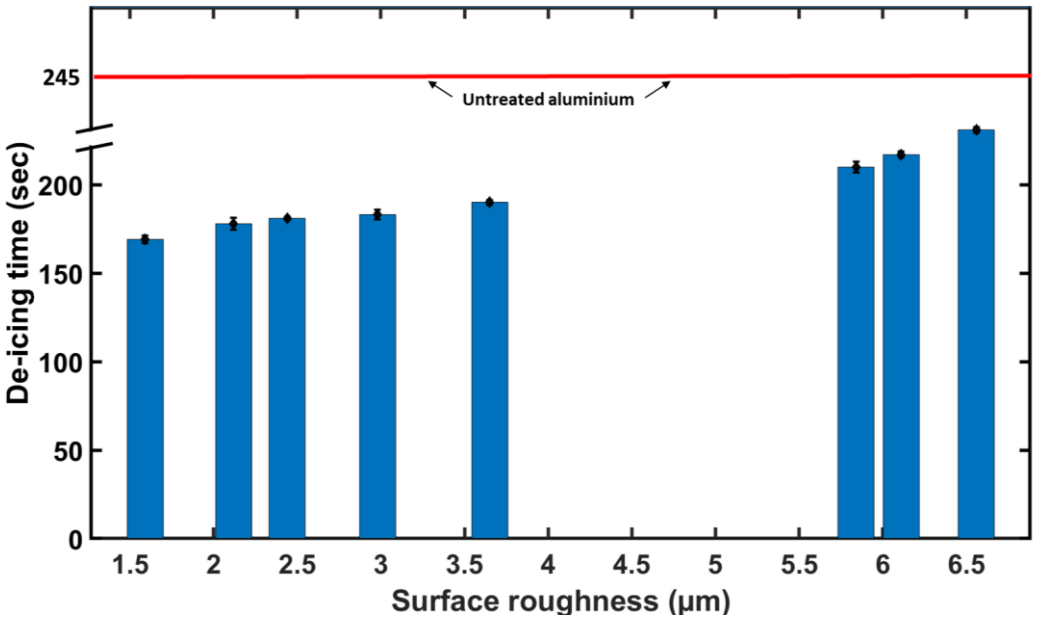


Figure 6-20. Variation of de-icing time for anodised aluminium substrates coated with a PFA emulsion containing 1:1:1 molar ratio of styrene, acrylic acid and heptafluorobutyl acrylate as a function of surface roughness.

Figure 6-20 shows variation of de-icing time on anodised aluminium substrate as a function of surface roughness. All the samples were coated with the same PFA emulsion containing 1:1:1 molar ratio of styrene, acrylic acid and heptafluorobutyl acrylate. The specifications of the de-icing tests are given in section 3.10. The average de-icing time of uncoated and untreated aluminium substrate was 245 s and that is taken as reference to compare reduction in de-icing time. For anodised aluminium samples the surface roughness varies to large extend 1.4 to 6.6 μm and hard to control. It is observed at lower surface roughness the de-icing time reduced to 170 s, with the increase in surface roughness the de-icing time gradually increases but remains below 200 s . When the surface roughness goes beyond 6 μm the de-icing time increases drastically beyond 200 and becomes almost comparable to that of uncoated aluminium of 240 s. This supports the theory that with high surface roughness the cavities become large and when water

molecule freezes it anchors in those cavities and hence hard to remove from the surface.

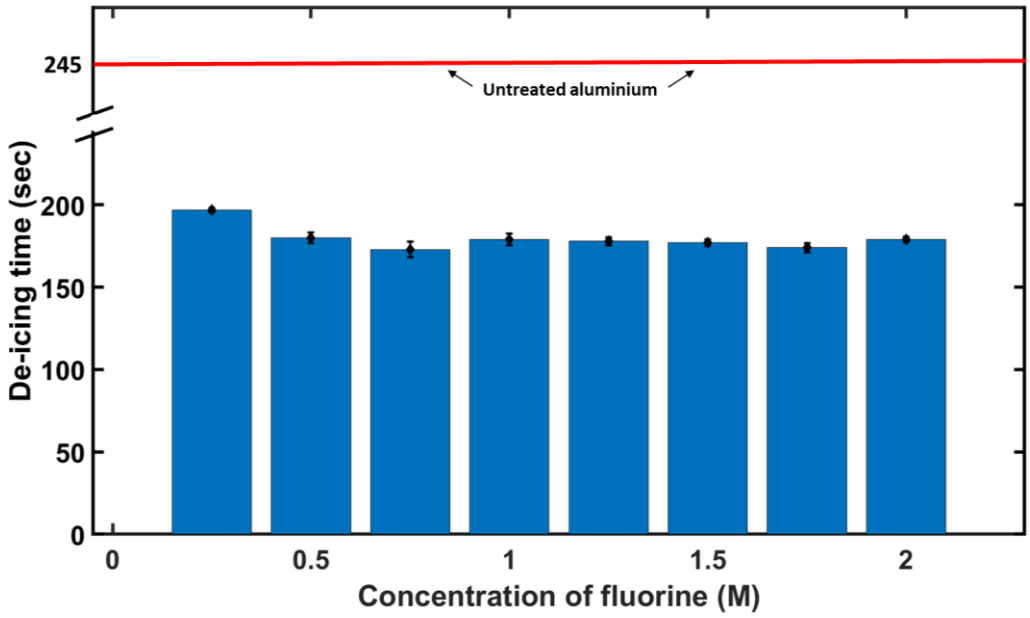


Figure 6-21. Variation of de-icing time for anodised aluminium substrates coated with a PFA emulsion containing 1:1 molar ratio of styrene, acrylic acid and various concentrations of heptafluorobutyl acrylate with surface roughness ranging from 1.6 to 1.85 μm.

All the aluminium samples under same anodising conditions and the surface roughness ranges between 1.6 to 1.85 μm. The concentration of fluorine was varied between 0.25 to 2 M and corresponding de-icing time was measured as shown in Figure 6-21. Initially when the concentration of fluorine is 0.25 M the de-icing time was ~ 200 s, with further increase in concentration of fluorine to 0.5 M the de-icing time decreases to 170 s . It remains almost constant with any further increase in concentration of fluorine. In all these cases the surface roughness also plays an important role for the de-icing time as the surface roughness range is quite high, so sole effect of concentration of fluorine is difficult to be evaluated.

6.3.2.2 De-icing test for chemically etched samples

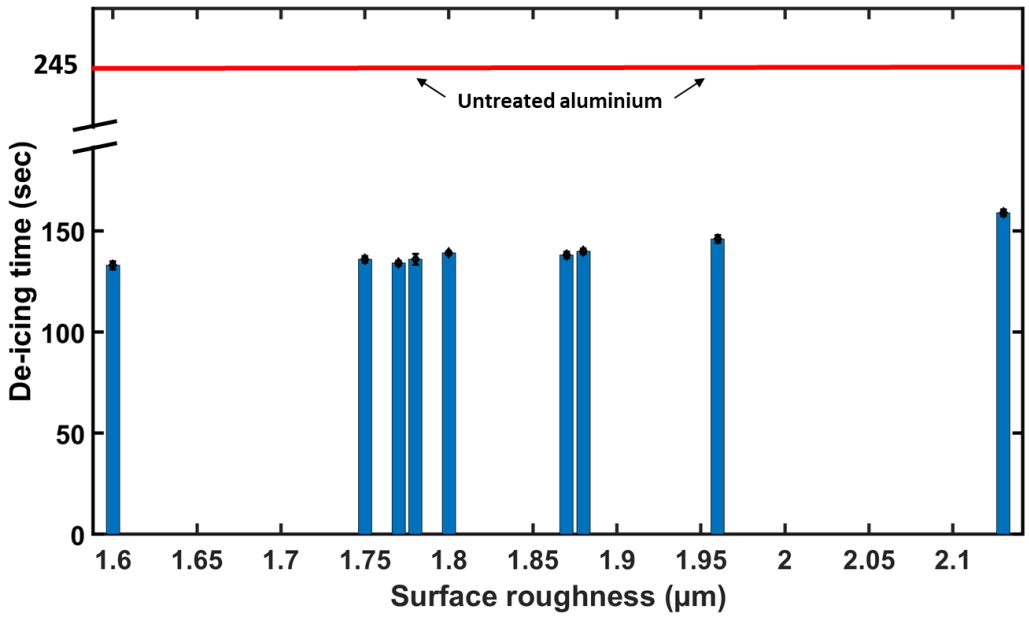


Figure 6-22. Variation of de-icing time for chemically etched aluminium substrates coated with a PFA emulsion containing 1:1:1 molar ratio of styrene, acrylic acid and heptafluorobutyl acrylate as a function of surface roughness.

Figure 6-22 shows variation of de-icing time for chemically etched aluminium substrates as a function of surface roughness. The surface roughness ranges from 1.6 μm to 2.3 μm, the de-icing time also ranges between 130 to 160 s. When surface roughness is in the range of 1.6 to 1.9 μm the de-icing time ranges between 130 to 140 s, with further increase in surface roughness the de-icing time gradually increases. The highest of 159 s of de-icing time obtained when surface roughness is 2.2 μm. In all the cases PFA emulsion is used containing 1:1:1 molar ratio of styrene, acrylic acid and heptafluorobutyl acrylate.

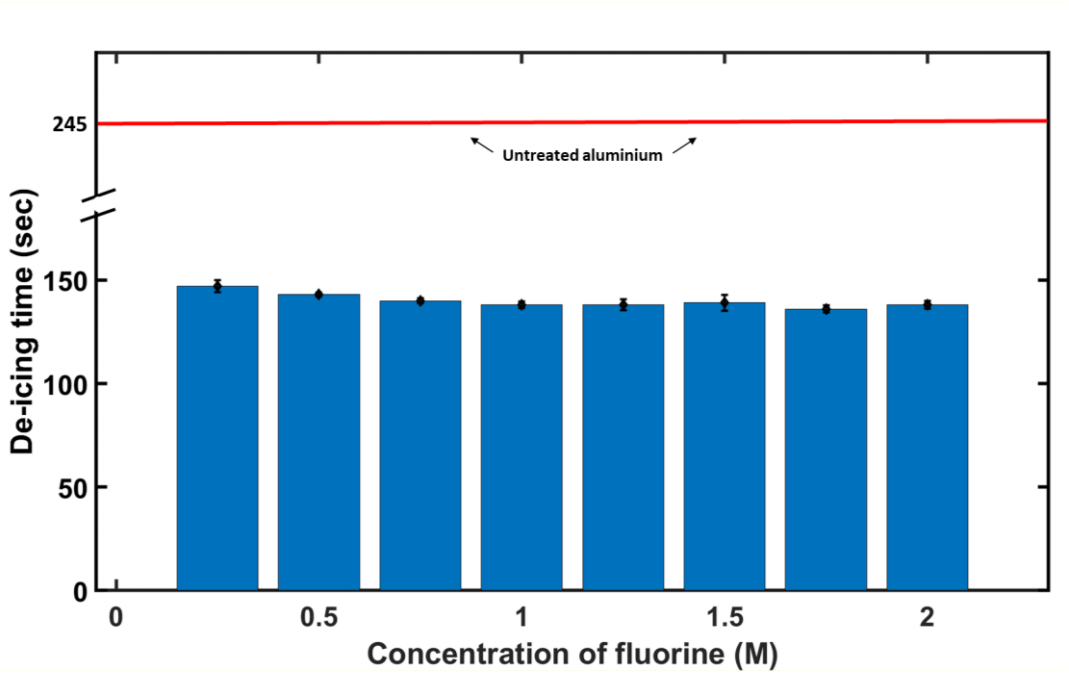


Figure 6-23. Variation of de-icing time for chemically etched substrates coated with a PFA emulsion containing 1:1 molar ratio of styrene, acrylic acid and various concentrations of heptafluorobutyl acrylate with surface roughness ranging from 1.6 to 1.7 μm.

PFA emulsions with different molar concentration of fluorine concentration were deposited on the chemically etched aluminium substrate and the variation of de-icing time was observed. The surface roughness was maintained between 1.6 to 1.7 μm. The molar concentration of fluorine was varied between 0.25 to 2 M. It is observed that concentration of fluorine has no drastic effect on the de-icing time. In all the cases the de-icing time ranges between 130 to 150 s. With lower concentration of fluorine at 0.25 M the de-icing time is higher and with further increase in concentration of fluorine the de-icing time slightly decreases as shown in Figure 6-23. When the molar concentration of fluorine reaches to 1 M the de-icing time becomes ~ 140 s and almost remains constant with further increase in fluorine content.

6.3.2.3 De-icing test for nanoparticle deposited samples

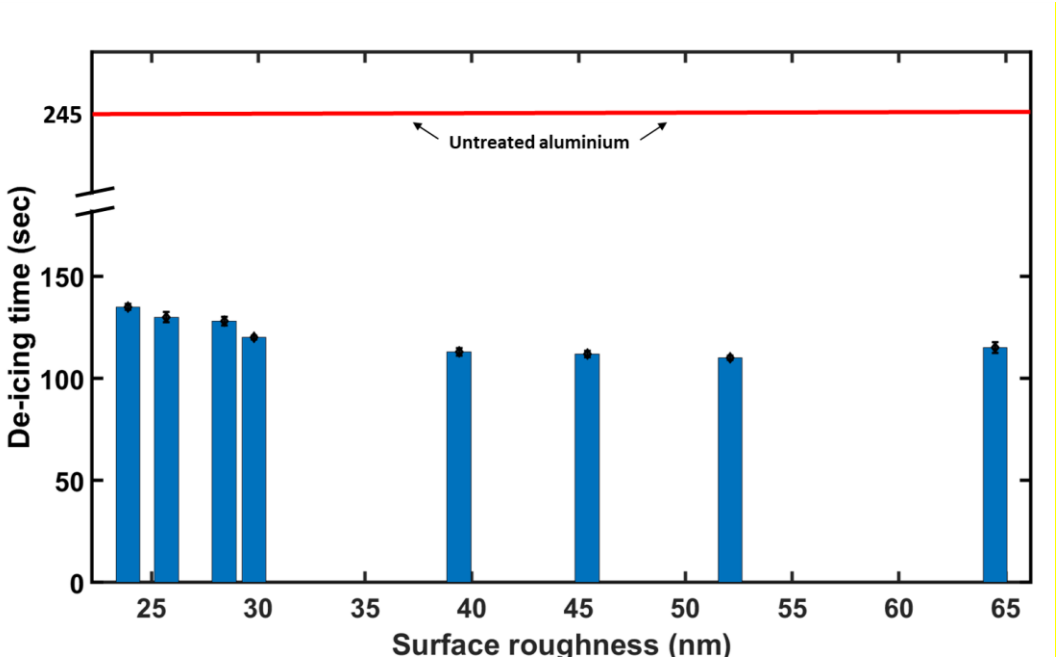


Figure 6-24. Variation of de-icing time for nanoparticle deposited aluminium substrates coated with a PFA emulsion containing 1:1:1 molar ratio of styrene, acrylic acid and heptafluorobutyl acrylate as a function of surface roughness.

Aluminium substrate surface with spin coated with a composite coating of PFA emulsion with different amount of Cu –nanoparticles to get various surface roughness. The de-icing time was measured and plotted against surface roughness as shown in Figure 6-24 .The surface roughness is in nanometer range as compared to micrometer range for anodised and chemical etched substrates. The surface roughness ranges between 20 to 70 nm. The de-icing time is also much lower as compared to anodised and chemically etched coated substrates. The de-icing time varies between 135 to 110 s. It is evident that with the increase in surface roughness the de-icing time gradually decreases. The increase in surface roughness is directly proportional to the Cu-nanoparticle content in the coating and the Cu-nanoparticles are conductive and can conduct electricity as heat through the coating making removal of ice easier and hence reduction in de-icing time.

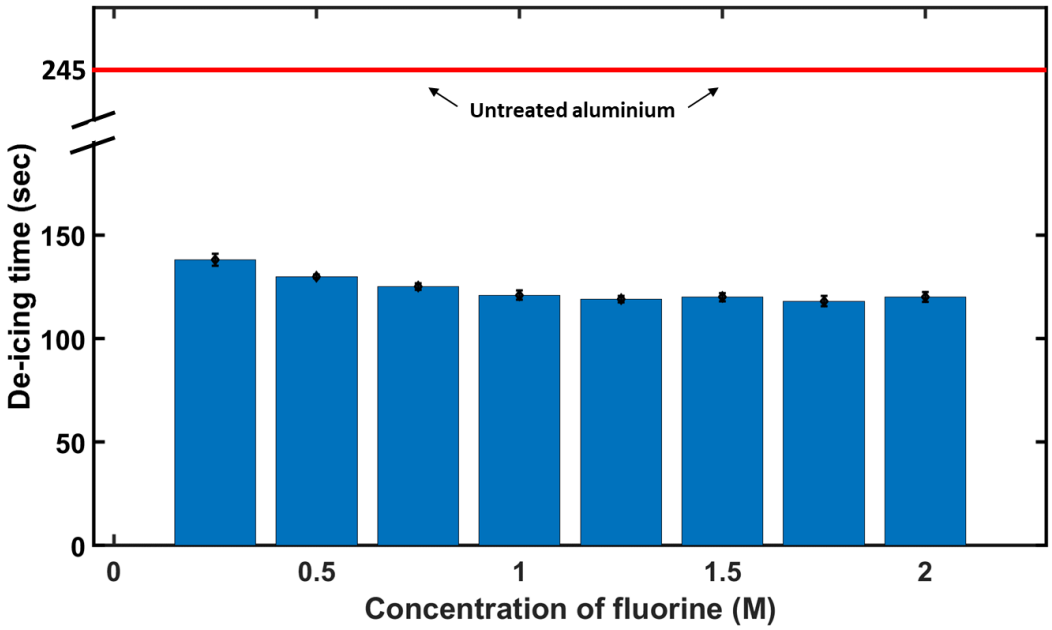


Figure 6-25. Variation of de-icing time for nanoparticle deposited samples coated with a PFA emulsion containing 1:1 molar ratio of styrene, acrylic acid and various concentrations of heptafluorobutyl acrylate with surface roughness ranging 40 to 50 nm.

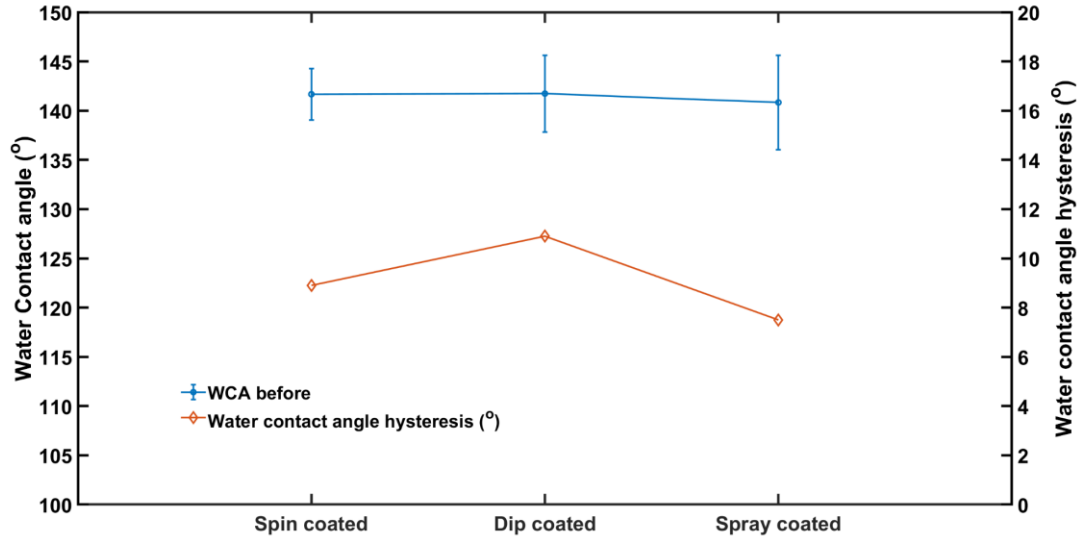
Figure 6-25 shows variation of de-icing time on nanoparticle deposited aluminium substrate as a function of fluorine content in the PFA emulsion. The surface roughness was maintained between 40 to 50 nm. The concentration of fluorine varied between 0.25 to 2 M. The concentration of styrene and acrylic acid is maintained constant at 1:1. Initially when the concentration of fluorine is 0.25 M the de-icing time was relatively high 138 s, with increase in fluorine content the de-icing time gradually increases indicating lower ice adhesion strength. When the fluorine content reaches to 1 M the de-icing time becomes 118 s and almost remains constant with further increase in fluorine content in the PFA emulsion.

6.4 Discussion

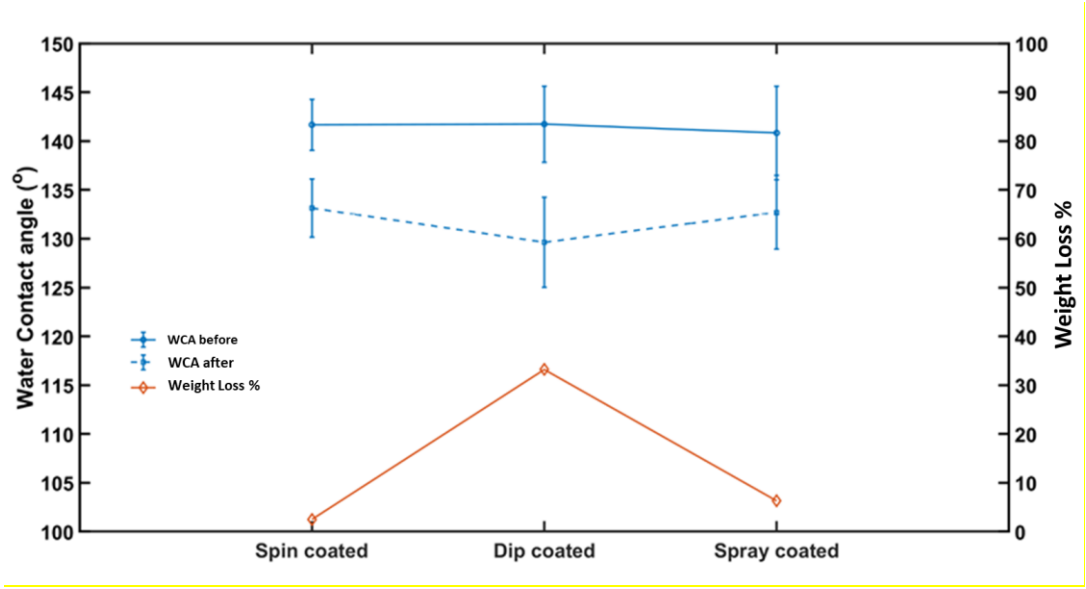
6.4.1 Effect of different coating process

For the deposition of the polymer three different coating methods were used including spin coating, dip coating and spray coating. The details of the coating processes are given in section 3.4.2. A polyfluoroacrylate emulsion containing 1:1:1 molar ratio of styrene, acrylic acid and heptafluorobutyl acrylate was deposited separately on chemically etched aluminium substrates with a surface roughness in the range of 1.7 to 1.9 μm by all three above mentioned methods. The curing temperature, the rate of heating during the curing process and the curing duration all were kept same for all the processes.

The water contact angle (WCA) and contact angle hysteresis (CAH) were measured to compare the surface hydrophobicity. The erosion resistance of the coating and coating adhesion strength were also compared for different coating processes.



(a)



(b)

Figure 6-26. Compared between spin, dip and spray coated aluminium substrates (a) static water contact angle and contact angle hysteresis measurement and (b) contact angle before and after water impinging test and loss in weight for the polymer coating.

Figure 6-26 (a) and (b) shows the comparison of hydrophobicity and erosion resistance of aluminium substrates coated by polyfluoroacrylate emulsion

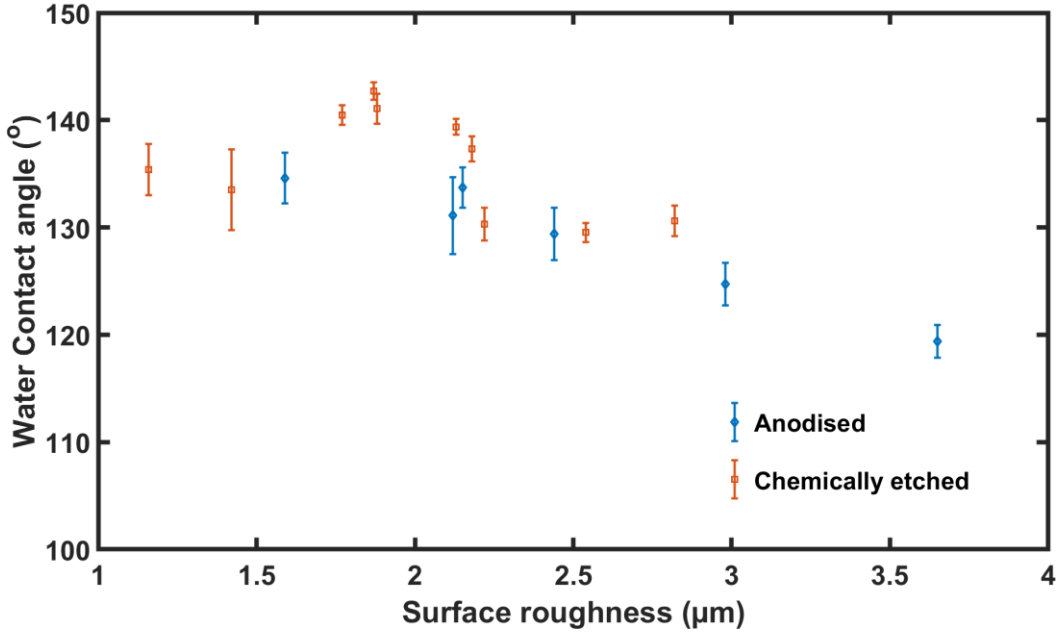
containing 1:1:1 molar ratio of styrene, acrylic acid and heptafluorobutyl acrylic acid by three different coating methods spin, dip and spray. The average surface roughness of the aluminium substrates ranges between 1.7 to 1.8 μm. The surface hydrophobicity for all the surfaces are almost same and average static water contact angle (WCA) is above 140° as shown in Figure 6-26 (a). The contact angle hysteresis (CAH) measurement shows the value is almost same for spray and spin coating process 7-8° but the CAH value is slightly higher for dip coated substrate ~11° indicating the water droplet has higher adhesion strength on the dip coated aluminium substrate.

After water impinging tests the WCA values are measured along with change in weight of the coating. It is observed that the surface remains hydrophobic although the WCA decreases in each case after the impinging test. In the case of dip coated aluminium the WCA decreases from 141.73 to 129.63°, for the spin and spray coated substrates the WCA decreases from 141.67 to 133.13° and 140.83 to 132.7° respectively. The loss in weight of the coating is 332 mg which is much higher for dip coated coating sample while weight loss for spin and spray coated coating sample are 25 and 63 mg only. So for dip coating the erosion resistance is not as high as the other two kinds of coatings as loss in weight is higher.

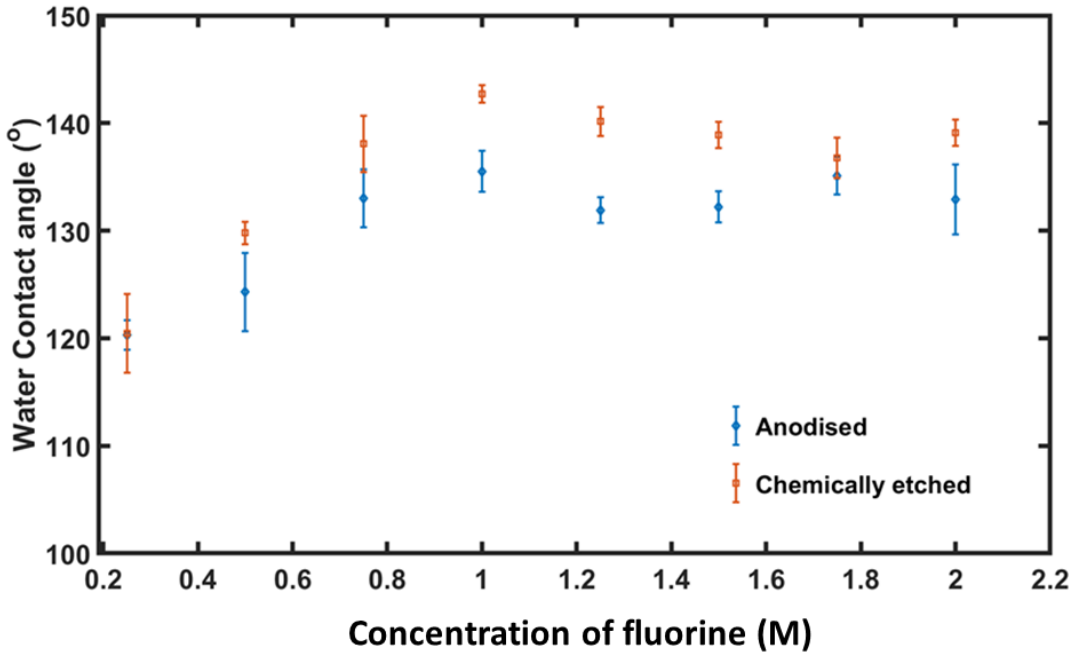
6.4.2 Comparison of hydrophobicity of different surfaces

Surface hydrophobicity is evaluated using static water contact angle (WCA) and contact angle hysteresis (CAH) measurement. The influence of surface roughness and content of fluorine on the surface hydrophobicity is shown in section 6.2. It is observed that both the components influences the surface hydrophobicity as well as adhesion strength of the water droplet on the substrate surface. In the case of anodised substrates the surface roughness value ranges from 1.5 to 7 μm while that for chemical etching varies between 1 to 3 μm depending on anodisation and etching conditions. When the surface roughness is beyond 3 μm the contact angle

drastically drops and hence not included in the comparison studies. In both cases concentration of fluorine has no substantial effect on WCA when the molar ratio of heptafluorobutyl acrylate goes beyond 3 so that the molar ratio is kept at 1.



(a)

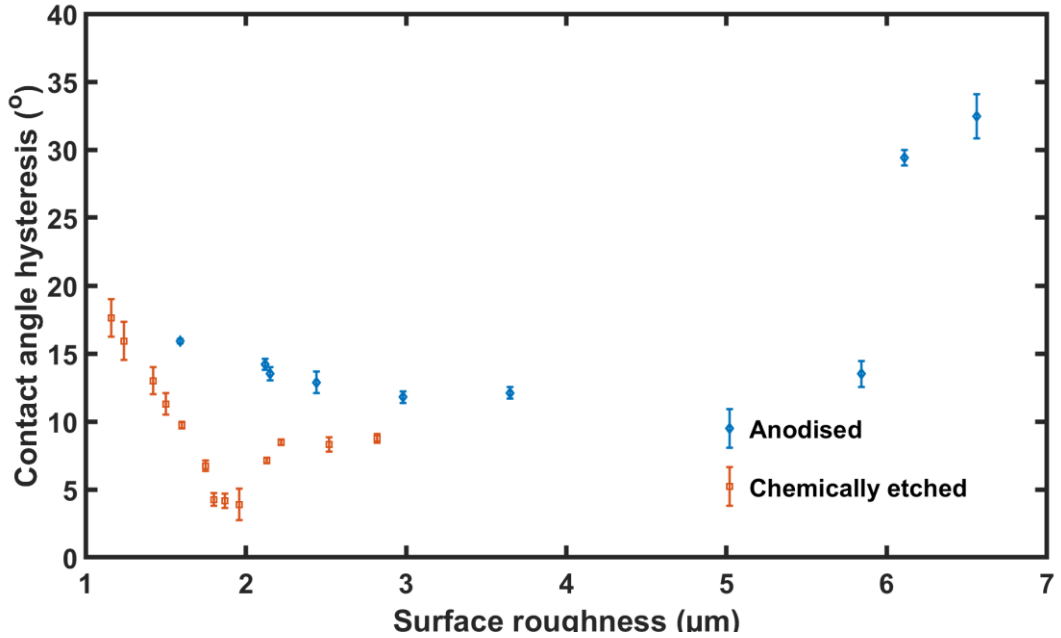


(b)

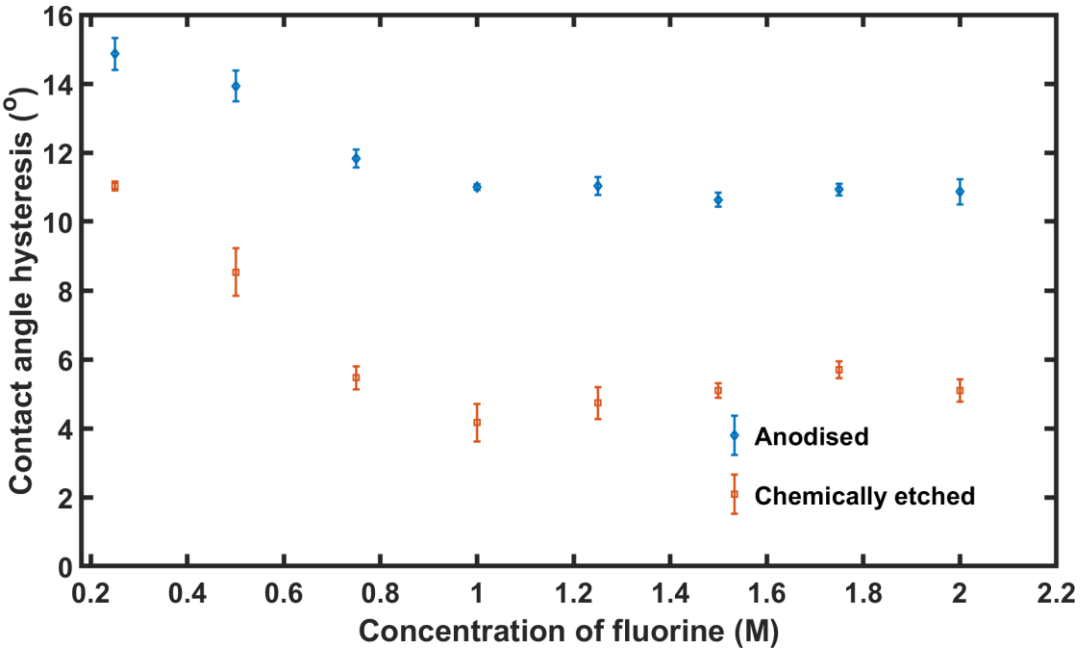
Figure 6-27. Comparison of static water contact angle for anodised and chemically etched aluminium substrates (a) with variation of surface roughness and (b) with variation of concentration of fluorine in the deposited PFA emulsion.

Figure 6-27 (a) shows the comparison of static water contact angle value for anodised and chemical etched modified surfaces with a surface roughness ranging

between 0 to 4 μm and coated with a polyfluoroacrylate emulsion containing 1:1:1 molar ratio of styrene, acrylic acid and heptafluorobutyl acrylate. It is observed that average water contact angle is higher for chemically etched aluminium substartes as compared to anodised substrates for similar surface roughness. The surface roughness for chemically etched samples ranges between 1 to 2.8 μm while average surface roughness for anodised samples are higher and ranges between 1.6 to 3.7 μm. The surface roughness for etched samples are relatively uniform and hence the water contact angles are relatively higher. For anodisied samples the cavities are larger and surface roughness is not uniform throughout and hence the water droplets and get into the cavities decreasing the water contact angle. Similarly when the concentration of fluorine increased from 0.25 M to 2 M in the PFA emulsion the water contact angle gradually increases until reaches 1 M concentration and then becomes almost constant with further increase in fluorine content as shown in Figure 6-27 (b). As before for the same concentration of fluorine in the PFA emulsion the water contact angle is slightly higher for the etched samples as the surface is uniform and average surface roughness is slightly lower than the anodised samples.



(a)



(b)

Figure 6-28. Comparison of water contact angle hysteresis for anodised and chemical etched aluminium substrates (a) with variation of surface roughness and (b) with variation of concentration of fluorine in the deposited PFA emulsion.

Figure 6-28 (a) and (b) shows comparison of contact angle hysteresis of anodised and chemically etched samples as variation of surface roughness and concentration of fluorine in the PFA emulsion. The surface roughness range varies from 1 to 3 μm for etched samples and goes upto 7 μm for anodised sample. It is clear that the average CAH is lower for etched sample than anodised samples for same surface roughness. As described for the variation of water contact angle, anodised sample surfaces are not totally uniform throughout and cavities are bigger in size and hence water droplet goes inside the cavities and hard to remove so higher CAH. This is also consistent with the fact that for anodised samples when the surface roughness is high ~ 6.5 μm the CAH value reaches to 35° indicating the water droplet anchors to the surface cavities as shown in Figure 6-28 (a). When the concentration of fluorine in the PFA emulsion was changed and deposited on the anodised and etched substarte surface the CAH value also varies. For anodised samples the roughness value ranged between 1.75 to 2 μm and that for etched samples ranged between 1.8-1.9 μm. The CAH for etched samples are below 10° indicating that water droplet can easily be removed from the surface, the CAH value for anodised samples higher than 10° but below 16°. Though the average CAH value of anodised samples are higher than etched samples but still the droplets can relatively easy to remove. In both the cases low value of CAH is obtained when the concentration of fluorine in PFA emulsion is 1 M. beyond 1 M concentration the CAH value almost remains same.

6.4.3 Comparison of icephobicity of different surfaces

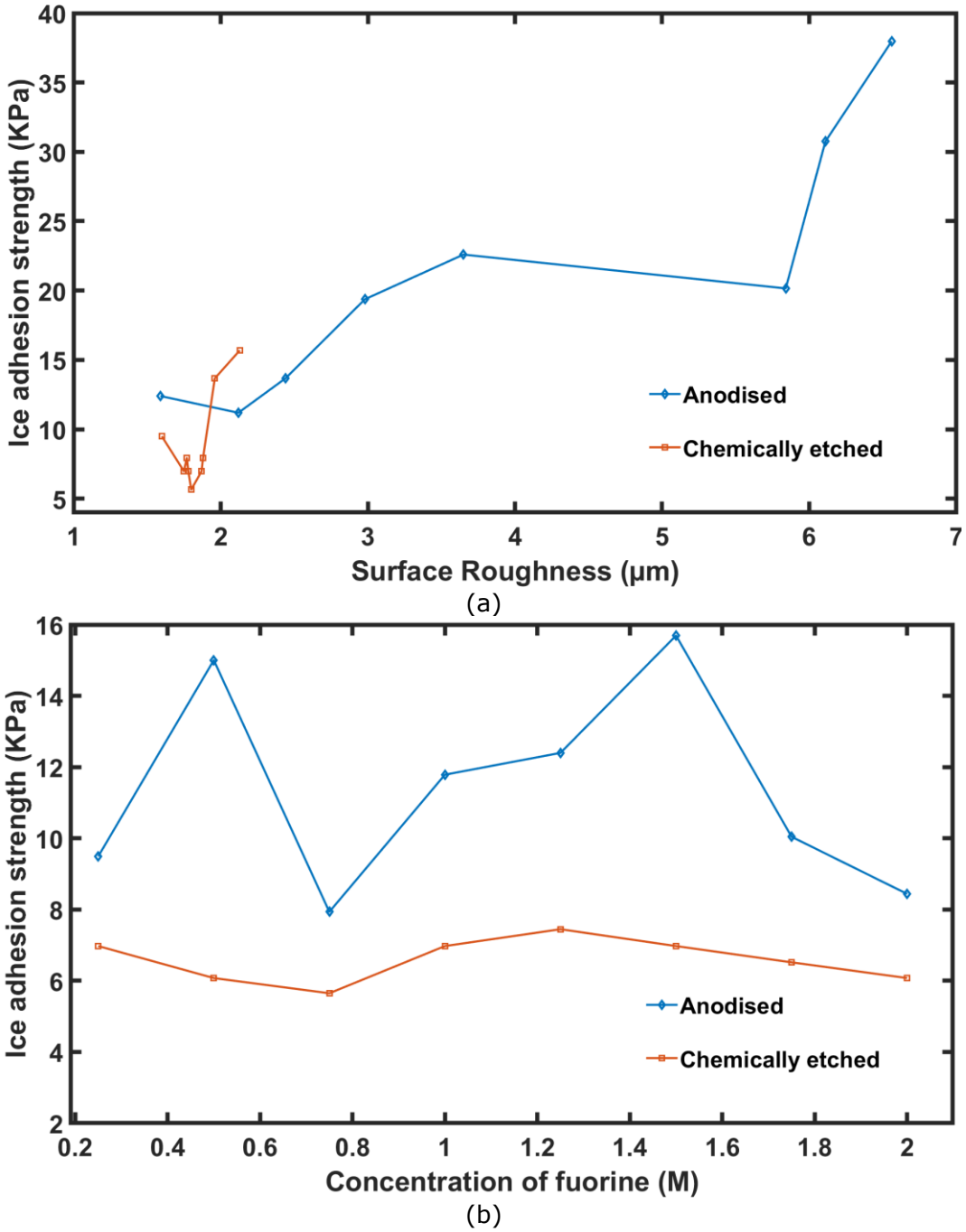
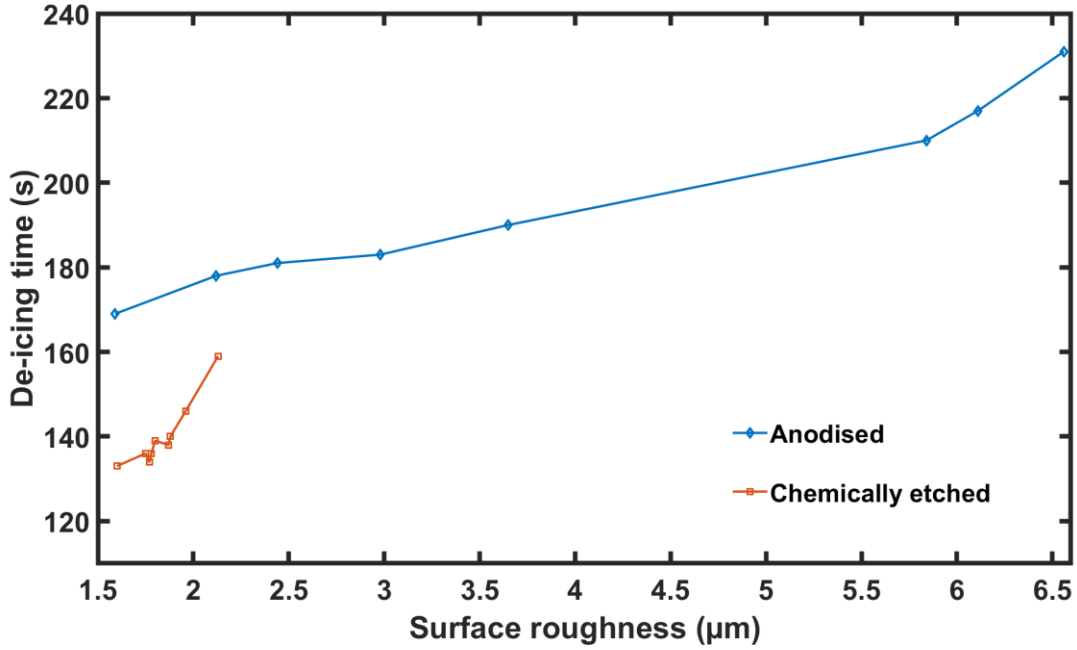


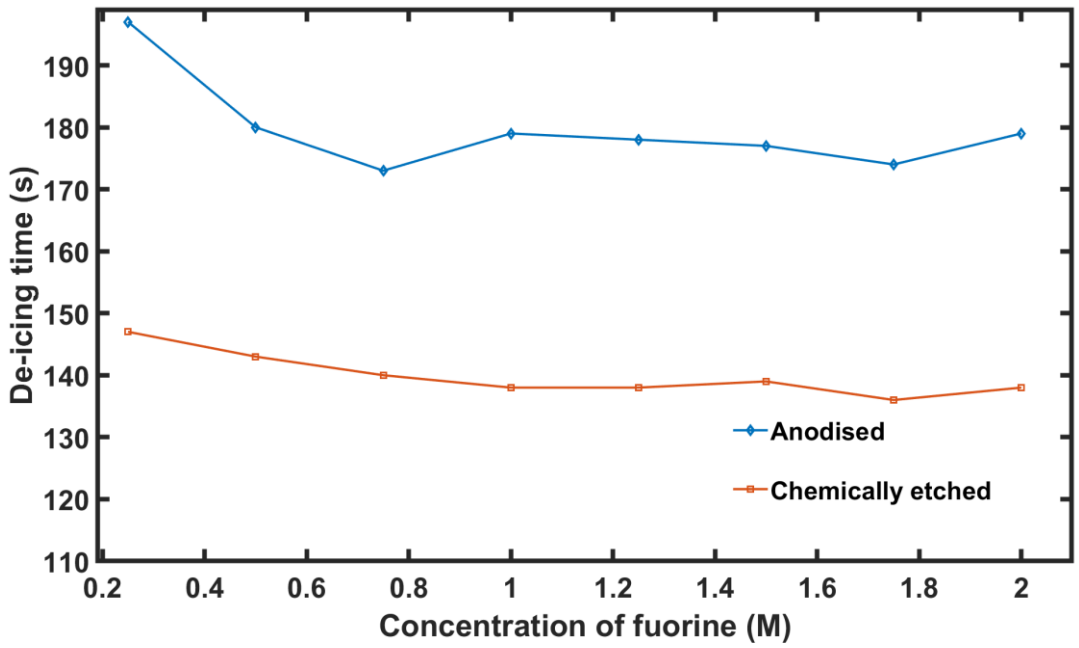
Figure 6-29. Comparison of Ice adhesion strength for anodised and chemically etched aluminium substrates (a) with variation in surface roughness and (b) with variation in fluorine content in the PFA emulsion.

Figure 6-29 (a) shows the comparison of ice adhesion strength of anodised and chemically etched samples with surface roughness. The PFA emulsion was kept

same in all the cases containing 1:1:1 molar ratio of styrene, acrylic acid and heptafluorobutyl acrylate. The surface roughness of anodised samples ranges from 1.5 to 7 μm with slight alteration of anodising conditions, so its crucial to maintain precise anodising conditions. Alternatively the surface roughness for etched samples are in the range of 1.5 to 2.2 μm with different etching conditions and much easier to control. It is noticed that for same surface roughness below 2 μm the ice adhesion strength of etched samples are lower than the anodised samples and below 10 KPa. As discussed in the previous cases for anodised samples the surface roughness is not uniform throughout For anodised samples the ice adhesion strength value is always above 10 KPa which increases gradually with increase in surface roughness indicating that the ice is anchoring inside the large cavities of the anodised sample surface hence harder to remove from the surface and greater ice adhesion strength. Effect on concentration of fluorine in the PFA emulsion also effects the ice adhesion strength as shown in Figure 6-29 (b). The concentration of fluorine varied between 0.25 to 2.5 M, the ice adhesion strength for chemically etched samples ranges between 6 to 8 KPa and that for anodised samples varied between 7 to 16 KPa. The surface roughness range for anodised samples is broad 1.6 to 1.8 μm resulting broad range in ice adhesion strength as well. The surface roughness for chemically etched samples ranges between 1.5 to 1.6 μm. As ice adhesion strength dependent on both surface roughness and surface energy thus a wide range of values obtained. But overall the ice adhesion strength value for anodised samples is higher than etched samples due to the fact that in the later the surface is more uniform than the former.



(a)



(b)

Figure 6-30. Comparison of de-icing time for anodised and chemically etched aluminium substrates (a) with variation in surface roughness and (b) with variation in fluorine content in the PFA emulsion.

Figure 6-30 (a) and (b) shows the variation of de-icing times for anodised and chemically etched samples with variation of surface roughness and fluorine content in the PFA emulsion respectively. The surface roughness for anodised samples ranges between 1.5 to 7 μm and that for chemically etched samples ranges

between 1.5 to 2.2 μm. The de-icing time for pure aluminium samples without any coating or surface treatment was found at 240 s. At lower surface roughness both for the anodised substrates and chemically etched surface the de-icing time decreased significantly. For the same surface roughness the de-icing time for chemically etched samples are still lower 130 to 160 s as compared to anodised samples 170 -180 s. For chemically etched samples the average decrease in de-icing time is ~38 % while that for anodised samples is ~ 27 % at low surface range. For anodised samples with the increase in surface roughness the de-icing time gradually increases as shown in Figure 6-30 (a) and when the surface roughness goes in the range of 6.5 to 7 μm the de-icing time becomes comparable to that of uncoated and untreated substarte. At high surface roughness the cavities on the surface become large and the ice can mechanically interlock inside the cavities required high energy and time to remove the ice. The concentration of fluorine in the PFA emulsion has minimal effect on de-icing time for chemically etched samples with the de-icing time ranging between 135 to 150 s as shown in Figure 6-30 (b). For anodised samples the de-icing time initially decreases from 200 to 180 s when the concentration of fluorine in PFA emulsion increases from 0.25 M to 0.5 M, after that the de-icing time almost becomes constant ranging between 170 to 180 s. During the de-icing experiment electricity was passed through the substrate which in turn produces heat and thus the ice detaches from the surface. In case of all the coated samples a very thin layer of PFA emulsion was deposited on the surface and thus doesn't effect the thermal conduction of the substrates, so the fluorine content has insignificant effect on the de-icing time.

6.5 Summary

Water contact angle and contact angle hysteresis measurements were performed to determine the hydrophobicity of the coating surface. Ice adhesion test and de-icing time test were carried out to study the icephobicity of the surface. Three

different processes spin, spray and dip coating were used to coat the samples and corresponding results were compared. The hydrophobity and icephobicity were also compared for anodised and chemically etched surfaces.

Samples coated with spin coating , dip coating and spray coating processes shows almost similar water contact angle (WCA) but for dip coating process the contact angle hysteresis value is a bit higher than other two processes indicating more adhesion of water on the substrate surface. The water contact angle results after the water impinging test also shows greater decrease in WCA value than the other two processes. Due to the simplicity and feasibility spin coating process was used for further samples. For dip coating process, the substrates were dipped in the PFA emulsion mixture and dried, and the process was continued for 3 times, so the successive polymer layers were not directly attached to the substrate rather than the previous polymer layer and hence could be removed easily. The coating thickness is in the range of 1-2 μm in each case.

As described before the WCA value is highly dependent on surface roughness as well as surface energy. Since in all the cases thin PFA polymer coating is used hence the surface energy is same, the only variation is for surface roughness and hence different WCA and CAH values. The PFA emulsion was of low surface energy and hence high water contact angle values were obtained. Comparison of coatings on anodised and chemical etched surface shows lower WCA and higher CAH for etched samples as compared to anodised samples. For anodised samples, the coating surface roughness is not uniform throughout, at some places it has large cavities and hence the water molecules have more interaction on the substrate surface. Also the average coating surface roughness on etched surface is low as compared to that on anodised surface, hence less tendency for water to go inside the cavities. For chemically etched samples, the coating surface roughness is uniform throughout and hence higher WCA and lower CAH are obtained as

compared to anodised samples. Nanoaprticle deposited substrates show higher WCA and low CAH as compared to both anodised and chemically etched surface. For nanoparticle deposited surface the surface roughness is in nanometer range unlike anodised and etched surface where the surface roughness is in micrometer range hence no large cavities for water to deposit.

Ice adhesion strength of the PFA coatings shows that anodised samples have the highest ice adhesion strength while nanoparticle deposited samples have the least. Due to high surface roughness value of the anodised substrate surface the ice can get attached to the surface cavities and get attached strongly by mechanical interlocking. The process is less for chemically etched process since not many large cavities are present and almost absent for nanoparticle deposited samples since the surface roughness is in the nanometer range. Again the de-icing time is also the lowest for nanoparticle deposited surface, due to the presence of Cu-nanoparticles which facilitates the thermal conduction through the coating layer, and thus reducing the de-icing time significantly offering better energy efficiency.

7 Conclusions

The research work in this project is primarily focused on (i) synthesis of a low surface energy polymer by a simple one-step polymerisation method with low curing temeparature, (ii) producing micro/nanoscale surface roughness on aluminium substrate, (iii) depositing the low surface energy polymer on the modified aluminium surface for hydrophobic and icephobic applications.

Styrene based low surface energy polymer was synthesized by a one-step polymerisation method. Acrylic acid and hepatfluorobutylacrylate were used with styerene as monomer units. The detailed study of the synthesis mechanism shows that the synthesis goes via random radical polymerization. The number of monomer units in a polymer chain cannot be precisely predicted. NMR and FTIR study confirms the inclusion of each monomer unit in the polymer chain. The curing temperature of the synthesized PFA emulsion was found around 80 °C. TGA and DSC analysis indicates the thermal stability of the polymer upto 300 °C. The average surface energy of the PFA emulsion was 19 N/m while that of conventionally used PTFE is 21 N/m, so slightly lower surface energy obtained. Tensile test was used to measure the ultimate tensile strength of the PFA polymer and it was found to be comparable to that of PTFE and that is ~ 35 MPa. The polymer was found to be thermoset in nature and hence once cured cannot be melted again.

Anodisation, chemical etching and Cu-nanoparticle deposition processes were used to obtain micro and nanoscale surface morphology on the aluminium surface. For anodisation and chemical etching, microscale surface roughness was obtained, and nanoscale surface roughness observed on Cu-nanoparticle deposited surface. For the anodisation process, temperature plays an important role on surface roughness and hence the range of surface roughness was quite broad (0-7 μm). When the anodisation temperature was controlled below 10 °C, the surface roughness

maintained below 2 μm. For chemical etching process, the process parameters also plays a key role and the average surface roughnes was below 2 μm. The Cu-nanoparticle deposition produces nanoscale surface roughness, and the roughness value averages between 20-50 nm, depending on the concentration of the Cu-nanoparticles. The SEM images show that the most uniform surface morphology was obtained on the chemically etched aluminium surfaces. For anodised samples, due to the variation of current density and temperature, the surface roughness is not uniform. The Cu-nanoparcticle deposited surfaces seem to have the most non uniform surface morphology, as the Cu-nanoparticles tend to aggromelate in the solution. The effect of temperature, current and time on surface morphology and surface roughness were observed and compared for anodising process. The effect of concentration of etching solution, etching time and temperature was also studied for chemically etched substrates. For nanoparticle deposited surfaces, the effect of concentration of nanoparticles and curing temperature was determined. The PFA coatings were deposited on the substrate surface by spin coating method and the final surface roughness was also evaluated. Erosion resistance of the coating was investigated via water impinging test and it was observed that nanoparticle deposited surfaces has the lowest erosion resistance due to the poor adhesion of the nanparticles on the substrate surface.

Finally, the hydrophobicity of the substrate surface was studied using water contact angle and icephobicity of the surface was evaluated by ice adhesion test. De-icing time value on the coating surface was studied via thermal de-icing method which determined the energy efficieny of the coating as compared to uncoated surface. It was observed that the hydrophobicity was quite consistent on chemically etched and Cu-nanoparticle deposited surfaces. For the anodised coated samples, the surface hydrophobicity varied due to the variation of the surface roughness. With increase in surface roughness the hydrophobicity decreases gradually as the water molecules may go inside the large cavities on the surface, increasing the contact

area of the water droplet on the surface. For the same reason, anodised samples showed higher ice adhesion strength as compared to the etched and nanoparticle deposited surfaces. The water droplet reached inside the cavities and freezed thus anchoring on the substrate surface by mechanical interlocking. Hence it was hard to remove the ice from the substrate surface and higher ice adhesion strength occured. For Cu-nanoparticle deposited and chemically etched surface, since the surface roughness was not as high as the anodised surfaces, lower ice adhesion strength was obtained. Average ice adhesion strength for chemically etched and Cu-nanoparticle deposited surfaces were below 10 KPa. Thermal de-icing test showed high energy efficiency for Cu-nanoparticle deposited coatings as compared to those for the anodised and etched surfaces. As the anodised and etched surfaces are not conductive hence higher energy (heat) required to remove the ice from the substrate surface and hence lower efficiency. Due to incorporation of Cu-nanoparticles in the coating, the thermal conductivity of the coating increases, lowering the de-icing time and increasing energy efficiency.

The thin film PFA coating can potentially be used for aerospace and turbine industries, where icing problems are great challenges. The synthesised PFA coating has significant lower processing temperature (80 °C) as compared to commercially available PTFE (400 °C). The ice adhesion strength of the synthesised polymer is comparable to that of PTFE . The polymer can also be used for high temperature application upto (300 °C). The performance of the polymer coatings can be enhanced by tailoring the proper surface morphology. Incoporation of nanoparticle can significantly reduce the de-icing time and provide better energy efficiency.

The future work related to the main theme of this project aims to further enhance the icephobicity, hydrophobicity and durability of the coating. Durability of the coating may be enhanced by increasing the adhesion of the coating on the substrate surface. It is evident from this study that PFA coating on Cu-nanoparticle

deposited substrate may potentially be used as icephobic coating as it can potentially decrease the ice adhesion strength, and also the energy efficiency for de-icing process increases substantially as compared to uncoated substrates. The only drawback is that the coating adhesion strength is not enough as it can easily be damaged during water impinging test. The adhesion of the Cu-nanoparticle can be increased by incorporating a primer layer, and modifying the synthesised polymer. More test required to evaluate the erosion resistance of the coating with certain icing and de-icing cycles. Also the coating can be incorporated with self-healing property, which can significantly increase the lifecycle of the coating and its application for aircraft and other infrastructure applications.

References

1. Boinovich, L.B., Emelyanenko, A.M., Ivanov, V.K. and Pashinin, A.S., *Durable Icephobic Coating for Stainless Steel.* ACS Applied Materials & Interfaces, 2013. **5**(7): p. 2549-2554.

2. Menini, R., Ghalmi, Z. and Farzaneh, M., *Highly resistant icephobic coatings on aluminum alloys.* Cold Regions Science and Technology, 2011. **65**(1): p. 65-69.

3. Zhang, P. and Lv, F.Y., *A review of the recent advances in superhydrophobic surfaces and the emerging energy-related applications.* Energy, 2015. **82**: p. 1068-1087.

4. Zhang, X., Shi, F., Niu, J., Jiang, Y. and Wang, Z., *Superhydrophobic surfaces: from structural control to functional application.* Journal of Materials Chemistry, 2008. **18**(6): p. 621-633.

5. Brassard, J.-D., Sarkar, D.K. and Perron, J., *Synthesis of Monodisperse Fluorinated Silica Nanoparticles and Their Superhydrophobic Thin Films.* ACS Applied Materials & Interfaces, 2011. **3**(9): p. 3583-3588.

6. Feng, L., Li, S., Li, Y., Li, H., Zhang, L., Zhai, J., Song, Y., Liu, B., Jiang, L. and Zhu, D., *Super‐hydrophobic surfaces: from natural to artificial.* Advanced materials, 2002. **14**(24): p. 1857-1860.

7. Wolfs, M., Darmanin, T. and Guittard, F., *Superhydrophobic fibrous polymers.* Polymer Reviews, 2013. **53**(3): p. 460-505.

8. Koch, K. and Barthlott, W., *Superhydrophobic and superhydrophilic plant surfaces: an inspiration for biomimetic materials.* Philosophical Transactions of the Royal Society A: Mathematical, Physical and Engineering Sciences, 2009. **367**(1893): p. 1487-1509.

9. Gao, X. and Jiang, L., *Biophysics: water-repellent legs of water striders.* Nature, 2004. **432**(7013): p. 36.

10. Otten, A. and Herminghaus, S., *How plants keep dry: a physicist's point of view.* Langmuir, 2004. **20**(6): p. 2405-2408.

11. Menini, R. and Farzaneh, M., *Elaboration of Al2O3/PTFE icephobic coatings for protecting aluminum surfaces.* Surface and Coatings Technology, 2009. **203**(14): p. 1941-1946.

12. Kim, P., Wong, T.-S., Alvarenga, J., Kreder, M.J., Adorno-Martinez, W.E. and Aizenberg, J., *Liquid-infused nanostructured surfaces with extreme anti-ice and anti-frost performance.* ACS nano, 2012. **6**(8): p. 6569-6577.

13. Guo, P., Zheng, Y., Wen, M., Song, C., Lin, Y. and Jiang, L., *Icephobic/anti‐icing properties of micro/nanostructured surfaces.* Advanced materials, 2012. **24**(19): p. 2642-2648.

14. Jung, S., Tiwari, M.K., Doan, N.V. and Poulikakos, D., *Mechanism of supercooled droplet freezing on surfaces.* Nature communications, 2012. **3**: p. 615.

15. Zheng, L., Li, Z., Bourdo, S., Khedir, K.R., Asar, M.P., Ryerson, C.C. and Biris, A.S., *Exceptional superhydrophobicity and low velocity impact icephobicity of acetone-functionalized carbon nanotube films.* Langmuir, 2011. **27**(16): p. 9936-9943.

16. Pike, W.S., *Extreme warm frontal icing on 25 February 1994 causes an aircraft accident near Uttoxeter.* Meteorological Applications, 1995. **2**(3): p. 273-279.

17. Marwitz, J., Poiitovich, M., Bernstein, B., Ralph, F., Neiman, P., Ashenden, R. and Bresch, J., *Meteorological conditions associated with the ATR72 aircraft accident near Roselawn, Indiana, on 31 October 1994.* Bulletin of the American Meteorological Society, 1997. **78**(1): p. 41-52.

18. Coffman, H.J., *Helicopter Rotor Icing Protection Methods.* Journal of the American Helicopter Society, 1987. **32**(2): p. 34-39.

19. Itagaki, K., *Mechanical Ice Release Processes: I. Self-shedding from high-speed rotors*. Vol. 83. 1983: Cold Regions Research and Engineering Laboratory.

20. Hejazi, V., Sobolev, K. and Nosonovsky, M., *From superhydrophobicity to icephobicity: forces and interaction analysis.* Scientific Reports, 2013. **3**: p. 2194.

21. Zhang, H.Y., Yang, Y.L., Pan, J.F., Long, H., Huang, L.S. and Zhang, X.K., *Compare study between icephobicity and superhydrophobicity.* Physica B: Condensed Matter, 2019. **556**: p. 118-130.

22. Wang, Y., Xue, J., Wang, Q., Chen, Q. and Ding, J., *Verification of Icephobic/Anti-icing Properties of a Superhydrophobic Surface.* ACS Applied Materials & Interfaces, 2013. **5**(8): p. 3370-3381.

23. Jung, S., Dorrestijn, M., Raps, D., Das, A., Megaridis, C.M. and Poulikakos, D., *Are Superhydrophobic Surfaces Best for Icephobicity?* Langmuir, 2011. **27**(6): p. 3059-3066.

24. Farhadi, S., Farzaneh, M. and Kulinich, S.A., *Anti-icing performance of superhydrophobic surfaces.* Applied Surface Science, 2011. **257**(14): p. 6264-6269.

25. Cao, L., Jones, A.K., Sikka, V.K., Wu, J. and Gao, D., *Anti-Icing Superhydrophobic Coatings.* Langmuir, 2009. **25**(21): p. 12444-12448.

26. Momen, G. and Farzaneh, M., *Simple process to fabricate a superhydrophobic coating.* Micro & Nano Letters, 2011. **6**(6): p. 405-407.

27. Jafari, R., Menini, R. and Farzaneh, M., *Superhydrophobic and icephobic surfaces prepared by RF-sputtered polytetrafluoroethylene coatings.* Applied Surface Science, 2010. **257**(5): p. 1540-1543.

28. Zhao, Y., Li, J., Hu, J. and Grzybowski, S. *Icing performances of super-hydrophobic PDMS/Nano-silica hybrid coating on insulators*. in *2010 International Conference on High Voltage Engineering and Application*. 2010. IEEE.

29. He, M., Wang, J., Li, H., Jin, X., Wang, J., Liu, B. and Song, Y., *Super-hydrophobic film retards frost formation.* Soft Matter, 2010. **6**(11): p. 2396-2399.

30. Mishchenko, L., Hatton, B., Bahadur, V., Taylor, J.A., Krupenkin, T. and Aizenberg, J., *Design of ice-free nanostructured surfaces based on repulsion of impacting water droplets.* ACS nano, 2010. **4**(12): p. 7699-7707.

31. Heinz, A., Haszler, A., Keidel, C., Moldenhauer, S., Benedictus, R. and Miller, W.S., *Recent development in aluminium alloys for aerospace applications.* Materials Science and Engineering: A, 2000. **280**(1): p. 102-107.

32. Moutarlier, V., Gigandet, M.P., Pagetti, J. and Ricq, L., *Molybdate/sulfuric acid anodising of 2024-aluminium alloy: influence of inhibitor concentration on film growth and on corrosion resistance.* Surface and Coatings Technology, 2003. **173**(1): p. 87-95.

33. Zhang, J.-s., Zhao, X.-h., Zuo, Y. and Xiong, J.-p., *The bonding strength and corrosion resistance of aluminum alloy by anodizing treatment in a phosphoric acid modified boric acid/sulfuric acid bath.* Surface and Coatings Technology, 2008. **202**(14): p. 3149-3156.

34. Wang, H., Xue, Y., Ding, J., Feng, L., Wang, X. and Lin, T., *Durable, Self-Healing Superhydrophobic and Superoleophobic Surfaces from Fluorinated-Decyl Polyhedral Oligomeric Silsesquioxane and Hydrolyzed Fluorinated Alkyl Silane.* Angewandte Chemie International Edition, 2011. **50**(48): p. 11433-11436.

35. Zhou, H., Wang, H., Niu, H., Gestos, A., Wang, X. and Lin, T., *Fluoroalkyl Silane Modified Silicone Rubber/Nanoparticle Composite: A Super Durable, Robust Superhydrophobic Fabric Coating.* Advanced Materials, 2012. **24**(18): p. 2409-2412.

36. Woodward, I., Schofield, W.C.E., Roucoules, V. and Badyal, J.P.S., *Super-hydrophobic Surfaces Produced by Plasma Fluorination of Polybutadiene Films.* Langmuir, 2003. **19**(8): p. 3432-3438.

37. Verma, G., Kaushik, A. and Ghosh, A.K., *Comparative assessment of nano-morphology and properties of spray coated clear polyurethane coatings reinforced with different organoclays.* Progress in Organic Coatings, 2013. **76**(7): p. 1046-1056.

38. West, J.O.F., Critchlow, G.W., Lake, D.R. and Banks, R., *Development of a superhydrophobic polyurethane-based coating from a two-step plasma-fluoroalkyl silane treatment.* International Journal of Adhesion and Adhesives, 2016. **68**: p. 195-204.

39. Liu, J., Wang, J., Memon, H., Fu, Y., Barman, T., Choi, K.-S. and Hou, X., *Hydrophobic/icephobic coatings based on thermal sprayed metallic layers with subsequent surface functionalization.* Surface and Coatings Technology, 2019. **357**: p. 267-272.

40. Ozbay, S., Yuceel, C. and Erbil, H.Y., *Improved Icephobic Properties on Surfaces with a Hydrophilic Lubricating Liquid.* ACS Applied Materials & Interfaces, 2015. **7**(39): p. 22067-22077.

41. Fu, Q., Wu, X., Kumar, D., Ho, J.W.C., Kanhere, P.D., Srikanth, N., Liu, E., Wilson, P. and Chen, Z., *Development of Sol–Gel Icephobic Coatings: Effect of Surface Roughness and Surface Energy.* ACS Applied Materials & Interfaces, 2014. **6**(23): p. 20685-20692.

42. Petrenko, V.F. and Peng, S., *Reduction of ice adhesion to metal by using self-assembling monolayers (SAMs).* Canadian Journal of Physics, 2003. **81**(1-2): p. 387-393.

43. Sarkar, D.K., Farzaneh, M. and Paynter, R.W., *Superhydrophobic properties of ultrathin rf-sputtered Teflon films coated etched aluminum surfaces.* Materials Letters, 2008. **62**(8–9): p. 1226-1229.

44. Su, X., Li, H., Lai, X., Zhang, L., Liang, T., Feng, Y. and Zeng, X., *Polydimethylsiloxane-Based Superhydrophobic Surfaces on Steel Substrate: Fabrication, Reversibly Extreme Wettability and Oil–Water Separation.* ACS Applied Materials & Interfaces, 2017. **9**(3): p. 3131-3141.

45. Gerard, M., Bowen, C.R. and Osman, F.H., *Processing and properties of PTFE-FEP-PTFE ferroelectret Films.* Ferroelectrics, 2011. **422**(1): p. 59-64.

46. Law, K.-Y., *Definitions for Hydrophilicity, Hydrophobicity, and Superhydrophobicity: Getting the Basics Right.* The Journal of Physical Chemistry Letters, 2014. **5**(4): p. 686-688.

47. Song, J. and Rojas, O.J., *Approaching super-hydrophobicity from cellulosic materials: A Review.* Nord. Pulp Pap. Res. J, 2013. **28**(2): p. 216-238.

48. Yuan, Y. and Lee, T.R., *Contact angle and wetting properties*, in *Surface science techniques*. 2013, Springer. p. 3-34.

49. Choi, W., Tuteja, A., Mabry, J.M., Cohen, R.E. and McKinley, G.H., *A modified Cassie–Baxter relationship to explain contact angle hysteresis and anisotropy on non-wetting textured surfaces.* Journal of Colloid and Interface Science, 2009. **339**(1): p. 208-216.

50. Han, T.-Y., Shr, J.-F., Wu, C.-F. and Hsieh, C.-T., *A modified Wenzel model for hydrophobic behavior of nanostructured surfaces.* Thin Solid Films, 2007. **515**(11): p. 4666-4669.

51. Extrand, C.W., *Contact Angles and Hysteresis on Surfaces with Chemically Heterogeneous Islands.* Langmuir, 2003. **19**(9): p. 3793-3796.

52. Chen, W., Fadeev, A.Y., Hsieh, M.C., Öner, D., Youngblood, J. and McCarthy, T.J., *Ultrahydrophobic and Ultralyophobic Surfaces: Some Comments and Examples.* Langmuir, 1999. **15**(10): p. 3395-3399.

53. Akram Raza, M., Kooij, E.S., van Silfhout, A. and Poelsema, B., *Superhydrophobic Surfaces by Anomalous Fluoroalkylsilane Self-Assembly on Silica Nanosphere Arrays.* Langmuir, 2010. **26**(15): p. 12962-12972.

54. Ono, S., Saito, M. and Asoh, H., *Self-ordering of anodic porous alumina formed in organic acid electrolytes.* Electrochimica Acta, 2005. **51**(5): p. 827-833.

55. Zhang, F., Zhao, L., Chen, H., Xu, S., Evans, D.G. and Duan, X., *Corrosion resistance of superhydrophobic layered double hydroxide films on aluminum.* Angewandte Chemie, 2008. **120**(13): p. 2500-2503.

56. Liu, T., Yin, Y., Chen, S., Chang, X. and Cheng, S., *Super-hydrophobic surfaces improve corrosion resistance of copper in seawater.* Electrochimica Acta, 2007. **52**(11): p. 3709-3713.

57. Xu, W., Song, J., Sun, J., Lu, Y. and Yu, Z., *Rapid Fabrication of Large-Area, Corrosion-Resistant Superhydrophobic Mg Alloy Surfaces.* ACS Applied Materials & Interfaces, 2011. **3**(11): p. 4404-4414.

58. Mates, J.E., Bayer, I.S., Palumbo, J.M., Carroll, P.J. and Megaridis, C.M., *Extremely stretchable and conductive water-repellent coatings for low-cost ultra-flexible electronics.* Nature communications, 2015. **6**: p. 8874.

59. Samuel, J.D.J.S., Ruther, P., Frerichs, H.P., Lehmann, M., Paul, O. and Rühe, J., *A simple route towards the reduction of surface conductivity in gas sensor devices.* Sensors and Actuators B: Chemical, 2005. **110**(2): p. 218-224.

60. Zimmermann, J., Reifler, F.A., Fortunato, G., Gerhardt, L.-C. and Seeger, S., *A Simple, One-Step Approach to Durable and Robust Superhydrophobic Textiles.* Advanced Functional Materials, 2008. **18**(22): p. 3662-3669.

61. Xue, C.-H., Chen, J., Yin, W., Jia, S.-T. and Ma, J.-Z., *Superhydrophobic conductive textiles with antibacterial property by coating fibers with silver nanoparticles.* Applied Surface Science, 2012. **258**(7): p. 2468-2472.

62. Chesnokova, M.G., Shalaj, V.V., Kraus, J.A. and Mironov, A.J., *Assessment of Soil Biocorrosion Severeness on the Pipeline Locations.* Procedia Engineering, 2015. **113**: p. 57-61.

63. Bagihalli, G.B., Avaji, P.G., Patil, S.A. and Badami, P.S., *Synthesis, spectral characterization, in vitro antibacterial, antifungal and cytotoxic activities of Co(II), Ni(II) and Cu(II) complexes with 1,2,4-triazole Schiff bases.* European Journal of Medicinal Chemistry, 2008. **43**(12): p. 2639-2649.

64. Ayliffe, G.A.J., Collins, B.J., Lowbury, E.J.L., Babb, J.R. and Lilly, H.A., *Ward floors and other surfaces as reservoirs of hospital infection.* Epidemiology and Infection, 2009. **65**(4): p. 515-536.

65. Islander, R.L., Devinny, J.S., Mansfeld, F., Postyn, A. and Shih, H., *Microbial Ecology of Crown Corrosion in Sewers.* Journal of Environmental Engineering, 1991. **117**(6): p. 751-770.

66. Shateri Khalil-Abad, M. and Yazdanshenas, M.E., *Superhydrophobic antibacterial cotton textiles.* Journal of Colloid and Interface Science, 2010. **351**(1): p. 293-298.

67. Chung, J.-S., Kim, B.G., Shim, S., Kim, S.-E., Sohn, E.-H., Yoon, J. and Lee, J.-C., *Silver-perfluorodecanethiolate complexes having superhydrophobic, antifouling, antibacterial properties.* Journal of Colloid and Interface Science, 2012. **366**(1): p. 64-69.

68. Privett, B.J., Youn, J., Hong, S.A., Lee, J., Han, J., Shin, J.H. and Schoenfisch, M.H., *Antibacterial Fluorinated Silica Colloid Superhydrophobic Surfaces.* Langmuir, 2011. **27**(15): p. 9597-9601.

69. Tang, P., Zhang, W., Wang, Y., Zhang, B., Wang, H., Lin, C. and Zhang, L., *Effect of Superhydrophobic Surface of Titanium on Staphylococcus aureus Adhesion.* Journal of Nanomaterials, 2011. **2011**: p. 8.

70. Ozkan, E., Crick, C.C., Taylor, A., Allan, E. and Parkin, I.P., *Copper-based water repellent and antibacterial coatings by aerosol assisted chemical vapour deposition.* Chemical Science, 2016. **7**(8): p. 5126-5131.

71. Hwang, G.B., Page, K., Patir, A., Nair, S.P., Allan, E. and Parkin, I.P., *The Anti-Biofouling Properties of Superhydrophobic Surfaces are Short-Lived.* ACS Nano, 2018. **12**(6): p. 6050-6058.

72. Song, X., Zhai, J., Wang, Y. and Jiang, L., *Fabrication of Superhydrophobic Surfaces by Self-Assembly and Their Water-Adhesion Properties.* The Journal of Physical Chemistry B, 2005. **109**(9): p. 4048-4052.

73. Mahadevan, L. and Pomeau, Y., *Rolling droplets.* Physics of Fluids, 1999. **11**(9): p. 2449-2453.

74. Feng, L., Li, S., Li, Y., Li, H., Zhang, L., Zhai, J., Song, Y., Liu, B., Jiang, L. and Zhu, D., *Super-Hydrophobic Surfaces: From Natural to Artificial.* Advanced Materials, 2002. **14**(24): p. 1857-1860.

75. Zhang, X., Shi, F., Yu, X., Liu, H., Fu, Y., Wang, Z., Jiang, L. and Li, X., *Polyelectrolyte Multilayer as Matrix for Electrochemical Deposition of Gold Clusters: Toward Super-Hydrophobic Surface.* Journal of the American Chemical Society, 2004. **126**(10): p. 3064-3065.

76. Iroh, J.O. and Mark, J., *Polymer data handbook*. 1999, Oxford University Press, New York.

77. Macleod, H. and Filters, T.-F.O., *American Elsevier Publishing Company.* Inc., New York, New York, pp. ix-x, 1969: p. 37-42.

78. Tahk, D., Kim, T.-i., Yoon, H., Choi, M., Shin, K. and Suh, K.Y., *Fabrication of antireflection and antifogging polymer sheet by partial photopolymerization and dry etching.* Langmuir, 2010. **26**(4): p. 2240-2243.

79. Wang, S.-D. and Shu, Y.-Y., *Superhydrophobic antireflective coating with high transmittance.* Journal of Coatings Technology and Research, 2013. **10**(4): p. 527-535.

80. Ko, J., Gong, D., Pillai, K., Lee, K.-S., Ju, M., Choi, P., Kim, K.-R., Yi, J. and Choi, B., *Double layer SiNx: H films for passivation and anti-reflection coating of c-Si solar cells.* Thin solid films, 2011. **519**(20): p. 6887-6891.

81. Jeong, S., McDowell, M.T. and Cui, Y., *Low-temperature self-catalytic growth of tin oxide nanocones over large areas.* ACS nano, 2011. **5**(7): p. 5800-5807.

82. Xiong, J., Das, S.N., Shin, B., Kar, J.P., Choi, J.H. and Myoung, J.-M., *Biomimetic hierarchical ZnO structure with superhydrophobic and antireflective properties.* Journal of colloid and interface science, 2010. **350**(1): p. 344-347.

83. Soeno, T., Inokuchi, K. and Shiratori, S., *Ultra-water-repellent surface: fabrication of complicated structure of SiO2 nanoparticles by electrostatic self-assembled films.* Applied Surface Science, 2004. **237**(1-4): p. 539-543.

84. Bravo, J., Zhai, L., Wu, Z., Cohen, R.E. and Rubner, M.F., *Transparent superhydrophobic films based on silica nanoparticles.* Langmuir, 2007. **23**(13): p. 7293-7298.

85. Tarwal, N. and Patil, P., *Superhydrophobic and transparent ZnO thin films synthesized by spray pyrolysis technique.* Applied surface science, 2010. **256**(24): p. 7451-7456.

86. Li, G., Wang, B., Liu, Y., Tan, T., Song, X. and Yan, H., *Fabrication of superhydrophobic ZnO/Zn surface with nanowires and nanobelts structures using novel plasma assisted thermal vapor deposition.* Applied Surface Science, 2008. **255**(5): p. 3112-3116.

87. Yang, J., Zhang, Z., Men, X. and Xu, X., *Fabrication of stable, transparent and superhydrophobic nanocomposite films with polystyrene functionalized carbon nanotubes.* Applied surface science, 2009. **255**(22): p. 9244-9247.

88. Meng, L.-Y. and Park, S.-J., *Effect of fluorination of carbon nanotubes on superhydrophobic properties of fluoro-based films.* Journal of colloid and interface science, 2010. **342**(2): p. 559-563.

89. Li, G.-X., Liu, Y., Wang, B., Song, X.-M., Li, E. and Yan, H., *Preparation of transparent BN films with superhydrophobic surface.* Applied Surface Science, 2008. **254**(17): p. 5299-5303.

90. Deng, X., Mammen, L., Zhao, Y., Lellig, P., Müllen, K., Li, C., Butt, H.J. and Vollmer, D., *Transparent, thermally stable and mechanically robust superhydrophobic surfaces made from porous silica capsules.* Advanced materials, 2011. **23**(26): p. 2962-2965.

91. Latthe, S.S., Imai, H., Ganesan, V., Kappenstein, C. and Rao, A.V., *Optically transparent superhydrophobic TEOS-derived silica films by surface silylation method.* Journal of sol-gel science and technology, 2010. **53**(2): p. 208-215.

92. Nakajima, A., Hashimoto, K., Watanabe, T., Takai, K., Yamauchi, G. and Fujishima, A., *Transparent superhydrophobic thin films with self-cleaning properties.* Langmuir, 2000. **16**(17): p. 7044-7047.

93. Wang, S.-D. and Shu, Y.-Y., *Superhydrophobic antireflective coating with high transmittance*. Vol. 10. 2013.

94. Meuler, A.J., McKinley, G.H. and Cohen, R.E., *Exploiting Topographical Texture To Impart Icephobicity.* ACS Nano, 2010. **4**(12): p. 7048-7052.

95. Laforte, C., Blackburn, C. and Perron, J., *A review of icephobic coating performances over the last decade*. 2015, SAE Technical Paper.

96. Ruan, M., Li, W., Wang, B., Deng, B., Ma, F. and Yu, Z., *Preparation and Anti-icing Behavior of Superhydrophobic Surfaces on Aluminum Alloy Substrates.* Langmuir, 2013. **29**(27): p. 8482-8491.

97. Shen, Y., Tao, J., Tao, H., Chen, S., Pan, L. and Wang, T., *Superhydrophobic Ti 6 Al 4 V surfaces with regular array patterns for anti-icing applications.* RSC Advances, 2015. **5**(41): p. 32813-32818.

98. Varanasi, K.K., Deng, T., Smith, J.D., Hsu, M. and Bhate, N., *Frost formation and ice adhesion on superhydrophobic surfaces.* Applied Physics Letters, 2010. **97**(23): p. 234102.

99. Li, K., Xu, S., Shi, W., He, M., Li, H., Li, S., Zhou, X., Wang, J. and Song, Y., *Investigating the Effects of Solid Surfaces on Ice Nucleation.* Langmuir, 2012. **28**(29): p. 10749-10754.

100. He, M., Li, H., Wang, J. and Song, Y., *Superhydrophobic surface at low surface temperature.* Applied Physics Letters, 2011. **98**(9): p. 093118.

101. He, M., Zhou, X., Zeng, X., Cui, D., Zhang, Q., Chen, J., Li, H., Wang, J., Cao, Z. and Song, Y., *Hierarchically structured porous aluminum surfaces for high-efficient removal of condensed water.* Soft Matter, 2012. **8**(25): p. 6680-6683.

102. Sexton, B.A., *Vibrational spectra of water chemisorbed on platinum (111).* Surface Science, 1980. **94**(2-3): p. 435-445.

103. Starke, U., Materer, N., Wander, A., Van Hove, M.A. and Somorjai, G.A., *Low-energy electron diffraction study of a disordered monolayer of H20 on Pt(111) and an ordered thin film of ice grown on Pt(111).* Journal of Vacuum Science and Technology A: Vacuum, Surfaces and Films, 1992. **10**(4): p. 2521-2528.

104. Firment, L.E. and Somorjai, G.A., *Low-energy electron diffraction studies of molecular crystals: The surface structures of vapor-grown ice and naphthalene.* The Journal of Chemical Physics, 1975. **63**(2): p. 1037-1038.

105. Thiel, P.A. and Madey, T.E., *The interaction of water with solid surfaces: Fundamental aspects.* Surface Science Reports, 1987. **7**(6-8): p. 211-385.

106. Fletcher, N., *Size effect in heterogeneous nucleation.* The Journal of chemical physics, 1958. **29**(3): p. 572-576.

107. Farzaneh, M., *Atmospheric icing of power networks*. 2008: Springer Science & Business Media.

108. Nosonovsky, M. and Hejazi, V., *Why Superhydrophobic Surfaces Are Not Always Icephobic.* ACS Nano, 2012. **6**(10): p. 8488-8491.

109. Dalili, N., Edrisy, A. and Carriveau, R., *A review of surface engineering issues critical to wind turbine performance.* Renewable and Sustainable Energy Reviews, 2009. **13**(2): p. 428-438.

110. Seifert, H. *Technical requirements for rotor blades operating in cold climate*. in *VI BOREAS Conference, Pyhatunturi, Finland*. 2003.

111. Anderson, D.N. and Reich, A.D., *Tests of the performance of coatings for low ice adhesion*. 1997: National Aeronautics and Space Administration.

112. Jelle, B.P., Gao, T., Mofid, S.A., Kolås, T., Stenstad, P.M. and Ng, S., *Avoiding Snow and Ice Formation on Exterior Solar Cell Surfaces – A Review of Research Pathways and Opportunities.* Procedia Engineering, 2016. **145**: p. 699-706.

113. Lin, Y., Chen, H., Wang, G. and Liu, A., *Recent progress in preparation and anti-icing applications of superhydrophobic coatings.* Coatings, 2018. **8**(6): p. 208.

114. Plummer, D.M., Göke, S., Rauber, R.M. and Di Girolamo, L., *Discrimination of Mixed- versus Ice-Phase Clouds Using Dual-Polarization Radar with Application to Detection of Aircraft Icing Regions.* Journal of Applied Meteorology and Climatology, 2009. **49**(5): p. 920-936.

115. Laakso, T. and Peltola, E., *Review on blade heating technology and future prospects.* BOREAS VII, Saariselka, Finland, 2005.

116. Hochart, C., Fortin, G., Perron, J. and Ilinca, A., *Wind turbine performance under icing conditions.* Wind Energy: An International Journal for Progress and Applications in Wind Power Conversion Technology, 2008. **11**(4): p. 319-333.

117. Biswas, S. and Vijayan, K., *Friction and wear of PTFE—a review.* Wear, 1992. **158**(1-2): p. 193-211.

118. Volat, C., Farzaneh, M. and Leblond, A., *De-icing/Anti-icing Techniques for Power Lines: Current Methods and Future Direction*. 2005.

119. Vasilyev, G.P., Leskov, V.A., Mitrofanova, N.V., Gornov, V.F., Kolesova, M.V., Esaulov, G.V. and Tabunshchikov, Y.A., *Technical Solution for Protection of Heat Pump Evaporators Against Freezing the Moisture Condensed.* MATEC Web of Conferences, 2016. **40**: p. 05002.

120. Yan, W.-M., Li, H.-Y., Wu, Y.-J., Lin, J.-Y. and Chang, W.-R., *Performance of finned tube heat exchangers operating under frosting conditions.* International Journal of Heat and Mass Transfer, 2003. **46**(5): p. 871-877.

121. Liu, D., Zhao, F.-Y. and Tang, G.-F., *Frosting of heat pump with heat recovery facility.* Renewable Energy, 2007. **32**(7): p. 1228-1242.

122. Chen, Y., Lu, P., Shen, C. and Zhang, Q., *Experimental study on frost formation on a cold surface in low atmospheric pressure.* Applied Thermal Engineering, 2015. **90**: p. 86-93.

123. Rahman, M.A. and Jacobi, A.M., *Condensation, Frost Formation, and Frost Melt-Water Retention Characteristics on Microgrooved Brass Surfaces Under Natural Convection.* Heat Transfer Engineering, 2013. **34**(14): p. 1147-1155.

124. Song, M., Deng, S., Dang, C., Mao, N. and Wang, Z., *Review on improvement for air source heat pump units during frosting and defrosting.* Applied Energy, 2018. **211**: p. 1150-1170.

125. Joppolo, C.M., Molinaroli, L., De Antonellis, S. and Merlo, U., *Experimental analysis of frost formation with the presence of an electric field on fin and tube evaporator.* International Journal of Refrigeration, 2012. **35**(2): p. 468-474.

126. Gou, Y., Liu, Z., Liu, Y., Huang, L. and Zhang, M., *The study of frost formation under magnetic field.* Journal of Engineering Thermophysics, 2009. **30**(3): p. 465-467.

127. Wang, D., Tao, T., Xu, G., Luo, A. and Kang, S., *Experimental study on frosting suppression for a finned-tube evaporator using ultrasonic vibration.* Experimental Thermal and Fluid Science, 2012. **36**: p. 1-11.

128. Wang, Z.-J., Kwon, D.-J., Lawrence DeVries, K. and Park, J.-M., *Frost formation and anti-icing performance of a hydrophobic coating on aluminum.* Experimental Thermal and Fluid Science, 2015. **60**: p. 132-137.

129. Sojoudi, H., Wang, M., Boscher, N., McKinley, G.H. and Gleason, K.K., *Durable and scalable icephobic surfaces: similarities and distinctions from superhydrophobic surfaces.* Soft matter, 2016. **12**(7): p. 1938-1963.

130. Dotan, A., Dodiuk, H., Laforte, C. and Kenig, S., *The Relationship between Water Wetting and Ice Adhesion.* Journal of Adhesion Science and Technology, 2009. **23**(15): p. 1907-1915.

131. Nosonovsky, M. and Bhushan, B., *Phase behavior of capillary bridges: towards nanoscale water phase diagram.* Physical Chemistry Chemical Physics, 2008. **10**(16): p. 2137-2144.

132. Yang, S.H., Nosonovsky, M., Zhang, H. and Chung, K.-H., *Nanoscale water capillary bridges under deeply negative pressure.* Chemical Physics Letters, 2008. **451**(1): p. 88-92.

133. Nosonovsky, M., *Slippery when wetted.* Nature, 2011. **477**: p. 412.

134. Stone, H.A., *Ice-Phobic Surfaces That Are Wet.* ACS Nano, 2012. **6**(8): p. 6536-6540.

135. Tang, Y., Zhang, Q., Zhan, X. and Chen, F., *Superhydrophobic and anti-icing properties at overcooled temperature of a fluorinated hybrid surface prepared via a sol–gel process.* Soft Matter, 2015. **11**(22): p. 4540-4550.

136. Wang, L., Gong, Q., Zhan, S., Jiang, L. and Zheng, Y., *Robust Anti-Icing Performance of a Flexible Superhydrophobic Surface.* Advanced Materials, 2016. **28**(35): p. 7729-7735.

137. Shen, Y., Wang, G., Tao, J., Zhu, C., Liu, S., Jin, M., Xie, Y. and Chen, Z., *Anti-Icing Performance of Superhydrophobic Texture Surfaces Depending on Reference Environments.* Advanced Materials Interfaces, 2017. **4**(22): p. 1700836.

138. Rezayi, T. and Entezari, M.H., *Toward a durable superhydrophobic aluminum surface by etching and ZnO nanoparticle deposition.* Journal of Colloid and Interface Science, 2016. **463**: p. 37-45.

139. Feng, L., Zhang, H., Wang, Z. and Liu, Y., *Superhydrophobic aluminum alloy surface: Fabrication, structure, and corrosion resistance.* Colloids and Surfaces A: Physicochemical and Engineering Aspects, 2014. **441**: p. 319-325.

140. Huang, Y., Sarkar, D.K. and Grant Chen, X., *Superhydrophobic aluminum alloy surfaces prepared by chemical etching process and their corrosion resistance properties.* Applied Surface Science, 2015. **356**: p. 1012-1024.

141. Sarkar, D.K., Zhou, X.J., Tannous, A. and Leung, K.T., *Growth Mechanisms of Copper Nanocrystals on Thin Polypyrrole Films by Electrochemistry.* The Journal of Physical Chemistry B, 2003. **107**(13): p. 2879-2881.

142. Nakajima, A., Fujishima, A., Hashimoto, K. and Watanabe, T., *Preparation of transparent superhydrophobic boehmite and silica films by sublimation of aluminum acetylacetonate.* Advanced Materials, 1999. **11**(16): p. 1365-1368.

143. Guo, Z., Zhou, F., Hao, J. and Liu, W., *Stable Biomimetic Super-Hydrophobic Engineering Materials.* Journal of the American Chemical Society, 2005. **127**(45): p. 15670-15671.

144. Sarkar, D.K. and Farzaneh, M., *Fabrication of PECVD-grown fluorinated hydrocarbon nanoparticles and circular nanoring arrays using nanosphere lithography.* Applied Surface Science, 2008. **254**(13): p. 3758-3761.

145. Saleema, N., Sarkar, D.K., Paynter, R.W. and Chen, X.G., *Superhydrophobic Aluminum Alloy Surfaces by a Novel One-Step Process.* ACS Applied Materials & Interfaces, 2010. **2**(9): p. 2500-2502.

146. Thünemann, A.F., Lieske, A. and Paulke, B.-R., *Low Surface Energy Coatings from Waterborne Nano-Dispersions of Polymer Complexes.* Advanced Materials, 1999. **11**(4): p. 321-324.

147. Marouani, S., *Investigation of the resistance welding of multilayers aluminum-coated polymer complexes used as envelopes of vacuum insulation panels.* Materials & Design (1980-2015), 2012. **36**: p. 546-556.

148. CS, N.S.a.H. *Hydrophobic and superhydrophobic Organic-Inorganic Hybrids and their Applications*. 2014. **1**, DOI: 07.07.2014.

149. Yao, W., Li, Y. and Huang, X., *Fluorinated poly(meth)acrylate: Synthesis and properties.* Polymer, 2014. **55**(24): p. 6197-6211.

150. Thomas, R.R., Anton, D.R., Graham, W.F., Darmon, M.J., Sauer, B.B., Stika, K.M. and Swartzfager, D.G., *Preparation and Surface Properties of Acrylic Polymers Containing Fluorinated Monomers.* Macromolecules, 1997. **30**(10): p. 2883-2890.

151. Domercq, B., Hreha, R.D., Zhang, Y.-D., Larribeau, N., Haddock, J.N., Schultz, C., Marder, S.R. and Kippelen, B., *Photo-Patternable Hole-Transport Polymers for Organic Light-Emitting Diodes.* Chemistry of Materials, 2003. **15**(7): p. 1491-1496.

152. Basu, B.J. and Dinesh Kumar, V., *Fabrication of Superhydrophobic Nanocomposite Coatings Using Polytetrafluoroethylene and Silica Nanoparticles.* ISRN Nanotechnology, 2011. **2011**: p. 6.

153. Wu, R., Liang, S., Liu, J., Pan, A., Yu, Y. and Tang, Y., *Fabrication of the micro/nano-structure superhydrophobic surface on aluminum alloy by sulfuric acid anodizing and polypropylene coating.* Journal of nanoscience and nanotechnology, 2013. **13**(3): p. 2362-2368.

154. Xie, Q., Fan, G., Zhao, N., Guo, X., Xu, J., Dong, J., Zhang, L. and Zhang, Y., *Facile Creation of a Bionic Super-Hydrophobic Block Copolymer Surface.* Advanced materials, 2004. **16**(20): p. 1830-1833.

155. Woodward, I., Schofield, W., Roucoules, V. and Badyal, J., *Super-hydrophobic surfaces produced by plasma fluorination of polybutadiene films.* Langmuir, 2003. **19**(8): p. 3432-3438.

156. Hancer, M. and Arkaz, H., *A facile fabrication of superhydrophobic nanocomposite coating with contact angles approaching the theoretical limit.* Applied Surface Science, 2015. **354, Part B**: p. 342-346.

157. Liu, S., Liu, X., Latthe, S.S., Gao, L., An, S., Yoon, S.S., Liu, B. and Xing, R., *Self-cleaning transparent superhydrophobic coatings through simple sol–gel processing of fluoroalkylsilane.* Applied Surface Science, 2015. **351**: p. 897-903.

158. Qian, B. and Shen, Z., *Fabrication of Superhydrophobic Surfaces by Dislocation-Selective Chemical Etching on Aluminum, Copper, and Zinc Substrates.* Langmuir, 2005. **21**(20): p. 9007-9009.

159. Arnold, J.C., *6.06 - Environmental Effects on Crack Growth in Polymers*, in *Comprehensive Structural Integrity*, I. Milne, R.O. Ritchie, and B. Karihaloo, Editors. 2003, Pergamon: Oxford. p. 281-319.

160. Matyjaszewski, K., Gaynor, S.G. and Müller, A.H.E., *Preparation of Hyperbranched Polyacrylates by Atom Transfer Radical Polymerization. 2. Kinetics and Mechanism of Chain Growth for the Self-Condensing Vinyl Polymerization of 2-((2-Bromopropionyl)oxy)ethyl Acrylate.* Macromolecules, 1997. **30**(23): p. 7034-7041.

161. Zheng, Y., Li, S., Weng, Z. and Gao, C., *Hyperbranched polymers: advances from synthesis to applications.* Chemical Society Reviews, 2015. **44**(12): p. 4091-4130.

162. Hawker, C.J. and Piotti, M.E., *Nitroxide-mediated Free Radical Polymerization*, in *Encyclopedia of Materials: Science and Technology*, K.H.J. Buschow, et al., Editors. 2001, Elsevier: Oxford. p. 6164-6177.

163. Riley, A., *12 - Basics of polymer chemistry for packaging materials*, in *Packaging Technology*, A. Emblem and H. Emblem, Editors. 2012, Woodhead Publishing. p. 262-286.

164. Corradini, P., Barone, V., Fusco, R. and Guerra, G., *Analysis of models for the Ziegler-Natta stereospecific polymerization on the basis of non-bonded interactions at the catalytic site—I. The Cossee model.* European Polymer Journal, 1979. **15**(12): p. 1133-1141.

165. Wang, M., Guo, L. and Sun, H., *Manufacture of Biomaterials*, in *Encyclopedia of Biomedical Engineering*, R. Narayan, Editor. 2019, Elsevier: Oxford. p. 116-134.

166. Padsalgikar, A.D., *3 - Speciality Plastics in Cardiovascular Applications*, in *Plastics in Medical Devices for Cardiovascular Applications*, A.D. Padsalgikar, Editor. 2017, William Andrew Publishing. p. 53-82.

167. Kwon, M.H., Shin, H.S. and Chu, C.N., *Fabrication of a super-hydrophobic surface on metal using laser ablation and electrodeposition.* Applied Surface Science, 2014. **288**: p. 222-228.

168. Hwang, S.-K., Jeong, S.-H., Hwang, H.-Y., Lee, O.-J. and Lee, K.-H., *Fabrication of highly ordered pore array in anodic aluminum oxide.* Korean Journal of Chemical Engineering, 2002. **19**(3): p. 467-473.

169. Aerts, T., Dimogerontakis, T., De Graeve, I., Fransaer, J. and Terryn, H., *Influence of the anodizing temperature on the porosity and the mechanical properties of the porous anodic oxide film.* Surface and Coatings Technology, 2007. **201**(16–17): p. 7310-7317.

170. Chi, C.-S., Lee, J.-H., Kim, I. and Oh, H.-J., *Effects of Microstructure of Aluminum Substrate on Ordered Nanopore Arrays in Anodic Alumina.* Journal of Materials Science & Technology, 2015. **31**(7): p. 751-758.

171. Kikuchi, T., Nakajima, D., Kawashima, J., Natsui, S. and Suzuki, R.O., *Fabrication of anodic porous alumina via anodizing in cyclic oxocarbon acids.* Applied Surface Science, 2014. **313**: p. 276-285.

172. Kikuchi, T., Yamamoto, T. and Suzuki, R.O., *Growth behavior of anodic porous alumina formed in malic acid solution.* Applied Surface Science, 2013. **284**: p. 907-913.

173. Kostov, G., Rousseau, A., Boutevin, B. and Pascal, T., *Novel fluoroacrylated copolymers: synthesis, characterization and properties.* Journal of Fluorine Chemistry, 2005. **126**(2): p. 231-240.

174. Seyfi, J., Jafari, S.H., Khonakdar, H.A., Sadeghi, G.M.M., Zohuri, G., Hejazi, I. and Simon, F., *Fabrication of robust and thermally stable superhydrophobic nanocomposite coatings based on thermoplastic polyurethane and silica nanoparticles.* Applied Surface Science, 2015. **347**: p. 224-230.

175. Manoudis, P.N., Karapanagiotis, I., Tsakalof, A., Zuburtikudis, I. and Panayiotou, C., *Superhydrophobic Composite Films Produced on Various Substrates.* Langmuir, 2008. **24**(19): p. 11225-11232.

176. Ding, X., Zhou, S., Gu, G. and Wu, L., *A facile and large-area fabrication method of superhydrophobic self-cleaning fluorinated polysiloxane/TiO2 nanocomposite coatings with long-term durability.* Journal of Materials Chemistry, 2011. **21**(17): p. 6161-6164.

177. Bolis, V., Busco, C., Ciarletta, M., Distasi, C., Erriquez, J., Fenoglio, I., Livraghi, S. and Morel, S., *Hydrophilic/hydrophobic features of TiO2 nanoparticles as a function of crystal phase, surface area and coating, in relation to their potential toxicity in peripheral nervous system.* Journal of Colloid and Interface Science, 2012. **369**(1): p. 28-39.

178. Soeno, T., Inokuchi, K. and Shiratori, S., *Ultra Water-Repellent Surface Resulting from Complicated Microstructure of SiO~ 2 nano particles.* TRANSACTIONS-MATERIALS RESEARCH SOCIETY OF JAPAN, 2003. **28**(4): p. 1207.

179. Zhai, L., Cebeci, F.Ç., Cohen, R.E. and Rubner, M.F., *Stable Superhydrophobic Coatings from Polyelectrolyte Multilayers.* Nano Letters, 2004. **4**(7): p. 1349-1353.

180. Liu, J., Li, X. and Jiao, S., *A kinetic study on emulsion copolymerization of butyl acrylate and styrene using cationic emulsifier.* Acta Polymerica Sinica, 1995. **4**.

181. Casazza, E., Mariani, A., Ricco, L. and Russo, S., *Synthesis, characterization, and properties of a novel acrylic terpolymer with pendant perfluoropolyether segments.* Polymer, 2002. **43**(4): p. 1207-1214.

182. Yao, L., Yang, T. and Cheng, S., *Study of nano-silica/fluorinated acrylate copolymer hybrid emulsion and the polymerization kinetics.* Acta Polymerica Sinica, 2008. **3**: p. 221.

183. Park, J.-Y. and Shim, J.-J., *Emulsion stability of PMMA particles formed by dispersion polymerization of methyl methacrylate in supercritical carbon dioxide.* The Journal of supercritical fluids, 2003. **27**(3): p. 297-307.

184. Zhang, K., Feng, H., Pan, Z. and LIU, D., *Synthesis and properties of polyacrylate emulsions modified by fluorine-containing emulsion.* JOURNAL-TSINGHUA UNIVERSITY, 2001. **41**(12): p. 50-52.

185. Hore, P., *Nuclear magnetic resonance*. 2015: Oxford University Press, USA.

186. Haasch, R.T., *X-Ray Photoelectron Spectroscopy (XPS) and Auger Electron Spectroscopy (AES)*, in *Practical Materials Characterization*, M. Sardela, Editor. 2014, Springer New York: New York, NY. p. 93-132.

187. Griffiths, P.R. and De Haseth, J.A., *Fourier transform infrared spectrometry*. Vol. 171. 2007: John Wiley & Sons.

188. Thomas, B., *X-Ray Fluorescence Spectroscopy INSTRUMENTATION.* Industrial & Engineering Chemistry, 1954. **46**(3): p. 93A-96A.

189. Packham, D.E., *Surface energy, surface topography and adhesion.* International journal of adhesion and adhesives, 2003. **23**(6): p. 437-448.

190. Janjua, Z.A., Turnbull, B., Choy, K.-L., Pandis, C., Liu, J., Hou, X. and Choi, K.-S., *Performance and durability tests of smart icephobic coatings to reduce ice adhesion.* Applied Surface Science, 2017. **407**: p. 555-564.

191. Zhang, J., Li, J. and Han, Y., *Superhydrophobic PTFE Surfaces by Extension.* Macromolecular Rapid Communications, 2004. **25**(11): p. 1105-1108.

192. Hansen, N.M.L., Jankova, K. and Hvilsted, S., *Fluoropolymer materials and architectures prepared by controlled radical polymerizations.* European Polymer Journal, 2007. **43**(2): p. 255-293.

193. Junyan, L., Ling, H. and Yuansuo, Z., *Synthesis and property investigation of three core-shell fluoroacrylate copolymer latexes.* Journal of Applied Polymer Science, 2009. **112**(3): p. 1615-1621.

194. Han, C.D., *Rheology in polymer processing*. Vol. 4. 1976: Academic press New York.

195. Wessling, R. *The polymerization of xylylene bisdialkyl sulfonium salts*. in *Journal of Polymer Science: Polymer Symposia*. 1985. Wiley Online Library.

196. Biesenberger, J.A. and Sebastian, D.H., *Principles of polymerization engineering*. 1983: Wiley-Interscience.

197. Patrick, C.R., *Thermal Stability of Polytetrafluoroethylene.* Nature, 1958. **181**: p. 698.

198. Tannenbaum, H.P., *Non-stick coating system with PTFE-FEP for concentration gradient*. 1993, Google Patents.

199. Naghash, H., Karimzadeh, A., Momeni, A., Massah, A. and Alian, H., *Preparation and Properties of Triethoxyvinylsilane-Modified Styrene -Butyl Acrylate Emulsion Copolymers*. Vol. 31. 2007.

200. Ayat, M., Belbachir, M. and Rahmouni, A., *Selective Synthesis, Characterization and Kinetics Studies of poly(α-Methyl styrene) induced by Maghnite-Na+ Clay (Algerian MMT)*. Vol. 11. 2016. 376.

201. Ismail, O., Beyribey, B. and Turhan, K., *Removal of Water in Liquid Fuel with a Super Absorbent Copolymer*. Vol. 33. 2011. 1669-1677.

202. Socrates, G., *Infrared and Raman characteristic group frequencies: tables and charts*. 2004: John Wiley & Sons.

203. Pretsch, E., Buehlmann, P., Affolter, C., Pretsch, E., Bhuhlmann, P. and Affolter, C., *Structure determination of organic compounds*. 2000: Springer.

204. Solcà, N. and Dopfer, O., *Protonated benzene: IR spectrum and structure of C6H7+.* Angewandte Chemie International Edition, 2002. **41**(19): p. 3628-3631.

205. Lin-Vien, D., Colthup, N.B., Fateley, W.G. and Grasselli, J.G., *The handbook of infrared and Raman characteristic frequencies of organic molecules*. 1991: Elsevier.

206. Silverstein, R.M. and Bassler, G.C., *Spectrometric identification of organic compounds.* Journal of Chemical Education, 1962. **39**(11): p. 546.

207. Pretsch, E., Clerc, T., Seibl, J. and Simon, W., *Tables of spectral data for structure determination of organic compounds*. 2013: Springer Science & Business Media.

208. Svensson, A., Fex, T. and Kihlberg, J., *Use of 19F NMR spectroscopy to evaluate reactions in solid phase organic synthesis.* Tetrahedron letters, 1996. **37**(42): p. 7649-7652.

209. Gilman, J.W., Jackson, C.L., Morgan, A.B., Harris, R., Manias, E., Giannelis, E.P., Wuthenow, M., Hilton, D. and Phillips, S.H., *Flammability properties of polymer−layered-silicate nanocomposites. Polypropylene and polystyrene nanocomposites.* Chemistry of materials, 2000. **12**(7): p. 1866-1873.

210. Lin, H.-R., *Solution polymerization of acrylamide using potassium persulfate as an initiator: kinetic studies, temperature and pH dependence.* European Polymer Journal, 2001. **37**(7): p. 1507-1510.

211. Kinoshita, K., Takano, Y., Ohkouchi, N. and Deguchi, S., *Free-Radical Polymerization of Acrylic Acid under Extreme Reaction Conditions Mimicking Deep-Sea Hydrothermal Vents.* ACS Omega, 2017. **2**(6): p. 2765-2769.

212. Masayoshi, O. and Toshiyuki, M., *The decomposition of potassium persulphate used as initiator in emulsion polymerization.* Makromolekulare Chemie. Macromolecular Symposia, 1990. **31**(1): p. 143-156.

213. Bornside, D., Macosko, C. and Scriven, L., *MODELING OF SPIN COATING.* Journal of imaging technology, 1987. **13**(4): p. 122-130.

214. Chang, J.-F., Sun, B., Breiby, D.W., Nielsen, M.M., Sölling, T.I., Giles, M., McCulloch, I. and Sirringhaus, H., *Enhanced mobility of poly (3-hexylthiophene) transistors by spin-coating from high-boiling-point solvents.* Chemistry of Materials, 2004. **16**(23): p. 4772-4776.

215. Makower, B. and Bray, W.C., *The rate of oxidation of hydrogen peroxide by chlorine in the presence of hydrochloric acid.* Journal of the American Chemical Society, 1933. **55**(12): p. 4765-4776.

216. Castner, D.G., Grainger, D.W., Pellerite, M. and Anton, D., *Fluorinated surfaces, coatings, and films*. 2001: ACS Publications.

217. de Gennes, P.-G., Brochard-Wyart, F. and Quere, D., *Capillarity and Wetting Phenomena: Drops.* Bubbles, Pearls, Waves, 2004. **291**.

218. Gao, L. and McCarthy, T.J., *The "Lotus Effect" Explained: Two Reasons Why Two Length Scales of Topography Are Important.* Langmuir, 2006. **22**(7): p. 2966-2967.

219. Patankar, N.A., *Mimicking the Lotus Effect: Influence of Double Roughness Structures and Slender Pillars.* Langmuir, 2004. **20**(19): p. 8209-8213.

220. Brandon, S., Haimovich, N., Yeger, E. and Marmur, A., *Partial wetting of chemically patterned surfaces: The effect of drop size.* Journal of Colloid and Interface Science, 2003. **263**(1): p. 237-243.

221. Xu, Y. and Liu, M., *Soiling and corrosion behaviors on fluorinated anodized TiO2 surface infused by perfluoropolyether.* Surface and Coatings Technology, 2016. **307**: p. 332-344.